Extraction of the CP Violating Angle ϕ_3 using $B^- \to DK^-$ decay at Belle

and

Determination of the CP content of $D \to h^-h^+\pi^0 (h = \pi/K)$ at CLEO-c

A THESIS
submitted by

Minakshi Nayak

for the award of the degree
of

DOCTOR OF PHILOSOPHY

DEPARTMENT OF PHYSICS
INDIAN INSTITUTE OF TECHNOLOGY
MADRAS
October 2014

THESIS CERTIFICATE

This is to certify that the thesis titled **Extraction of the CP Violating Angle ϕ_3 using $B^- \to DK^-$ decay at Belle and Determination of the CP content of $D \to h^-h^+\pi^0(h = \pi/K)$ at CLEO-c**, submitted by **Minakshi Nayak**, to the Indian Institute of Technology, Madras, for the award of the degree of **Doctor of Philosophy**, is a bona fide record of the research work done by her under my supervision. The contents of this thesis, in full or in parts, have not been submitted to any other Institute or University for the award of the degree.

Dr. James Frederick Libby
Research Guide
Associate Professor
Dept. of Physics
IIT-Madras, 600 036
Place: Chennai
Date: 20th October 2014

ACKNOWLEDGEMENTS

I express my deep gratitude to my supervisor, Dr. Jim Libby for providing me the opportunity to work in Experimental High Energy Physics at Belle and CLEO-c. I am sincerely thankful to him for his constant guidance, encouragement and support from the beginning of my PhD, the time when I did not have any idea to work in data analysis. I appreciate his resourceful ideas due to which I did not feel pain of PhD. I feel lucky to have him as my supervisor.

I sincerely express my thanks to Dr. Karim Trabelsi, who also had supervised me during my analysis on Belle Project. I have learnt many data analysis techniques from him. I am grateful to him for his constant encouragements in carrying out a good research.

My sincere thanks to Prof. Guy Wilkinson for his guidance throughout my analysis on CLEO-c project and for all the supports during my Oxford visit. It is my privilege to thank to Dr. Sneha Malde and Dr. Chris Thomas for the help and discussions during the analysis.

I am also thankful to Belle India Group for many helps and supports during Belle Analysis Workshops. I really learnt many things during these meetings. I am thankful to Dr. Gagan Mohanty for arranging the first Belle India Group meeting at TIFR and for the useful discussions during my Belle analysis.

I am thankful to Belle Collaboration for allowing me to join the collaboration and work in KEK and for the excellent service to do data analysis. I had a very pleasant time at KEK visit. My thanks to Anu, Deepanwita, Nisar, Saurabh and Vipin.

I would specially thank my friends and juniors: Sreenath, Pranati, Chiki, Monalisha, Archana, Dibya, Preeti, Prasanth, Basith, Resmi, Krishnakumar, Udaya, Rebin, Pramod, Subeesh, Madhusmita, Ajit, Guru, Bhaskar and all the friends at IITM, for their support in one way or other and making a pleasant time at IIT Madras.

I will not forget to say thanks to my M.Sc. teachers for their excellent teaching and seriousness to shape each student's carrier. My special thanks to retired Prof. L.P. Singh who strongly inspired me to pursue research in physics and especially at the time when I was about to choose my carrier as a Higher Secondary School teacher.

My parents are the biggest source of inspiration in my life. I would specially acknowledge my mother for making me what I am today and my father for his support and teaching which inspired me to choose science as a carrier.

I would also acknowledge my paternal grandmother who is the real gem of my life. I feel blessed to have her in my life. I also remember my late grandfather who had

inspired in many ways. I always bow down for the love and the care they have given to their grandchildren and specially to me.

I am thankful to all the individuals who helped me in one way or other. My special thanks to the Department of Physics, IIT Madras for giving me the opportunity to pursue research at IITM.

Last but not least, my greatest regards to the Almighty God for all he has given.

ABSTRACT

We perform a study of the suppressed decay $B^- \to DK^-$, $D \to K^+\pi^-\pi^0$, where D denotes either a D^0 or a $\bar{D}^0$ meson. The decay is sensitive to the CP-violating parameter ϕ_3. Using a data sample of 772×10^6 $B\bar{B}$ pairs collected at the $\Upsilon(4S)$ resonance with the Belle detector, located at the interaction point of the e^+e^- asymmetric energy (3.5 GeV on 8 GeV) collider at the KEK-B factory, we measure the branching-fraction ratio R_{DK} and CP-asymmetry A_{DK} as:

$$\begin{aligned} R_{DK} &\equiv \frac{B(B^- \to [K^+\pi^-\pi^0]_D K^-) + B(B^+ \to [K^-\pi^+\pi^0]_D K^+)}{B(B^- \to [K^-\pi^+\pi^0]_D K^-) + B(B^+ \to [K^+\pi^-\pi^0]_D K^+)} \\ &= [1.98 \pm 0.62(\text{stat.}) \pm 0.24(\text{syst.})] \times 10^{-2} \end{aligned}$$

$$\begin{aligned} A_{DK} &\equiv \frac{B(B^- \to [K^+\pi^-\pi^0]_D K^-) - B(B^+ \to [K^-\pi^+\pi^0]_D K^+)}{B(B^- \to [K^+\pi^-\pi^0]_D K^-) + B(B^+ \to [K^-\pi^+\pi^0]_D K^+)} \\ &= 0.41 \pm 0.30(\text{stat.}) \pm 0.05(\text{syst.}) \end{aligned}$$

The value of R_{DK} indicates the first evidence of the signal for this suppressed decay with a significance of 3.2 standard deviations. We also report measurements for the analogous quantities $R_{D\pi}$ and $A_{D\pi}$ for the decay $B^- \to D\pi^-$, $D \to K^+\pi^-\pi^0$.

We also perform the first measurements of F_+, the fractional CP-even content of the self-conjugate decays $D \to \pi^-\pi^+\pi^0$ and $D \to K^-K^+\pi^0$ using quantum-correlated $D\bar{D}$ decays collected by the CLEO-c experiment at the $\psi(3770)$. Values of $0.968 \pm 0.017 \pm 0.006$ and $0.731 \pm 0.058 \pm 0.021$ are obtained for $\pi^-\pi^+\pi^0$ and $K^-K^+\pi^0$, respectively. It is demonstrated how modes of this sort can be cleanly included in measurements of the unitarity triangle ϕ_3 using $B^\mp \to DK^\mp$ decays. The high CP-even content of $D^0 \to \pi^-\pi^+\pi^0$, in particular, makes this a promising mode for improving the precision on ϕ_3.

Contents

List of Tables

List of Figures

Chapter 1

Introduction

In the standard model (SM) of particle physics, nature is invariant under $SU(3) \otimes SU(2)_L \otimes U(1)_Y$ gauge group symmetry, also known as the symmetry of the strong interaction unified with the electro-weak interaction. However nature is not invariant under some discrete symmetry transformation. An example is the violation of CP symmetry, the combined operation of C (charge-conjugation) and P (parity) symmetry, which is a discrete symmetry of nature. Tests of SM CP violation, which occur because of weak interaction among quarks are an important task in the hand of physicists.

In the SM, coupling of quark fields via the weak interaction is described by a 3×3 mixing matrix called the Cabibbo-Kobayashi-Maskawa (CKM) matrix [1] named after Nicola Cabibbo, who introduced the idea of quark mixing in 2-generations of quarks and Makoto Kobayashi and Toshihide Maskawa, who in 1973 extended this idea to 3-generations of quarks by introducing the third quark family (t, b). This CKM matrix gives a free complex phase parameter, which provides a mechanism to explain CP violation in the SM. For this work, Kobayashi and Maskawa received the Noble Prize in 2008.

Tests of CP violation in the SM are equivalent to measurement of the independent parameters of the unitary CKM matrix, some of which are related to the unitary angles ϕ_1, ϕ_2, ϕ_3 of an unitary triangle in the complex plane. To date, the angle ϕ_3 is least precisely measured. The goal of this thesis is to measure the observables used to constrain ϕ_3 and to find out new effective modes to be studied for the measurement of ϕ_3.

Using the so-called ADS method [2], for $B^- \to DK^-$ ($D = \bar{D}^0$ or D^0), with $D \to K^-\pi^+\pi^0$ decay, we measure, the ratio of the suppressed to favored branching fractions:

$$R_{ADS} = \frac{\mathcal{B}([K^+\pi^-\pi^0]_D K^-) + \mathcal{B}([K^-\pi^+\pi^0]_D K^+)}{\mathcal{B}([K^-\pi^+\pi^0]_D K^-) + \mathcal{B}([K^+\pi^-\pi^0]_D K^+)}; \tag{1.1}$$

and the direct CP asymmetries,

$$A_{ADS} = \frac{\mathcal{B}([K^+\pi^-\pi^0]_D K^-) - \mathcal{B}([K^-\pi^+\pi^0]_D K^+)}{\mathcal{B}([K^+\pi^-\pi^0]_D K^-) + \mathcal{B}([K^-\pi^+\pi^0]_D K^+)}, \tag{1.2}$$

which are related to the angle ϕ_3. We extract the above observables using a maximum likelihood fit to the data collected by the Belle experiment at KEK, Japan. This analysis has been published in Reference [3].

We also demonstrate how modes like $D \to \pi^-\pi^+\pi^0$ and $D \to K^-K^+\pi^0$ can be cleanly included in the ϕ_3 measurement using $B^- \to DK^-$ decays. We measure the CP content the above two modes using quantum-correlated data collected by CLEO-c experiment. This work has been submitted to Reference [4].

The rest of the thesis has been organised as follows. We give a review to standard model and CP violation in Chapter 2. Experimental setup is discussed in Chapter 3. Chapter 4 describes the event selection and continuum suppression. Signal yield determination is described in Chapter 5. Measurement of observables relative to angle ϕ_3 are presented in Chapter 6. We discuss about the CLEO-c analysis in Chapter 7 and finally conclusion is given in Chapter 8.

Chapter 2

Standard Model and CP Violation

2.1 Short review of gauge theory of fundamental particles

The Standard Model (SM) of particle physics, based upon relativistic quantum field theory, concerns the dynamics of fundamental particles via electromagnetic, weak and strong interactions. In the language of relativistic quantum field theory, it is a non-abelian gauge theory described by the $SU(3)\otimes SU(2)_L\otimes U(1)_Y$ gauge group. This theory combines the theory of strong interactions of colored quarks and gluons (QCD) based on the $SU(3)$ gauge symmetry describing the strong interactions, with the unified theory of electroweak interactions, based on gauge symmetry $SU(2)_L\otimes U(1)_Y$ describing the weak and electromagnetic interactions. Here the subscript L represents left handed particle in the $SU(2)$ group and subscript Y reperesents weak hypercharge. The standard model Lagrangian remains invariant under the local transformation of the above gauge group. To understand the above gauge groups explicitly, we consider the physical interpretation of an $SU(n)$ gauge group which has n^2-1 generators, which means a fundamental force with n^2-1 gauge bosons. There are 8 types of gluons, G^a where $a \in 1,..,8$, carrying color and anti-color charges and having coupling constant g_a that mediate the strong force, is described by an $SU(3)$ group. Glashow, Salam and Weinberg [5, 6, 7] found that in fact the electromagnetic and weak forces can be described as the physical manifestations of the underlying 'electroweak' force, which has a gauge group $SU(2)\otimes U(1)$. The gauge bosons of this group are the $W^{1,2,3}$ for the $SU(2)$ group, and the B for the $U(1)_Y$ group. The neutral electroweak W and B bosons mix to produce γ and Z bosons. Their respective coupling constants are g and g', and the degree of mixing is expressed in terms of weak mixing angle, θ_W. The symmetry of the above gauge group is spontaneously broken via the Higgs mechanism, which has the effect of giving mass to the weak gauge bosons, $W^{\pm}$ and Z^0, while leaving the electromagnetic gauge boson, the photon, massless. In the SM, all known matter particles are composites of two types of fundamental particles: fermions and force carrier bosons. A fermion is any particle with half-integer spin while a boson is one having integer spin. The fermions of the SM are

six quarks and six leptons and the SM bosons are the gauge particles that mediate the interactions, as described above. Quarks carrying color charge are differentiated from leptons which do not carry any color charge, via the charge, quarks having fractional electric charge where as leptons have unit charge and quarks experience all the four fundamental forces but leptons experience only three; they do not interact via the strong interaction. All fermions interact via the weak gauge bosons, which in most cases mediate the decay of heavier particles to lighter particles.
The arrangement and the properties of all the above listed quarks and leptons and gauge bosons are shown in Table 2.1, 2.2 and 2.3.

Table 2.1: The quarks and their mass, charge, spin-parity, baryon number and isospin [8].

Quark	Symbol	Mass [MeV/c^2]	Charge Q/e	Spin-parity J^P	Baryon number B	Isospin I
up	u	$2.3^{+0.7}_{-0.5}$	$+\frac{2}{3}$	$\frac{1}{2}^+$	$\frac{1}{3}$	$\frac{1}{2}$
down	d	$4.8^{+0.5}_{-0.3}$	$-\frac{1}{3}$	$\frac{1}{2}^+$	$\frac{1}{3}$	$\frac{1}{2}$
charm	c	1275 ± 25	$+\frac{2}{3}$	$\frac{1}{2}^+$	$\frac{1}{3}$	0
strange	s	95 ± 5	$-\frac{1}{3}$	$\frac{1}{2}^+$	$\frac{1}{3}$	0
top	t	$173210 \pm 510 \pm 710$	$+\frac{2}{3}$	$\frac{1}{2}^+$	$\frac{1}{3}$	0
bottom	b	4180 ± 30	$-\frac{1}{3}$	$\frac{1}{2}^+$	$\frac{1}{3}$	0

Table 2.2: The leptons and their mass, charge, spin and lifetime [8].

Leptons	Symbol	Mass [MeV/c^2]	Charge Q/e	Spin	Lifetime
electron	e	0.511	-1	$\frac{1}{2}$	stable
electron neutrino	ν_e	225×10^{-6}(CL = 95%)	0	$\frac{1}{2}$	stable
muon	μ	105.658	-1	$\frac{1}{2}$	2.197×10^{-6} s
muon neutrino	ν_μ	< 0.19(CL = 90%)	0	$\frac{1}{2}$	stable
tau	τ	1776.82±0.16	-1	$\frac{1}{2}$	$(291 \pm 1.5)^{-15}$ s
tau neutrino	ν_τ	< 18.2(CL = 95%)	0	$\frac{1}{2}$	stable

Table 2.3: The Gauge Bosons and their mass and width [8].

Gauge Bosons	Symbol	Mass (GeV/c^2)	Width (GeV)
photon	γ	$< 10^{-24}$	stable
gluon	G	0	stable
weak boson	$W^{\pm}$	80.385 ± 0.015	$\Gamma = 2.07 \pm 0.06$
weak boson	Z^0	91.188 ± 0.002	$\Gamma = 2.49 \pm 0.01$

2.2 Symmetry and conservation laws

Symmetry is a phenomenon that leaves a physical system unchanged under a certain transformation. The existence of such a symmetry implies a conservation law of some kind. For example, invariance of a system under translation or rotation in space leads to the conservation of linear and angular momentum, respectively. These transformations can be either continuous or discrete which in turn gives rise to continuous or discrete symmetries, respectively. Translation or rotation in space are examples of continuous symmetry. Spatial inversion through the origin of the coordinates is known as the parity operation, which is an example of a discrete symmetry.

2.3 CP violation

The theoretical symmetry between matter and anti-matter is known as CP symmetry which is a discrete symmetry of nature. Our nature has treated matter and anti-matter differently, commonly known as dominance of matter over anti-matter. This is believed to have started within the first second after the Big Bang. The existence of CP violation, violation of the combined operation of C that changes matter to anti-matter and vice-versa and P that reverses space-coordinates, is one of the most important reasons for dominance of matter over antimatter.
If we apply C to the $|\pi^+\rangle = |u\bar{d}\rangle$ meson, we will find a $|\pi^-\rangle = |\bar{u}d\rangle$ meson under the charge conjugation process. In general terms, charge conjugation maps matter into anti-matter. C-symmetry is a discrete symmetry of physical laws under the charge-conjugation transformation. Parity is also a physical transformation which inverts the space-coordinates, $(t, x) \rightarrow (t, -x)$, producing a mirror image of reality. It only changes the handedness of a particle by reversing its momentum and leaving its spin unchanged. Until 1956, it was believed parity is conserved in all interactions. In 1956, Lee and Yang [9] proposed an experiment with β decay of Cobalt-60 that confirmed parity violation in weak decays [10]. Even though P violation had been found, it was believed that all fundamental interactions were invariant under CP, the combined operation of C and P. Eventually CP violation was observed in neutral Kaon decays in 1964 [10] which began a series of search for CP violation in the Kaon system, followed by a search for CP violation in B and D meson decay.

2.4 CP-Violation in the Standard Model and the CP-Violating Angle ϕ_3/γ

The SM has a natural place for CP violation. CP violating effects may originate from the charged-current interactions of quarks, having the structure: $U \to DW^+$, where $U = (u, c, t)$ represents up-type quarks and $D = (d, s, b)$ represents the down-type quarks. The above structure means the weak interaction in the SM mediated by $W^\pm$ boson changes the flavor of the quarks. An up-type quark can only be changed to a down-type quark by emitting or absorbing the $W^\pm$ boson or vice versa. This flavor-changing charged current transition occurs because of the difference between the quark-mass eigenstates and the weak eigenstates. In the SM two-generation quark case, the familiar Cabibbo rotation, gives the following charged current coupling mediated by $W^\pm$ bosons:

$$-L_{W^\pm} = \frac{g}{\sqrt{2}}(\overline{u}, \overline{c})_L \gamma^\mu \begin{pmatrix} \cos\theta_c & \sin\theta_c \\ -\sin\theta_c & \cos\theta_c \end{pmatrix} \begin{pmatrix} d \\ s \end{pmatrix}_L W_\mu^+ + h.c., \tag{2.1}$$

where θ_c is the Cabibbo angle. Since in this case the quark mixing matrix can be taken to be real, the unitary transformation is just an ordinary rotation.

In the three-generation, six-quark case, the mixing matrix is not just an ordinary orthogonal matrices. So the charged current Lagrangian is given by

$$-L_{W^\pm} = \frac{g}{\sqrt{2}} \overline{U}_L \gamma^\mu \mathbf{V}_{CKM} D_L W_\mu^+ + h.c., \tag{2.2}$$

where h.c. is the hermitian conjugate term, the subscript L represents left-handed chiral components of the quark spinors. $W^\pm$ is the field corresponding to the charged W boson. Here, g is the weak coupling strength and $\mathbf{V}_{CKM}$ is a 3×3 unitary matrix called Cabibbo-Kobayashi-Maskawa (CKM) matrix [11, 12]. The elements of $\mathbf{V}_{CKM}$ are named in terms of the quarks they couple together and is written as

$$\mathbf{V}_{CKM} = \begin{pmatrix} V_{ud} & V_{us} & V_{ub} \\ V_{cd} & V_{cs} & V_{cb} \\ V_{td} & V_{ts} & V_{tb} \end{pmatrix}. \tag{2.3}$$

The nine elements of the CKM matrix represent the couplings of the quarks to W bosons and the matrix relates the weak interaction eigenstates (d', s', b') of the down, strange and bottom quarks with their mass eigenstates (d, s, b) through the following unitary transformation:

$$\begin{pmatrix} d' \\ s' \\ b' \end{pmatrix} = \mathbf{V}_{CKM} \begin{pmatrix} d \\ s \\ b \end{pmatrix}. \tag{2.4}$$

Under the CP transformation, the $\mathcal{L}_{W^\pm}$ is invariant only when $\boldsymbol{V}_{CKM} = \boldsymbol{V}_{CKM}^*$, since

$$(CP)\mathcal{L}_{W^\pm}(CP)^\dagger = -\frac{g}{\sqrt{2}}\Big[\left(\overline{U}_L \gamma^\mu \boldsymbol{V}_{CKM}{}^* D_L\right) W_\mu^+ + \left(\overline{D}_L \gamma^\mu (\boldsymbol{V}_{CKM}{}^*)^\dagger U_L\right) W_\mu^-\Big], \tag{2.5}$$

which is supported by $(CP)W^+_\mu(CP)^\dagger = -W^-_\mu$ and $(CP)\bar{\psi}_{\rm a}\gamma^\mu\psi_{\rm b}(CP)^\dagger = -\bar{\psi}_{\rm b}\gamma^\mu\psi_{\rm a}$ with $\psi_{\rm a,b}$ being general fermion states. Therefore, CP violation can only occur if one or more elements of $\boldsymbol{V}_{CKM}$ are complex numbers. From the above two equations and for the three quark generations case, $\mathbf{V}_{CKM}$ can be parametrized by one imaginary and three real parameters. The unitarity of the CKM matrix provides constraints on six real and three imaginary quantities, leaving three real and six imaginary ones. Among the six phases, five are unphysical. Therefore only one complex and three real quantities (Euler-type angles) are required to describe the elements of $\mathbf{V}_{CKM}$ parametrizes:

$$V_{CKM} = \begin{pmatrix} \cos\theta_{12} & \sin\theta_{12} & 0 \\ -\sin\theta_{12} & \cos\theta_{12} & 0 \\ 0 & 0 & 1 \end{pmatrix} \begin{pmatrix} 1 & 0 & 0 \\ 0 & \cos\theta_{23} & \sin\theta_{23} \\ 0 & -\sin\theta_{23} & \cos\theta_{23} \end{pmatrix} \begin{pmatrix} \cos\theta_{13} & 0 & \sin\theta_{13}e^{-i\delta} \\ 0 & 1 & 0 \\ -\sin\theta_{13}e^{-i\delta} & 0 & \cos\theta_{13} \end{pmatrix}$$

In the standard parametrization advocated by the Particle Data Group (PDG) [8], the three generation CKM matrix takes the following form:

$$= \begin{pmatrix} c_{12}c_{13} & s_{12}c_{13} & s_{13}e^{-\imath\delta_{13}} \\ -s_{12}c_{23} - c_{12}s_{23}s_{13}e^{\imath\delta_{13}} & c_{12}c_{23} - s_{12}s_{23}s_{13}e^{\imath\delta_{13}} & s_{23}c_{13} \\ s_{12}s_{23} - c_{12}c_{23}s_{13}e^{\imath\delta_{13}} & -c_{12}s_{23} - s_{12}c_{23}s_{13}e^{\imath\delta_{13}} & c_{23}c_{13} \end{pmatrix} \qquad (2.6)$$

where $c_{ij} = \cos\theta_{ij}$ and $s_{ij} = \sin\theta_{ij}$ and i, j = 1,2,3 denotes the quark generations and δ is the complex phase. This parametrization has the advantage that the mixing between two chosen generations vanishes if the corresponding mixing angle θ_{ij} is set to zero. This complex phase allows to accommodate the CP violation phenomenon in the SM, as was pointed out by Kobayashi and Maskawa in 1973 [12]. The corresponding picture is referred to as the Kobayashi-Maskawa (KM) mechanism of CP violation. So, the extension of Cabibbo mixing matrix to accommodate the third-generation of quark is referred to as the Cabibbo-Kobayashi-Maskawa (CKM) matrix.

In the Wolfenstein parametrization [13] which expresses the CKM matrix as an expansion in powers of $\lambda \approx \sin\theta_c$,

$$\mathbf{V}_{CKM} = \begin{pmatrix} 1 - \frac{1}{2}\lambda^2 & \lambda & A\lambda^3(\rho - i\eta) \\ -\lambda & 1 - \frac{1}{2}\lambda^2 & A\lambda^2 \\ A\lambda^3[1 - (\rho + i\eta)] & -A\lambda^2 & 1 \end{pmatrix} + O(\lambda^4), \qquad (2.7)$$

where A is a scaling parameter $\sim$1, ρ and η are related to the CP violating phase. If $\eta = 0$ there would be no CP violation.

The unitarity of the CKM matrix, $(VV^\dagger)_{ij} = (V^\dagger V)_{ij} = \delta_{ij}$, leads to twelve distinct complex relations among the matrix elements. The six relations with $i \neq j$ can be represented geometrically as triangles in the complex plane. These so called unitarity

triangles are,

$$\underbrace{V_{ub}V_{us}^{\star}}_{\lambda}+\underbrace{V_{cd}V_{cs}^{\star}}_{\lambda}+\underbrace{V_{td}V_{ts}^{\star}}_{\lambda^5}=0 \tag{2.8}$$

$$\underbrace{V_{ud}V_{cd}^{\star}}_{\lambda}+\underbrace{V_{us}V_{cs}^{\star}}_{\lambda}+\underbrace{V_{ub}V_{cb}^{\star}}_{\lambda^5}=0 \tag{2.9}$$

$$\underbrace{V_{us}V_{ub}^{\star}}_{\lambda^4}+\underbrace{V_{cs}V_{cb}^{\star}}_{\lambda^2}+\underbrace{V_{ts}V_{tb}^{\star}}_{\lambda^2}=0 \tag{2.10}$$

$$\underbrace{V_{cd}V_{td}^{\star}}_{\lambda^4}+\underbrace{V_{cs}V_{ts}^{\star}}_{\lambda^2}+\underbrace{V_{cb}V_{tb}^{\star}}_{\lambda^2}=0 \tag{2.11}$$

$$\underbrace{V_{ud}V_{td}^{\star}}_{\lambda^3}+\underbrace{V_{us}V_{ts}^{\star}}_{\lambda^3}+\underbrace{V_{cb}V_{tb}^{\star}}_{\lambda^3}=0 \tag{2.12}$$

$$\underbrace{V_{ud}V_{ub}^{\star}}_{\lambda^3}+\underbrace{V_{cd}V_{cb}^{\star}}_{\lambda^3}+\underbrace{V_{td}V_{tb}^{\star}}_{\lambda^3}=0. \tag{2.13}$$

When there is no CP-violation, all six triangles lapse to a line on the real axis. The area of the triangles is, therefore, a measure of the degree of CP-violation in the SM. Each triangle has an equal area (A):

$$\mathrm{A}=\frac{|J|}{2}, \tag{2.14}$$

where J is defined as

$$J=Im(V_{ij}V_{kl}V_{il}^{*}V_{kj}^{*})=A^2\lambda^6\eta, \tag{2.15}$$

where i $\neq$ j , k $\neq$ l and i, j, k, l $\in \{1,2,3\}$.
The triangle corresponding to Eq. 2.13 is more interesting because the sides are of similar length, $O(\lambda^3)$ and angles which are all physical quantities that can be independently measured using B decays. The triangle corresponding to Eq. 2.13 is shown in Fig. 2.1,

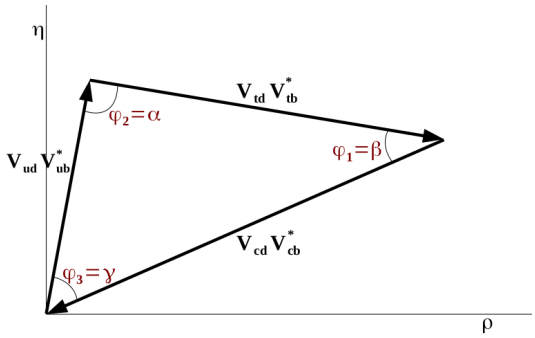

Figure 2.1: Unitarity triangle.

The angles of the triangle are:

$$\phi_1 \equiv arg\left(-\frac{V_{cd}V_{cb}^*}{V_{td}V_{tb}^*}\right) \simeq arg\left(-\frac{1}{1-\rho-i\eta}\right),$$

$$\phi_2 \equiv arg\left(-\frac{V_{td}V_{tb}^*}{V_{ud}V_{ub}^*}\right) \simeq arg\left(-\frac{1-\rho-i\eta}{\rho+i\eta}\right)$$

and

$$\phi_3 \equiv arg\left(-\frac{V_{ud}V_{ub}^*}{V_{cd}V_{cb}^*}\right) \simeq arg\left(\rho+i\eta\right).$$

2.5 Measurement of the angle ϕ_3 of the Unitary Triangle in $B^- \to DK^-$ decays

From the above definition of ϕ_3, complex phases appear only in V_{ub} as described in Eq. (2.7). Therefore, the angle ϕ_3 is expressed as

$$\phi_3 \sim -\arg(V_{ub}). \tag{2.16}$$

This means the measurement of ϕ_3 is equivalent to the extraction of the phase of V_{ub} relative to the phases of other elements associated with ϕ_3.

Various methods to determine ϕ_3 in the tree decay $B^- \to DK^-$, where D is a D^0 or $\bar{D}^0$ decaying to a common final state, have been proposed [2, 14, 15]. The schematic diagram of tree-dominated $B^- \to DK^-$ decay is shown in Figure 2.2. Since there is no loop contribution in the decay amplitude, it is theoretically clean sensitivity to ϕ_3. The two amplitudes contributing to the above decays are related by:

$$\frac{A(B^- \to \bar{D}^0 K^-)}{A(B^- \to D^0 K^-)} = r_B e^{i(\delta_B - \phi_3)}, \tag{2.17}$$

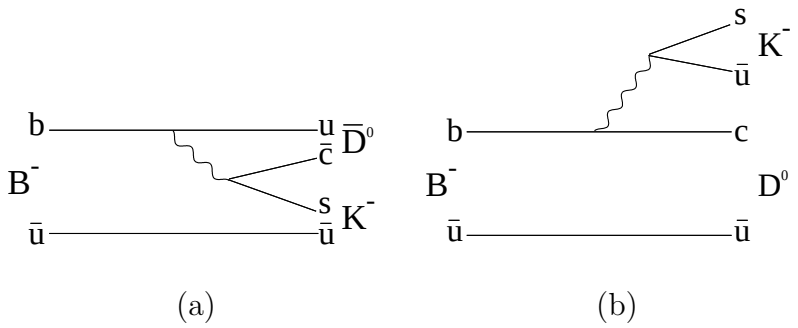

Figure 2.2: (a) Color suppressed $b \to u$ transition (b) Color favored $b \to c$ transition

where the magnitude of ratio of amplitudes r_B and the strong phase difference δ_B are defined as

$$r_B = \left|\frac{A(B^- \to \bar{D}^0 K^-)}{A(B^- \to D^0 K^-)}\right|, \ \delta_B = \delta(B^- \to \bar{D}^0 K^-) - \delta(B^- \to D^0 K^-). \tag{2.18}$$

The value of r_B is around 0.1 - 0.2, by taking a product of the ratio of the CKM matrix elements $|V_{ub}V_{cs}^*/V_{cb}V_{us}^*|$ and the color suppression factor of $\frac{1}{3}$.

In the sections below, we describe several techniques using different D decays. Note that the D^0–$\bar{D}^0$ mixings can safely be neglected for current precision of ϕ_3 [16].

2.5.1 GLW Method

In 1991, Gronau, London and Wyler (GLW) proposed a method [14] for measuring ϕ_3 using $B \to D_{CP\pm}K$ decay, where $D_{CP\pm}$ decays to a CP eigenstate $D_{CP\pm} = (D^0 \pm \bar{D}^0)/\sqrt{2}$ with eigenvalue ± 1. We can measure the amplitude of B decay as:

$$\sqrt{2}.A(B^+ \to D^0_{CP\pm}K^+) = A(B^+ \to D^0K^+) \pm A(B^+ \to \bar{D}^0K^+), \tag{2.19}$$
$$\sqrt{2}.A(B^- \to D^0_{CP\pm}K^-) = A(B^- \to D^0K^-) \pm A(B^- \to \bar{D}^0K^-). \tag{2.20}$$

One can also write the decay amplitude of a $b \to u$ process as:

$$A(B^+ \to D^0K^+) = |V_{ub}|e^{i\phi_3}|A|e^{i\alpha}, \tag{2.21}$$
$$A(B^- \to \bar{D}^0K^-) = |V_{ub}|e^{-i\phi_3}|A|e^{i\alpha}. \tag{2.22}$$

Comparing the above two relations, we obtain the following relation:

$$A(B^+ \to D^0K^+) = e^{2i\phi_3}A(B^- \to \bar{D}^0K^-). \tag{2.23}$$

Similarly we can establish the following relation for $b \to c$ process:

$$A(B^+ \to \bar{D}^0K^+) = A(B^- \to D^0K^-). \tag{2.24}$$

The above relations which lies in the heart of GLW method, can be represented in a complex plane as two triangles, as shown in Fig. 2.3. The difference between $|A(B^+ \to D^0_{CP\pm}K^+)|$ and $A(B^- \to D^0_{CP\pm}K^-)$ indicates the presence of CP violation. The phase difference between the amplitudes $A(B^- \to \bar{D}^0K^-)$ and $A(B^- \to D^0K^-)$ is $\delta_B - \phi_3$, while the one for B^+ decays is $\delta_B + \phi_3$. Thus, the phase $2\phi_3$ could be extracted by measuring three sides of the triangles in the complex plane.

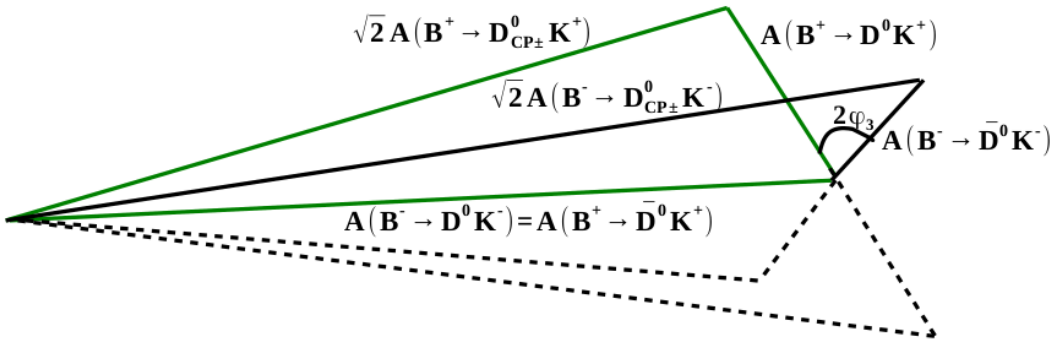

Figure 2.3: Complex GLW triangle.

The following observables are measured via GLW method which can be used to extract ϕ_3:

$$\begin{aligned} \mathcal{R}_{CP\pm} &\equiv \frac{\mathcal{B}(B^- \to D_{CP\pm}K^-) + \mathcal{B}(B^+ \to D_{CP\pm}K^+)}{\mathcal{B}(B^- \to D^0K^-) + \mathcal{B}(B^+ \to \bar{D}^0K^+)} \\ &= 1 + r_B^2 \pm 2r_B \cos\delta_B \cos\phi_3, \qquad (2.25) \\ \mathcal{A}_{CP\pm} &\equiv \frac{\mathcal{B}(B^- \to D_{CP\pm}K^-) - \mathcal{B}(B^+ \to D_{CP\pm}K^+)}{\mathcal{B}(B^- \to D_{CP\pm}K^-) + \mathcal{B}(B^+ \to D_{CP\pm}K^+)} \\ &= \pm 2r_B \sin\delta_B \sin\phi_3 / R_{CP\pm}. \qquad (2.26) \end{aligned}$$

The above four observables are measured to constrain the three unknowns r_B, δ_B and ϕ_3. The effects of the CP violation to the observables are limited because of the small value of r_B. Precise measurements of the observables are needed for obtaining an effective constraint on ϕ_3. CP eigenstates like $D \to K^+K^-$, $\pi^+\pi^-$, $K_S\pi^0$ are used to extract ϕ_3 via the above method.

2.5.2 ADS Method

In the Atwood-Dunietz-Soni (ADS) method [2], ϕ_3 is measured from the study of $B \to DK$ decays with D meson decaying to flavored eigenstates. In this method the decay of B meson to its final state can proceed in two ways: 1) favored B decay ($b \to c$) followed by a doubly Cabibbo-suppressed D decay ($D^0 \to f$ or $\bar{D}^0 \to \bar{f}$), 2) suppressed B decay ($b \to u$) followed by a Cabibbo-favored D decay ($D^0 \to \bar{f}$ or $\bar{D}^0 \to f$). Since in the

above case the two interfering decay amplitudes are of the same order of magnitude, so one can expect large interference effects, which in turn give significant information on ϕ_3 by enhancing CP violation effects. Denoting the final state of the D decay as f, the comparable magnitudes of $A(B^- \to [f]_{\bar{D}^0} K^-)$ and $A(B^- \to [f]_{D^0} K^-)$ provide a relatively large interference effect on $A(B^- \to [f]_D K^-)$ as shown in Figure 2.4.

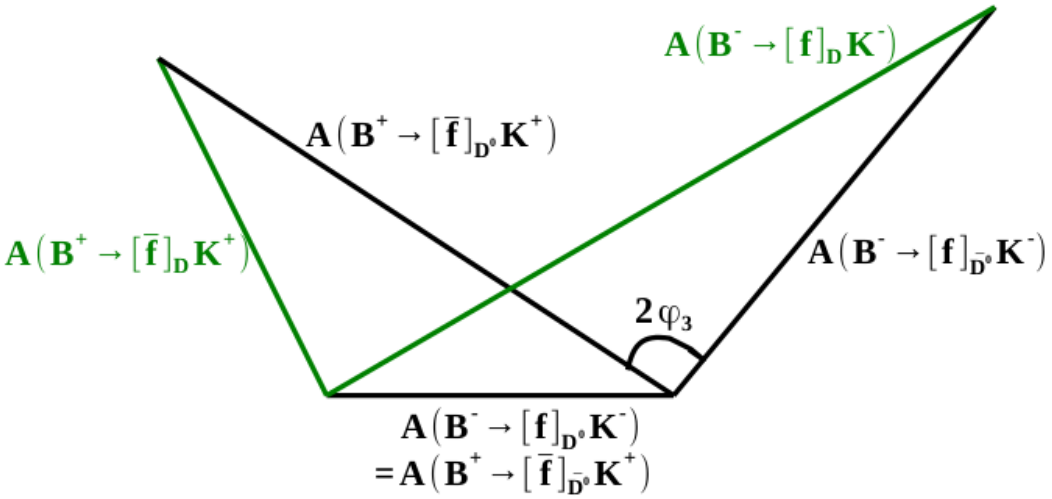

Figure 2.4: Complex ADS triangle.

The following observables are measured via ADS method:

$$\begin{aligned} \mathcal{R}_{\rm ADS} &\equiv \frac{\mathcal{B}(B^- \to [f]_D K^-) + \mathcal{B}(B^+ \to [\bar{f}]_D K^+)}{\mathcal{B}(B^- \to [\bar{f}]_D K^-) + \mathcal{B}(B^+ \to [f]_D K^+)} \\ &= r_B^2 + r_D^2 + 2 r_B r_D \cos(\delta_B + \delta_D) \cos\phi_3, \qquad (2.27) \\ \mathcal{A}_{\rm ADS} &\equiv \frac{\mathcal{B}(B^- \to [f]_D K^-) - \mathcal{B}(B^+ \to [\bar{f}]_D K^+)}{\mathcal{B}(B^- \to [f]_D K^-) + \mathcal{B}(B^+ \to [\bar{f}]_D K^+)} \\ &= 2 r_B r_D \sin(\delta_B + \delta_D) \sin\phi_3 / R_{\rm ADS}, \qquad (2.28) \end{aligned}$$

where $r_D = |A(D^0 \to f)/A(\bar{D}^0 \to f)|$, the ratio of the magnitudes of the suppressed and favored D decays to a particular final state and $\delta_D = \delta(\bar{D}^0 \to f) - \delta(D^0 \to f)$, the strong phase difference between them. By adding the above two hadronic parameters of D meson, ϕ_3 can be extracted. The most important CP non-eigenstates are $D \to K^+\pi^-$, $K^+\pi^-\pi^+\pi^-$, $K^+\pi^-\pi^0$; the latter is one of the subjects of this thesis.

2.5.3 Dalitz Method

In 2003, Giri, Grossman, Soffer, and Zupan (GGSZ) proposed a new method that involves three-body D decays [15]. Their idea is to observe γ through the interference between $B \to D^0 K$ and $B \to \bar{D}^0 K$ decays with D^0 and $\bar{D}^0$ decay to the self-conjugate Cabibbo-allowed final states $K_S\pi^+\pi^-$, $K_S K^+ K^-$ and $K_S\pi^+\pi^-\pi^0$.

2.5.4 ϕ_3 Result as of Winter 2014

The CKMfitter group provide a global measurement of determining the CKM parameters [1] in the SM frame work and beyond. After reviewing all the recent experimental and theoretical informations, the global CKMfit result as of winter 2014 is shown in Figure 2.5. All the measurements are consistent with each other. The combined results

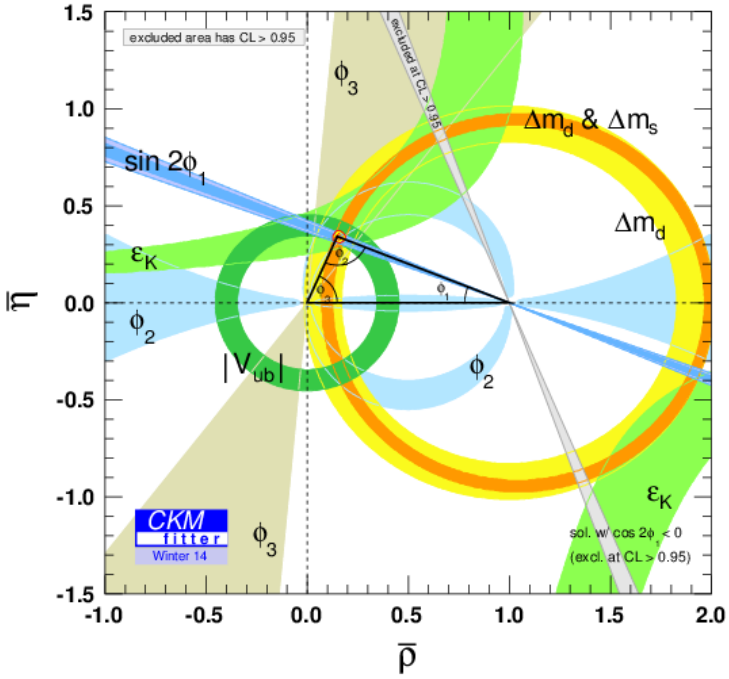

Figure 2.5: Constraints on unitarity triangle from various measurements, as of winter of 2014.

on direct measurements of the unitarity triangle angles from all experiments is:

$$\phi_1 = 21.5^\circ \, ^{+0.8^\circ}_{-0.7^\circ}, \tag{2.29}$$
$$\phi_2 = 85.4^\circ \, ^{+4.0^\circ}_{-3.8^\circ}, \tag{2.30}$$
$$\phi_3 = 73.2^\circ \, ^{+6.3^\circ}_{-7.0^\circ}. \tag{2.31}$$

The error of ϕ_3 is much larger than ϕ_1 in particular. Measurements of ϕ_3 with high precision is required to constrain further the the CKM picture. Any significant discrepancy between the measured parameters from the expected values would be a signature of new physics.

2.6 Motivation to Analyze $B^- \to [K^+\pi^-\pi^0]_D K^-$

In the Atwood-Dunietz-Soni (ADS) method [2], we consider the decay channel $B^- \to DK^-$, followed by $D \to K^+\pi^-\pi^0$. The D decay has a significantly larger branching fraction $[(13.9 \pm 0.5)\%]$ than $D \to K^-\pi^+$ $[(3.89 \pm 0.05)\%]$ [8], making it potentially very sensitive to ϕ_3 despite a reduced acceptance owing to the presence of a π^0 meson in the final state. We search for $B^- \to [K^+\pi^-\pi^0]_D K^-$ events for the first time in Belle, where the favored $B^- \to D^0 K^-$ decay followed by the doubly Cabibbo-suppressed $D^0 \to K^+\pi^-\pi^0$ decay interferes with the suppressed $B^- \to \bar{D}^0 K^-$ decay followed by the Cabibbo-favored $\bar{D}^0 \to K^+\pi^-\pi^0$ decay. The interference between the two amplitudes can lead to a large direct CP asymmetry between the suppressed decays.

The observables measured are the ratio of the suppressed to allowed branching ratios

$$\begin{aligned} R_{DK} &= \frac{B(B^- \to [K^+\pi^-\pi^0]_D K^-) + B(B^+ \to [K^-\pi^+\pi^0]_D K^+)}{B(B^- \to [K^-\pi^+\pi^0]_D K^-) + B(B^+ \to [K^+\pi^-\pi^0]_D K^+)} \\ &= r_B^2 + r_D^2 + 2 r_B r_D R_{K\pi\pi^0} \cos\phi_3 \cos(\delta_B + \delta_D^{K\pi\pi^0}), \end{aligned} \tag{2.32}$$

and the direct CP asymmetry,

$$\begin{aligned} A_{DK} &= \frac{B(B^- \to [K^+\pi^-\pi^0]_D K^-) - B(B^+ \to [K^-\pi^+\pi^0]_D K^+)}{B(B^- \to [K^+\pi^-\pi^0]_D K^-) + B(B^+ \to [K^-\pi^+\pi^0]_D K^+)} \\ &= \frac{2 r_B r_D R_{K\pi\pi^0} \sin\phi_3 \sin(\delta_B + \delta_D^{K\pi\pi^0})}{r_B^2 + r_D^2 + 2 r_B r_D R_{K\pi\pi^0} \cos\phi_3 \cos(\delta_B + \delta_D^{K\pi\pi^0})} \end{aligned} \tag{2.33}$$

where, $\delta_D^{K\pi\pi^0}$ and $R_{K\pi\pi^0}$ are the average strong-phase difference and the coherence factor for the $D^0 \to K^-\pi^+\pi^0$ decay, respectively. Here, the ratio of DCS and CF D decays is defined as

$$r_D^2 \equiv \frac{\Gamma(D^0 \to K^+\pi^-\pi^0)}{\Gamma(D^0 \to K^-\pi^+\pi^0)} = \frac{\int d\vec{\mathbf{m}} A_{DCS}^2(\vec{\mathbf{m}})}{\int d\vec{\mathbf{m}} A_{CF}^2(\vec{\mathbf{m}})}, \tag{2.34}$$

and the average strong-phase difference and coherence factor as

$$R_{K\pi\pi^0} e^{i\delta_D^{K\pi\pi^0}} \equiv \frac{\int d\vec{\mathbf{m}} A_{DCS}(\vec{\mathbf{m}}) A_{CF}(\vec{\mathbf{m}}) e^{i\delta(\vec{\mathbf{m}})}}{\sqrt{\int d\vec{\mathbf{m}} A_{DCS}^2 \int d\vec{\mathbf{m}} A_{CF}^2}}, \tag{2.35}$$

where $A_{CF}(\vec{\mathbf{m}})$ and $A_{DCS}(\vec{\mathbf{m}})$ are the magnitude of the CF and DCS amplitudes, respectively, $\delta(\vec{\mathbf{m}})$ is the relative strong phase, and $\vec{\mathbf{m}}$ indicates a point in the Dalitz plane $\vec{\mathbf{m}} = [m_{K\pi}^2, m_{K\pi^0}^2]$. The parameter $R_{K\pi\pi^0}$ can take values in the interval [0,1]. A coherence factor value close to one indicates a single or several kinematically-isolated intermediate final states dominating the decay. A coherence factor close to zero indicates many interfering intermediate resonances contributing to the amplitude. If $R_{K\pi\pi^0}$ is large, measurements of R_{DK} and A_{DK} for $B \to [K\pi\pi^0]_D K$, can improve the determination of ϕ_3 when combined with other measurements sensitive to r_B, δ_B and

ϕ_3. Furthermore, the coherence factor and average strong-phase difference have been reported by the CLEO collaboration [17]:

$$\begin{aligned} R_{K\pi\pi^0} &= 0.82 \pm 0.07 \,, \\ \delta_D^{K\pi\pi^0} &= \left(164^{+20}_{-14}\right)^\circ \,, \text{where } C\,|D^0\rangle = |\bar{D}^0\rangle \,. \end{aligned}$$

These values indicate significant coherence and can be used to constrain ϕ_3 from the measured observables.

Previous measurements of $B \to [K\pi\pi^0]_D K$ have been made by BABAR [18, 19]. Using 431 fb^{-1} of data, the total signal yield from $B \to D_{fav}K$ decay and $B \to D_{sup}K$ decay is found to be 1981 ± 57 and constraint on R_{ADS} is $R_{ADS} < 21 \times 10^{-3}$ at 90% confidence level.

2.7 Motivation to $D \to h^+h^-\pi^0(h = K/\pi)$ analysis

The current world average precision on ϕ_3 is significantly worse than that of the other angles of the unitarity triangle [8]. Therefore, including additional D-meson final states in $B^- \to DK^-$ decay is desirable to reduce the statistical uncertainty on ϕ_3 at current and future facilities. Our goal is to measure the CP content of $D \to h^+h^-\pi^0(h = K/\pi)$ decay. If the decay is found to be a CP state to good approximation, then one can use GLW method to extract ϕ_3. In the case that the D does not decay to a pure CP eigenstate, information is required on the strong decay dynamics in order to relate the CP-violating observables to ϕ_3. This information can be obtained from studies of quantum-correlated $D\bar{D}$ mesons produced in e^+e^- collisions at an energy corresponding to the mass of the $\psi(3770)$ [15, 20, 21].

The decay $D \to \pi^-\pi^+\pi^0$ is a promising candidate to be added to the suite of modes used in the ϕ_3 measurement. Its Dalitz plot has been studied by the BaBar collaboration using flavor-tagged D^0 decays and exhibits a strikingly symmetric distribution that suggests the decay may be dominated by a single CP eigenstate [22]. An isospin analysis [23] of the amplitude model for $D \to \pi^+\pi^-\pi^0$ presented in Ref. [22] concludes that the final state is almost exclusively $I = 0$. Therefore, given that the parity and G-parity of the three-pion final state is odd and $G = (-1)^I C$, the final state is expected to be $C = -1$ and $CP = +1$. The decay $D \to K^-K^+\pi^0$ has also been studied and possesses similar characteristics [24]. We analyse these decay modes for the first time using quantum-correlated $D\bar{D}$ decays, and measured their CP content, making use of the CLEO-c $\psi(3770)$ data set. These measurements allow the inclusive decays to be included in future $B^- \to DK^-$ analyses in a straightforward and model-independent manner, thus allowing for an improved determination of the angle ϕ_3. The effects of CP violation in charm mesons are neglected, which is a good assumption given theoretical expectations and current experimental limits [8].

Chapter 3

Experimental setup

The principal analysis is based on a data sample of 772×10^6 $B\bar{B}$ pairs collected at the $\Upsilon(4S)$ resonance with the Belle detector at the KEKB asymmetric-energy e^+e^- (3.5 GeV on 8 GeV) collider in the High Energy Accelerator Research Organization (KEK) in Tsukuba, Japan. In this chapter we describe briefly the KEKB Accelerator and Belle Detector.

3.1 KEKB Accelerator

The configuration of the KEKB accelerator [25] is shown in Figure 3.1. KEKB consists of two storage rings: the ring for 8 GeV electrons is called the High Energy Ring (HER), and that for 3.5 GeV positrons is called the Low Energy Ring (LER). The two rings are around 3 km in circumference, located 11 meters below ground level and constructed side by side in the tunnel used originally for TRISTRAN.[1] Electron and positron beams are injected from a linear accelerator (linac) in to these two storage rings at the Fuji area. The two beams collide with a finite horizontal crossing angle of ± 11 mrad at the interaction point (IP) in KEKB. In order to compensate the crossing angle at the IP by tilting the bunch horizontally and thus increasing luminosity, special super conducting radio-frequency (RF) cavities (crab cavities), which kick each beam sideways in the horizontal plane, were installed in KEKB to make the head-on collisions while retaining the crossing angle of beams. A crab crossing is shown in Figure 3.2. Beam operation with crab crossing began in February 2007. The center-of-mass (CM) energy is 10.58 GeV, which coincides with the mass of $\Upsilon(4S)$ resonance,

$$E_{\rm CM} = 2\sqrt{E_{\rm HER}E_{\rm LER}} = 10.58 \text{ GeV} \sim \mathrm{M}_{\Upsilon(4S)}.$$

This is just above $B\bar{B}$ production threshold as shown in Figure 3.3. On June 17, 2009, after the installation of special skew sextupoles that correct chromatic coupling, the KEKB broke the world luminosity record and achieved a peak luminosity of 2.11

[1] A symmetric electron-positron particle accelerator at KEK, Japan. This was built in 1981-1986 with the aim to search for $t\bar{t}$. The CM energy attained was 64 GeV.

$\times 10^{34}$ cm^{-2}s^{-1} using these new accelerator devices. This new record is more than a factor of two higher than the original design luminosity of KEKB. While this luminosity was being recorded, the backgrounds were good and the data were recorded smoothly in the Belle experiment. The integrated luminosity recorded by Belle detector reached 1000 fb^{-1} by the end of summer 2010.

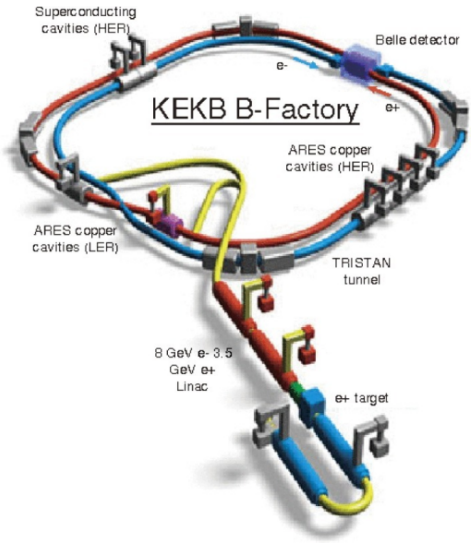

Figure 3.1: Schematic view of KEKB accelerator complex. Taken from Reference [26].

3.2 Belle Detector

Figure 3.4 shows the configuration of the Belle detector [27]. The detector is configured around a 1.5 T superconducting solenoid and iron structure surrounding the KEKB beams at the Tsukuba interaction region. B-meson decay vertices are reconstructed by a double-sided silicon vertex detector (SVD) situated around a cylindrical beryllium beam pipe. There were two inner detector configurations used: SVD1 (three layers before the summer of 2003) and SVD2 (four layers from summer of 2013). Precision tracking of charged particle is provided by a central drift chamber (CDC). Particle identification is provided by the energy loss (dE/dx) measurements in the CDC, information from aerogel Cerenkov counters (ACC) and time of flight information from the IP to the time-of-flight counters (TOF), situated radially outside of the CDC. Electromagnetic particles are detected by an electromagnetic calorimeter (ECL) composed of CsI(Tl) crystals, located inside the super-conducting solenoid coil. Muons and KL mesons are identified by arrays of resistive plate counters (KLM) interspersed in the iron yoke present outside the solenoid.

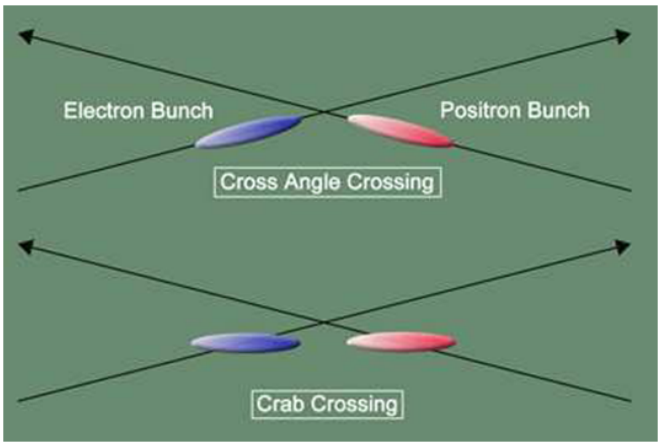

Figure 3.2: Schematic view of a crab crossing. Taken from Reference [28].

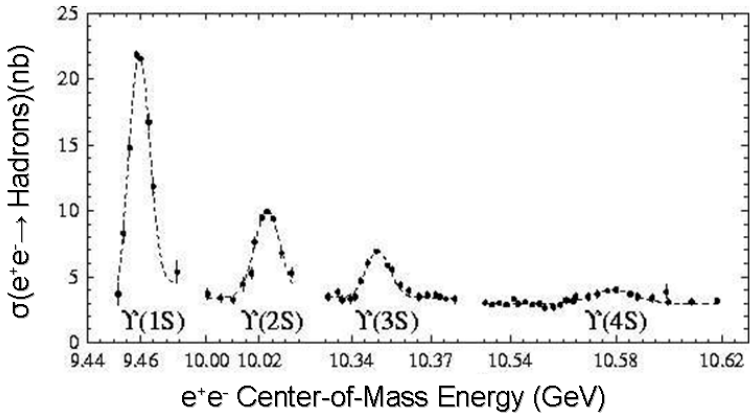

Figure 3.3: Hadronic cross-section in e^+e^- collisions at the center-of-mass energy of around 10 GeV/c^2. Taken from Reference [29].

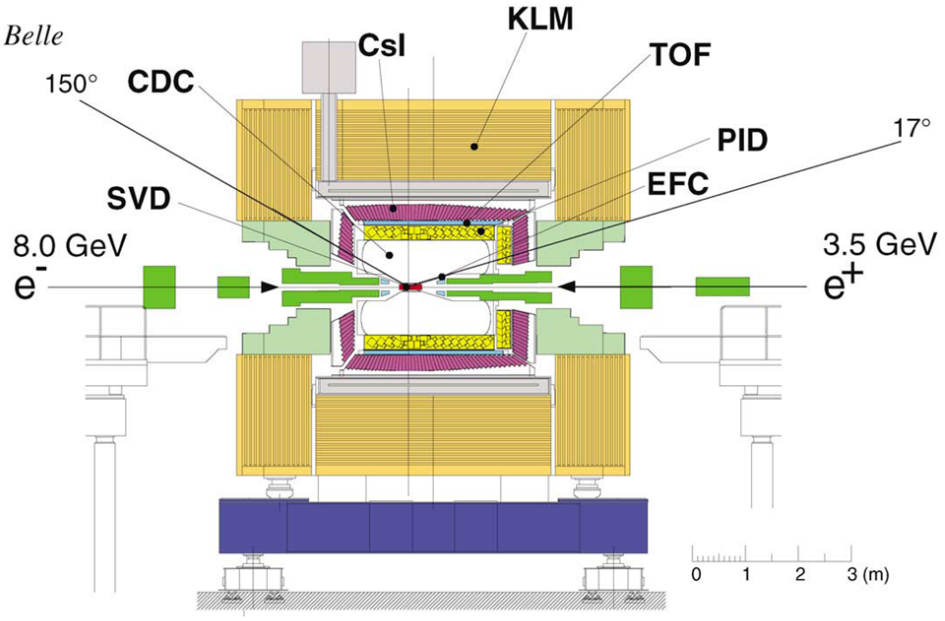

Figure 3.4: Side view of the Belle detector. Taken from Reference [27].

The conventional definition of the coordinate system in Belle are given as follows: the origin is defined as the position of the nominal IP, the x axis is in the horizontal direction pointing outward from the center of the KEKB ring, the y axis is along the vertical direction (upward), the z axis is aligned opposite to the positron beam direction, the radial distance is defined as $r = \sqrt{x^2 + y^2}$, the polar angle θ and the azimuthal angle ϕ are measured with respect to the z and x axes, respectively. The following subsections provide a detailed description of each sub-detector.

3.2.1 Silicon Vertex Detector (SVD)

An accurate determination of the distance between decay vertices of the two B mesons is a crucial point in the study of time-dependent CP asymmetry. Due to 100μm precision of SVD [30], the choice of asymmetric collider to have average decay distance 200μm. The SVD is also useful for identifying and measuring the decay vertices of D and τ particles. Furthermore, the SVD contributes to the charged particle tracking.

Figure 3.5 shows the geometrical configuration of the SVD. It consists of three concentric cylindrical layers of double-sided silicon strip detectors (DSSDs) and covers the polar angle range $23° < \theta < 139°$, which corresponds to 86% of the full solid angle. The radii of the three layers are 30 mm, 45.5 mm and 60.5 mm. The inner, middle and outer layers are constructed from 8, 10, and 14 independent ladders, respectively.

All the ladders are made of identical DSSDs with identical aluminum nitride ceramic hybrid preamplifier cards. The ladders are reinforced by boron nitride support ribs. Each ladder consists of 2/3/4 DSSDs for layer 1/2/3, respectively. The DSSD size is $57.5 \times 33.5 \times 0.3$ mm^3 and in total 102 DSSDs are used and the total number of readout channels is 81,920. The readout chain for DSSDs is based on the VA1 integrated circuit. The VA1 has a very good noise performance ($200e^- + 8e^-$/pF) and reasonably good radiation tolerance of 500 kRad.

A DSSD is a depleted pn junction. A charged particle passing through the junction produces electron-hole pairs along its trajectory. The applied electric field leads to the charges being collected on the p^+ and n^+ strips located on the surface of the DSSD. The charge distributions on the strips allow one to determine three-dimensional hit positions and, hence, to reconstruct the particle track. The n^+ strips aligned perpendicularly to the beam axis measure the z coordinate. The p^+ strips are aligned along the beam axis and therefore measure the azimuthal angle ϕ about the z axis.

The SVD measures the impact parameter resolutions in $r\phi$ and z coordinates. The momentum and angular dependences of the impact parameter resolution are given by:

$$\sigma_{r\phi} = \sqrt{19.2^2 + \left(\frac{54.0}{p\beta \sin^{3/2}\theta}\right)^2}\ \mu\text{m},\ \ \sigma_z = \sqrt{42.2^2 + \left(\frac{44.3}{p\beta \sin^{5/2}\theta}\right)^2}\ \mu\text{m}, \qquad (3.1)$$

where r is the distance from the z axis, p is the momentum in GeV/c and β is the velocity divided by c of the particle.

A new vertex detector, SVD2, was installed in 2003 [31], which has been used ever since. Figure 3.6 shows the configuration of SVD2. It consists of a four-layer structure, where 6, 12, 18, and 18 ladders comprise the first, second, third, and fourth layers, respectively. It has larger coverage of $17^\circ < \theta < 150^\circ$ than SVD1, which corresponds to 92% of the full solid angle. It has significantly improved the impact parameter resolution in both the $r\phi$ and z directions. The impact parameter resolutions are

$$\sigma_{r\phi} = \sqrt{17.4^2 + \left(\frac{34.3}{p\beta \sin^{3/2}\theta}\right)^2}\ \mu\text{m},\ \ \sigma_z = \sqrt{26.3^2 + \left(\frac{32.9}{p\beta \sin^{5/2}\theta}\right)^2}\ \mu\text{m}. \qquad (3.2)$$

The performance is better than the one of SVD1, mainly because of the smaller radius of the first layer.

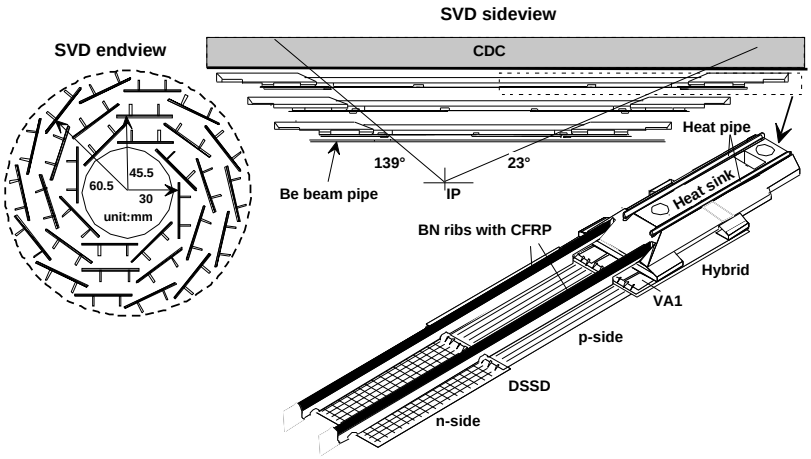

Figure 3.5: Configuration of SVD1 [30].

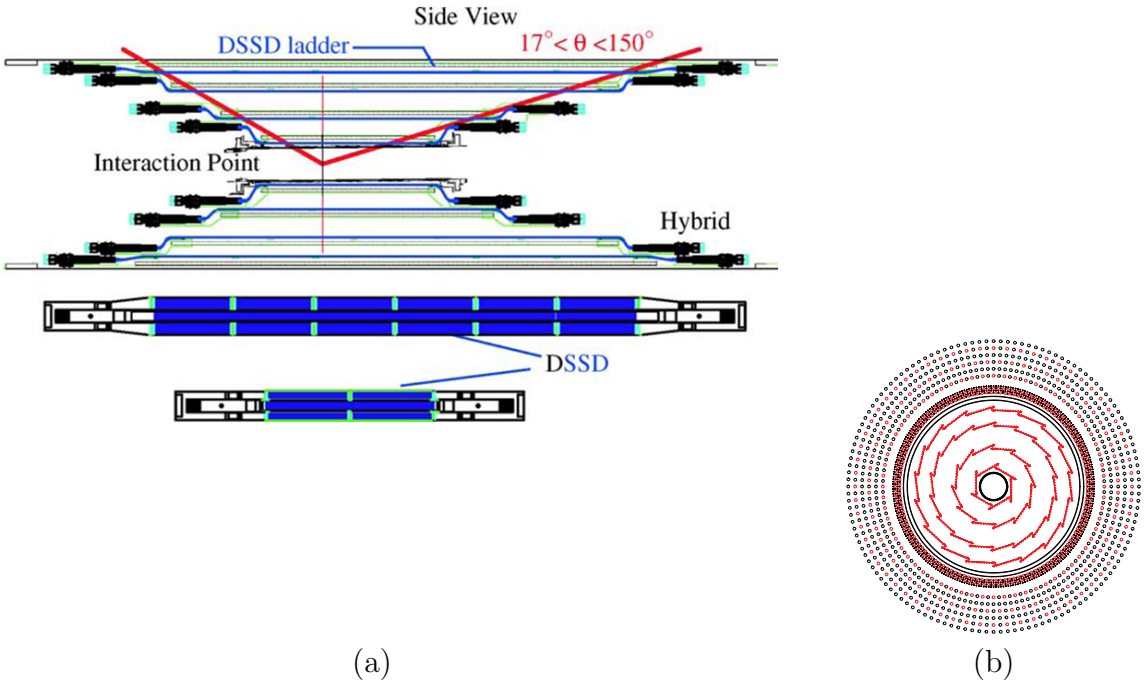

(a) (b)

Figure 3.6: Configuration of SVD2 [32]: (a) side view, (b) end view.

3.2.2 Central Drift Chamber (CDC)

The main functions of the CDC [33] are the efficient reconstruction of charged particle tracks, precise determination of their momenta and to provide the particle identification information by precise energy loss (dE/dx) measurements.
The structure of CDC is shown in Figure 3.7. It is asymmetric in the z direction and several other places in order to provide an angular coverage of $17° < \theta < 150°$. The chamber has 50 cylindrical layers, each containing between three and six either axial or small-angle-stereo layers, and three cathode strip layers. CDC has a total of 8400 drift cells of which 5280 are axial and 3120 are stereo. The cathode strips are divided into eight segments in ϕ and 64 segments (8.2 mm pitch) in z to provide z-coordinate information for the fast trigger.

Since the majority of the decay products of a B meson have momenta lower than 1 GeV/c, the minimization of multiple Coulomb scattering is important for preserving the momentum resolution. Therefore, a 50% helium - 50% ethane gas mixture is chosen, which still retains a good dE/dx resolution. The average spatial resolution for the entire drift space is measured to be approximately 130 μm in the $r - \phi$ direction.

The rate of energy loss (dE/dx) of a charged particle is given by the Bethe-Bloch formula:

$$-dE/dx = 2\pi N_a r_e^2 m_e c^2 \rho \frac{Z}{A}\frac{z^2}{\beta^2}\left[\ln(\frac{2m_e\gamma^2\nu^2 W_{max}}{I^2}) - 2\beta^2 - \delta/2\right], \qquad (3.3)$$

where N_a is the Avogadro's number, r_e is the classical electron radius, m_e is the electron mass, Z and A are the atomic number and mass number of the materials of the medium, z and v are the charge and velocity of the particle, $\beta = v/c, \gamma = 1/\sqrt{1-\beta^2}, I \simeq 16Z^{-0.19}$ eV is the mean excitation potential of the medium, δ is the density correction factor, W_{max} is the maximum energy transfer in a collision, and x is the path length in the medium, measured in gcm^{-2}. The above equation shows that dE/dx is independent of the mass of the particle and only depends on the parameter, β. Therefore one can estimate β from the measurement of dE/dx. The measurement of β can provide a useful method for estimating the rest mass and hence measuring momentum of the particle species. Figure 3.8 shows the scattered plot between measured dE/dx as a function of momentum. The separation between pions, kaons, protons and electrons are clearly seen. The resolution of dE/dx is measured to be 7.8% for pions in the momentum range from 0.4 to 0.6 GeV/c and 6% for energetic electrons and muons. The dE/dx information provides $\geq 3\sigma$ K/π separation up to 0.8 GeV/c. The dE/dx for kaons and pions has a crossover around 1 GeV/c, however the CDC can provide some discrimination between kaons and pions above 2 GeV/c. It also provides more than 3σ e/π separation for the momentum range from 0.3 GeV/c to 3 GeV/c.

3.2.3 Aerogel Cherenkov Counter (ACC)

Particle identification, specifically of $K^\pm$ and $\pi^\pm$ is very important for studying CP violation in the B system. The aerogel Cerenkov counter is designed for $K^\pm$ and $\pi^\pm$

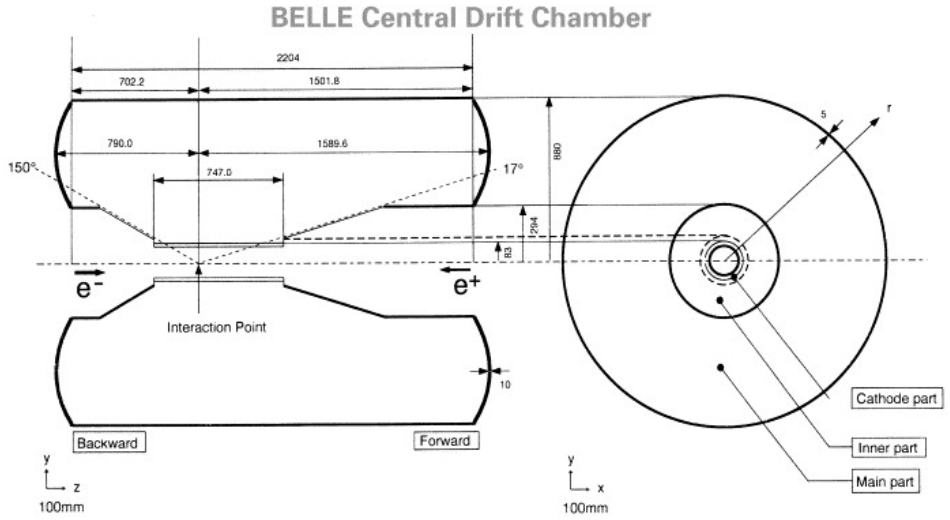

Figure 3.7: Overview of the CDC structure. Taken from Reference [33].

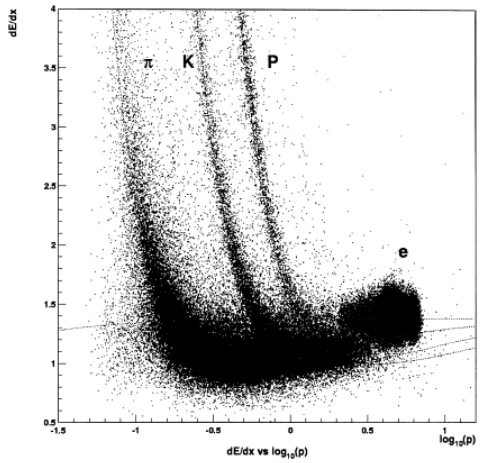

Figure 3.8: dE/dx versus momentum distribution. The separation between π, K, p and e are clearly seen. Taken from Reference [27].

separation with momentum between 1.2 GeV/c and 3.5 GeV/c, which is not covered by the dE/dx measurement by CDC and time-of-flight information on TOF. The ACC based on the Cherenkov principle detects the Cerenkov radiation emitted when a particle travels faster than the speed of light in a material.
For a medium of refractive index n, Cherenkov radiation is emitted if the velocity of the particle β, satisfies:

$$n > \frac{1}{\beta} = \sqrt{1 + \left(\frac{m}{p}\right)^2}. \tag{3.4}$$

where m and p are the mass and momentum of the particle, respectively. Thus, depending on the refractive index of the medium, there is a momentum region where pions emit Cherenkov light while another heavier particles such as kaons do not. Thus, the Cherenkov detector can identify charged particles having different masses by choosing the refractive index n of the matter for the interested range of momentum. For example, for momentum 2 GeV/c, pions emit Cerenkov light in the matter if $n > 1.002$ while kaons emit radiation if $n > 1.030$.

The configuration of ACC [34], in the central part of the Belle detector is shown in Figure 3.9. It consists of 960 counter modules segmented into 60 cells in ϕ for the barrel part and 228 modules arranged in five concentric layers for the forward end-cap part of the detector. All the counters are arranged in a semi-tower geometry, pointing to the interaction point and covering a total θ range from 17° to 127°. In order to obtain a good pion/kaon separation for the whole kinematical range, the refractive indices of aerogels are selected to be between 1.01 and 1.03, depending on the polar angle. An ACC module consists of five aerogel tiles stacked in a 0.2 mm thick aluminum box of approximate dimensions $(12 \times 12 \times 12)$ cm^3. Cherenkov photons are detected effectively by fine mesh-type photomultiplier tubes (FM-PMTs), which are operated in a magnetic field of 1.5 T and are attached directly to the aerogel stacks at the sides of the box.

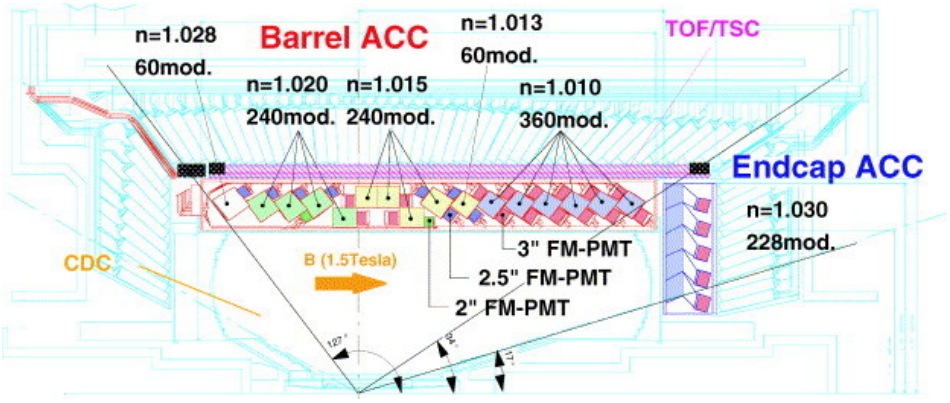

Figure 3.9: The arrangement of ACC. Taken from Reference [27].

3.2.4 Time-of-Flight Counter (TOF)

The TOF detector system [35] is used to provide particle identification information for momenta below about 1.2 GeV/c, which is not covered by the CDC and ACC. It encompasses 90% of the particles produced in $\Upsilon(4S)$ decays and also provides fast timing signals for the Belle trigger system.

The TOF system consists of 128 TOF counters and 64 trigger scintillation counter (TSC) counters. Two trapezoidally shaped TOF counters and one TSC counter, with a 1.5 cm radial gap, form one module. There are 64 modules located at a radius of 1.2 m from the interaction point, covering a polar angle range of $34° < \theta < 120°$. Scintillation counters utilize the ionization produced by charged particles to generate optical photons. Scintillation light is collected by the fine mesh-type photo-multiplier tubes (FM-PMT). Two FM-PMTs are mounted directly on the scintillator and one FM-PMT on the TSC.

The TOF detector measures the time interval between a collision and the passage of a particle through it. Particles need only about 3 ns to travel the distance between the IP and the TOF counters. The time resolution of the TOF counters is about 100 ps, allowing 3σ separation between kaons and pions in the low momentum range below 1 GeV/c. The time of flight t of a particle is expressed as

$$t = \frac{l}{c\beta} = \frac{l}{c}\sqrt{1 + c^2(m/p)^2}, \tag{3.5}$$

where l, β, p, and m are the path length, the velocity, the momentum and the mass of the particle, respectively. Given the values of l and p, the measurement of t by the TOF counter provides identification of particles by calculating m. Figure 3.10 shows the configuration of a TOF module and Figure 3.11 shows the particle mass distribution calculated from TOF measurements for the particles with momentum less than 1.2 GeV/c. Clear peaks corresponding to $\pi^{\pm}$, $K^{\pm}$, and proton mass can be seen.

3.2.5 Electromagnetic Calorimeter (ECL) and extreme forward calorimeter (EFC)

The main purpose of the electromagnetic calorimeter (ECL) is the detection of photons from B meson decays with high efficiency and good energy and position resolution. It also plays a very important role in the electron identification as it depends on charged particle momentum and the energy deposit in the ECL. At high energy, when an electron or a photon hits a crystal, it produces an electromagnetic shower by pair production and bremsstrahlung. The ECL utilizes the generated shower for measuring the energy deposition and the position.

The ECL is a highly segmented array of 8736 tower-shaped CsI(Tl) crystals with silicon photodiode readout installed inside a superconducting 1.5 T solenoid magnet. The overall configuration of the ECL is shown in Figure 3.12. It consists of the barrel section of 3.0 m in length with an inner radius of 1.25 m and the annular end-caps at

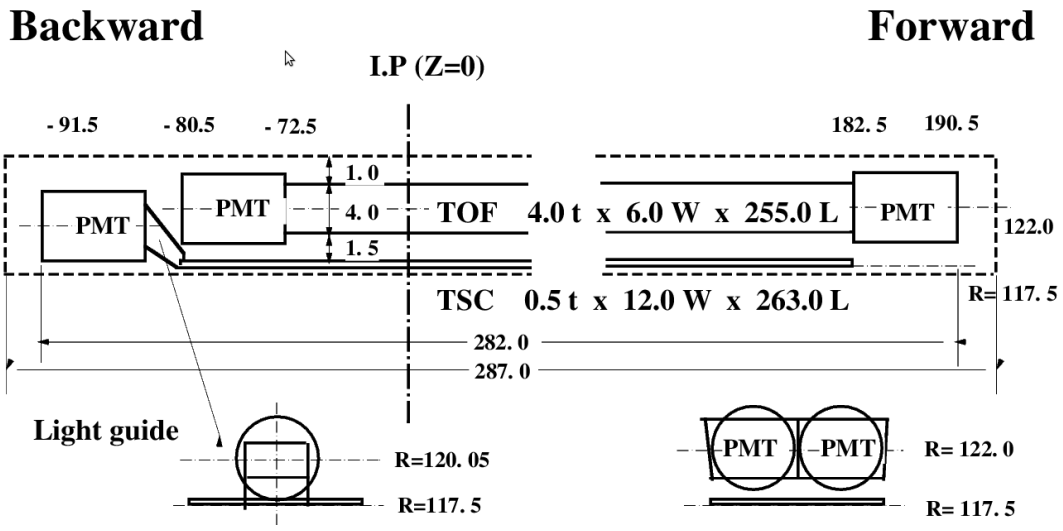

Figure 3.10: Configuration of a TOF module. Taken from Reference [27].

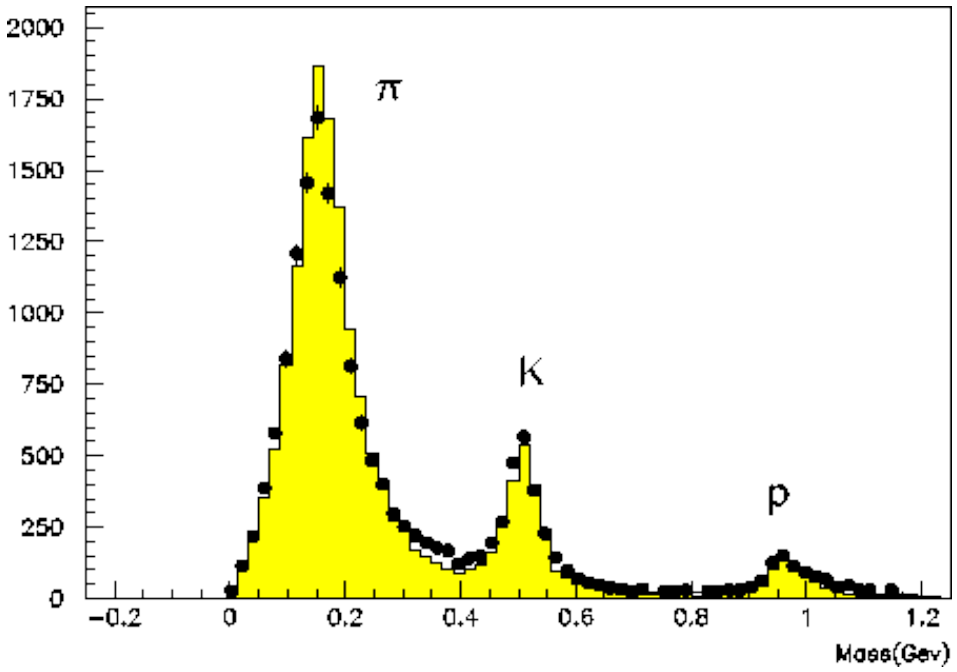

Figure 3.11: Mass distribution from TOF measurements for momenta below 1.2 GeV/c. Taken from Reference [36].

$z = +2.0$ and -1.0 m from the interaction point, covering the polar angle region of $17° < \theta < 150°$. The ECL has a total solid-angle coverage of 91% of 4π. The readout is based on an independent pair of silicon PIN (positive-intrinsic-negative) photodiodes and charge-sensitive preamplifiers attached at the end of each crystal.

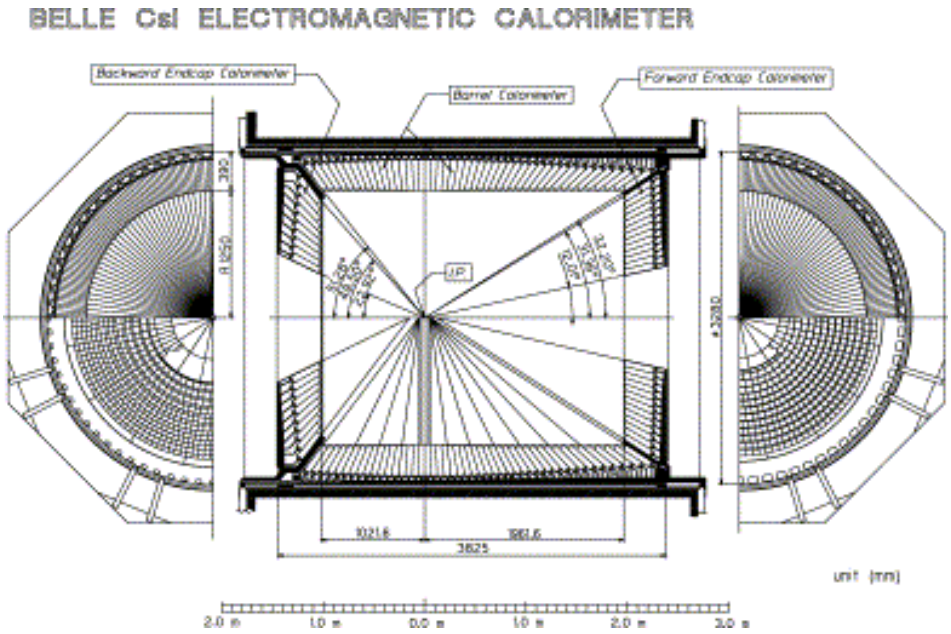

Figure 3.12: Configuration of a ECL module. Taken from Reference [27].

The designed energy and position resolutions as a function of photon energy E (GeV) are given by

$$\frac{\sigma_E}{E}\ (\%) = \frac{0.066}{E} \oplus \frac{0.81}{E^{1/4}} \oplus 1.34. \tag{3.6}$$

$$\sigma_{\rm pos} = \left(0.27 + \frac{3.4}{E^{1/2}} + \frac{1.8}{E^{1/4}}\right) \text{mm}. \tag{3.7}$$

Here, the first term is due to the contribution from electronic noise, second and a part of the third term comes from the shower leakage fluctuations and third term includes systematic effects such as the uncertainty of the calibration on crystals. After commissioning of KEKB collider, The energy resolution was achieved to be 1.7% for the barrel ECL, 1.74% and 2.85% for the forward and backward ECL, respectively [27].

The ECL is described in more detail in reference [37]. The extreme forward calorimeter (EFC) [38] extends the polar angle coverage from that of the ECL. The EFC covers an angular range from $6.4° < \theta < 11.5°$ in the forward direction and $163.3° < \theta < 171.2°$ in the backward direction to detect electrons and photons very close to the beam pipe. It also serves as a mask to reduce beam backgrounds in the CDC. In addition, the EFC is used for a beam monitor for KEKB and a luminosity monitor for Belle.

The schematic view of EFC is shown in Figure 3.13. The EFC is required to be radiation hard, since it is placed in a very high radiation level area around the beam pipe near the interaction point. So, the $Bi_4Ge_3O_{12}$ (BGO) crystal has been chosen which has the property of radiation hardness at the megarad level and has excellent e/γ energy resolution of $(0.3 - 1.0)\%/\sqrt{E}$ GeV. Both parts of EFC are composed of BGO crystals arranged into 5 regions in θ and 32 regions in the ϕ in order to provide better position resolution.

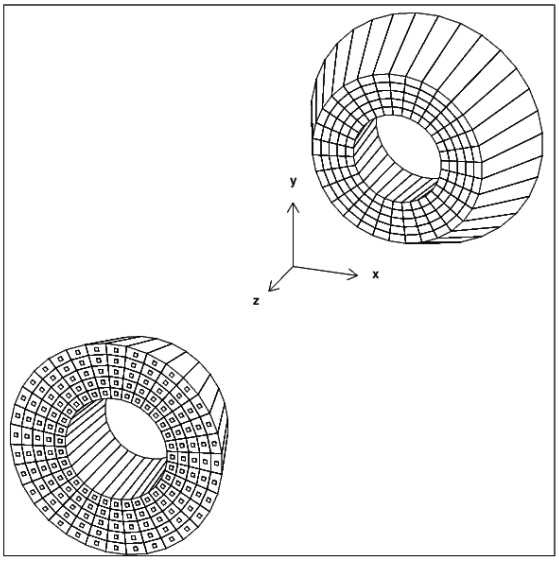

Figure 3.13: Configuration of an EFC module. Taken from Reference [27].

3.2.6 K_L and Muon Detector (KLM)

The KLM system [39] was designed to identify K_L^0 mesons and muons with high efficiency and low fake rate over a broad momentum range above 600 MeV/c. It consists of alternating layers of resistive plate counters (RPCs) also known as charged particle detectors and 4.7 cm thick iron plates. It is divided into a barrel KLM and end-caps (backward and forward) KLM. The barrel shaped region around the interaction point covers an angular range 45°- 125° in the polar angle and is made of 15 detector layers and 14 iron layers. The end-caps in the forward and backward directions extend this range to 20°- 155° and contains 14 detector and 14 iron layers. It is the only detector which is present outside the solenoid magnetic field. The RPCs have two parallel plate electrodes separated by a gas-filled gap. An ionizing particle traversing the gap induces a streamer in the gas that results in a local discharge. The discharge generates a signal on external pickup strips which can be used to record the location and the time of ionization.

Table 3.1: Trigger rates from various physics processes at $\Upsilon(4S)$ with $L = 10^{34}\text{cm}^{-2}\text{s}^{-1}$ [41].

Physics Process	Rate (Hz)
$\Upsilon(4S) \to B\bar{B}$	10.5
Hadron production from $e^+e^- \to q\bar{q}$	28
$e^+e^- \to e^+e^-$ and $e^+e^- \to \gamma\gamma$ (prescaled by 100)	5
$e^+e^- \to \mu^+\mu^-$ and $e^+e^- \to \tau^+\tau^-$	16
Beam background	$O(100)$
Cosmic ray background	20
Two-photon processes ($p_t > 0.3$ GeV/c)	35

The KLM iron plates provide 3.9 interaction length of material in addition to the 0.8 interaction length of the ECL. A K_L that interacts in the iron plates or ECL produces a shower of ionizing particles which is used to determine the flight direction of the K_L assuming that it comes from the IP. Compared to other strongly interacting hadrons, muons travel much farther with smaller deflections on average. This enables the multiple layers of charged particle detectors and iron to discriminate between muons and other charged hadrons based upon their range and transverse scattering.

The Muon identification efficiency is typically around 90% with a fake rate of around 3%.

3.3 The Trigger

The acquisition and storage of data from the Belle detector is carried out by the trigger. The role of the trigger is to store the interested physics events with high efficiency and forward them to the Data Acquisition (DAQ) system, at a rate less than the bandwidth of the data acquisition system, 700 Hz, and reject the uninteresting background events. The main source of such backgrounds come from collisions of beams with residual gas or with the beam-pipe, synchrotron radiation and cosmic ray. The DAQ transfers the interesting physics events such as hadronic, Bhabha, μ-pair, τ-pair and two photon events from the detector to the data storage system for further processing and analysis. The total trigger rate at an instantaneous luminosity of 10^{34} $\text{cm}^{-2}\text{s}^{-1}$ from various physical processes of interest at the $\Upsilon(4S)$ are listed in Table 3.1. At an instantaneous luminosity of 10^{34} $\text{cm}^{-2}\text{s}^{-1}$, the trigger rate for physics events of interest is around 100 Hz and the total rate is about 220 Hz. The rate of beam background events depends on the accelerator condition. To accommodate higher backgrounds, the trigger is designed to operate up to 500 Hz. Belle trigger system consists of level-1 (L1) hardware trigger and level-3 (L3) and level-4 (L4) software triggers.

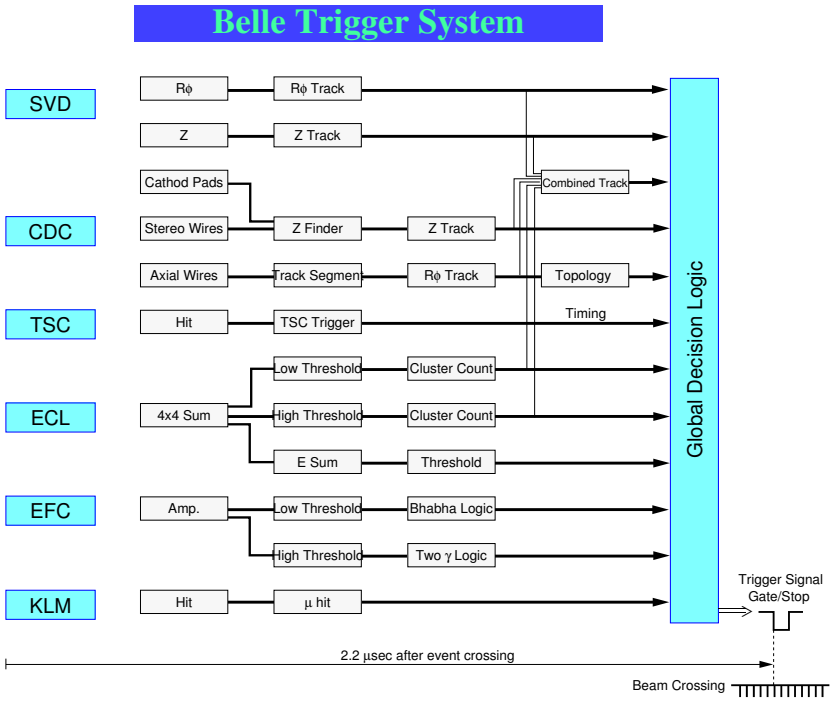

Figure 3.14: An overview of the L1 trigger. Taken from Reference [42].

3.3.1 The Level-1 (L1) Trigger

A schematic layout of the L1 trigger system is shown in Figure 3.14. It consists of the sub-trigger system governed by a central trigger system called the Global Decision Logic (GDL) [40]. By design, the GDL receives sub-detector triggers within 1.85 μs after the collision occurs. The L1 final trigger provides the trigger signal 2.2 μs after the collision. The GDL receives up to 48 trigger signals from sub-detectors and makes global correlations among them. There are trigger signals from the CDC, TOF, ECL, KLM and EFC systems as shown in Figure 3.14. The CDC is used to obtain trigger signals for charged particles. The TOF produces trigger signals for charged particles, based on the hit multiplicity and back-to-back topology. The ECL trigger consists of trigger cells (TC) composed of adjacent 4×4 crystals. ECL provides two kinds of trigger schemes: total energy trigger which is sensitive to events with high electromagnetic energy deposits and a cluster counting trigger sensitive to multi-hadronic events that contains low-energy clusters and minimum ionizing particles. The KLM detects muon hits using four layers of barrel and two layers of endcap parts and sends the trigger signals to the GDL. The EFC provides triggers on Bhabha ($e^+e^- \to e^+e^-$) and two-photon ($e^+e^- \to \gamma\gamma$) events.
GDL performs trigger logic operations and generates up to 48 types of event trigger signals. The GDL issues the final trigger 2.2 μs after the e^+e^- collision. The GDL has four main triggers that constitute the hadronic trigger:

- Two-track triggers: these triggers take the following information from the CDC-two tracks with $r-\phi$ and at least one track with z triggers and an open angle of at least 135°. This trigger also requires TOF hits and ECL clusters.
- Multi-track triggers: this is similar to the two-track trigger, but the CDC $r-\phi$ information is required for three or more tracks.
- Isolated clusters counting triggers: requires four or more isolated ECL clusters to suppress Bhabha events.
- Total energy triggers: these are based on the ECL energy sum triggers and vetoed by the ECL Bhabha and cosmic triggers.

Each of the multi-track, total energy, and isolated cluster counting triggers provide more than 96% efficiency for multi-hadronic samples and the combined multi-hadronic efficiency from all the triggers is found to be more than 99.5%.

3.3.2 Level-3 (L3) Triggers

The L3 trigger is a software trigger which stores raw data containing all sub-detector information. The L3 trigger first checks the L1 trigger information and passes some categories of events, such as Bhabha events and random trigger events. If an event does not belong to these categories, the L3 trigger performs a fast reconstruction and rejects events having no track with impact parameter $|z| < 5$ cm and events with energy less than 3 GeV deposited in the ECL. A large part of the beam background events are discarded by this procedure, which results in a 50% reduction of stored events while retaining an efficiency of more than 90% for hadronic and τ-pair events.

3.4 Data Acquisition System (DAQ)

The overview of the Belle DAQ system [43] is shown in Figure 3.15. The DAQ system records the L1 triggered events upto its limit of 500 Hz. To handle the data from each subdetector, the DAQ system is segmented into seven subsystems. In most subdetectors, signals correspond to pulses proportional to the deposited energy in the detector. These pulses are converted to times through a charge-to-time (Q-to-T) converter and these times are then digitized by a time-to-digital converter (TDC). Only the SVD uses flash analogue-to-digital converter (FADCs) instead of TDCs. For the KLM, only the timing information of the shower is recorded, hence a Q-to-T converter is not needed. When the sequence controller, receives a final GDL trigger signal, the data from each subdetector are combined into a single event by the event-builder, which converts "detector-by-detector" parallel data streams into "event-by-event" data. The output data of the event-builder is then transferred through the L3 trigger to the online computer farm. The quality of the data is monitored by the online data quality monitor in the online computer farm. Finally, the data is sent via optical fibers to the mass

storage system at the KEK computing center. The size of a typical hadronic event is about 30 kB, which corresponds to a maximum data transfer rate of 15 MB/s.

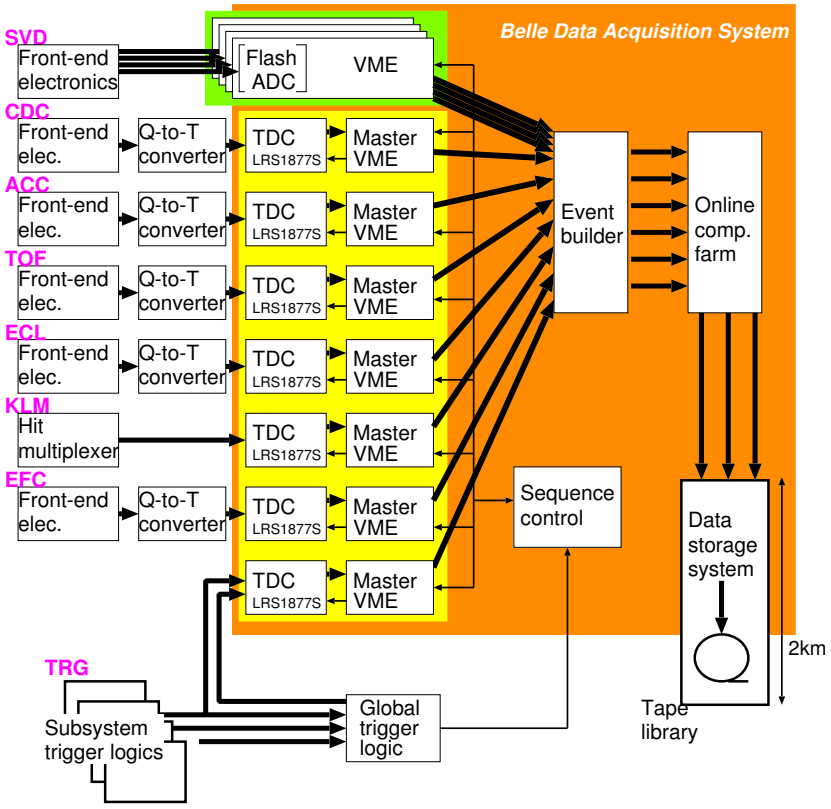

Figure 3.15: An overview of the DAQ system. Taken from Reference [27].

3.5 Level-4 trigger (L4) and Data Summary Tapes (DST) production

The L4 trigger is applied in the online computer farm to filter events from the raw data. It computes particle tracks, photon candidates and likelihoods for particle identification. The events filtered by the L4 trigger are reconstructed and the information is stored on data summary tapes (DST). The above trigger requires events with more than 4 GeV of energy deposited in the ECL and with at least one track with a transverse momentum greater than 300 MeV/c and impact parameter $|dr| < 1$ cm and $|dz| < 4$ cm. The L4 trigger then rejects about 78% of triggered events while keeping nearly 100% of B meson events. Events are then classified into several categories based on certain loose selection criteria and stored as skimmed data in Mini-DST (MDST) files. The analysis presented in this document uses HadronB skim data. The production and analysis of

the (M)DST data are performed in a C++ framework, known as the Belle Analysis Framework (BASF). BASF is also used for simulating data.

3.5.1 Monte Carlo (MC) simulation

Monte Carlo (MC) simulation plays an important role in physics analysis. The detector is simulated using the MC techniques. Events are generated for a specific physics process using EvtGen program [44] and then they are reconstructed as simulated data using the response of the Belle detector modeled by a GEANT3-based full-simulation program [45]. The simulated data are then analyzed with the same procedure as is used for the real data by preparing standard reconstruction module for each subdetector. Using this information, reconstruction codes are written to identify specific decay channels and to produce physics outputs.
There are around 29 streams of simulated data stored for analysis, where one stream corresponds to simulated data whose luminosity is equivalent to $\Upsilon(4S)$ real data set. One can create one full stream of simulated data by adding one stream of charged (B^+B^-) with one stream of neutral ($B^0\bar{B}^0$) and continuum ($q\bar{q}$) simulated events.

Chapter 4

Event selection and continuum suppression

In this chapter, we discuss the reconstruction of B mesons for the favored and suppressed $B^{\pm} \to DK^{\pm}$ modes. We also analyzed favored and suppressed $B^{\pm} \to D\pi^{\pm}$ modes as reference mode because of the kinematic similarity to $B^{-} \to DK^{-}$ and its much larger branching fraction. The observables for the $B^{\pm} \to D\pi^{\pm}$ mode are $R_{D\pi}$ and $A_{D\pi}$. They can be defined using Eqs. 2.32 and 2.34 with the following substitutions: $K \to \pi$ for the B daughter, $r_B \to r_B^{D\pi}$, and $\delta_B \to \delta_B^{D\pi}$. Here, $r_B^{D\pi}$ and $\delta_B^{D\pi}$ are the absolute ratio and strong-phase difference between the suppressed and favored $B^{-} \to D\pi^{-}$ decay amplitudes. The sensitivity to ϕ_3 is reduced in this mode because $r_B^{D\pi}$ is approximately an order of magnitude smaller than r_B.

Possible backgrounds are analyzed and their suppression is also studied. We implement special multivariate technique to reject the huge continuum background relative to the above suppressed decays.

4.1 Event selection

The event selection criteria are determined by an optimization technique using MC events. The selection criteria are the same for both favored and suppressed modes.

4.1.1 Data and Monte Carlo samples

The data sample used in the analysis is that of the full Belle running at the $\Upsilon(4S)$. It corresponds to 772×10^6 $B\overline{B}$ pairs.

Signal Monte Carlo (MC) samples are produced using the EvtGen program for event generation [46, 47]. Generated events are passed through the detector simulation using gsim (Detector response GEANT3 simulation) [46, 47] package. We generate 10^6 events for each of the favored and suppressed $B^{\pm} \to DK^{\pm}$ modes. We also generate 10^6 events for each of the favored and suppressed $B^{\pm} \to D\pi^{\pm}$ control channel. Samples of generic

$B\overline{B}$ and continuum MC are also used to develop the selection and fitting algorithms. Table 4.1 lists the various generic MC samples used in the analysis.

Table 4.1: Summary of generic MC samples that are used. The number of available streams is also given.

Generic MC Type	Number of streams Used	Available
$q\overline{q}$	5	6
B^+B^-	5	10
$B^0\overline{B}^0$	5	10

4.1.2 Event Reconstruction

To begin we give a brief overview of the selection procedure. We reconstruct signal candidates, by first identifying well measured $K^\pm$, $\pi^\pm$ and π^0 candidates. These particles are used to reconstruct $D \to K^\pm\pi^\mp\pi^0$ candidates, which are then combined with either K^+ or π^+ to form $B^+ \to DK^+$ or $B^+ \to D\pi^+$ candidates. At this stage a single B candidate is retained in each event. The dominant background arises from $e^+e^- \to q\overline{q}$ continuum events. This background is suppressed by using a multivariate discriminant. The overall approach is similar to that for the measurement of $B \to [K\pi]_D K$ [48].

Track Selection

We define good charged tracks by requiring $|dr| < 0.2$ cm and $|dz| < 1.5$ cm, where dr and dz represent the distance of closest approach to the nominal interaction point in the x-y plane and along the z-axis, respectively. This eliminates poorly reconstructed tracks or tracks that do not come from the interaction region.

Reconstruction of the π^0 mesons

π^0 meson candidates used to reconstruct the neutral D meson decaying to $K^\pm\pi^\mp\pi^0$ final state, are reconstructed from photon pairs detected in the ECL. The energy of each photon is greater than 50 MeV in the barrel and endcap ECL and the pair has an invariant mass between 120 MeV/c^2 $< M_{\gamma\gamma} <$ 145 MeV/c^2 which corresponds to approximately $\pm 3.2\sigma$ in resolution around the nominal π^0 mass [8]. The π^0 mass (M_{π^0}) distribution for signal MC and data are shown in Fig. 4.1. The momentum of a π^0 candidate in the e^+e^- center-of-mass (CM) frame is required to be greater than 400 MeV/c. We apply a mass-constrained fit to the π^0 candidate to improve its momentum resolution.

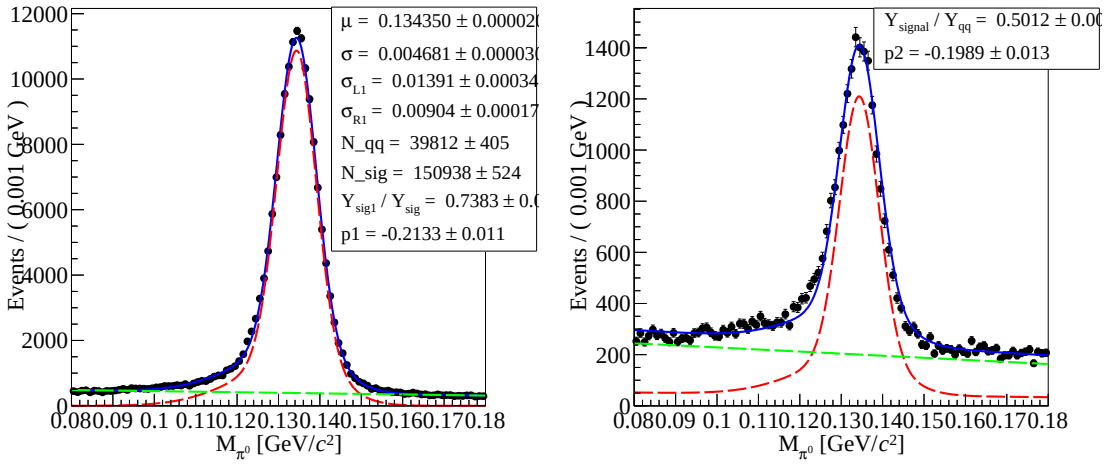

Figure 4.1: Distribution of M_{π^0} without mass constraint fit using signal MC (left) and data (right). Signal PDF parameter values in data have been fixed from signal MC. For signal MC, the blue line shows the total fit, the red line shows the fit to true signal candidates and green line shows the combinatoric events. For data, the blue line shows the total fit, the red line shows the fit to signal candidates and green line shows the continuum events.

Reconstruction of the neutral D mesons

The D meson candidates are reconstructed from pairs of oppositely charged tracks and a π^0 candidate. Each track must have a distance of closest approach to the interaction point of less than 0.2 cm in the plane transverse to the positron beam direction and less than 1.5 cm along the positron beam axis. We also define L_K (L_π), the likelihood of a track being a kaon (pion), based on particle identification (PID) information [49] from the ACC and the TOF, combined with specific ionization measured in the CDC. We apply likelihood-ratio requirements of $L(K/\pi) = \frac{L_K}{L_K+L_\pi} > 0.6$ for a kaon candidate and $L(K/\pi) < 0.4$ for a pion candidate. The efficiency to identify a kaon (pion) is approximately 83% (88%) averaged over momentum and the probability of misidentifying a pion (kaon) as a kaon (pion) is approximately 8% (7%). The D mass (M_D) distribution for signal MC and data are shown in Fig. 4.2. The correctly reconstructed signal distribution is modeled by the Crystal Ball function [50], whereas combinatoric D^0 candidate distribution is modeled by a 2$^{\text{nd}}$-order Chebyshev polynomial. Using the results of the fit to the M_D distribution to these two functions we define the asymmetric signal region around $\pm 2.5\sigma$ around the nominal mass: $1.804\ \text{GeV}/c^2 < M_D < 1.885\ \text{GeV}/c^2$. For selected candidates a D-mass constraint fit is applied to improve the four momenta resolution of the daughters.

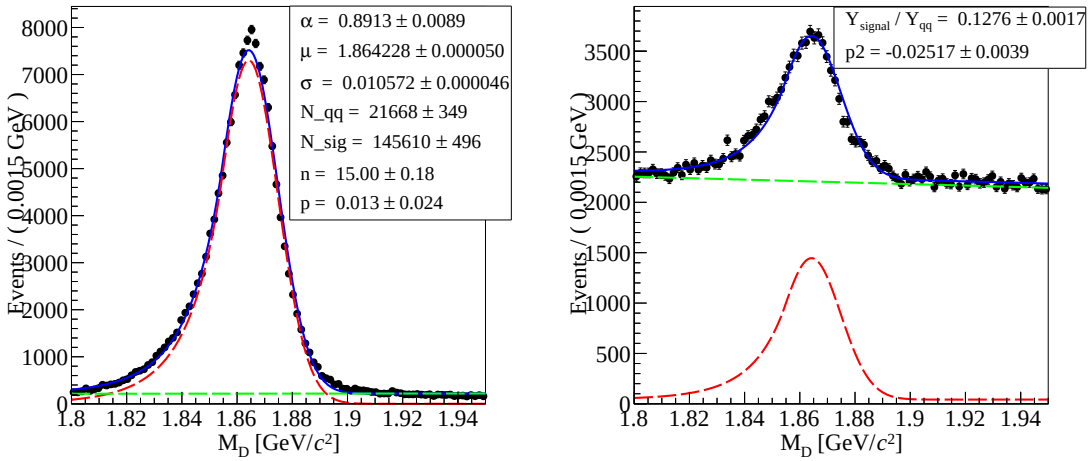

Figure 4.2: Distribution of M_D without mass constraint fit using signal MC (left) and data (right). Signal PDF parameter values in data have been fixed from signal MC. For signal MC, the blue line shows the total fit, the red line shows the fit to true signal candidates and green line shows the combinatoric events. For data, the blue line shows the total fit, the red line shows the fit to signal candidates and green line shows the continuum events.

Reconstruction of the charged B mesons

A B meson candidate is reconstructed by combining D meson candidate with a charged K or π meson. The PID likelihood cut is also applied to B daughters. The B meson is identified by using two independent variables: the beam-energy-constrained mass ($M_{\rm bc}$) and the energy difference (ΔE) defined in the CM frame, as $M_{\rm bc} = c^{-2}\sqrt{E^2_{\rm beam} - |\vec{p}_B|^2c^2}$ and $\Delta E = E_B - E_{\rm beam}$, where $E_{\rm beam}$ is the beam energy and $\overrightarrow{p}_B$ (E_B) is the momentum (energy) of the B meson candidates. For $B \to Dh$ ($h = K/\pi$) decays, $M_{\rm bc}$ peaks at the nominal mass of the B meson [8] A typical $M_{\rm bc}$ and ΔE distributions for signal MC events are shown in Fig. 4.3. Continuum background events have a different $M_{\rm bc}$ and ΔE distribution. A typical distribution for continuum events, obtained using off-resonance data, is shown in Fig. 4.4. We select signal B candidates in the ranges $5.27\ {\rm GeV}/c^2 < M_{\rm bc} < 5.29\ {\rm GeV}/c^2$ and $-0.1\ {\rm GeV} < \Delta E < 0.2\ {\rm GeV}$.

Best Candidate Selection

After applying all selection criteria there are sometimes multiple candidates per event. The distribution of the candidate multiplicity in signal MC is shown in Fig. 4.5. The average candidate multiplicity is 1.065. We require one candidate per event selected on

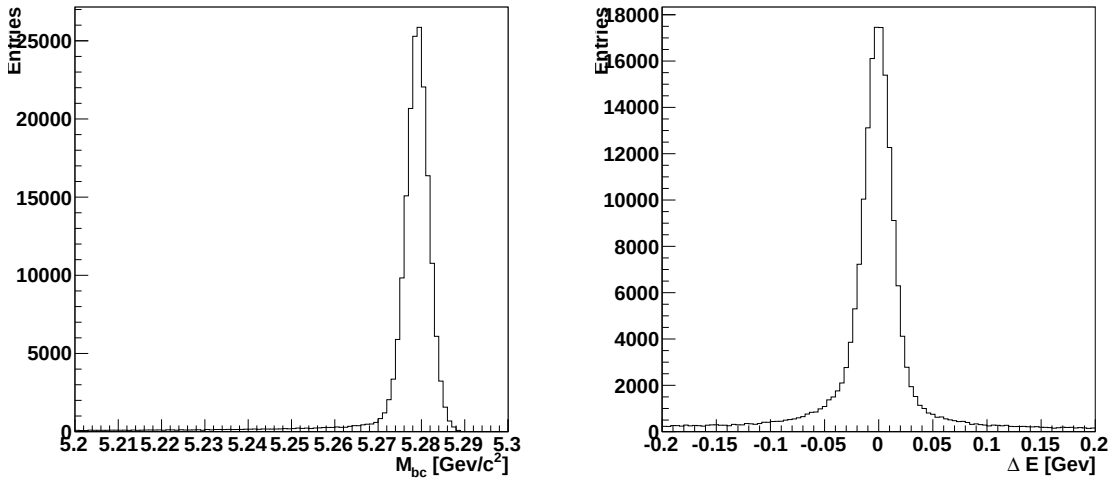

Figure 4.3: $M_{\rm bc}$ (left) and Δ E (right) distribution obtained using signal MC.

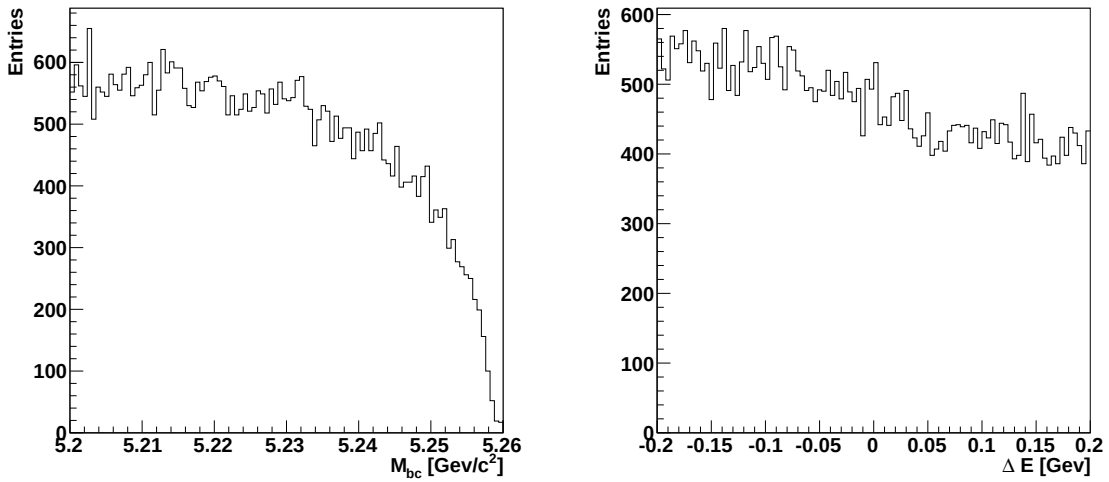

Figure 4.4: $M_{\rm bc}$ (left) and Δ E (right) distribution obtained using off-resonance data.

the basis of minimum χ^2 defined as

$$\chi^2 = \left(\frac{M_D - \mu_D}{\sigma^+{}_D}\right)^2 + \left(\frac{M_{\rm bc} - \mu_{bc}}{\sigma_{\rm bc}}\right)^2 \ (M_D > \mu_D) \tag{4.1}$$

and

$$\chi^2 = \left(\frac{M_D - \mu_D}{\sigma^-{}_D}\right)^2 + \left(\frac{M_{\rm bc} - \mu_{\rm bc}}{\sigma_{\rm bc}}\right)^2 \ (M_D < \mu_D)\ , \tag{4.2}$$

where μ_D ($\sigma_D^{\pm}$) is the mean (width) of the Crystal Ball fit to the M_D distribution described in Sec. 4.1.2, $\mu_{\rm bc}$ ($\sigma_{\rm bc} = 2.68$ MeV/c^2) is the mean (width) of a Gaussian fit to the signal MC $M_{\rm bc}$ distribution. Here $\sigma_D^+ = 8.95$ MeV/c^2 and $\sigma_D^- = 22.13$ MeV/c^2.

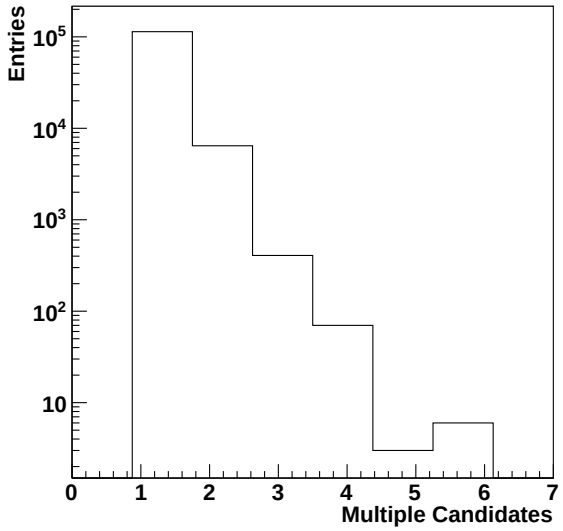

Figure 4.5: B candidate multiplicity in log scale using signal MC.

Background vetoes

Two vetoes are applied to remove specific backgrounds. These vetoes reject combinatoric events where the D^0 comes from a $D^{*\pm}$ decay and events where both the K^- and π^+ daughters of the D^0 are misidentified. We refer to the second type of background as double mis-ID.

***D*$^{*\pm}$ veto:** To suppress the background coming from $D^{*\pm} \to D\pi^{\pm}$ decays in $e^+e^- \to c\bar{c}$, we use a variable ΔM defined as the mass difference between the $D^{*\pm}$ and D^0 candidates. We reconstructed $D^{*\pm}$ from the D meson used for B reconstruction and a $\pi^{\pm}$ candidate not used in B reconstruction. If there are multiple $\pi^{\pm}$ candidates, we select a $\pi^{\pm}$ candidate so that the ΔM value is very close to 0.142. No PID cut is applied

on $\pi^{\pm}$ because of its low momentum when coming from the $D^{*\pm}$ decay. By applying the requirement $\Delta M > 0.15$ GeV/c^2, we remove 99% of $D^{*\pm}$ backgrounds and 17% of all $c\bar{c}$ backgrounds. The relative loss of signal efficiency is 3.4%. Fig. 4.6 shows the distribution of ΔM for signal and $c\bar{c}$ background.

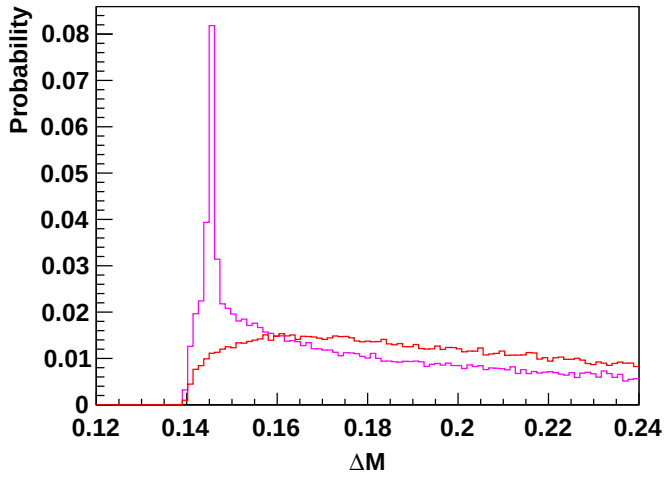

Figure 4.6: Distribution of ΔM for signal (red) and $c\bar{c}$ background (magenta). The distribution is not truth matched, so signal has a long tail just when a slow pion not from the $D^{*\pm}$ is combined with the D candidate to form ΔM.

Double mis-ID veto: A possible source of peaking background is the favored $B^- \to [K^-\pi^+\pi^0]_D h^-$ ($h = K$ or π) decay, which can contribute to the signal region of the respective suppressed decay and vice versa, due to misidentification of both the K^- and π^+ mesons in the D decay. To reject this background, we veto events satisfying 1.804 GeV/c^2 $< M_{K\pi\pi^0} <$ 1.885 GeV/c^2 when the mass assignments of the K^- and π^+ are exchanged. This criterion reduces the background to a negligible level with a relative loss of signal efficiency of around 17%. Fig. 4.7 shows the distribution of ΔE for the peaking background in the suppressed modes before and after applying vetoes. The fitting function used to extract the background yield from the ΔE distribution is described in Section 5.2.

Table 4.2 gives the efficiency and background before and after applying double-mis-ID veto. Though we do not need double-mis-ID veto for favored $B \to Dh$ decays, it is still applied to keep the efficiency consistent with the suppressed $B \to Dh$ decays. The remaining double mis-ID background is at a negligible level after the application of the veto.

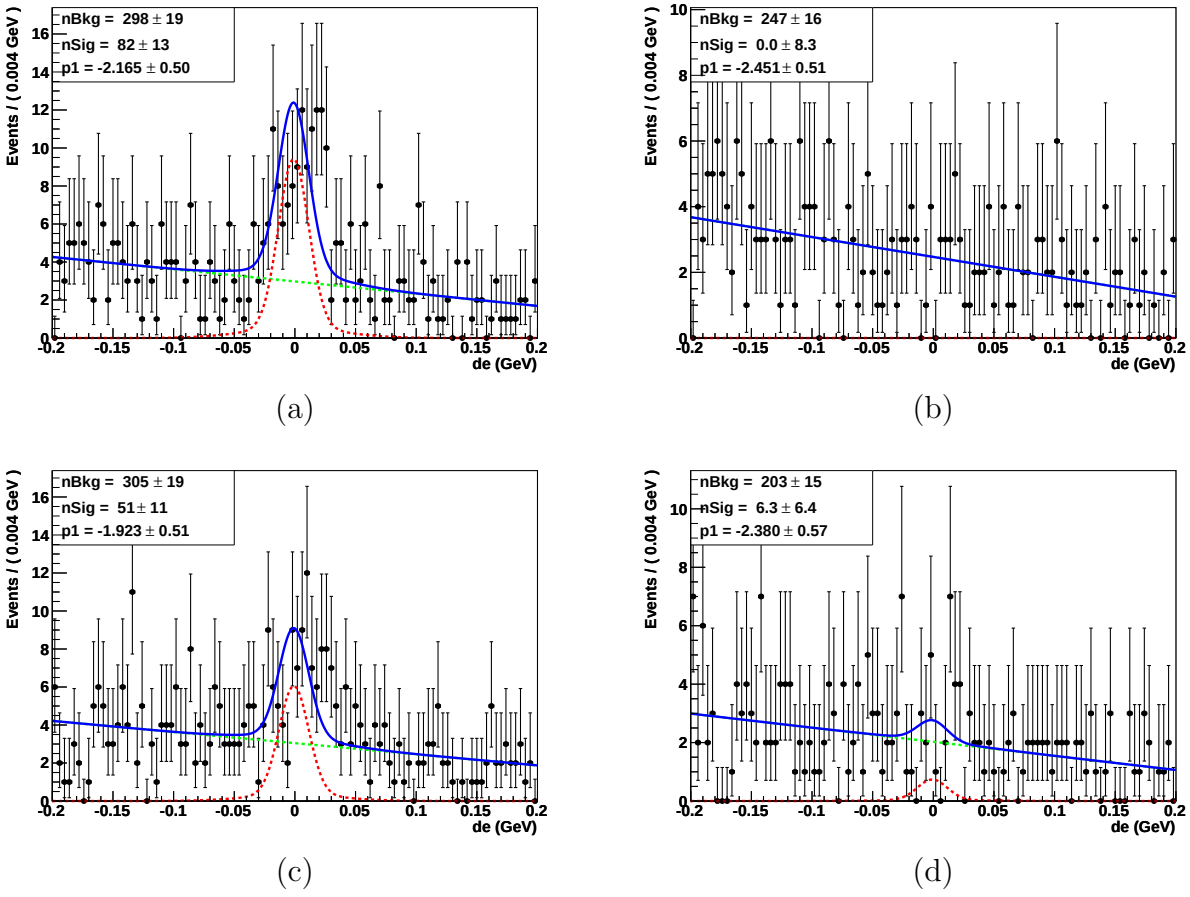

Figure 4.7: Distributions of the double mis-ID peaking background (a) [(c)] before and (b) [(d)] after the application of the veto for the suppressed $B^- \to D\pi^-$ and $[B^- \to DK^-]$ decays, using signal MC.

Table 4.2: Efficiency and expected peaking background yield before and after the double mis-ID veto. The expected background is scaled to the luminosity of the data set. The yield for the $D\pi$ peaking background in data is about two times larger than the MC result. The ratio is found to be 1.89±0.07, using the Belle-official PID calibration factor, which uses $D \to K\pi$ data to calibrate the misidentification rates. So the possible data/MC difference (1.89) in $M(K\pi\pi^0)_{\text{exchange}}$ distribution is taken in to account.

Decay	Efficiency (%)		Peaking background yield	
	Before veto	After veto	Before veto	After veto
$B \to D\pi$ favored	15.3	12.6	0.54 ± 0.05	0.25 ± 0.03
$B \to D\pi$ suppressed	15.4	12.7	85.82 ± 13.62	0.0 ± 8.7
$B \to DK$ favored	14.0	11.6	0.034 ± 0.003	0.005 ± 0.002
$B \to DK$ suppressed	14.0	11.6	4.06 ± 0.87	0.50 ± 0.51

4.2 Continuum Suppression

The dominant background comes from $e^+e^- \to q\bar{q}$ ($q = u,\ d,\ s,$ or c) continuum events. For continnum events a small proportion of beam enerngy goes towards initial $q\bar{q}$ production, so these events have higher momentum and hence topologically different from $B\overline{B}$. Therefore, $B\overline{B}$ events are spherical in the $\Upsilon(4S)$ rest frame for signal and jet-like for continuum events as shown in Fig. 4.8. To distinguish between the signal

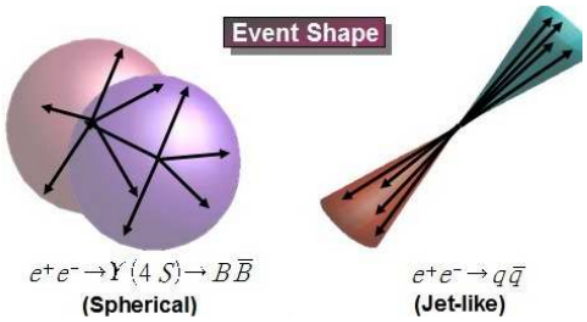

Figure 4.8: Event shape distribution of $B\overline{B}$ (left) and $q\bar{q}$ (right)

and the background we use a neural-network method based on nine variables that are described below [48, 53].

4.2.1 Variables used to suppress continuum

- ROOKSFW: are shape variables called Kakuno-san's modified Super Fox Wolfram moments [51]. The ROOT-based ROOKSFW package is used to calculate the moments. In calculating the KSFW moments, the missing momentum is treated as one additional particle. The variable definition is given in Appendix A. We define a likelihood ratio of KSFW (LR(KSFW)) defined as $L^{\rm sig}_{\rm KSFW}/(L^{\rm sig}_{\rm KSFW} + L^{\rm bkg}_{\rm KSFW})$. The distribution is peaked at one for the signal and zero for the background.

- ΔQ: is the difference between the sum of the charges of particles in the hemisphere about the D candidate direction and the sum of charges in the opposite hemisphere. Particles used for the reconstruction of B mesons are excluded from the calculation. Signal events peak around zero while $c\bar{c}$ are slightly shifted from zero.

- $Q_B Q_K$: is the product of the charge of the B candidate and the sum of the charges of all kaons not used for the reconstruction of the B candidate. $q\bar{q}$ events peak around zero while signal events are slightly lower than zero.

- $\cos\theta_B$: the cosine of the angle between the B-flight direction and the beam axis. For the $e^+e^- \to B\overline{B}$ decay the polar angle distribution of the B candidate in the CoM frame follows a $1 - \cos^2\theta$ distribution, whereas for continuum events it is flat.

- Δz: is the vertex separation between the B candidate and the remaining tracks. The absolute value tends to be larger for the signal than the background, since the B meson has a larger lifetime.

- $|\cos\theta_T|$: is the absolute value of the cosine of the angle in CoM frame between the thrust axis of the B decay and the one of the other particles in the event. The distribution is flat for signal events, but has a strong peak towards one for continuum events.

- $|r|$: is the absolute value of B flavor tagging information [52]. It also uses information about charge of leptons and kaons not associated with the signal decay. Signal have more events with $|r| \sim 1$ than background. $|r| \to 1$ indicate the candidate is likely to be a B event, while $|r| \to 0$ is continuum.

- $\cos\theta_D^K$: is the cosine of the angle between the daughter K direction and the opposite direction to B in the D-rest frame. Signal events have a uniform distribution while $q\overline{q}$ events accumulate near ± 1.

- $\cos\theta_B^D$: is the cosine of the angle between D direction and the opposite direction to $\Upsilon(4S)$ in the B-rest frame. The distribution is nearly flat for the signal, while it peaks slightly around one for the continuum background.

The distributions of all the variables used for discrimination are shown in Fig. 4.9. Due to the presence of continuum background within the signal region the data do not match the MC events. Therefore, 23% scaled continuum MC is added to the signal MC so that the distributions can be better compared to the data.

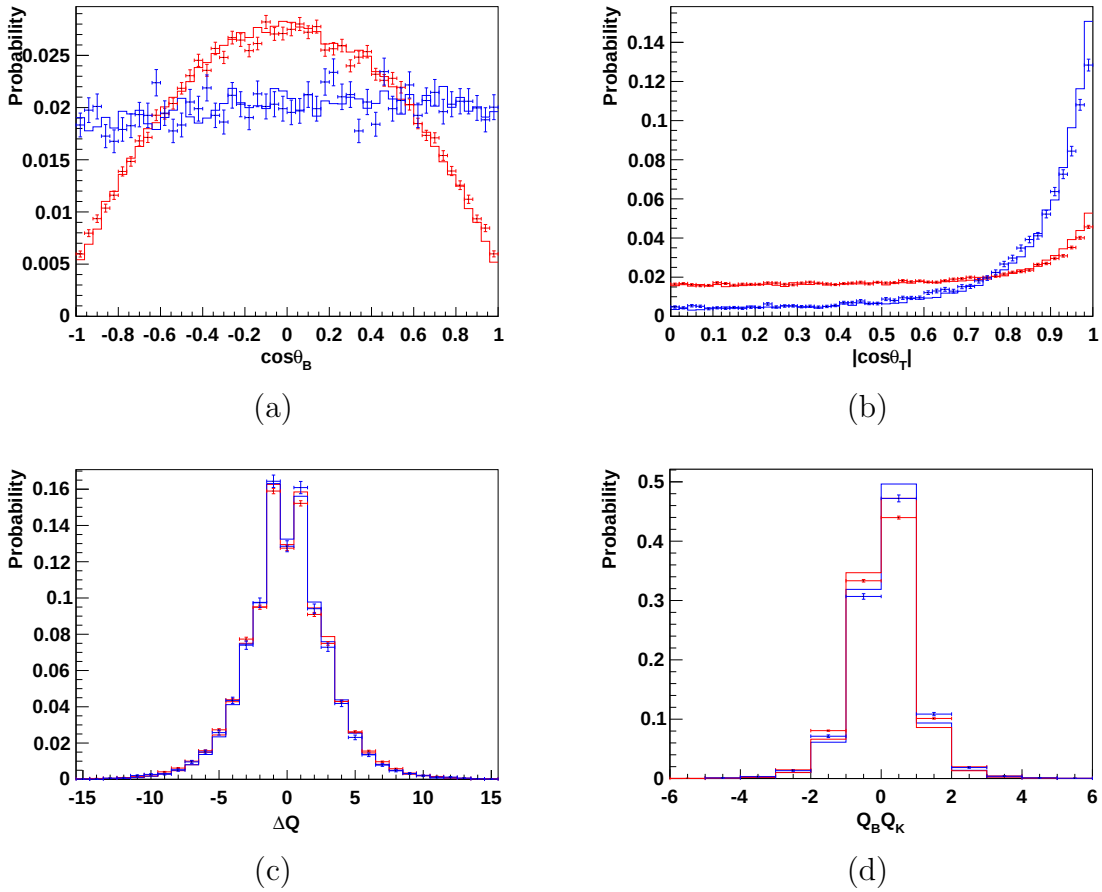

Figure 4.9: Distributions of the shape variables: (a) $\cos\theta_B$, (b) $|\cos\theta_T|$, (c) ΔQ, (d) $Q_B Q_K$. Red curve corresponds to signal MC, blue curve for $q\overline{q}$ ($q = u, d, s, c$), red points with error bars for favored $B \to D\pi$ data sample ($|\Delta E| < 0.05$ GeV) and blue points with error bars for sideband in the favored $B \to D\pi$ data sample ($\Delta E > 0.15$ GeV). Here in order to match MC and data we added appropriately scaled continuum to the signal MC and appropriated scaled combinatorial $B\overline{B}$ background to the continuum MC.

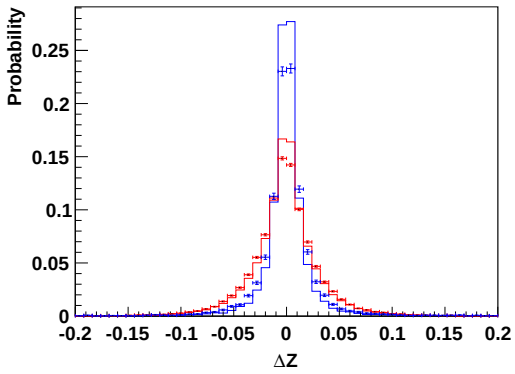

(e)

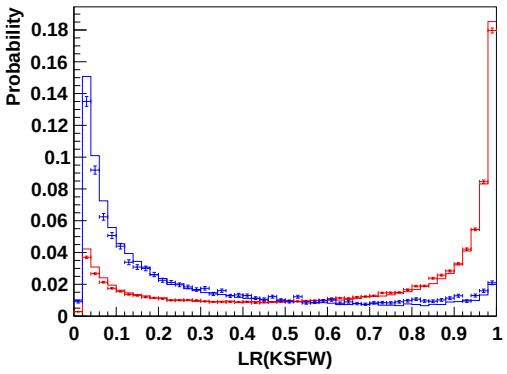

(f)

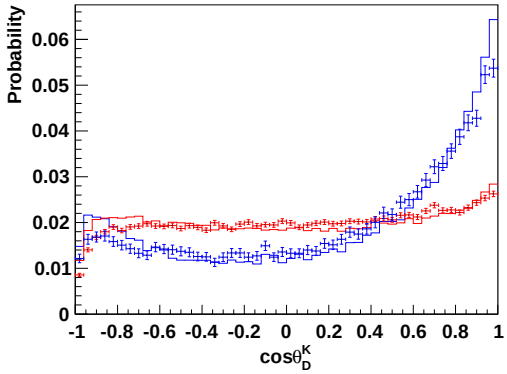

(g)

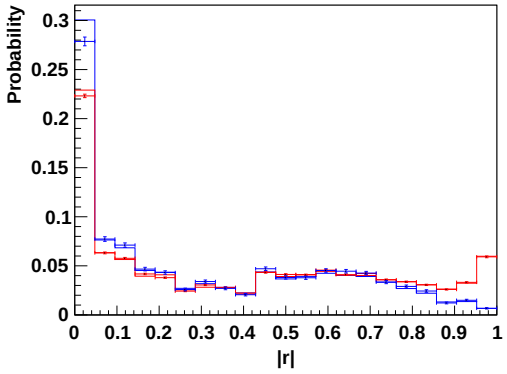

(h)

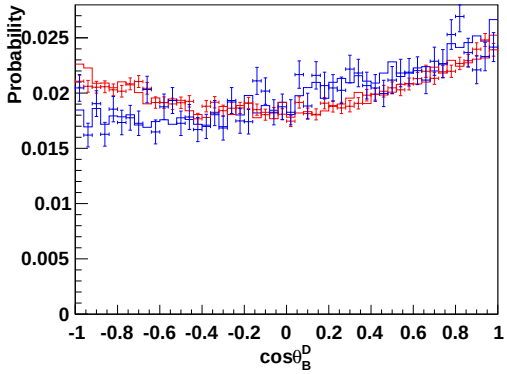

(i)

Figure 4.10: Distributions of the shape variables: (e) Δz, (f) RooKSFW likelihood ratio, (g) $\cos\theta_D^K$, (h) $|r|$ and (i) $\cos\theta_B^D$. The color legend and histogram components are the same as those in Fig. 4.9.

4.2.2 Neural Network Method

Neurobayes Neural Network package [53] is a multivariate algorithm used for the analysis of many variables which may be correlated. A simple cut based selection to reduce the background using these variables would lead to a very low efficiency. This is a good tool to maximize the separation between the signal and background. First the network topology and the input variables are set up. Then the training patterns are read in and the actual training is performed. After the training is completed, the network is saved for further use. The network consists of three layers (input, hidden, and output layers) that are combined with the preprocessors of the input variables to provide a powerful classification between the variables and to give a stable output. The output which is the function of all the input variables gives a very good discrimination between signal and background. The preprocessors used, compute the significance of the variables and rank them according to their importance. The result of NeuroBayes output (NB) is shown in Fig. 4.11.

The samples used for the training are the signal and the $q\overline{q}$ MCs, each of which contains 133,898 events after the event-selection requirements described in Sec. 4.1.2.

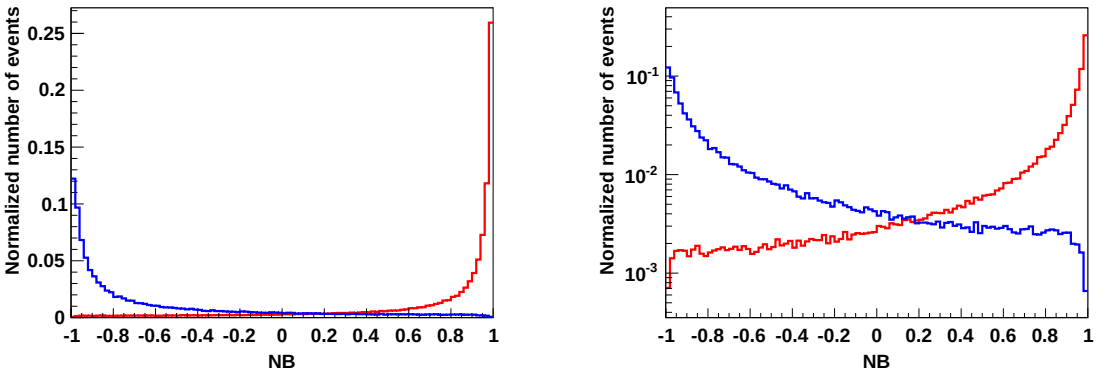

(a) (b)

Figure 4.11: (a) Distribution of NeuroBayes output (NB) for signal (red) and $q\overline{q}$ (blue) MC samples. (b) Same distribution with a log scale.

Significance of the variables used for training

Table 4.3 shows the significance of the variables used for training. In the table "Only this" means the significance of the single variable and "Signi. loss" means the significance loss when removing that variable while using the remaining eight. Significance is more for the variables which show a clear separation between signal and background.

Table 4.3: Significance of the variables input to the neural network.

Variables	Only this (σ)	Signi. loss (σ)	Correlation
LR(KSFW)	0.886	0.329	0.80
$\lvert\cos\theta_T\rvert$	0.787	0.142	0.78
Δz	0.499	0.243	0.28
$\cos\theta_D^K$	0.387	0.171	0.23
$\lvert r\rvert$	0.320	0.093	0.40
$\lvert\cos\theta_B\rvert$	0.323	0.145	0.20
$\cos\theta_B^D$	0.030	0.014	0.06
$Q_B Q_K$	0.061	0.003	0.29
ΔQ	0.023	0.004	0.14

Overtraining check

Overtraining is defined as a bias in the network output due to the limited statistics of the training sample. To check for overtraining of the network we produce the distribution of the neural network output for samples not used in the training. Figure 4.12 compares these samples to the output from the training sample. Given that the two distributions are in agreement there is no evidence for overtraining.

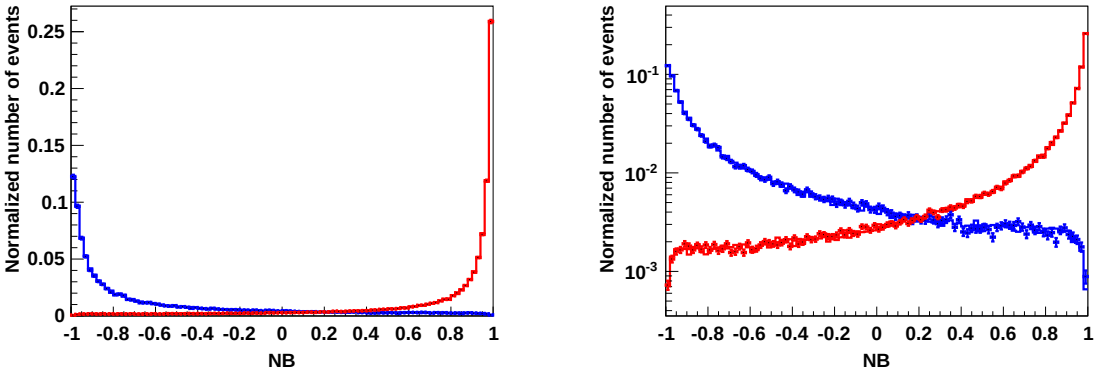

(a) (b)

Figure 4.12: (a) Training output result (histogram) and test result for independent MC sample (points with error bars) for signal (red) and $q\overline{q}$ background (blue). (b) Same figure on a logarithmic scale.

Transformation of the NB output

Ideally the NB output should be in a form that is easy to describe using an analytic probability density function in the fit to extract the signal yield (see Chapter 5). Therefore, the neural network output NB is transformed to a new variable (NB′) using:

$$\mathrm{NB}' \;=\; \log\left(\frac{\mathrm{NB}-\mathrm{NB}_{\mathrm{low}}}{\mathrm{NB}_{\mathrm{high}}-\mathrm{NB}}\right) \;,$$

where $\mathrm{NB}_{\mathrm{low}} = -0.6$ and $\mathrm{NB}_{\mathrm{high}} = 0.9995$. Figure 4.13 shows the distribution of NB′ for signal and background. Applying a cut on NB at $\mathrm{NB}_{\mathrm{low}} = -0.6$, we reject 70% of background at a 3% loss of the signal efficiency. The distribution of NB′ can be easily described by Gaussian or bifurcated-Gaussian functions.

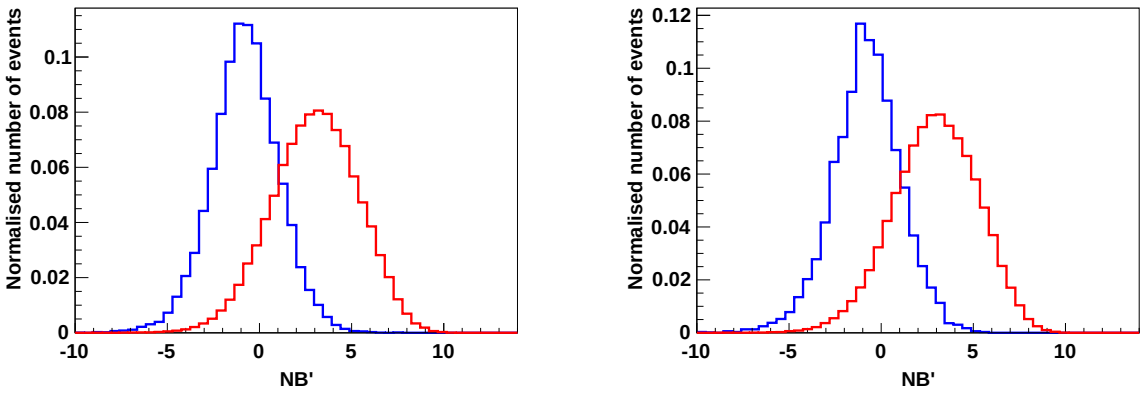

(a) (b)

Figure 4.13: The transformed NB distribution for (a) $B \to [K\pi\pi^0]_D\pi$ and (b) $B \to [K\pi\pi^0]_D K$. Red curve corresponds to signal MC, blue curve for continuum MC.

Chapter 5

Signal Yield Determination

In this chapter we give a brief introduction into the concept of the maximum likelihood fit, which is used to obtain the values of the physical observables presented here. We then discuss about the parametrization of different components of the two independent variables, ΔE and NB$'$. We first fit each component to MC samples of the appropriate type to decide the PDF to use. The components of the whole MC sample are divided in to the Dh signal, peaking background, $B\overline{B}$ background and $q\overline{q}$ background. Then we describe the signal yield extraction, which uses unbinned extended maximum-likelihood fits to ΔE and NB$'$. Separate fits are performed for favored and suppressed modes. Finally, we describe the estimation of the rare peaking background in the signal region and the fit-bias check for the suppressed D modes.

5.1 Introduction to Maximum Likelihood Fit method

The maximum likelihood (ML) is a powerful method for estimating the parameters of a given statistical model. For a model $f(x;\lambda)$, with x being a set of observables in the data, λ is the unknown parameter whose value is to be estimated, the likelihood method estimates the best fit of the model to the data distribution. For a continuous random sample $x_1, x_2, ..., x_n$, we define

$$f(x_1, x_2, ..., x_n; \lambda) = f(x_1; \lambda).....f(x_n; \lambda). \tag{5.1}$$

Here $f(x_1, ..., x_n; \lambda)$ is the joint density function also called as likelihood function often denoted as:

$$L(x_1, x_2, ..., x_n; \lambda) = f(x_1, x_2, ..., x_n; \lambda) = \prod_{i=1}^{n} f(x_i; \lambda) \tag{5.2}$$

For our convenience, we use the logarithm of the likelihood function, called the log-likelihood:

$$\ln L(x_1, x_2, ..., x_n; \lambda) = \sum_{i=1}^{n} \ln f(x_i; \lambda) \tag{5.3}$$

We use the minimum of the negative log-likelihood function to obtain the most likely estimator for the parameters of interest λ. Furthermore, we use an extension of the the likelihood function, if data distribution consists of several components, such as signal and background, each with its own model. Taking this into account, we define the log-likelihood function of an unbinned extended ML fit, as it is used in this analysis:

$$\mathcal{L}(\lambda) = \ln L(\lambda) = \sum_{i=1}^{n} \ln\left\{ \sum_{j=1}^{x} N_j f_j(x_i;\lambda) \right\} - \sum_{j=1}^{x} N_j - \ln(\mathrm{N!}), \tag{5.4}$$

where x is the number of different components present in the data set, N_j is the expected number of events for the j^{th} component, f_j is the model/PDF for the j^{th} component, and N is a constant. The extended ML estimator for the parameter λ_k, is that value of λ_k for which extended $\mathcal{L}(\lambda_k)$ is maximum. The above can be obtained by solving the equation:

$$\frac{d(\mathcal{L}(\lambda_k))}{d\lambda_k} = 0, \text{where } \mathcal{L}(\lambda_\mathrm{k}) = \ln\mathrm{L}(\lambda_\mathrm{k}) = \sum_{\mathrm{i}=1}^{\mathrm{n}} \ln\left\{ \sum_{\mathrm{j}=1}^{\mathrm{x}} \mathrm{N_j f_j}(\mathrm{x_i};\lambda_\mathrm{k}) \right\} - \sum_{\mathrm{j}=1}^{\mathrm{x}} \mathrm{N_j} \tag{5.5}$$

The solution of the above equation is known as the extended ML estimator for the parameter λ_k.

We need to decide the correct PDF for the ML fit to work properly. To decide a correct PDF for the data distribution, we need to parametrize the simulated data for each component. For our analysis we use RooFit [54] package of the ROOT [55] framework. The RooFit package provides a large set of PDFs that can be used to build a model for data distributions. It also normalizes the PDFs and visualizes the fit results. The functional form of the PDFs used for modeling the specific components of ΔE and NB$'$ are:

- symmetric Gaussian function (G_S)

$$G_S(x;\mu,\sigma) = \frac{1}{\sqrt{2\pi}\sigma}\exp\left[-\frac{1}{2}\left(\frac{x-\mu}{\sigma}\right)^2\right], \tag{5.6}$$

  where μ is the mean and σ is the width;

- symmetric double Gaussian function (G_D)

$$G_D(x;\mu,\sigma_1,\sigma_2) = f_1 G_S(x;\mu,\sigma_1) + (1-f_1) G_S(x;\mu,\sigma_2), \tag{5.7}$$

  where μ is the mean, σ_1, σ_2 are the width of the two Gaussians and f_1 is the weight factor;

- asymmetric Gaussian function

$$G_{\pm}(x;\mu,\sigma_{\pm}) = \frac{\sqrt{2}}{\sqrt{\pi}(\sigma_{+}+\sigma_{-})} \begin{cases} \exp\left[-\frac{1}{2}\left(\frac{x-\mu}{\sigma_{+}}\right)^2\right] & \text{if } x \geq \mu \\ \exp\left[-\frac{1}{2}\left(\frac{x-\mu}{\sigma_{-}}\right)^2\right] & \text{if } x < \mu \end{cases} \tag{5.8}$$

  and μ is the mean, σ_{+} is the width if $x \geq \mu$ and σ_{-} is the width if $x < \mu$;

- Exponential function (E)

$$E(x;\alpha) = \alpha e^{-\alpha x}, \tag{5.9}$$

  where α is a free parameter.

- The Chebyshev polynomials are a set of orthogonal polynomials which can be defined as:

$$P_{n+1}(x) = 2xP_n(x) - P_{n-1}(x), \tag{5.10}$$

  Chebyshev Polynomial of the First order (P_1)

$$P_1(x) = x, \tag{5.11}$$

  where the polynomial is orthogonal in the interval [-1,1].

Using the PDFs described above, we perform a two-dimensional ML fit to extract the signal. ΔE and NB$'$ have negligible correlation, so we describe the two-dimensional PDF as a product of two one-dimensional PDFs as:

$$\mathcal{P}_i = \mathcal{L}_i(\Delta E;\lambda) \times \mathcal{L}_i(\mathrm{NB}';\lambda). \tag{5.12}$$

Here i varies from $1-n$ depending upon the category of events. The parametrizations of each category of events combined to build the model (total PDF) for the events that have been reconstructed. The total PDF is a sum of each categories PDF:

$$\mathcal{P} = \sum_{i=1}^{n} \mathcal{P}_i. \tag{5.13}$$

5.2 Parametrization of PDFs used in the fit

In this section, we discuss the parametrization of ΔE and NB$'$ PDFs for signal and background events, which have very small correlation between them. The small correlation between the two is shown in Table 5.1. The parametrization have been obtained using simulated events.

Table 5.1: Correlation between ΔE and NB$'$ for various MC samples in $B \to D_{\rm fav}\pi$ decay.

Components	Correlation factor
signal	-0.01
$q\bar{q}$ background	0.01
$B\overline{B}$ background	-0.07

5.2.1 Functions for ΔE

The parametrization of ΔE PDF for signal and background components are described below.

Dh signal

Dh signal has been parametrized by a double Gaussian function with a common mean. The parametrization is checked by a fit to signal MC samples as shown in Fig. 5.1.

For $D\pi$ signal, due to differences between data and the MC, we floated all the shape parameters for the favored $D\pi$ mode. For DK signal, due to slight difference in $D\pi$ and DK signal component, all shape parameters except width of Gaussian having greater width (σ_1), are fixed to the parameter from the fit to $D\pi$.

Peaking background

Peaking background is only seen in the DK mode arising from the more abundant $D\pi$ decays. We parametrize the above background by using a sum of asymmetric Gaussian to fit the core and a Gaussian to fit the tails as shown in Fig. 5.2. Area fraction of asymmetric Gaussian and Gaussian, right width (σ_R) and fraction of left width to right width (σ_L/σ_R) of asymmetric Gaussian are fixed from the fit to the favored $D\pi$ mode both in MC and data where the kaon mass is assigned to the prompt pion. The remaining parameters, are floated in the fit to the favored modes since the different particle-identification requirement effects the values of the parameters slightly.

$B\bar{B}$ background

The $D_{\rm fav}h$ $B\bar{B}$ background is parametrized by a sum of an exponential function and a Chebychev polynomial of $1^{\rm st}$ order. The exponential function is used mainly to fit the tail of the peaking contribution from $B^- \to D^*h^-$ and $B^- \to D\rho^-$ that peaks in the region $\Delta E < -0.1$ GeV and the Chebychev polynomial takes care of the combinatorial background located in whole region. The parametrization is checked by a fit to the $B\bar{B}$ MC sample as shown in Fig. 5.3 (a). PDF parameters obtained from $D\pi$ mode can not be used in DK case, due to the difference in $B\bar{B}$ background shape between $D\pi$ and DK as shown in Fig. 5.3 (b). This is due to less $B\overline{B}$ background that peaks around ΔE

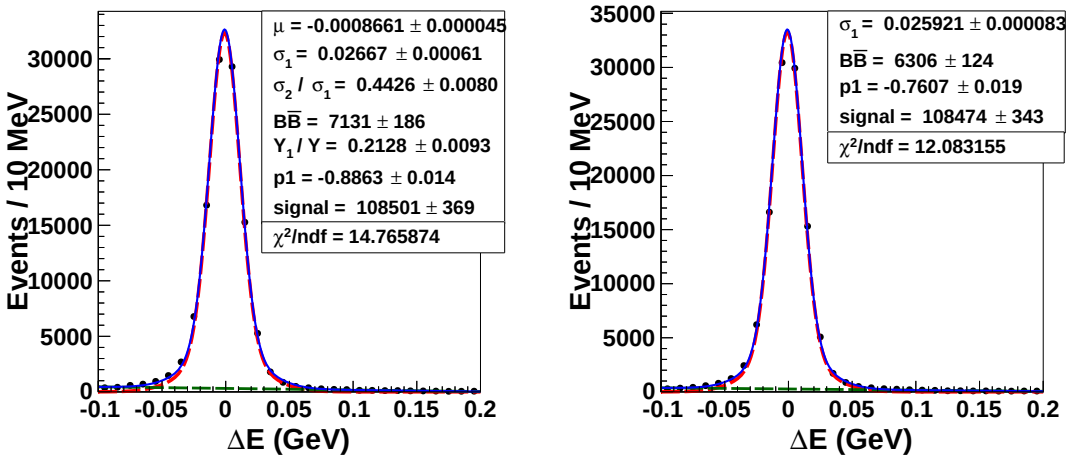

(a) (b)

Figure 5.1: (a) The ΔE distribution for the signal MC on the mode $B^- \to [K^-\pi^+\pi^0]_D\pi^-$(b) ΔE distribution for the signal MC when $B^- \to [K^-\pi^+\pi^0]_D\pi^-$ PDF used on $B^- \to [K^-\pi^+\pi^0]_D K^-$ with floated σ_1.

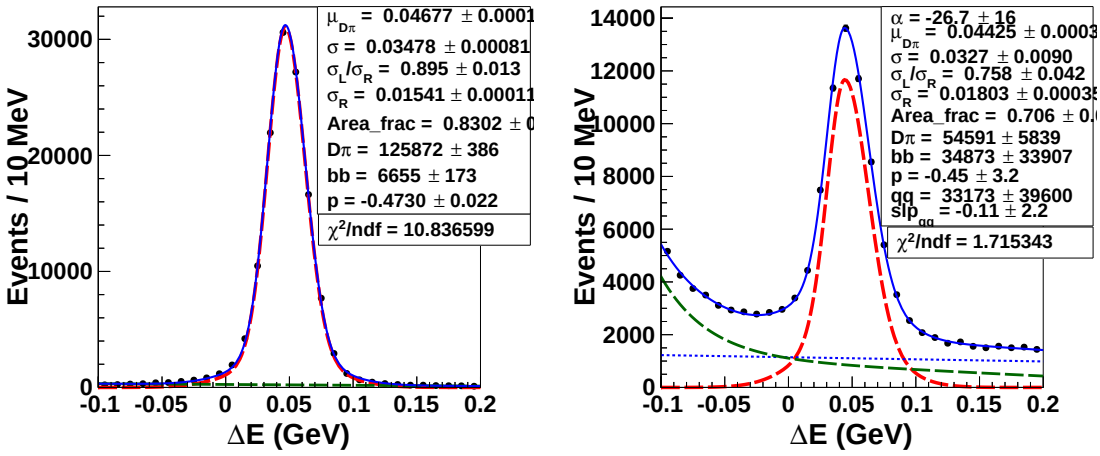

(a) (b)

Figure 5.2: (a) The ΔE distribution for signal MC sample of $B^- \to [K^-\pi^+\pi^0]_D\pi^-$ where kaon-mass hypothesis is assigned for the prompt pion. (b) ΔE distribution for the data sample of the mode $B^- \to [K^-\pi^+\pi^0]_D\pi^-$ where kaon-mass hypothesis is assigned for the prompt pion. The dashed curves show $D\pi$ (red), $B\bar{B}$ (green), $q\bar{q}$ (blue) components and solid blue curve shows total fit.

$= -0.1$ GeV and relatively more combinatorial $B\bar{B}$ background being present in the suppressed Dh modes (Fig. 5.3 (a)-(d)). Therefore, the ΔE PDF parameters obtained from favored Dh mode do not fit well to the corresponding suppressed mode. So we use a free exponential function to better fit the $B\overline{B}$ ΔE component of the suppressed Dh mode.

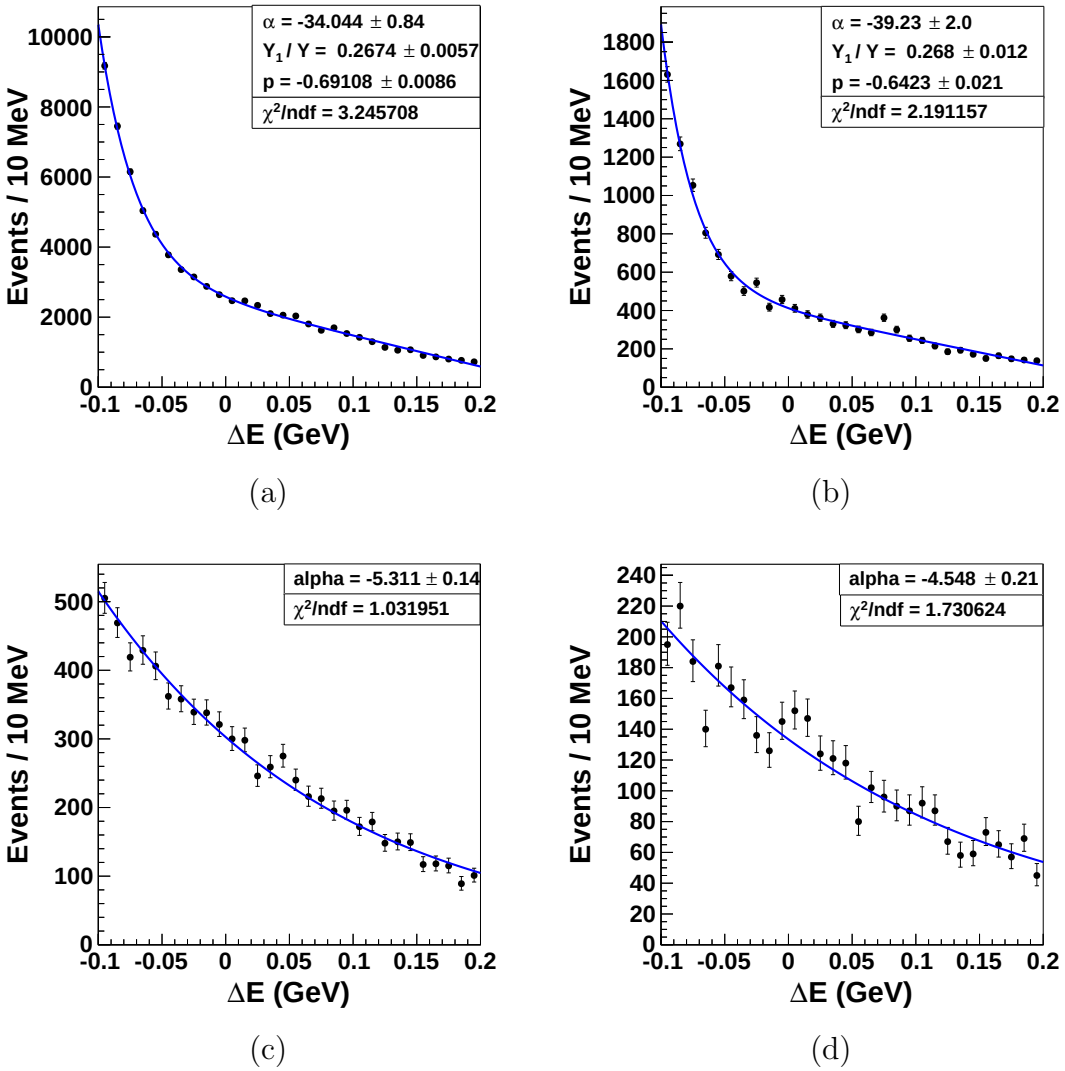

Figure 5.3: ΔE distribution for six streams of $B\overline{B}$ MC: (a) $D_{\rm fav}\pi$ mode (b) $D_{\rm fav}K$ mode (c) $D_{\rm sup}\pi$ mode (d) $D_{\rm sup}K$ mode.

$q\bar{q}$ background

We use a Chebychev polynomial of 1st order, which is checked by a fit to $q\bar{q}$ MC sample as shown in Fig. 5.4. The shape and the normalisation are left free in all fits.

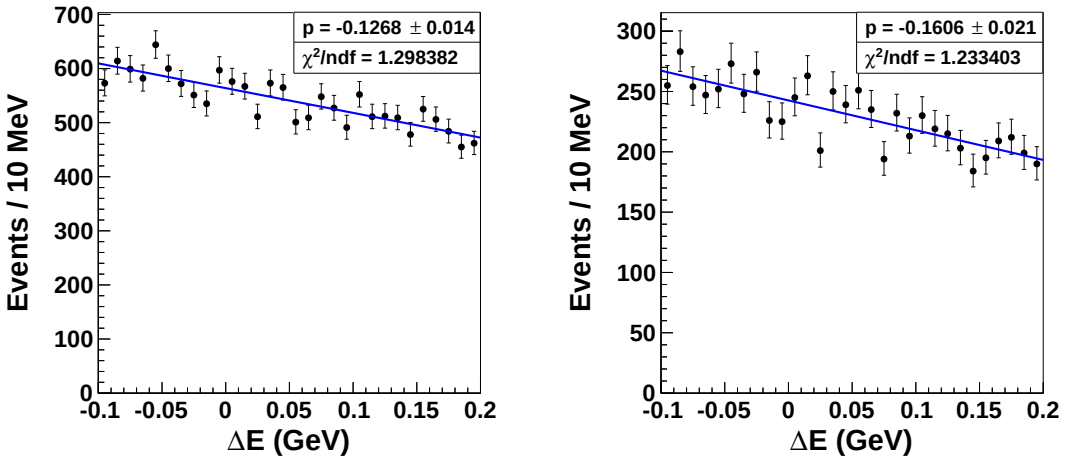

(a) (b)

Figure 5.4: (a) The ΔE distribution for $q\bar{q}$ MC on the mode $B^- \to [K^-\pi^+\pi^0]_D\pi^-$(b) ΔE distribution for $q\bar{q}$ MC on the mode $B^- \to [K^-\pi^+\pi^0]_D K^-$

5.2.2 Functions for NB′

NB′ as PDF for each components is described below.

Dh signal

We use a sum of a bifurcated Gaussian function and a Gaussian function with different means. The parametrization is checked by a fit to signal MC samples as shown in Fig. 5.5.

$D\pi$ signal: Due to difference between the data and MC, we floated all the shape parameters for the favored $D\pi$ mode. All the shape parameters in suppressed $D\pi$ mode are fixed from favored $D\pi$ result.

DK signal: For favored DK signal component we fixed the PDF parameter values from favored $D\pi$ result except the means (μ_1 and μ_2) of the two Gaussians, due to slight difference in $D\pi$ and DK shape. All the shape parameters in suppressed DK mode are fixed from favored DK result.

Peaking background

We use a sum of a bifurcated Gaussian function and a Gaussian function with different means. For the $D\pi$ mode we do not have any peaking background. Since the peaking background exists for DK mode only and it follows a similar distribution distribution as DK, we use the same PDF as we used for DK signal.

$B\bar{B}$ background

We use a Gaussian PDF to fit the $B\bar{B}$ background both for favored and suppressed Dh modes. The suitability of the PDF is checked by fit to four streams of $B\bar{B}$ MC sample as shown in Fig. 5.6. $B\overline{B}$ NB$'$ PDF obtained from favored $D\pi$ mode does not fit to suppressed Dh mode due to relatively more combinatorial and less peaking background (peaking around $\Delta E = -0.1$ GeV) in the suppressed Dh modes. Therefore, we fix the $B\overline{B}$ NB$'$ shape for the suppressed Dh mode by using five streams of $B\overline{B}$ MC as shown in Fig. 5.7. We fixed the shape parameter values both for data and MC to the validated MC result.

$q\bar{q}$ background

We use a double Gaussian with different means. For MC, the shape parameters are fixed from $q\bar{q}$ MC sideband sample: 5.2 GeV/c^2 $< M_{\rm bc} <$ 5.24 GeV/c^2, as shown in Fig. 5.8. It has been checked that the PDF obtained in the sideband region in $D_{\rm fav}\pi$ mode fits well to $D_{\rm fav}K$ and $D_{\rm sup}h$ mode in the same sideband region but the shape is slightly shifted when fixed using $q\overline{q}$ MC for $D_{\rm sup}h$ mode in signal region. This slight shift in NB$'$ shape from the data points, gives a systematic bias between $B\overline{B}$ and $q\overline{q}$ in $D_{\rm sup}h$. Therefore, to correct this we fixed all the $q\overline{q}$ NB$'$ PDF parameter values to the $D_{\rm fav}\pi$ mode except for the mean of the second Gaussian (μ) as shown in Fig. 5.9 and the result of the fit is discussed in Sec. 5.3.2. For data, the shape parameters are fixed to those obtained from a sideband data sample, 5.2 GeV/c^2 $< M_{\rm bc} <$ 5.24 GeV/c^2, as shown in Fig. 5.10.

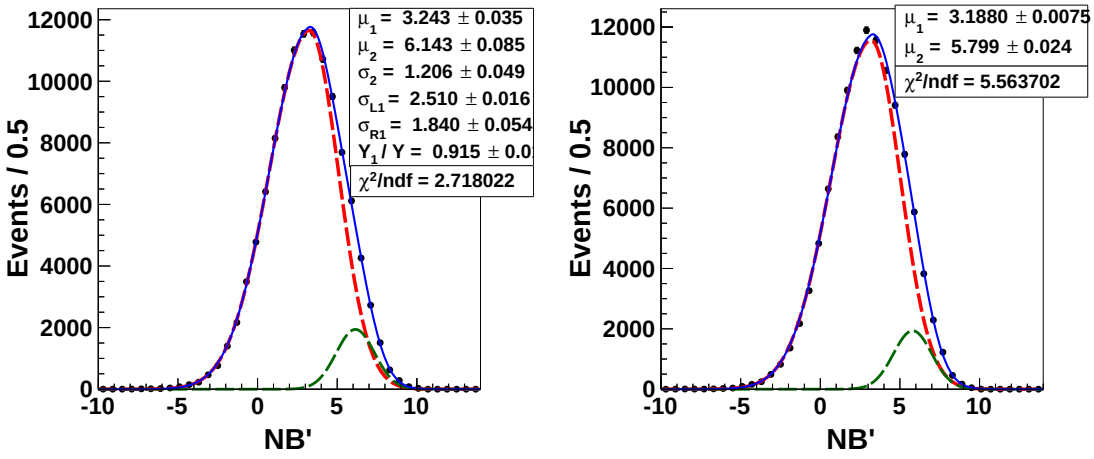

(a) (b)

Figure 5.5: (a) The NB′ distribution for the signal MC on the mode $B^- \to [K^-\pi^+\pi^0]_D\pi^-$(b) NB′ distribution for the signal MC with $B^- \to [K^-\pi^+\pi^0]_D\pi^-$ PDF used on the mode $B^- \to [K^-\pi^+\pi^0]_D K^-$ with floated μ_2/μ_1 and σ_{L2}/σ_{L1}.

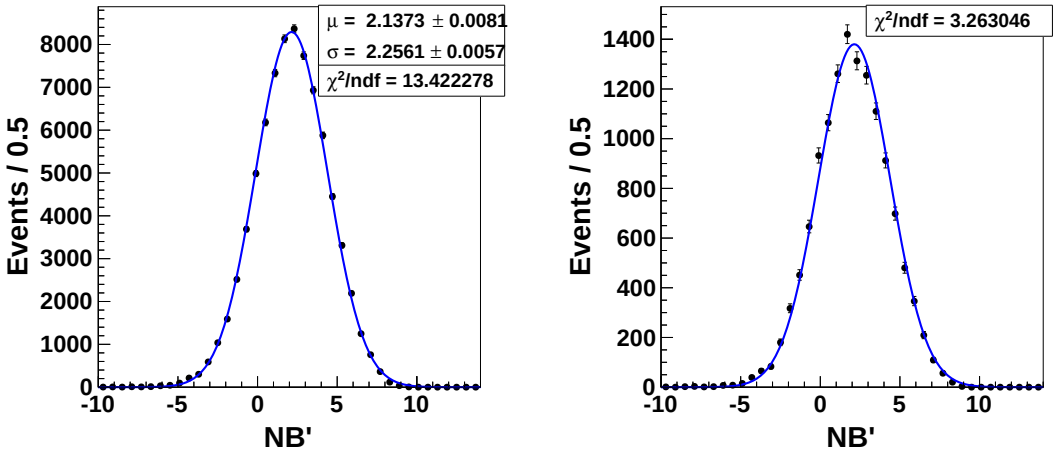

(a) (b)

Figure 5.6: (a) NB′ distribution using six streams of $B\bar{B}$ MC for the modes $B \to D_{\rm fav}\pi$ (b) NB′ distribution using five streams of $B\bar{B}$ MC with $B \to D_{\rm fav}\pi$ PDF used on $B \to D_{\rm fav}K$ mode.

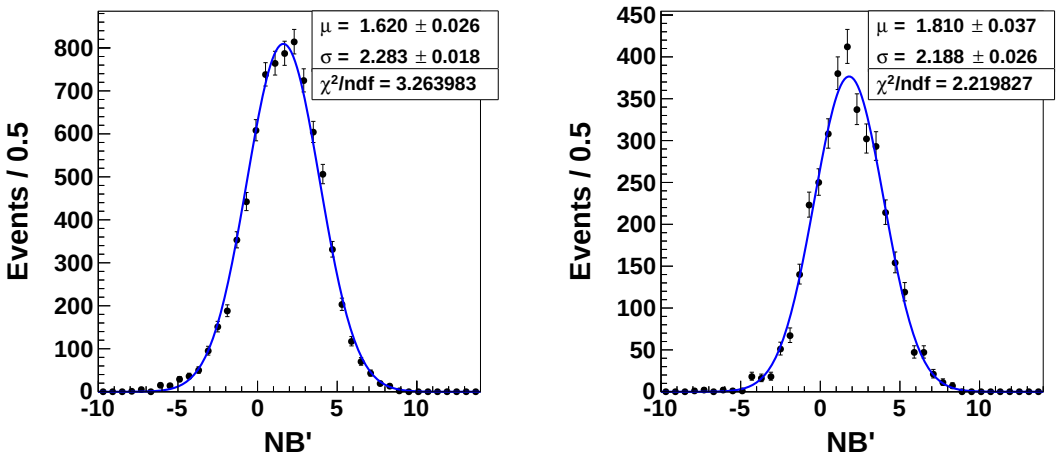

(a) (b)

Figure 5.7: The NB′ distribution using six streams of $B\bar{B}$ MC for the modes: (a) $B \to D_{\rm sup}\pi$ (b) $B \to D_{\rm sup}K$.

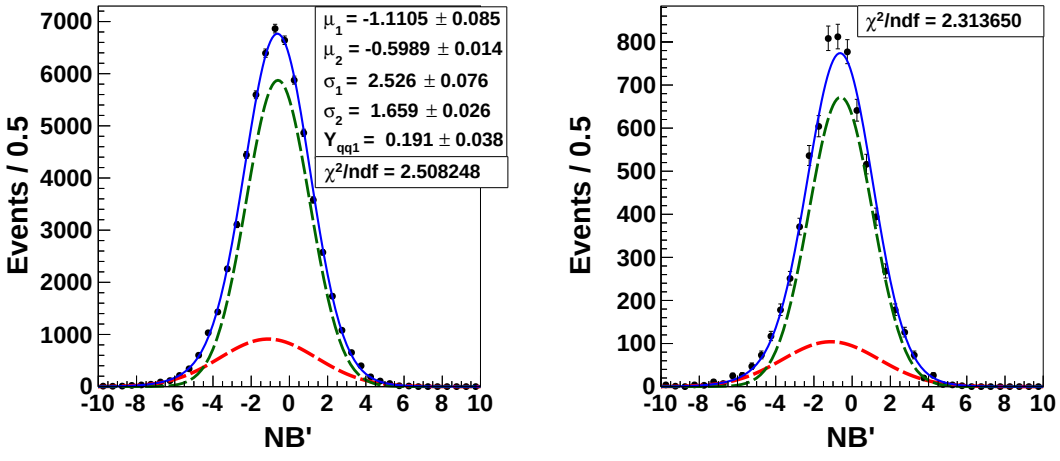

(a) (b)

Figure 5.8: (a) The NB′ distribution for $q\bar{q}$ MC on the mode $B^- \to [K^-\pi^+\pi^0]_D\pi^-$ (b) NB′ distribution for $q\bar{q}$ MC with $B^- \to [K^-\pi^+\pi^0]_D\pi^-$ PDF used on $B^- \to [K^-\pi^+\pi^0]_D K^-$ mode

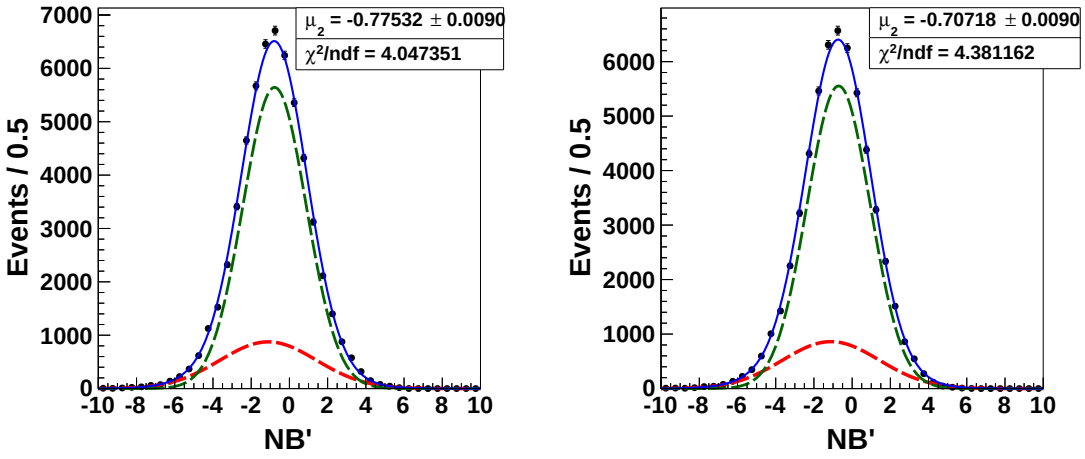

(a) (b)

Figure 5.9: (a) NB′ distribution for five streams of $q\bar{q}$ MC with $D_{\text{fav}}\pi$ PDF used on $D_{\text{sup}}\pi$ mode with floated μ_2 and (b) NB′ distribution for five streams of $q\bar{q}$ MC with $D_{\text{fav}}\pi$ PDF used on $D_{\text{sup}}K$ mode with floated μ_2.

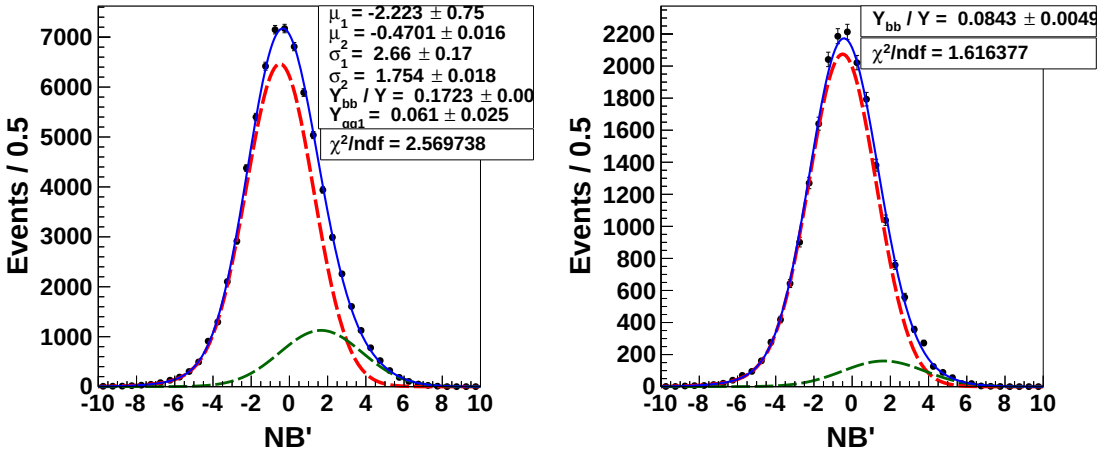

(a) (b)

Figure 5.10: (a) The NB′ distribution for sideband data on the mode $B^- \to [K^-\pi^+\pi^0]_D\pi^-$ (b) NB′ distribution for sideband data with $B^- \to [K^-\pi^+\pi^0]_D\pi^-$ PDF used on the mode $B^- \to [K^-\pi^+\pi^0]_D K^-$. Components of the fit are shown with red ($q\bar{q}$) and green ($B\bar{B}$), where all the parameters for the former are floated while those for the latter are fixed from $B\bar{B}$ MC sideband fit. The sum of two components is shown with the blue. From the fit it is clear that for case (a) $q\bar{q}$ is contaminated with 17% of $B\bar{B}$ combinatorial background and case (b) shows contamination of $B\bar{B}$ is around 8%.

5.3 Signal Extraction

Using the PDFs described above we fit to one stream of MC sample described in Appendix B and a data sample to extract signal yield. We use $\Upsilon(4S)$ sample of 772×10^6 $B\overline{B}$ pairs. We extract the signal yield by performing an unbinned extended maximum likelihood fit to ΔE and NB′ distributions. We perform separate fits to the suppressed and favored $B \to DK$ ($B \to D\pi$) modes as described below. The total PDF for each component is formed by multiplying the individual PDFs for ΔE and NB′. The ratio of branching fractions $DK/D\pi$ is found to be 0.082 ± 0.003 which compares well with the older Belle result [56].

5.3.1 Fit to Favored Modes

Fit to $B \to D_{\rm fav}\pi$ mode on data

Figure 5.11 shows the result of the fit to the favored modes on data. Projections for several regions are shown in Fig. 5.12 and Fig. 5.13. Reasonable quality of the fit is indicated by the values of χ^2/ndf. Table 5.2 shows the list of the parameters in the fit.

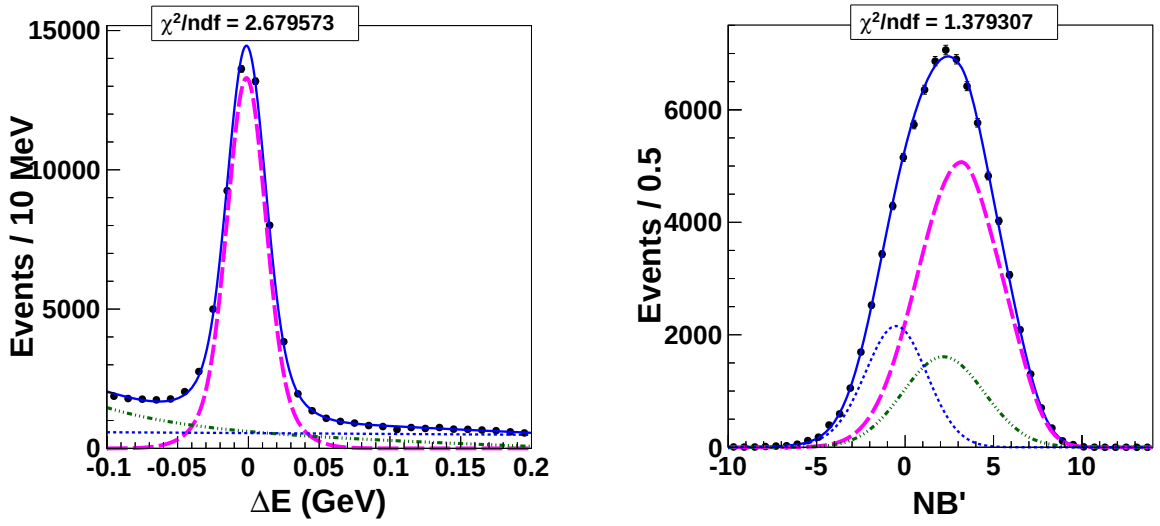

(a) (b)

Figure 5.11: (a) ΔE distribution and (b) NB′ distribution both of which are obtained by projecting all fitted regions. In these plots, points with error bars represent data while the total best-fit projection is shown with the solid blue curve, for which the components are shown with thinner dashed magenta ($D\pi$), dashed dot green ($B\bar{B}$ background) and dotted blue ($q\bar{q}$ background).

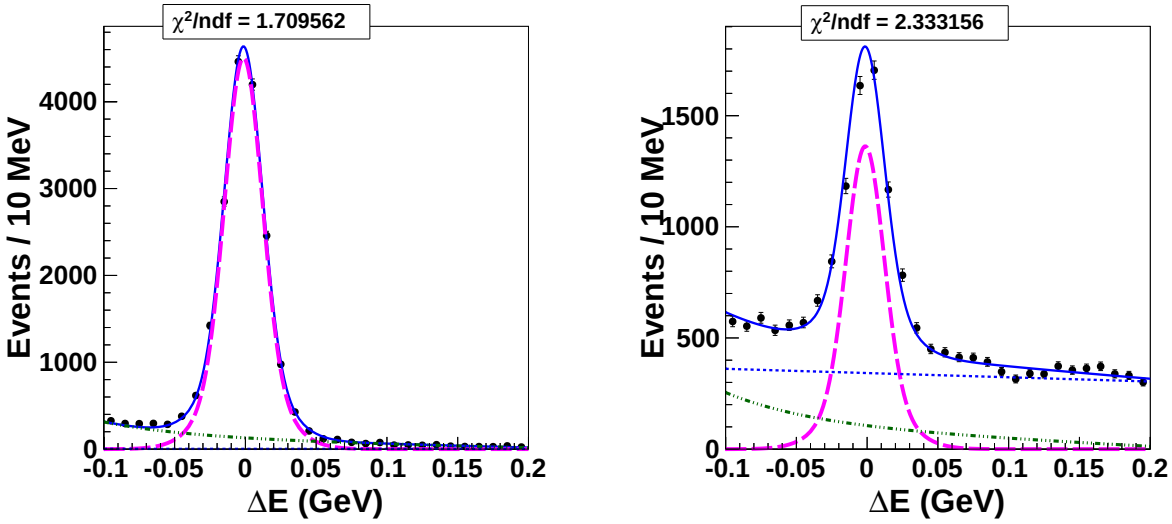

(a) (b)

Figure 5.12: The projections for the favored $D\pi$ data sample. The ΔE distributions for signal and $B\overline{B}$ enhanced (NB$'$ > 4), $q\overline{q}$ enhanced (NB$'$ < 0) are shown from left to right.

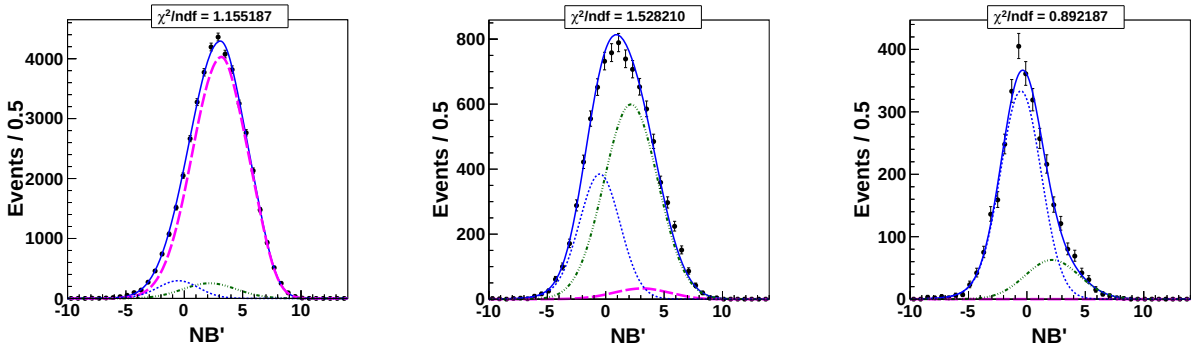

(a) (b) (c)

Figure 5.13: The projections for the favored $D\pi$ data sample. The NB$'$ distributions for signal enhanced ($-0.02 < \Delta E < 0.02$), $B\overline{B}$ enhanced ($-0.1 < \Delta E < -0.05$), $q\overline{q}$ enhanced ($\Delta E > 0.15$) are shown from left to right.

Table 5.2: Parameters values for the fit to $B \to D_{\rm fav}\pi$ data.

Component	PDF type	Parameters	Value
$D\pi$	General	Yield	49668±338
	G_D (ΔE)	μ	-0.0013367±0.000082
		σ_1	0.0244±0.0012
		σ_2/σ_1	0.531±0.019
		Area fraction	0.281±0.035
	$G_A + G_S$ (NB′)	Area fraction	0.901±0.023
		μ_1	3.09±0.06
		σ_{L1}	2.418±0.032
		σ_{R1}	1.862±0.076
		μ_2	6.02±0.12
		σ_2	1.246±0.059
$B\overline{B}$ in Dπ	General	Yield	15520±340
	$E + P_1$ (ΔE)	expo. coefficient α	-15.845±0.92
		Slope β	-0.81±0.03
		Area fraction	0.341 (fixed from $B\overline{B}$ MC)
	G_S (NB′)		fixed from $B\overline{B}$ MC PDF parameter values shown in Fig. 5.6:(a)
$q\overline{q}$ in Dπ	General	Yield	15997±216
	P_1	Slope	-0.0858±0.021
	G_D (NB′)		fixed from data sideband PDF parameter values shown in Fig. 5.10:(a)

Fit to $B \to D_{\rm fav}K$ on data

Figure 5.14 shows the result of the fit to favored modes on data. Projections for several regions are shown in Fig. 5.15 and Fig. 5.16. Good quality of the fit is indicated by the values of χ^2/ndf. Table 5.3 shows the list of the parameters in the fit. The yield for the $D\pi$ peaking background is about two times larger than the MC result. The ratio is found to be 1.92±0.08, which is consistent with the Belle-official PID calibration factor which is calculated to be 1.89±0.07.

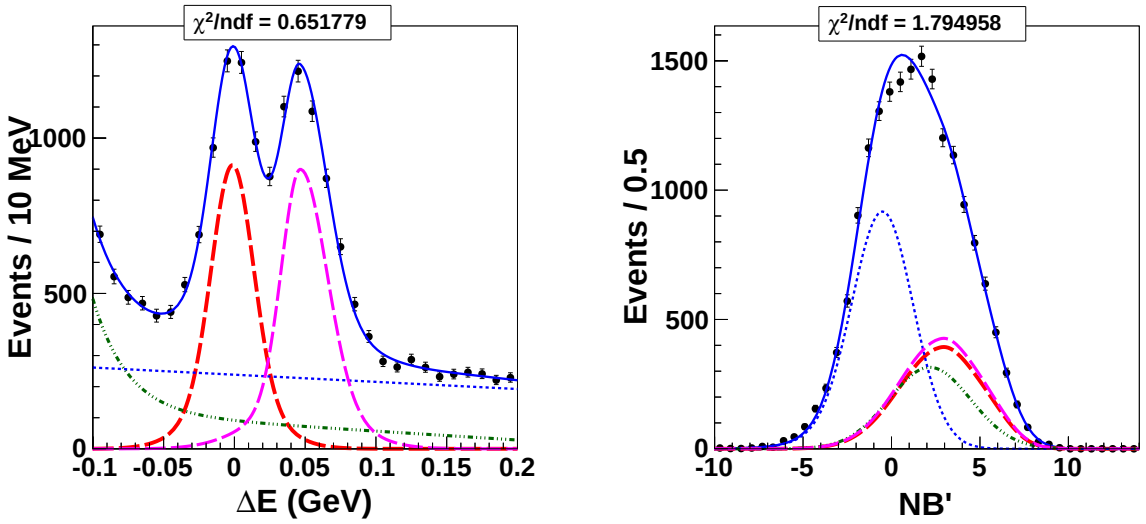

(a) (b)

Figure 5.14: (a) ΔE distribution and (b) NB$'$ distribution both of which are obtained by projecting all fitted regions. In these plots, points with error bars represent data while the total best-fit projection is shown with the solid blue curve, for which the components are shown with thicker dashed red (DK signal), thinner dashed magenta ($D\pi$), dashed dot green ($B\bar{B}$ background) and dotted blue ($q\bar{q}$ background).

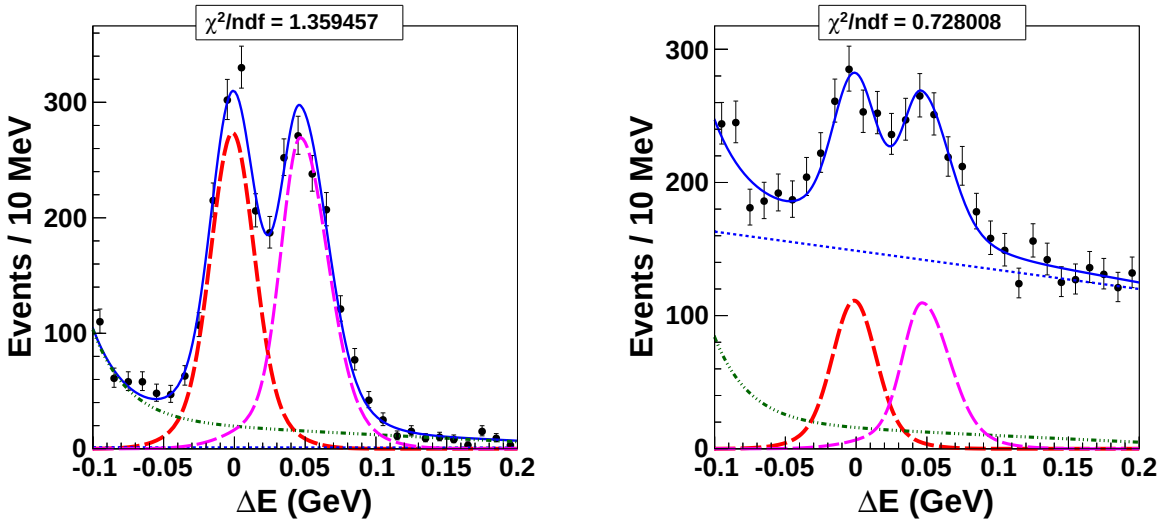

(a) (b)

Figure 5.15: The projections for the favored DK data sample. (a) shows the ΔE distribution for signal enhanced, $D\pi$ enhanced, $B\bar{B}$ enhanced region ($\mathrm{NB}' > 4$) and (b) shows the ΔE distribution for $q\bar{q}$ enhanced region ($\mathrm{NB}' < 0$)

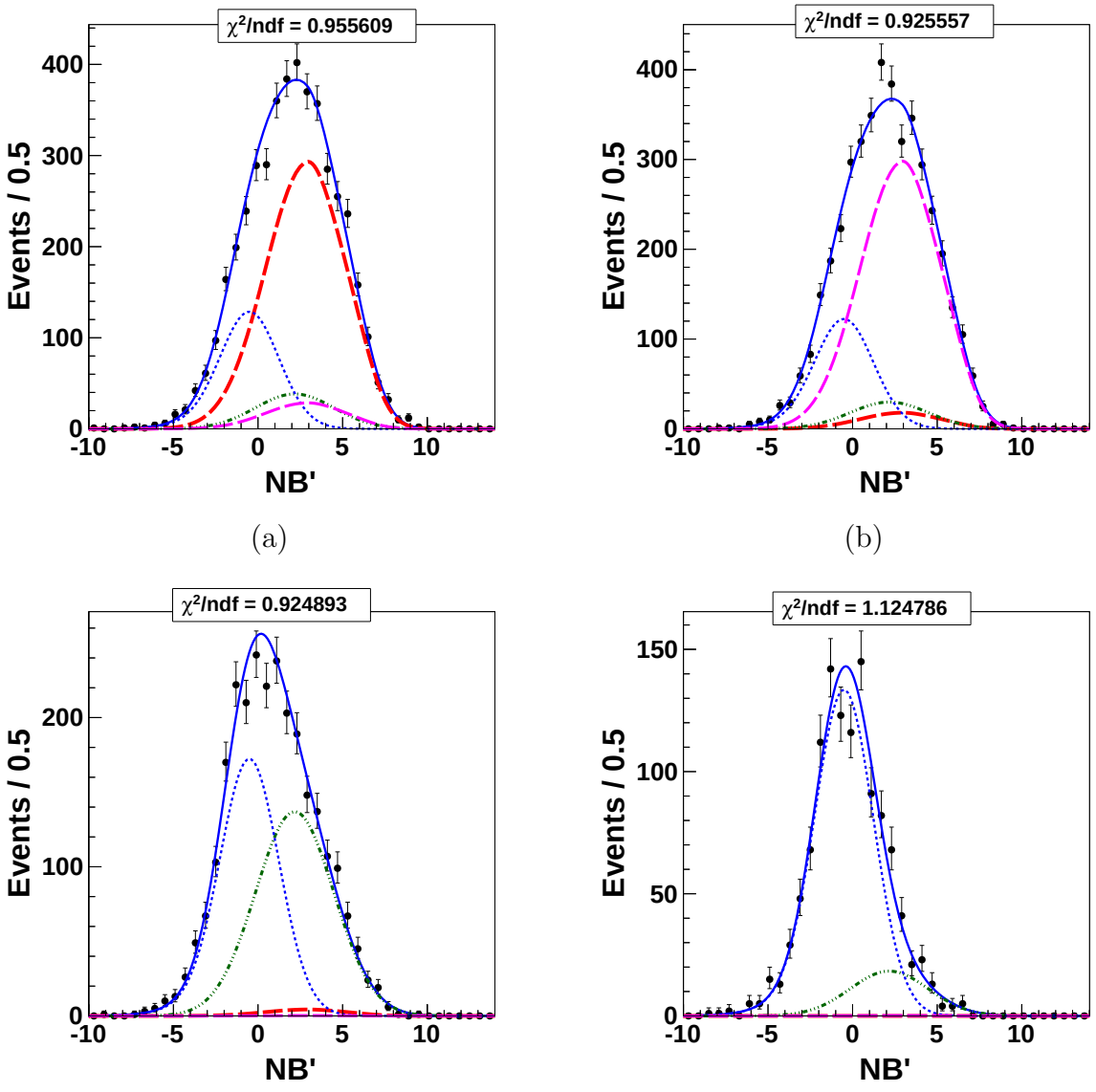

Figure 5.16: The projections for the favored DK data sample. The NB′ distributions for signal enhanced ($-0.02 < \Delta E < 0.02$), $D\pi$ enhanced ($0.03 < \Delta E < 0.07$), $B\bar{B}$ enhanced ($-0.1 < \Delta E < -0.05$), $q\bar{q}$ enhanced ($\Delta E > 0.15$) are shown from Figure (a) to (d).

Table 5.3: Parameters values for the fit to $B \to D_{\rm fav}K$ data.

Component	PDF type	Parameters	Value
DK	General	Yield	3844±125
	G_D (ΔE)	μ	-0.0013367 (fixed)
		σ_1	0.02747±0.00096
		σ_2/σ_1	0.531 (fixed)
		Area fraction	0.281 (fixed)
	$G_A + G_S$ (NB′)	Area fraction	0.901 (fixed)
		μ_1	2.845±0.042
		σ_{L1}	2.418 (fixed)
		σ_{R1}	1.862 (fixed)
		μ_2	5.66±0.08
		σ_2	1.246 (fixed)
$D\pi$ in DK	General	Yield	4171±111
	$G_A + G_S$ (ΔE)	μ	0.04659±0.00053
		σ	0.0333±0.0029
		σ_R	0.0183 (fixed)
		σ_L/σ_R	0.719 (fixed)
		Area fraction	0.716 (fixed)
	$G_A + G_S$ (NB′)		same as DK signal component
$B\overline{B}$ in DK	General	Yield	3036±126
	$E + P_1$ (ΔE)	expo. coefficient α	-40.76±4.1
		Slope β	-0.6025±0.066
		Area fraction	0.298 (fixed from $B\overline{B}$ MC)
	G_S (NB′)		fixed from $B\overline{B}$ MC PDF parameter values shown in Fig. 5.6:(a)
$q\overline{q}$ in DK	General	Yield	6807±129
	P_1	Slope	-0.1524±0.028
	G_D (NB′)		fixed from data sideband PDF parameter values shown in Fig. 5.10:(a)

5.3.2 Fit to Suppressed Modes

Fit to $B \to D_{\rm sup}\pi$ mode on data

Figure 5.17 shows the result of the fit to suppressed modes on data. Projections for several regions are shown in Fig. 5.18 and Fig. 5.19. Good quality of the fit is indicated by the values of χ^2/ndf. Table 5.4 shows the list of the parameters in the fit.

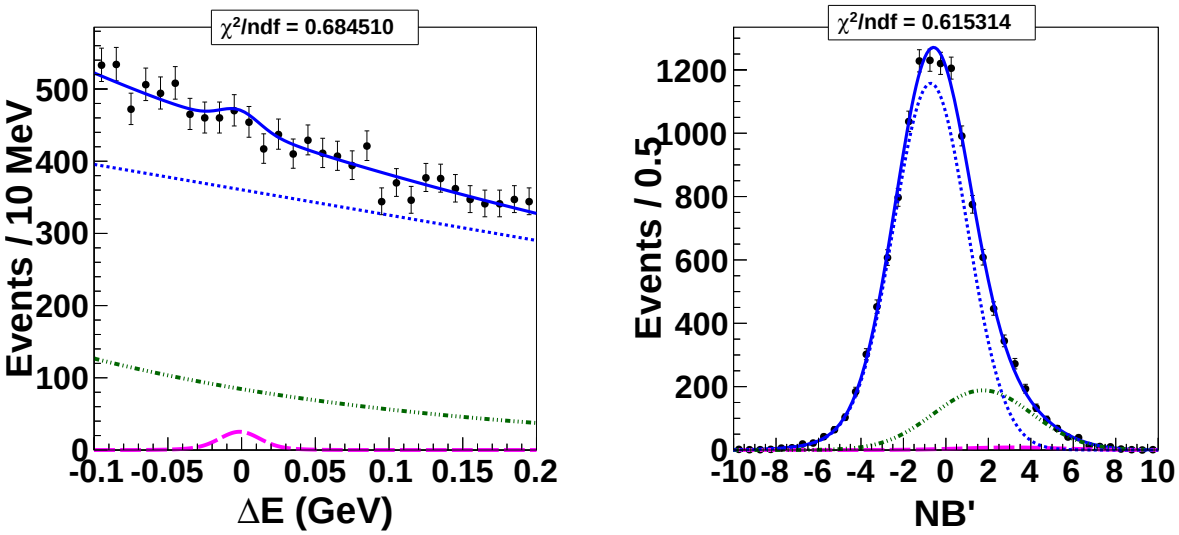

(a) (b)

Figure 5.17: (a) ΔE distribution and (b) NB′ distribution both of which are obtained by projecting all fitted regions. In these plots, points with error bars represent data while the total best-fit projection is shown with the solid blue curve, for which the components are shown with thinner dashed magenta ($D\pi$), dashed dot green ($B\bar{B}$ background) and dotted blue ($q\bar{q}$ background).

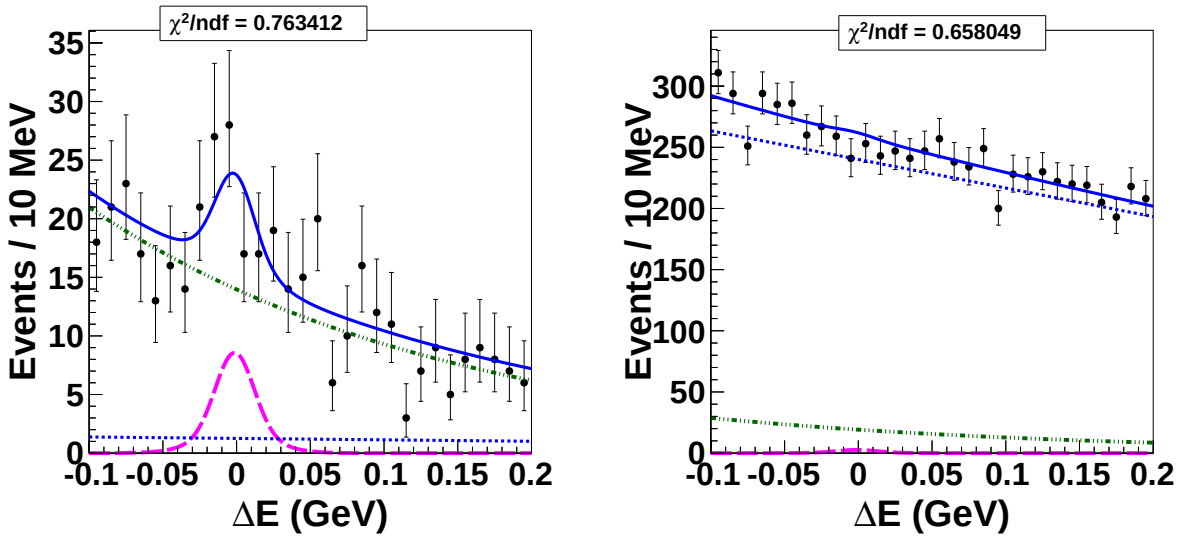

(a) (b)

Figure 5.18: The projections for the suppressed $D\pi$ data sample. The ΔE distributions for signal and $B\overline{B}$ enhanced (NB$' > 4$), $q\overline{q}$ enhanced (NB$' < 0$) are shown from left to right.

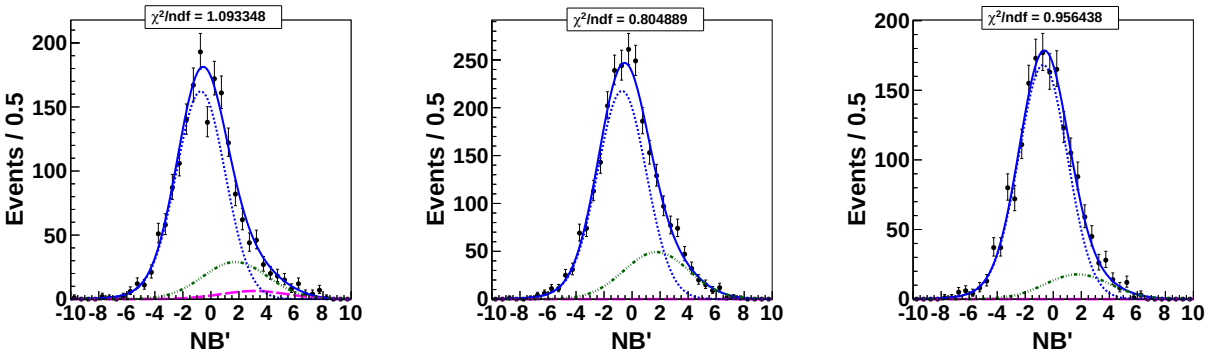

(a) (b) (c)

Figure 5.19: The projections for the suppressed $D\pi$ data sample. The NB$'$ distributions for signal enhanced ($-0.02 < \Delta E < 0.02$), $B\overline{B}$ enhanced ($-0.1 < \Delta E < -0.05$), $q\overline{q}$ enhanced ($\Delta E > 0.15$) are shown from left to right.

Table 5.4: Parameters values for the fit to $B \to D_{\rm sup}\pi$ data.

Component	PDF type	Parameters	Value
$D\pi$	General	Yield	94±27
		Asymmetry	0.16±0.27
	G_D	μ	-0.0013367 (fixed)
	(ΔE)	σ_1	0.0244 (fixed)
		σ_2/σ_1	0.531 (fixed)
		Area fraction	0.281 (fixed)
	$G_A + G_S$	Area fraction	0.901 (fixed)
	(NB′)	μ_1	3.09 (fixed)
		σ_{L1}	2.418 (fixed)
		σ_{R1}	1.862 (fixed)
		μ_2	6.02 (fixed)
		σ_2	1.246 (fixed)
$B\overline{B}$ in Dπ	General	Yield	2196±110
		Asymmetry	0 (fixed)
	E	expo. coefficient	-4.06±0.47
	(ΔE)		
	G_S		fixed from $B\overline{B}$ MC
	(NB′)		PDF parameter values shown in Fig. 5.7:(a)
$q\overline{q}$ in Dπ	General	Yield	10287±136
	P_1	Slope	-0.1536±0.02
	G_D		fixed from data sideband with free μ_2
	(NB′)		($\mu_2 = -0.688 \pm 0.027$)
			PDF parameter values shown in Fig. 5.10:(a)

Fit to $B \to D_{\rm sup}K$ on data

Figure 5.20 shows the result of the fit to suppressed modes on data. Projections for several regions are shown in Fig. 5.21 and Fig. 5.22. Good quality of the fit is indicated by the values of χ^2/ndf. Table 5.5 shows the list of the parameters in the fit. The yield for "$D\pi$ in DK" is about two times larger than the MC result, due to difference in $\pi \to K$ Mis-ID and Branching fractions.

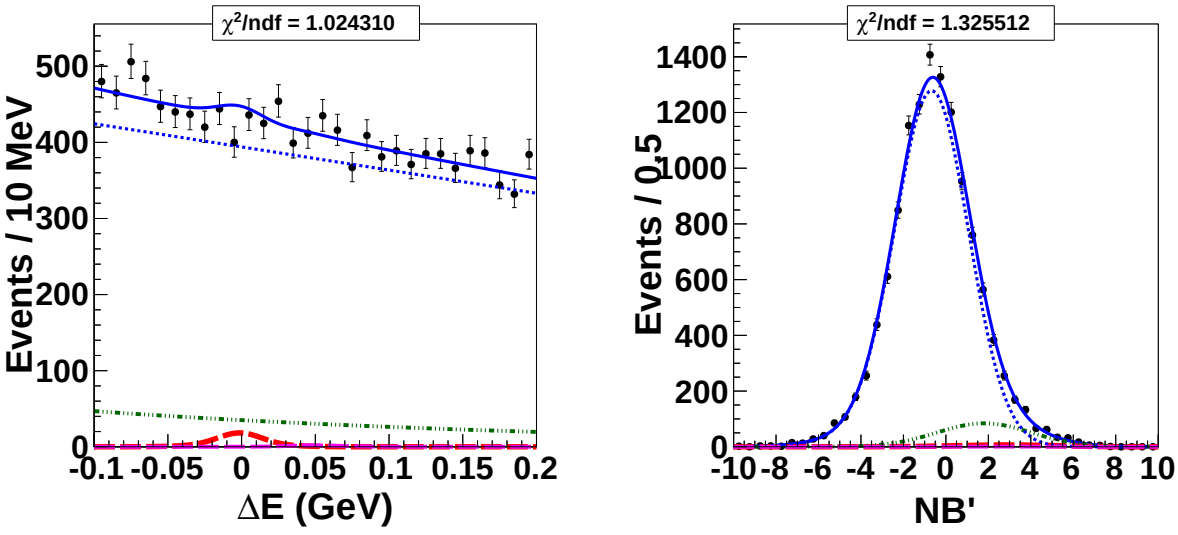

(a) (b)

Figure 5.20: (a) ΔE distribution and (b) NB$'$ distribution both of which are obtained by projecting all fitted regions. In these plots, points with error bars represent data while the total best-fit projection is shown with the solid blue curve, for which the components are shown with thicker dashed red (DK signal), thinner dashed magenta ($D\pi$), dashed dot green ($B\bar{B}$ background) and dotted blue ($q\bar{q}$ background).

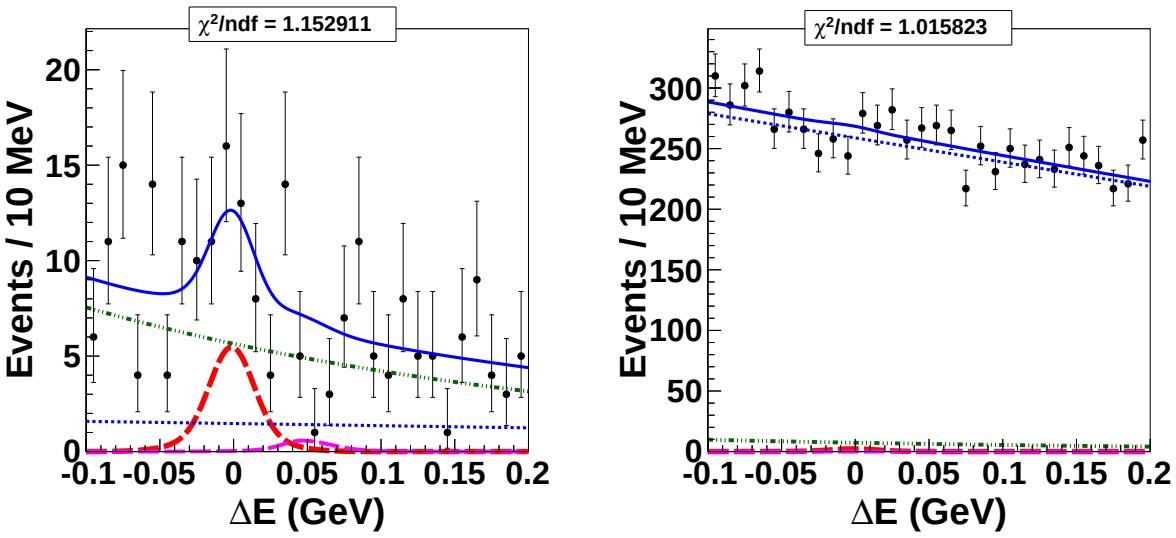

(a) (b)

Figure 5.21: The projections for the suppressed DK data sample. Figure (a) shows ΔE distribution for signal enhanced, Dπ enhanced, $B\bar{B}$ enhanced region (NB$' > 4$) and Figure (b) shows ΔE distribution for $q\bar{q}$ enhanced region (NB$' < 0$).

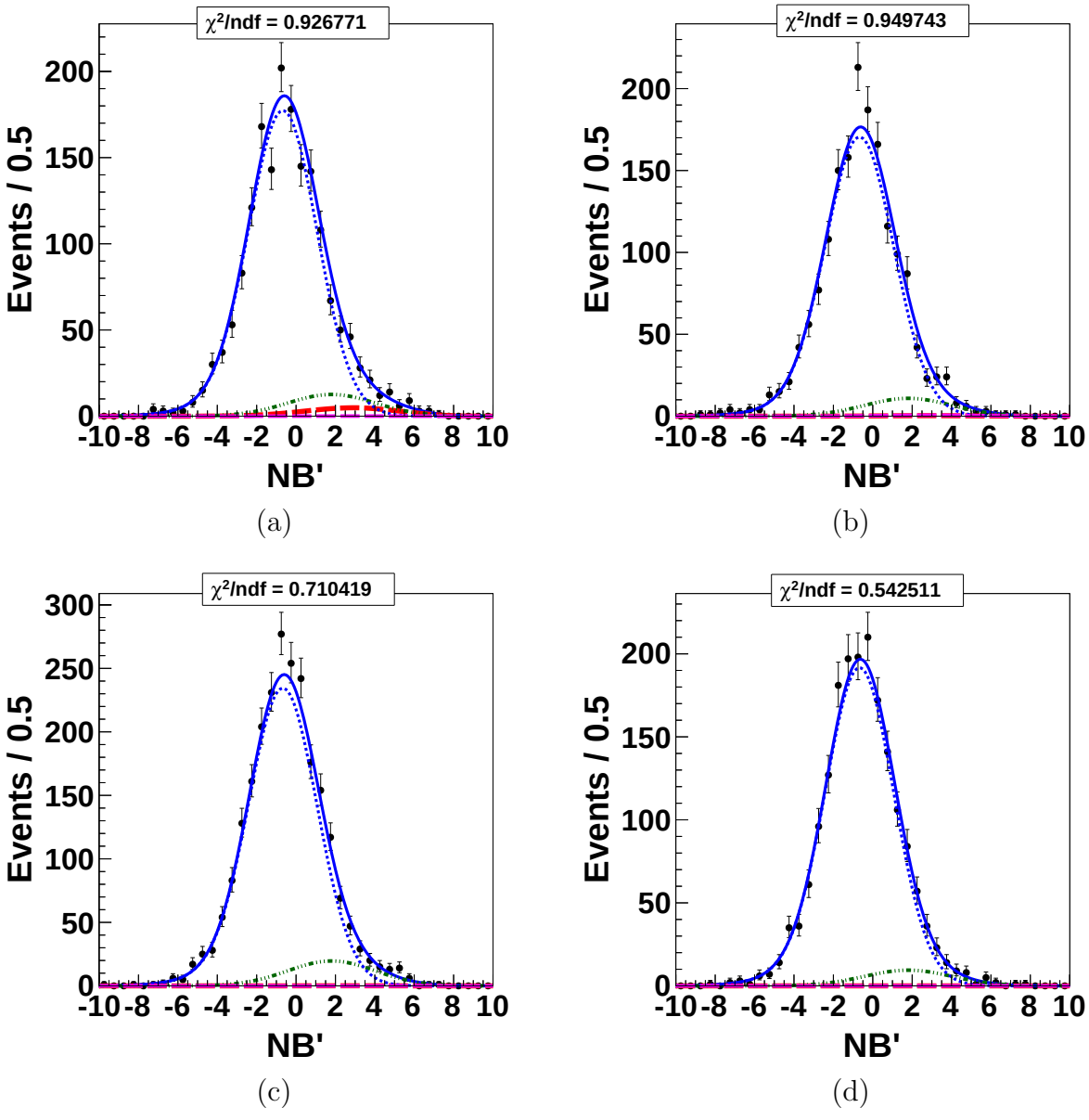

Figure 5.22: The projections for the suppressed DK data sample. The NB′ distributions for signal enhanced ($-0.02 < \Delta E < 0.02$), $D\pi$ enhanced ($0.03 < \Delta E < 0.07$), $B\bar{B}$ enhanced ($-0.1 < \Delta E < -0.05$), $q\bar{q}$ enhanced ($\Delta E > 0.15$) are shown from Figure (a) to (d).

Table 5.5: Parameters values for the fit to $B \to D_{\rm sup}K$ data.

Component	PDF type	Parameters	Value
DK	General	Yield	77±24
		Asymmetry	0.41±0.3
	G_D	μ	-0.0013367 (fixed)
	(ΔE)	σ_1	0.02747 (fixed)
		σ_2/σ_1	0.531 (fixed)
		Area fraction	0.281 (fixed)
	$G_A + G_S$	Area fraction	0.901 (fixed)
	(NB′)	μ_1	2.845 (fixed)
		σ_{L1}	2.418 (fixed)
		σ_{R1}	1.862 (fixed)
		μ_2	5.66 (fixed)
		σ_2	1.246 (fixed)
$D\pi$ in DK	General	Yield	8.8 (fixed)
		Asymmetry	0.16 (fixed)
	$G_A + G_S$	μ	0.04659 (fixed)
	(ΔE)	σ	0.0333 (fixed)
		σ_R	0.0183 (fixed)
		σ_L/σ_R	0.719 (fixed)
		Area fraction	0.716 (fixed)
	$G_A + G_S$		same as DK signal component
	(NB′)		
$B\overline{B}$ in DK	General	Yield	938±83
		Asymmetry	0 (fixed)
	E	expo. coefficient	-2.91±0.81
	G_S		fixed from $B\overline{B}$ MC
	(NB′)		PDF parameter values shown in Fig. 5.7:(b)
$q\overline{q}$ in DK	General	Yield	11365±127
		Asymmetry	-0.005±0.01
	P_1	Slope	-0.12±0.02
	G_D		fixed from data sideband with free μ_2
	(NB′)		($\mu_2 = -0.64 \pm 0.02$)
			PDF parameter values shown in Fig. 5.10:(a)

5.4 Estimation of the rare peaking background

In this chapter, we describe the estimation of the peaking background inside the signal window of ΔE and NB′. Since the background would come from the charmless B decay $B^- \to K^+K^-\pi^-\pi^0$, it is flat in the M_D distribution but can peak in the signal of ΔE and NB′ region. So, we estimated the peaking background using the M_D sideband data sample. We use 1.9 GeV/c^2 $< M_D <$ 2.25 GeV/c^2 for the upper sideband and 1.45 GeV/c^2 $< M_D <$ 1.8 GeV/c^2 for the lower sideband in both $B \to D_{\rm sup}\pi$ and $B \to D_{\rm sup}K$ channels. In addition, we constrain M_D to have a mass equal to the middle of the upper and lower sideband ranges, respectively. Figures 5.24 and 5.25 show the results of the fit, where we applied the same method as signal extraction to find the peaking backgrounds. We obtain an expected background yield of -91 ± 67 (-77 ± 63) for $D\pi^-$ (DK^-) in the sideband region. The normalized number of peaking backgrounds that can contribute in the signal region is found to be -10.5 ± 7.8 (-9 ± 7) for $D\pi^-$ (DK^-) mode.

We also did a similar test using six streams of generic $B\bar{B}$ MC (shown in Fig. 5.26 and Fig. 5.27) and found that the peaking contribution is 70±51 (104±44) events for $D\pi^-$ (DK^-) and the normalized number of peaking backgrounds for one stream of MC that can contribute in the signal region is found to be 9.5 ± 6.9 (14 ± 6) for $D\pi^-$ (DK^-) mode. Here in generic $B\bar{B}$ MC, we use 1.9 GeV/c^2 $< M_D <$ 1.95 GeV/c^2 for the upper sideband and 1.75 GeV/c^2 $< M_D <$ 1.8 GeV/c^2 for the lower sideband in both $B \to D_{\rm sup}\pi$ and $B \to D_{\rm sup}K$ channels (shown in Fig. 5.23).

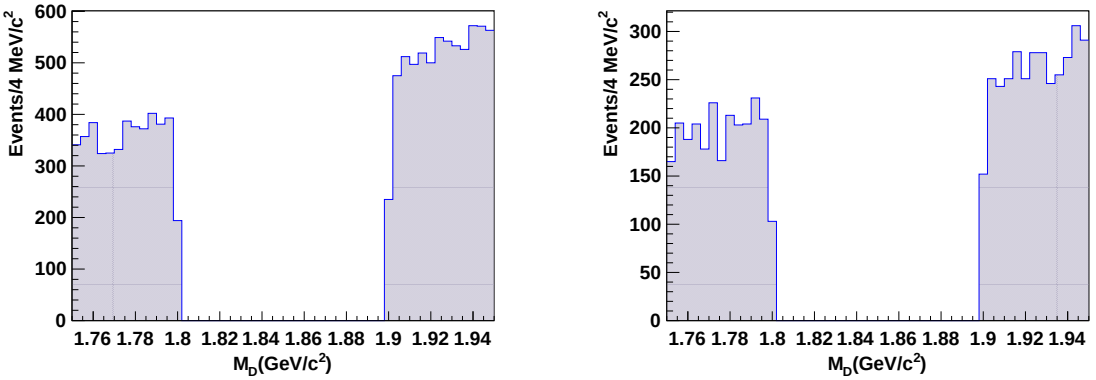

(a) (b)

Figure 5.23: D mass sideband distributions using 6 streams of $B\bar{B}$ MC for (a) $D_{\rm sup}\pi$ and (b) $D_{\rm sup}K$ decay.

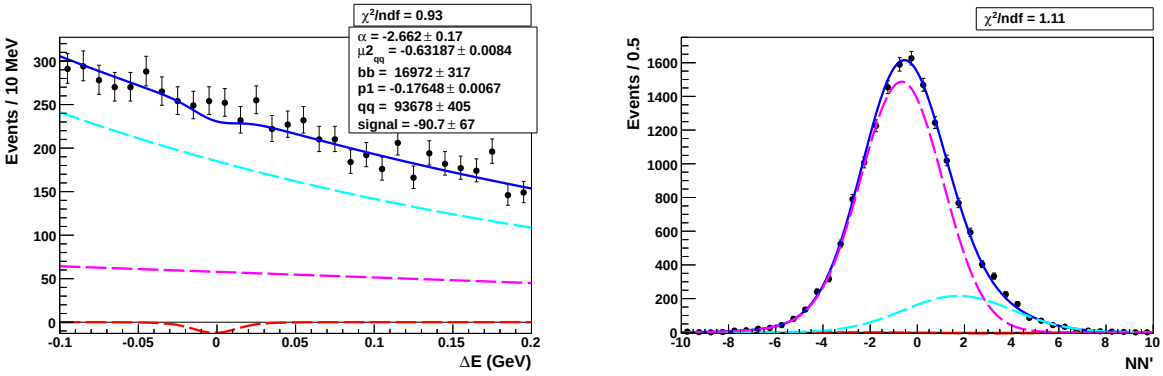

(a) (b)

Figure 5.24: (a) ΔE distributions ($4 < \mathrm{NB}' < 14$) and (b) NB′ distributions ($-0.02 < \Delta E < 0.02$) using M_D sideband data sample for $B \to D_{\mathrm{sup}}\pi$ decay. The fitted sample is shown by dots with error bars and the PDF is the solid blue curve, for which the components are: dashed red (DK), dashed cyan ($B\bar{B}$ background) and dashed magenta ($q\bar{q}$ background).

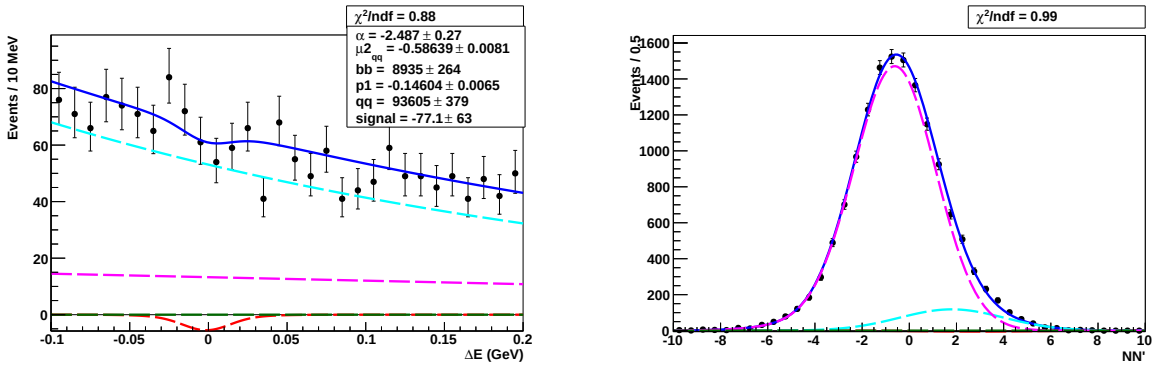

(a) (b)

Figure 5.25: (a) ΔE distributions ($4 < \mathrm{NB}' < 14$) and (b) NB′ distributions ($-0.02 < \Delta E < 0.02$) using M_D sideband sample of data for $B \to D_{\mathrm{sup}}K$ decay. The fitted sample is shown by dots with error bars and the PDF is the solid blue curve, for which the components are: dashed red (DK), dashed green ($D\pi$), dashed cyan ($B\bar{B}$ background) and dashed magenta ($q\bar{q}$ background).

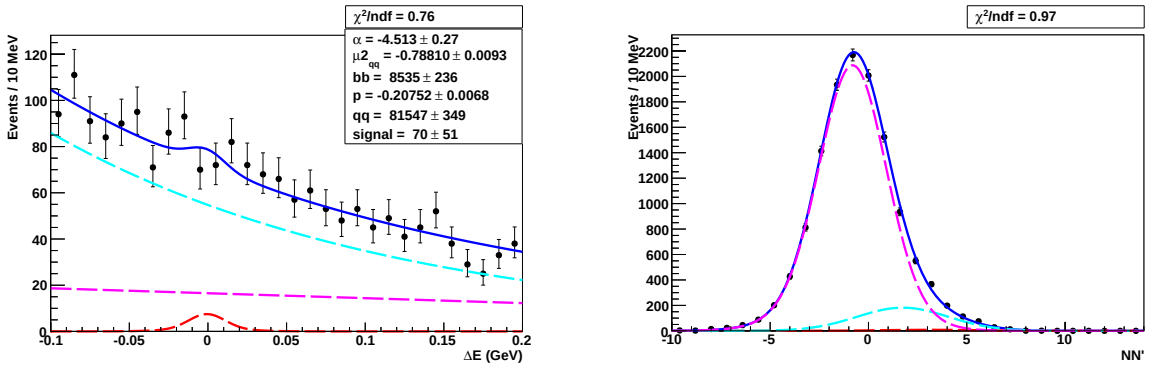

(a) (b)

Figure 5.26: (a) ΔE distributions ($4 < \mathrm{NB}' < 14$) and (b) NB′ distributions ($-0.02 < \Delta E < 0.02$) for reconstructed $D_{\mathrm{sup}}\pi$ candidates in M_D sideband region using six streams of MC. The fitted sample is shown by dots with error bars and the PDF is the solid blue curve, for which the components are: dashed red (DK), dashed cyan ($B\bar{B}$ background) and dashed magenta ($q\bar{q}$ background).

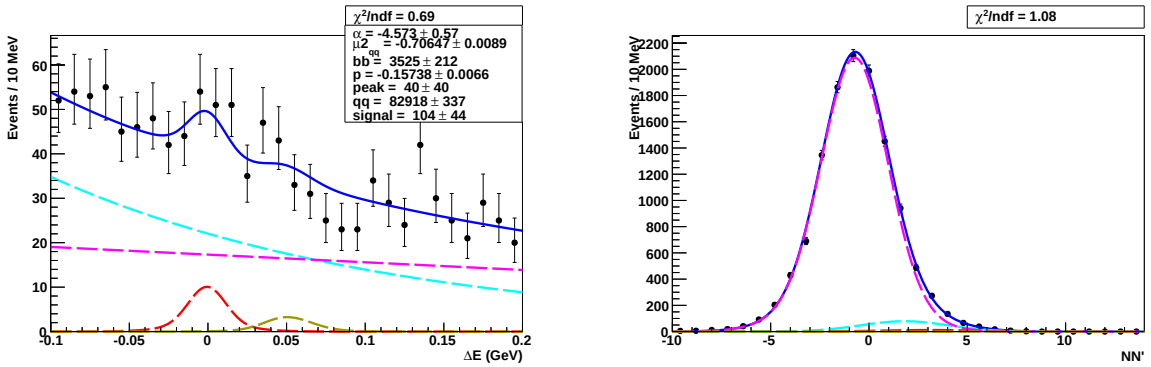

(a) (b)

Figure 5.27: (a) ΔE distributions ($4 < \mathrm{NB}' < 14$) and (b) NB′ distributions ($-0.02 < \Delta E < 0.02$) for reconstructed $D_{\mathrm{sup}}K$ candidates in M_D sideband region using six streams of MC. The fitted sample is shown by dots with error bars and the PDF is the solid blue curve, for which the components are: dashed red (DK), dashed yellow ($D\pi$), dashed cyan ($B\bar{B}$ background) and dashed magenta ($q\bar{q}$ background).

5.5 Fit bias check for $B \to D_{\rm sup}h$ mode

A possible bias in the fit to $B \to D_{\rm sup}K$ mode is checked by generating 10000 toy-experiments. Figure 5.28 shows, the pull and returned yield distribution obtained for 77 generated signal events. We find the fitted values to be normally distributed around the expected value and the pull distributions to be distributed around zero mean with unit width which confirms the bias is small. We also perform a linearity test between generated vs. fitted signal yield by varying it from 0 to 120 as shown in Fig. 5.29. We find the slope and intercept to be 1.001 ± 0.002 and 0.14 ± 0.16 respectively. We will take 0.14 events as a systematic uncertainty related to possible fit bias.

The possible bias on signal due to small bias on the $b\bar{b}$ and $q\bar{q}$ yields for $B \to D_{\rm sup}K$ mode is checked by generating 10000 toy-experiments. Figure 5.30 and Fig. 5.31 show, the pull distributions for 937 and 11365 generated $b\bar{b}$ and $q\bar{q}$ events respectively. The maximum possible bias of 3 events on 77 generated signal events is shown in Fig. 5.32.

Similarly we check for a possible bias in the fit to $B \to D_{\rm sup}\pi$ mode is checked by generating 10000 toy-experiments. Figure 5.33 shows, the pull and return yield distribution obtained for 94 generated signal events. We find the fitted values to be normally distributed around the expected value and the pull distributions to be distributed around zero mean with unit width which confirms the bias is very small (0.47).

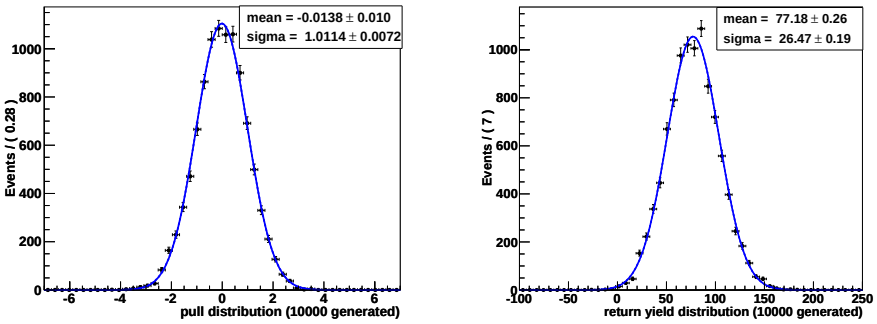

(a) (b)

Figure 5.28: (a) Pull and (b) yield distribution for 10000 experiments with an input signal yield of 77 events.

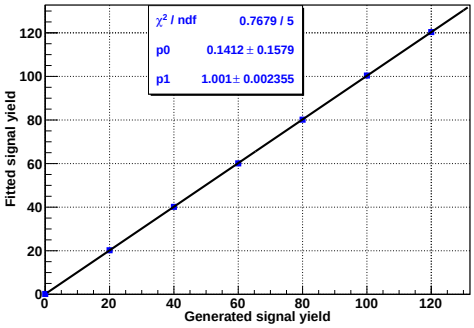

Figure 5.29: Linearity test for the $B \to D_{\rm sup}K$ yield. 10000 toy experiments have been generated at seven different input signal yields: 0, 20, 40, 60, 80, 100, 120.

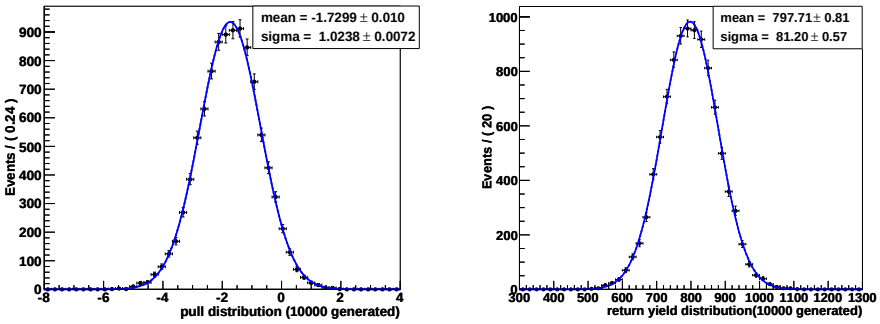

(a) (b)

Figure 5.30: (a) Pull and (b) yield distribution for 10000 experiments with an input $D_{\rm sup}K$ $b\overline{b}$ yield of 937 events.

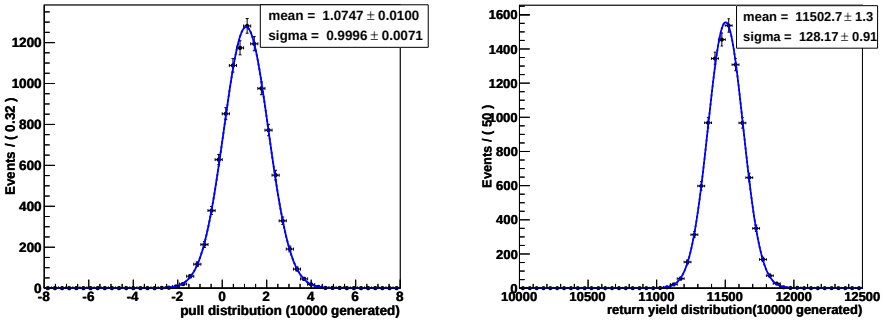

(a) (b)

Figure 5.31: (a) Pull and (b) yield distribution for 10000 experiments with an input $D_{\rm sup}K$ $q\overline{q}$ yield of 11365 events.

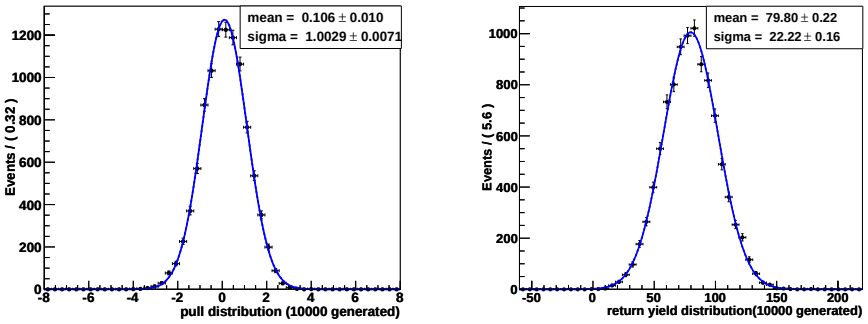

(a) (b)

Figure 5.32: (a) Pull and (b) yield distribution for 10000 experiments with an input $D_{\rm sup}K$ signal yield of 77 events.

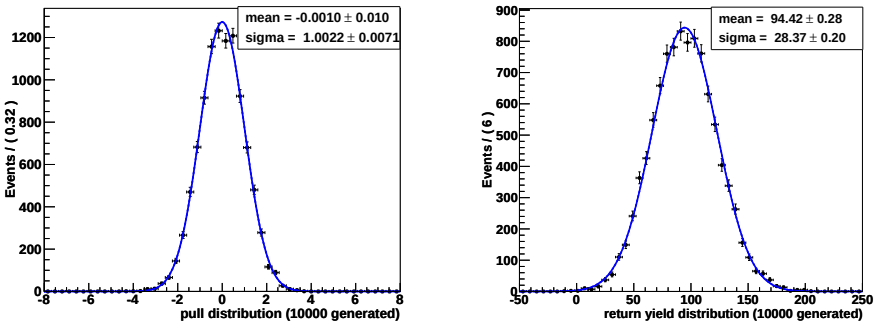

(a) (b)

Figure 5.33: (a) Pull and (b) yield distribution for 10000 experiments with an input $D_{\rm sup}\pi$ signal yield of 94 events.

Chapter 6

Measurement of Observables Relative to Angle ϕ_3

In this chapter we discuss about the calculation of suppressed to favored branching-fraction ratio, R_{ADS} and CP asymmetry, A_{ADS}. We also discuss the related systematic associated with these observables coming from PDF parameterization, bias in the fit, bias due to $b\bar{b}$ and $q\bar{q}$, uncertainties due to peaking background, due to efficiency and uncertainty due to $D\pi$ yields in DK.

6.1 Calculation of R_{ADS}

We calculate the branching-fraction ratio R_{ADS} as

$$\begin{aligned} R_{ADS} &\equiv \frac{B(B^{\mp} \to [K^{\pm}\pi^{\mp}\pi^0]_D h^{\mp})}{B(B^{\mp} \to [K^{\mp}\pi^{\pm}\pi^0]_D h^{\mp})} \\ &= \frac{N(B^{\mp} \to [K^{\pm}\pi^{\mp}\pi^0]_D h^{\mp})/\epsilon(B^{\mp} \to [K^{\pm}\pi^{\mp}\pi^0]_D h^{\mp})}{N(B^{\mp} \to [K^{\mp}\pi^{\pm}\pi^0]_D h^{\mp})/\epsilon(B^{\mp} \to [K^{\mp}\pi^{\pm}\pi^0]_D h^{\mp})} \end{aligned}$$

where N and ϵ are signal yield and detection efficiency, respectively. The efficiencies, corrected for data and MC differences in PID calibration between the modes. Corrections due to data MC differences in π^0 and charged track detection efficiencies cancel in the ratio. Using the above relation we obtain

$$R_{DK} = [1.98 \pm 0.62(\text{stat.}) \pm 0.24(\text{syst.})] \times 10^{-2}, \tag{6.1}$$

$$R_{D\pi} = [1.89 \pm 0.54(\text{stat.})^{+0.22}_{-0.25}(\text{syst.})] \times 10^{-3}. \tag{6.2}$$

The evaluation of systematic errors associated with R_{DK} and $R_{D\pi}$ are described in detail in Sec. 6.1.1

Table 6.1: Efficiencies for $D\pi$ and DK signals after PID calibration

Mode	MC efficiency (%)	PID correction[1]	total corrected efficiency (%)
$B \to D_{fav}\pi$	11.9±0.03	0.94±0.01	11.2±0.1
$B \to D_{sup}\pi$	11.9±0.03	0.94±0.01	11.2±0.1
$B \to D_{fav}K$	10.8±0.03	1.0±0.01	10.8±0.1
$B \to D_{sup}K$	10.9±0.03	1.0±0.01	10.9±0.1

6.1.1 Systematic uncertainties on R_{ADS}

In this section we describe the different systematic uncertainties on the measurement of R_{ADS}. The uncertainties considered relate to the PDF parameterization, possible bias due to the fit assumptions, determination of the peaking backgrounds and the error on efficiency. These are considered in turn below.

(1) ΔE and NB′-PDFs
The uncertainties associated with $B \to D_{\rm fav}h$ ($h = K/\pi$) and $B \to D_{\rm sup}h$ ($h = K/\pi$) mode, are obtained by varying each fixed parameter by $\pm 1\sigma$. The uncertainties associated with $B\overline{B}$ NB′ PDFs are obtained by varying the width and mean by 0.1 where, 0.1 is the maximum possible data-MC difference found from signal NB′-PDFs in $B \to D_{\rm fav}\pi$ decay. Table 6.2 shows the error associated with each fixed parameter for all the four modes ($B \to D_{\rm fav}h$ ($h = K/\pi$) and $B \to D_{\rm sup}h$ ($h = K/\pi$)). The total uncertainty, which is the quadratic sum of each individual uncertainty is also shown in the same table. Since there is no error associated with free PDF parameters, the uncertainty related to those PDFs are given as "−".

(2) Fit bias
The fit bias is checked by generating 10,000 toy experiments. The details have been discussed in Sec. 5.5. The fit bias on signal is estimated to be 0.14% (0.45%) for $D_{\rm sup}K(D_{\rm sup}\pi)$.

(3) Possible bias on signal due to bias between $b\bar{b}$ and $q\bar{q}$
Bias on signal yield due to small bias on $b\bar{b}$ and $q\bar{q}$ has been checked by generating 10,000 toy experiments. The details have been discussed in Sec. 5.5. We take the fit bias on signal to be 3% as a conservative limit for $D_{\rm sup}K$ mode.

(4) Peaking backgrounds
The uncertainty due to the backgrounds which peak under the signal was described in

[1]Considering the possible difference of PID (Particle Identification) efficiency between real data and MC, we need to add the PID correction factor to estimate the signal efficiency in real data.

Table 6.2: Systematic uncertainties due to variations in the fixed PDF parameters by one standard deviation in %.

Mode	Signal		Peaking	$B\overline{B}$		Continuum		**Total**
	ΔE	NB′	ΔE	ΔE	NB′	ΔE	NB′	
$D_{\rm fav}\pi$	–	–	–	–	$^{+0.24}_{-0.54}$	–	± 0.04	$^{\mathbf{+0.24}}_{\mathbf{-0.54}}$
$D_{\rm sup}\pi$	$^{+4.38}_{-2.81}$	$^{+1.50}_{-1.06}$	–	–	$^{+5.73}_{-9.09}$	–	$^{+3.83}_{-3.83}$	$^{\mathbf{+\ 8.30}}_{\mathbf{-10.31}}$
$D_{\rm fav}K$	$^{+0.85}_{-0.88}$	$^{+0.64}_{-0.56}$	± 0.3	–	$^{+0.28}_{-0.22}$	–	$^{+0.50}_{-0.47}$	$^{\mathbf{+1.25}}_{\mathbf{-1.20}}$
$D_{\rm sup}K$	$^{+3.89}_{-4.49}$	$^{+4.30}_{-3.18}$	0	–	$^{+1.84}_{-2.90}$	–	$^{+1.83}_{-3.18}$	$^{\mathbf{+6.35}}_{\mathbf{-6.99}}$

Sec. 5.4. The systematic error is estimated to be 9% (8%) for $D_{\rm sup}K$ ($D_{\rm sup}\pi$).

(5) Efficiency
Monte Carlo statistics and the uncertainties in the efficiencies of particle identifications can contribute to the systematic error in efficiency, which is estimated to be ±0.1% for all the four modes.

(6) $D_{\rm sup}\pi$ yield in $D_{\rm sup}K$
The uncertainty due to the $D\pi$ yields in DK is also checked by varying the $D\pi$ yield by $\pm 1\sigma$.[2] No change is observed in the DK yield due to changing the $D\pi$ yield. Therefore this systematic is negligible.

The total systematic error is the quadratic sum of the above uncertainties. The summary of all the systematic errors are given in Table 6.3.

We estimated the significance defined as $\sqrt{-2\ln(\mathrm{L}_0/\mathrm{L}_{\rm max})}$, where $\mathrm{L}_{\rm max}$ is the maximum likelihood and L_0 is the likelihood when the signal yield is constrained to be zero. In order to find the effect of systematic uncertainty on R_{DK} and $R_{D\pi}$, we convolute the likelihood using a symmetric Gaussian, whose width is taken as the systematic error of R_{DK} and an asymmetric Gaussian whose widths are the negative and positive systematic errors of $R_{D\pi}$, respectively. Figure 6.1 shows the distribution of $\sqrt{-2\ln(\mathrm{L}_0/\mathrm{L}_{\rm max})}$. We obtain a significance of 3.2σ and 3.3σ for R_{DK} and $R_{D\pi}$, respectively.

[2]The σ is the total error on $D_{\rm sup}\pi$ yield estimation in $D_{\rm sup}K$ decay by considering the error on $D_{\rm sup}\pi$ yield in $D_{\rm sup}\pi$ decay, error on π mis-ID rate and uncertainty on efficiency of identifying a π.

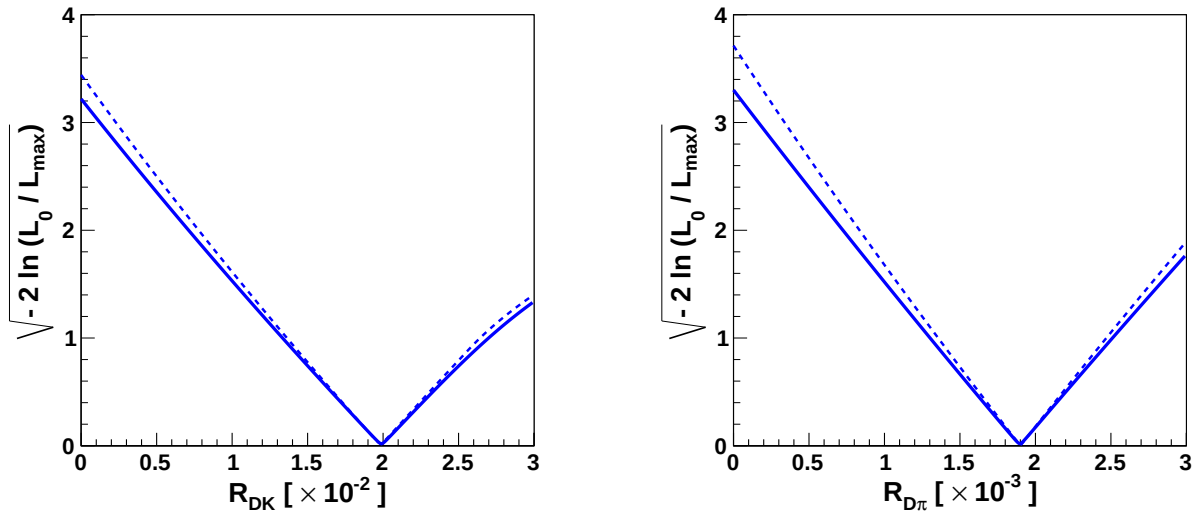

Figure 6.1: The distributions of $\sqrt{-2\ln(L_0/L_{max})}$ for R_{DK} (left) and $R_{D\pi}$ (right). The blue dashed curve shows the distribution obtained without including systematic error, while the blue solid curve shows the distribution obtained after including the systematic error.

6.2 CP-asymmetry (A_{Dh})

We also measure CP-asymmetry (A_{Dh}) in suppressed decays:

$$A_{Dh} \equiv \frac{B(B^- \to [K^+\pi^-\pi^0]_D h^-) - B(B^+ \to [K^-\pi^+\pi^0]_D h^+)}{B(B^- \to [K^+\pi^-\pi^0]_D h^-) + B(B^+ \to [K^-\pi^+\pi^0]_D h^+)}$$

as,

$$A_{DK} = 0.41 \pm 0.30(\text{stat.}) \pm 0.05(\text{syst.}), \quad (6.3)$$

$$A_{D\pi} = 0.16 \pm 0.27(\text{stat.})^{+0.02}_{-0.03}(\text{syst.}). \quad (6.4)$$

The ΔE projections for signal Dh^- and Dh^+ are shown in Fig. 6.2. The total systematic errors (Table 6.3) are subdivided as follows: the uncertainties related to fit are obtained in the same way as we get for R_{Dh}. The uncertainty due to the yield of the peaking background is obtained to be ± 0.04 (± 0.01) for A_{DK} ($A_{D\pi}$) which is taken as a multiplicative systematics on asymmetry. Possible bias due to the detector asymmetry is obtained by the data asymmetry result from favored modes, which is very small. We take the statistical error of the asymmetry, ± 0.02 (± 0.00) as a systematic for A_{DK} ($A_{D\pi}$). The total systematic is the sum in quadrature of the above individual systematic errors. Figure 6.3 shows the comparison between the $R_D(K\pi\pi^0)K$ and $A_D(K\pi\pi^0)K$ result from Belle with the expectations.

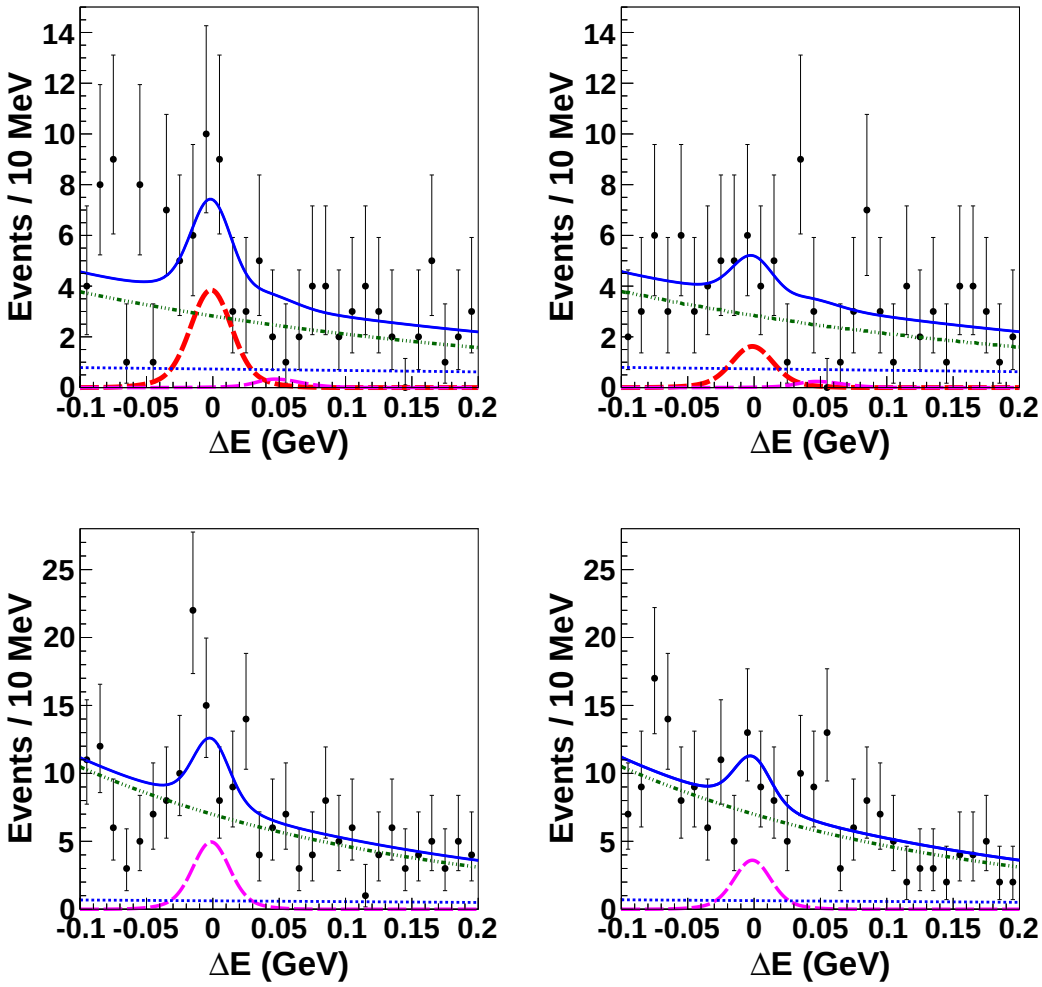

Figure 6.2: ΔE distributions (NB$' > 4$) for $D_{sup}K^-$ (left upper), $D_{sup}K^+$ (right upper), $D_{sup}\pi^-$ (left lower), $D_{sup}\pi^+$ (right lower). In these plots, points with error bars represent data while the total best-fit projection is shown with the solid blue curve, for which the components are shown with thicker dashed red (DK signal), thinner dashed magenta ($D\pi$), dashed dot green ($B\bar{B}$ background) and dotted blue ($q\bar{q}$ background).

Table 6.3: Summary of the systematic uncertainties for $D_{\rm fav}h$, $D_{\rm sup}h$, R_{Dh} and A_{Dh}.

Source	$D_{\rm fav}\pi$	$D_{\rm sup}\pi$	$D_{\rm fav}K$	$D_{\rm sup}K$	$R_{D\pi}$	R_{DK}	$A_{D\pi}$	A_{DK}
ΔE and NB$'$-PDFs	$^{+0.2}_{-0.5}\%$	$^{+8.3}_{-10.3}\%$	$^{+1.2}_{-1.2}\%$	$^{+6.3}_{-7.0}\%$	$^{+8.3}_{-10.3}\%$	$^{+6.5}_{-7.1}\%$	$^{+0.02}_{-0.03}$	$^{+0.03}_{-0.02}$
Fit bias	–	+0.4%	–	+0.1%	+0.4%	+0.1%	–	–
Due to $b\bar{b}$ and $q\bar{q}$ bias	–	–	–	±3.0%	–	±3.0%	–	–
Peaking background	–	±8.2%	–	±9.5%	±8.2%	±9.5%	±0.01	±0.04
Efficiency	±0.1%	±0.1%	±0.1%	±0.1%	±0.1%	±0.1%	–	–
Detector asymmetry	–	–	–	–	–	–	±0.02	±0.02
Combined	$^{+0.2}_{-0.5}\%$	$^{+11.7}_{-13.2}\%$	$^{+1.2}_{-1.2}\%$	$^{+11.8}_{-12.2}\%$	$^{+11.7}_{-13.2}\%$	$^{+11.9}_{-12.2}\%$	$^{+0.03}_{-0.04}$	±0.05

We perform a comparison between our result on R_{DK} and A_{DK} with the expectations of the standard model. The comparison plot is shown below. The result has some tension with the Standard Model prediction but its significance is less than 3 standard deviations. Therefore, more measurements at LHCb or Belle II are required to investigate this discrepancy further.

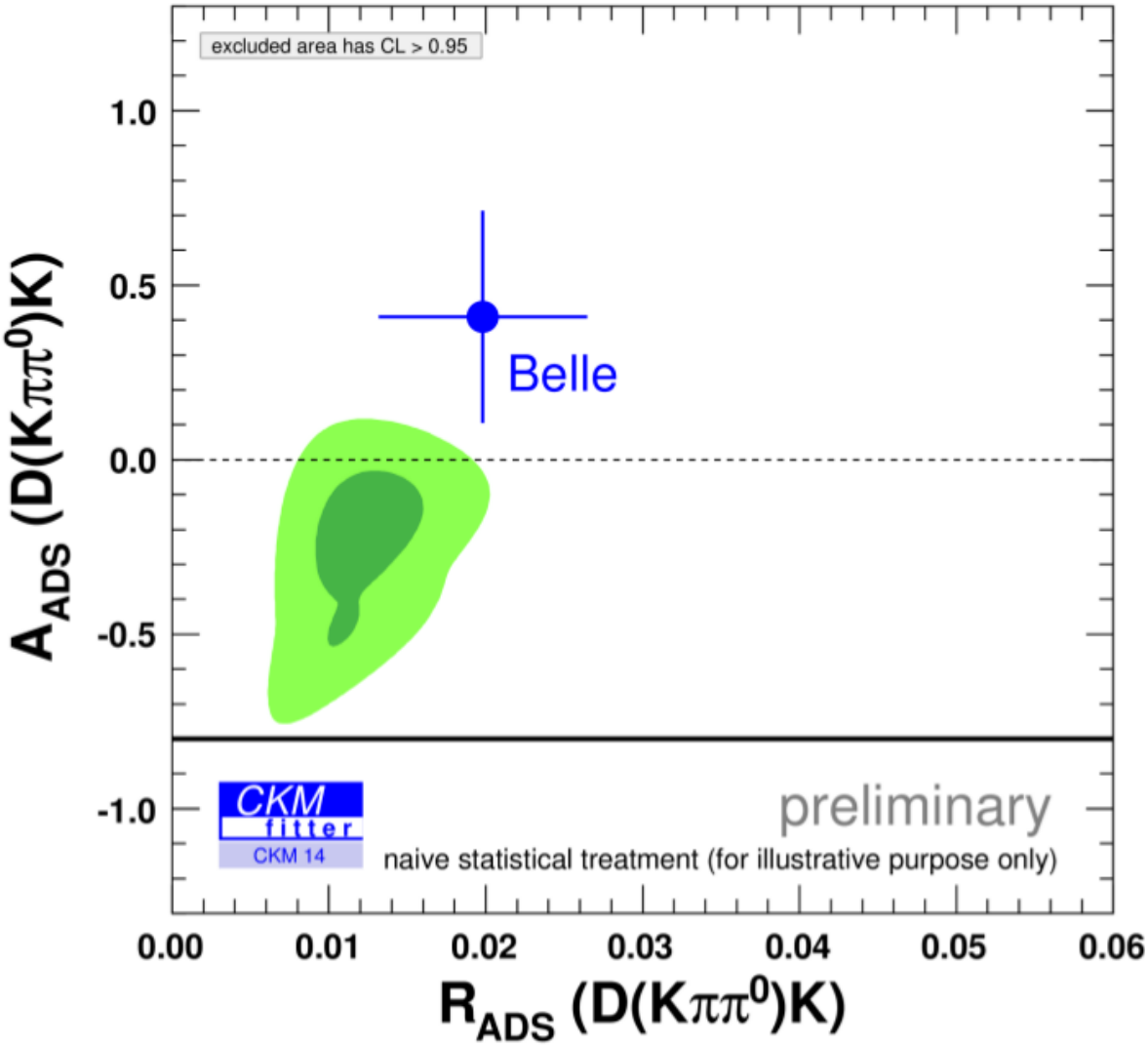

Figure 6.3: Plot comparing ADS $B \to D(K\pi\pi^0)K$ result from Belle with the expectations.

Chapter 7

CLEO-c Analysis

The outline of the chapter is structured as follows. First we discuss how quantum correlated D decays can be used to determine the CP content and predictions of the CP content from the Dalitz amplitude model. CESR and CLEO-c experiments are discussed shortly in the next section. Next we discuss the data and MC sample used for the analysis followed by event selection. Selection of double-tag, single-tag events by applying tight selection criteria are discussed then. Then we follow double-tag background evolution and double-tag yield determination followed by $h^-h^+\pi^0$ vs $h^-h^+\pi^0$ yield determination. We discuss the $K_L$tag background evolution followed by the signal $\pi^-\pi^+\pi^0$ vs. $K_L$tag yield determination. Next we extract the single-tag yield for non $K_L$tag decay. Finally determination of CP fraction (F^+) followed by systematic uncertainties and implication of the F^+ value for the ϕ_3 measurement.

7.1 Determination of the CP content of $D \to h^-h^+\pi^0(h = \pi/K)$ at CLEO-c

Since $\psi(3770)$ is a vector particle, so the decay $\psi(3770) \to D\bar{D}$ is an antisymmetric wavefunction:

$$\frac{(|D\rangle\,|\overline{D}\rangle - |\overline{D}\rangle\,|D\rangle)}{\sqrt{2}} \tag{7.1}$$

In the case when $\psi(3770)$ decays to two inclusive states F and G, the decay rate of the total final state [57]:

$$\begin{aligned}
\Gamma(F|G) &= \Gamma_0 \int_{\mathbf{x},\mathbf{y}} |A_F(\mathbf{x})\overline{A}_G(\mathbf{y}) - \overline{A}_F(\mathbf{x})A_G(\mathbf{y})|^2 d\mathbf{x}d\mathbf{y} && (7.2)\\
&= \Gamma_0 \int_{\mathbf{x},\mathbf{y}} (|A_F(\mathbf{x})|^2|\overline{A}_G(\mathbf{y})|^2 + |\overline{A}_F(\mathbf{x})|^2|A_G(\mathbf{y})|^2 \\
&\quad -2|A_F(\mathbf{x})C(\mathbf{y})\overline{A}_F(\mathbf{x})A_G(\mathbf{y})|\cos\left[\delta_D^G(\mathbf{x}) - \delta_D^F(\mathbf{x}]\right)d\mathbf{x}d\mathbf{y} && (7.3)\\
&= \Gamma_0\{A_F^2\overline{A}_G^2 + \overline{A}_F^2A_G^2 - 2R_FR_GA_F\overline{A}_FA_G\overline{A}_G \times \cos\left[\delta_D^G - \delta_D^F\right]\}\ , && (7.4)
\end{aligned}$$

where $\Gamma_0 = \Gamma(\psi(3770) \to D\bar{D})$ and $\mathbf{x}$ ($\mathbf{y}$) describe the kinematics of $D \to F$ ($\bar{D} \to G$), A_F and $\bar{A}_F$ (A_G and $\bar{A}_G$) are the average amplitudes of D and $\bar{D}$ decay to F (G), δ_D^F (δ_D^G) is the average strong phase difference for F (G) and R_F (R_G) is a measure of the coherence of F (G), where $0 < R_F(R_G) < 1$.

Let us consider the case when G is a CP eigenstate with eigen value, $\lambda_{CP} = +1$ or -1. When G is a CP eigenstate then $R_{CP} = 1$ and δ_D^{CP} is 0 or π. Therefore, the decay rate can be written as:

$$\Gamma(F|CP) \;=\; \Gamma_0|A_F|^2|A_{CP}|^2[1 + (r_D^F)^2 - 2\lambda_{CP} r_D^F R_F \cos\delta_D^F] \; . \tag{7.5}$$

Let's consider our case, $F \to h^-h^+\pi^0$, then the above equation can be expressed as:

$$\begin{aligned}\Gamma(h^-h^+\pi^0|CP) \;=\; & \Gamma_0|A_{h^-h^+\pi^0}|^2|A_{CP}|^2[1 + (r_D^{h^-h^+\pi^0})^2 \\ & -2\lambda_{CP} r_D^{h^-h^+\pi^0} R_{h^-h^+\pi^0} \cos\delta_D^{h^-h^+\pi^0}] \; .\end{aligned} \tag{7.6}$$

In the special case, if $h^-h^+\pi^0 \to$ a pure CP state, then $R_{h^-h^+\pi^0} \to 1$ and $\delta_D^{h^-h^+\pi^0} \to 0$ or π, then the above expression becomes,

$$\Gamma(h^-h^+\pi^0|CP) \;\to\; 2\Gamma_0|A_{h^-h^+\pi^0}|^2|A_{CP}|^2[1 - \lambda_{CP}\lambda'_{CP}] \; . \tag{7.7}$$

If F is a opposite CP state, then

$$\Gamma(h^-h^+\pi^0|CP) \;\to\; 4\Gamma_0|A_{h^-h^+\pi^0}|^2|A_{CP}|^2. \tag{7.8}$$

Thus, the double tagged decay rate will be maximally enhanced if F is a opposite CP state.
If F is in same CP state, then

$$\Gamma(h^-h^+\pi^0|CP) \;\to\; 0. \tag{7.9}$$

Thus, the double tagged decay rate will approach to zero if F is a same CP state.

With this quantum correlation idea, let's consider a $\psi(3770) \to D\bar{D}$ analysis to determine the CP content of signal $D \to h^-h^+\pi^0$. Let M^+ designate the number of "double-tagged" candidates, after background subtraction, where one D meson is reconstructed in the signal mode of interest, and the other is reconstructed in a CP-odd eigenstate. The quantum-numbers of the $\psi(3770)$ resonance require that the signal mode is in a CP-even state, hence the + superscript. The observable M^- is defined in an analogous manner. Let S^+ (S^-) designate the number of "single-tagged" CP-odd (CP-even) candidates in the data sample, where a D meson is reconstructed decaying to a CP eigenstate, with no requirement on the final state of the other D meson in the event. The small effects of $D^0\bar{D}^0$ mixing are eliminated from the measurement by correcting the measured single-tagged yields $S^{\pm}_{\rm meas}$ such that $S^{\pm} = S^{\pm}_{\rm meas}/(1 - \eta_{\pm} y_D)$, where $\eta_{\pm}$ is the CP eigenvalue of the mode, and $y_D \sim 10^{-2}$ is one of the well-known $D^0\bar{D}^0$ mixing parameters [58]. For a time-integrated measurement at the $\psi(3770)$ there are no effects on the double-tagged yields at leading order in the mixing parameters.

On the assumption that for double-tagged candidates the reconstruction efficiencies of each D meson are independent, then the quantity $N^+ \equiv M^+/S^+$ has no dependence on the branching fractions or reconstruction efficiencies of the CP-eigenstate modes, and can be directly compared with the analogous quantity N^- to gain insight into the CP-content of the signal mode. The CP fraction is defined

$$F_+ \equiv \frac{N^+}{N^+ + N^-} \tag{7.10}$$

and is 1 (0) for a signal mode that is fully CP-even (CP-odd).

Dalitz plot formalism

We use Amplitude models of $D^0 \to \pi^+\pi^-\pi^0$ and $D^0 \to K^+K^-\pi^0$ available from studies of flavor-tagged D^0 decays performed by the BaBar collaboration [22, 24], to measure the observable F_+.

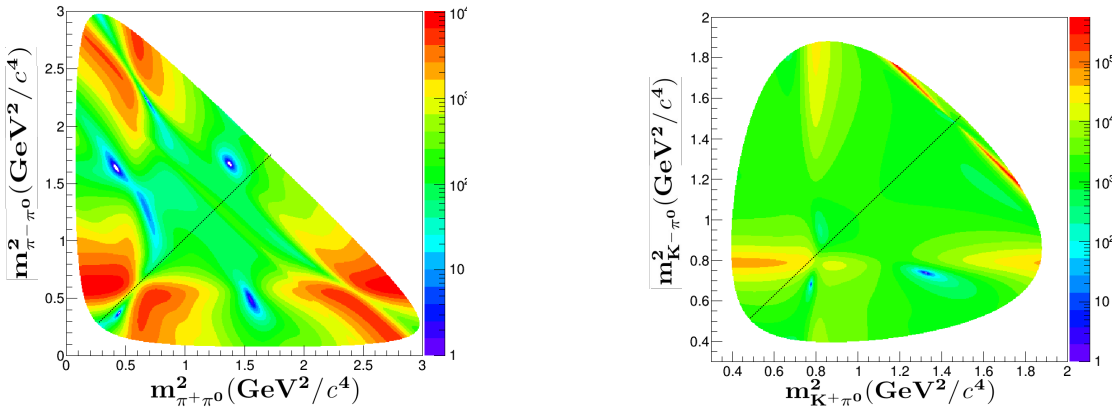

Figure 7.1: Amplitude squared distributions for $\pi^+\pi^-\pi^0$ (left), and $K^+K^-\pi^0$ (right) state. The diagonal line separates the positive and negative bins.

The observable F_+ can be interpreted making use of the formalism developed in Ref. [20] for binned analyses of self-conjugate three-body final states. Considering our case where $h^+h^-\pi^0$ Dalitz distribution is divided into two bins by the line $m^2_{h^+\pi^0} = m^2_{h^-\pi^0}$ as shown in Fig. 7.1. The bin for which $m^2(h^+\pi^0) > m^2(h^-\pi^0)$ is as labelled $-i$ and the opposite bin is labelled as $+i$. The CP-tagged events in these bins, $N_i^\pm$, normalised by the corresponding single CP-tag yields, is given by

$$\begin{aligned} N_i^\pm &= h_D(K_i \pm 2c_i\sqrt{K_iK_{-i}} + K_{-i}), \\ N_{-i}^\pm &= h_D(K_{-i} \pm 2c_i\sqrt{K_{-i}K_i} + K_i). \end{aligned} \tag{7.11}$$

Here h_D is a normalisation factor independent of bin number and CP-tag. The parameter K_i is the flavor-tagged fraction if D^0 is a flavor eigenstate defined as:

$$K_i \;=\; N_D \int_{\mathcal{D}} p_D \, d\mathcal{D}, \tag{7.12}$$

where N_D is the normalisation factor which depends on Dalitz plot amplitude. The parameter c_i is the cosine of the strong-phase difference between D^0 and $\bar{D}^0$ decays averaged in bin i and weighted by the absolute decay rate is defined as:

$$c_i \;=\; \frac{\int_{\mathcal{D}} \sqrt{p_D \bar{p}_D} \cos(\Delta\delta_D(m^2_{h^+\pi^0}, m^2_{h^-\pi^0}))\, d\mathcal{D}}{\sqrt{\int_{\mathcal{D}} p_D d\mathcal{D} \int_{\mathcal{D}} \bar{p}_D d\mathcal{D}}}, \tag{7.13}$$

where p_D and $\bar{p}_D$ are the absolute value of the square of the amplitude defined as,

$$p_D = |A_D(m^2_{h^+\pi^0}, m^2_{h^-\pi^0})|^2,$$
$$\bar{p}_D = |A_D(m^2_{h^-\pi^0}, m^2_{h^+\pi^0})|^2.$$

$\mathcal{D}_i$ is the Dalitz region and δ_D is the strong-phase difference between D^0 and $\bar{D}^0$ decays averaged in bin i. $\Delta\delta_D$ the strong phase difference between the symmetric Dalitz plot points can be obtained from the decay of D meson to CP eigenstates. Here we have used the convention $C\,|D^0\rangle = -\,|\bar{D}^0\rangle$. The Dalitz plot density of such decay to CP eigenstate is:

$$p_{CP} = |A_D \pm \bar{A}_D|^2 = p_D + \bar{p}_D \pm 2c\sqrt{p_D \bar{p}_D}. \tag{7.14}$$

This expression is used to find the CP-tagged yield as given in Eqn. 7.11. $m^2_{h^+\pi^0}$ and $m^2_{h^-\pi^0}$ are the invariant mass squared of the $h^+\pi^0$ and $h^-\pi^0$, respectively in the Dalitz plot. $A_D(m^2_{h^+\pi^0}, m^2_{h^-\pi^0})$ and $\bar{A}_D(m^2_{h^+\pi^0}, m^2_{h^-\pi^0})$ are the $D \to h^+h^-\pi^0$ and $\bar{D} \to h^+h^-\pi^0$ decay amplitudes, respectively. By making use of the relations $N^{\pm} = \sum_i N_i^{\pm}$, $\sum_i K_i = 1$ and $c_1 = c_{-1}$ it follows that

$$F_+ = \frac{1}{2}\left(1 \,+\, 2c_1\sqrt{K_i K_{-i}}\right). \tag{7.15}$$

Therefore the inclusive decay tends to a pure CP eigenstate in the limit that the Dalitz plot is symmetric, with $K_i = K_{-i} = 1/2$, and c_i is -1 or 1.

Result from Dalitz's analysis: The above Dalitz models along with Eq. 7.15, are used to calculate predictions for F_+ for each decay. We obtain $\mathbf{F}_+ = \mathbf{0.92}$ for $D \to \pi^+\pi^-\pi^0$ and $\mathbf{F}_+ = \mathbf{0.64}$ for $D \to K^+K^-\pi^0$ and the corresponding distribution is shown in Fig. 7.1. The amplitude models are fitted to time-integrated data and the $D^0\bar{D}^0$ mixing is included. The biases in the predicted values of F_+ arising from these effects are < 0.01.

The CP content of the state $D \to h^-h^+\pi^0$ also has consequences for the number of self tags M^{self}. Using the formalism of Ref. [20] for self-tagged events, and once more

considering a Dalitz plot divided into two, the number of self tag candidates in bins i and j is given by

$$M_{ij}^{\rm self} = 0.5R\,(K_iK_{-j} + K_{-i}K_j - 2\sqrt{K_iK_{-j}K_{-i}K_j}(c_ic_j + s_is_j)). \tag{7.16}$$

Here $R = N_{D\bar{D}}(BR_{h^-h^+\pi^0})^2\epsilon$, where $N_{D\bar{D}}$ is the number of $D\bar{D}$ pairs in the sample, $BR_{h^-h^+\pi^0}$ is the branching fraction of $D^0 \to h^-h^+\pi^0$ and ϵ is the detection efficiency. The parameter s_i is the sine of the strong-phase difference between D^0 and $\bar{D}^0$ decays averaged in bin i and weighted by the absolute decay rate. Employing the same relations as previously, together with $s_1 = -s_{-1}$ and $M^{\rm self} = \sum_{i,j} M_{ij}^{\rm self}$ it follows that

$$\begin{aligned} M^{\rm self} &= R\,(1 - 4c_1^2K_1K_{-1}) \\ &= 4R\,F_+(1-F_+). \end{aligned} \tag{7.17}$$

Hence the number of self tags vanishes in the case that the signal mode is a CP eigenstate.

7.2 CESR and CLEO-c experiment

Figure 7.2 shows the schematic view of Cornell Electron Storage Ring (CESR) [59] which is a symmetric energy e^+e^- machine at Cornell University, New York, United States. CESR started its operation in 1981 and got continuously upgraded till 2002. It operated at CM energy in the range: 3.5 GeV - 12 GeV. Now CESR is used as a X-ray source known as Cornell High Energy Synchrotron Source (CHESS). Particles were accelerated via three machines: a 30 m linear accelerator (LINAC), a synchrotron and the storage ring CESR. The circumference of CESR was 768 m. The LINAC produced electrons from a 120 kV electron gun. The electrons produced were accelerated up to 300 MeV using low-frequency RF cavities. A tungsten target inserted into the beam; so that electrons incident upon this target produced showers of particles including electrons, positrons and photons. Using magnets, the electrons can be bent one way and the positrons bent the other way, thus separating them from each other where as photons are unaffected by a magnet. The positrons captured are accelerated to 160 MeV. The electrons and positrons bunches are then accelerated in opposite direction and transfered to synchrotron. The synchrotron was used to accelerate the particles from LINAC to CESR energies. Particles were then bent from the synchrotron into CESR using dipole magnets which are present through out the ring. There are also quadrupole magnets used for focusing and defocusing the beam, and sextupole magnets to correct for energy dependent effects.
The bunches of particle collide at the interaction point (IP). The luminosity achieved dependents upon:

$$L \propto f\frac{N_B n_{e^-} n_{e^+}}{A}, \tag{7.18}$$

where N_B is the number of bunches, f is the revolution frequency of bunches, n_{e^+} and n_{e^-} are the number of e^- and e^+ in each bunch. Using the above relation, the instantaneous luminosity achieved by CESR by the CLEO-c detector was $O(10^{31})\text{cm}^{-2}\text{s}^{-1}$.

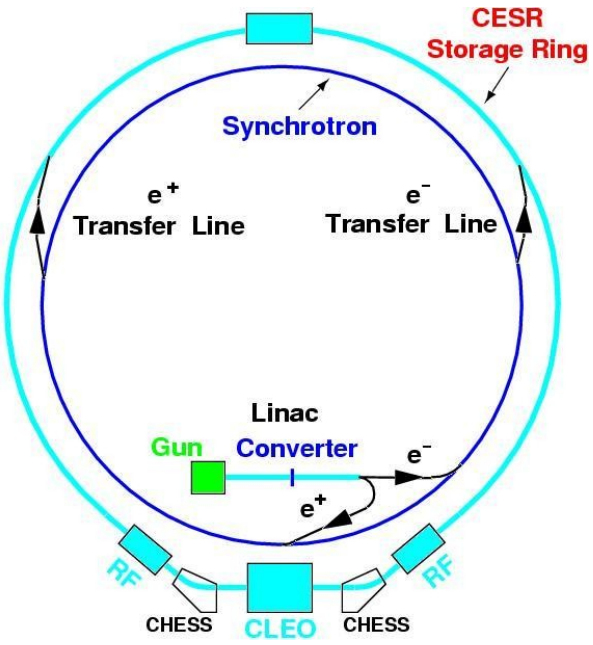

Figure 7.2: A schematic view of CESR showing the CHESS and CLEO-c detector areas. Taken from Reference [60].

7.2.1 CLEO-c

CLEO-c was a symmetric detector present at the collision point of the CESR, at 3.77 GeV. It covers approximately 93% of the 4π solid angle. It consists of subdetectors designed to measure kinematic properties of detected particles and distinguish between them. Figure 7.3 shows a 3D schematic view of the detector. It consists of a wire drift-chamber, a Ring Imaging Cherenkov (RICH) detector for identifying hadrons above 700 MeV/c, a crystal calorimeter known as electromagnetic calorimeter, a 1 T superconducting magnetic field and finally barrel muon chamber. In the following section we give brief flavor of the subdetectors used for our analysis.

Drift Chamber

The CLEO-c Drift Chamber consists of two cylindrical, concentric drift chambers: the inner Drift chamber (ZD) between the radii of 5.3 cm and 10.5 cm and the outer Drift chamber (DR) between 12 cm and 82 cm [62, 63]. In total, the tracking systems covers about 93% of 4π. The ZD replaced the silicon vertex detector that had been used in CLEO III, and used to detect low-momentum particles. Both ZD and DR were located

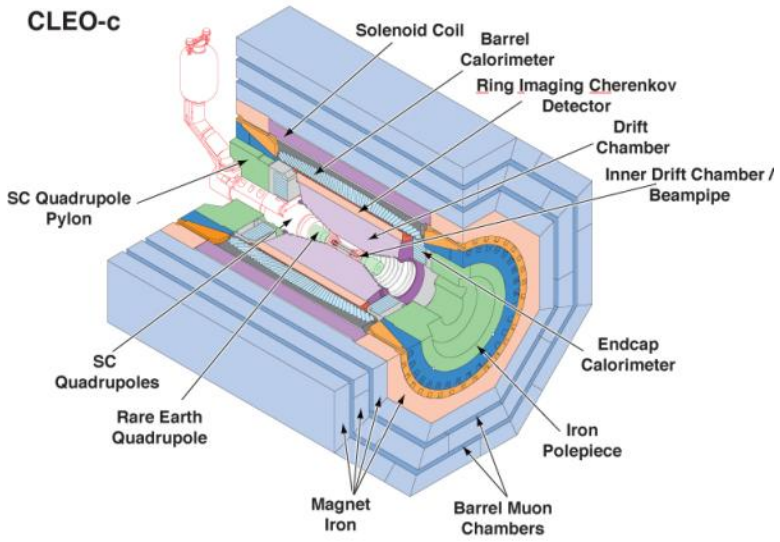

Figure 7.3: The CLEO-c detector. Taken from Reference [61].

in a 1 Tesla magnetic field. Charged particle's trajectories were curved in the $x-y$ plane because of the magnetic field present. A 60% : 40% helium (He) and propane (C_3H_{10}) gas mixture filled in ZD. It composed of 300 sensitive cells arranged into six layers and DR located between radii of 120 and 820 mm are arranged in 47 layers. The momentum resolution, σ_p/p, of the ZD, was about 0.4% for charged particles at normal incidence. Each cell consisting of a gold-plated tungsten sense wire of 20μm diameter and gold-plated aluminium field wire of diameter 130μm. The minimum distance between sense wire and field wire is 5mm for ZD and 7mm for DR. Sense wires are maintained at 2KV potential w.r.t. field wire. The overall positional resolution of the tracking detectors was about 100 μm. The momentum resolution σ_p/p was about 0.6% for 1 GeV/c tracks that traversed every layer of the ZD and DR. When an energetic charged particle passes through the chamber, it ionizes a track of gas. The electrons liberated are accelerated towards the sense wire. Since the electrons are energetic enough, so they produce local ionization around the sense wire which in turn create avalanche of electrons with an amplified signal. The time at which the avalanche occurred were recorded to find the distance of closest approach of the particles from the sense wires. To reconstruct the particles three dimensional trajectory inside the drift chamber, the distance of closest approach of the particle to the sense wire is fitted using minimum χ^2 fit and Kalman fitter to find the physical modes of interest excluding the background tracks or poorly reconstructed tracks. The curvature of the fitted track in the 1 T magnetic field allowed to determine the momentum of the charged particle.

Particle Identification: The trajectory of charged particles that passes through the tracking system can be determined by identifying the signal deposits in the sense wires. When a charged particle passes through the gas in the drift chamber, it ionises the gas, liberating electrons that drift towards a sense wire due to the electromagnetic field present in the chamber. Because of the strong electric field present near the anode, the

electrons ionise the gas further, creating an avalanche of e^- with an amplified signal. By determining the time at which the avalanche occurred and, from the information of bunch crossing time, one can calculate the time taken for the initial electron to reach the sense wire. The distance of closest approach could be determined from the time and position information of an e^- to reach the sense wire. The momentum ($|p|$) of the charged particle could be determined by combining the information from all the cells. For particles of momentum less than 700 MeV/c, the tracking system could be used to discriminate between hadrons by determining the energy loss (dE/dx), of a charged particle in the gas. The dE/dx of an incident particle is determined by measuring the avalanche created by the particle near the sense wire. By using Bethe Bloch formula [8], one can determine the mass of the parent particle by combining the dE/dx information with the measured $|p|$.

Ring Imaging Cherenkov (RICH) detector

The Ring Imaging CHerenkov (RICH) detector[64] is used to identify the charged particles of higher momentum. It is present between the Drift Chamber and Electromagnetic Calorimeter. The RICH covers 80% of 4π. The cross sectional view of RICH detector is shown in Fig. 7.4. When charged particles pass through LiF radiators with refractive index 1.5, they emit Cherenkov photons. To overcome the total internal reflection at normal incidence, the crystals near to the interaction point are equipped with sawtooth radiators. The Cherenkov photons produced travel through the nitrogen expansion gap and enter the multi-wire proportional chambers (MWPC) through CaF2 windows, filled with a gas mixture of methane (CH_4) and triethylamine(TEA). The Cherenkov photons lying in the range of 135-165 nm are converted into photo-electrons by ionisation of the gas. These photo-electrons are then amplified by the proportional wire chamber mechanism and detected by 7.5 mm $\times$ 8 mm cathode pads. Particle with momentum

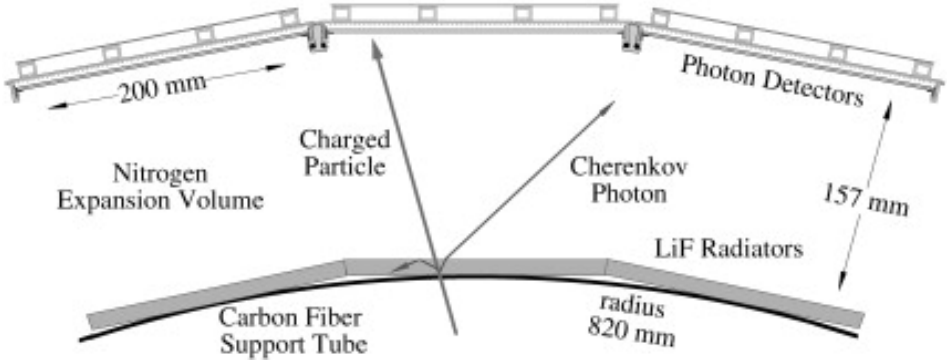

Figure 7.4: Cross sectional view of the CLEO-c RICH detector. Taken from Reference [65].

greater than 0.12 GeV/c which reaches RICH detector can be Identified. The operating principle of a RICH is that when a charged particle travelling faster than the speed of

light in a medium, it emits a cone of Cherenkov radiation. The Cherenkov light when incident upon photosensitive material is detected as a ring of hits. The opening angle of the Cherenkov light (θ_{Ch}) dependents upon the velocity of the particle (v) and the refractive index of the medium (n) as:

$$\begin{aligned} cos(\theta_{Ch}) &= \frac{c}{nv} \\ &= \frac{1}{n}\sqrt{1+\left(\frac{mc}{|\mathbf{p}|}\right)^2}, \end{aligned} \tag{7.19}$$

where m and $\mathbf{p}$ are the mass and momentum of the particle, respectively. The maximum Cherenkov angle approaches to $1/n$ with the limit $m \to 0$ and $p \to \infty$. v can be measured from the radius of the ring. combining this information with the momentum measurement, one can determine the mass of the particle.

Crystal calorimeter

The crystal calorimeter [66] was designed to identify e^-, γ, η, π^0, by measuring the energy of electromagnetic showers. It consists of around 7800 scintillating crystals covering about 93% of 4π. The crystals of ($5 \times 5 \times 30$) cm size are composed of CsI doped with 0.1% thallium. The crystals are located in the central barrel and in two endcap regions. The barrel crystals are tapered towards the front face, the endcap crystals are rectangular, but shaved near the outer radius to fit in the container and reduce leakage. Four photodiodes were located at the end of each crystal to detect scintillation light. Both photons and electrons produce narrow deposits of energy in the calorimeter. Photon candidates were detected as deposits of energy without having any tracks associated, whereas e^- are associated with tracks. The energy and position of each shower are used to measure photon momentum. The calorimeter achieves photon energy resolution, $\frac{\sigma_E}{E} = 1.5\%$ at 5 GeV, 4% at 100 MeV, and 7% at 30 MeV.

7.2.2 Data and Monte Carlo samples

Data samples

CLEO-c has taken data at various charmonium energies. A total of (818 ± 8) pb^{-1} data collected at 3.77 GeV, consisting of $\psi(3770) \to D^0\bar{D}^0$ pairs, were used in the analysis described below. The CLEO-c $\psi(3770)$ full data sample corresponds to the ten datasets: 31-33, 35-37 and 43-46. Table 7.1 gives the integrated luminosity for each data set. The cross section corresponding to the above decay is equal to $(3.66 \pm 0.06 \pm 0.03)$ nb.

MC samples

Generic, signal and continuum Monte Carlo data have been used in the analysis. The details of each Monte Carlo sample are given below. The generic $D\bar{D}$ simulation of

Table 7.1: The integrated luminosity $\int Ldt$ of the $\psi(3770)$ data used in the analysis.

Dataset	$\int Ldt(\text{pb}^{-1})$	Dataset	$\int Ldt(\text{pb}^{-1})$
31	20.631	37	111.467
32	32.959	43	116.648
33	6.657	44	173.987
35	50.883	45	108.192
36	71.582	46	137.084

the 281 pb^{-1} data sample corresponding to datasets 31-33 and 35-37 were studied to determine peaking backgrounds. The total integrated luminosity used in this study is 2936.11 pb^{-1} which is 10×281 pb^{-1} data sample.

Signal MC samples are generated for each $D^0\bar{D}^0$ double-tagged and single-tagged modes under study. For a given signal mode, the sample contains 50×10^3 events. These events were used to study selection criteria and estimate the reconstruction efficiencies.

We also studied continuum sample generated with a luminosity $5\times$ greater than the data events corresponding to datasets 31-33 and 35-37. This continuum sample is used to study background.

EVTGEN generator [67] package has been used to simulate the decays. The detector response is modelled using the GEANT software package [68].

7.2.3 Event Selection

We select fully reconstructed double-tagged events from two single-tag events, one reconstructed from D^0 and other from $\bar{D}^0$. For our analysis we use $\psi(3770) \to D^0\bar{D}^0$ double-tagged events where one D meson decays to $\pi^+\pi^-\pi^0$ and the other to specific CP eigenstate of interest. The decays of both D mesons are identified. All final state tracks and showers associated with both D meson decays are reconstructed. Selections are also performed for CP tags that involve a K^0_L meson. Due to the K^0_L mesons long lifetime and its subsequent tendency to decay outside the detector, a missing mass technique is applied to reconstruct the K^0_L meson and subsequently the tag. Reconstruction of all the modes are performed within the SUEZ software framework. For our analysis, we take pre-reconstructed, single-tag events called `DTags`. To reconstruct the double-tagged modes of interest, we combine the `DTag` object for each of the two constituent decay modes reconstructed within the same CLEO-c environment to form a composite, `DDoubleTag` object provided the two `DTag` objects do not share a common track or shower. The selection applied here is same as that given in Refs. [69, 17].

D-tag requirements

CLEO-c software is used to select the particles and combine them to form `DTag` objects during skimming procedure. The default selection criteria applied on the `DTag` objects

during skimming procedure are described below.

- **Charged Tracks**
  To determine good charged tracks, each charged track must satisfy the following selection criteria.

  - **χ^2 of Track Fit:**
    This refers to the performance of the Kalman filter that fits a track to the drift chamber wire hits. $\chi^2 < 100000$ is applied to remove the bad quality tracks/ghost tracks.
  - **Hit Fraction, f_{Hit} :**
    The ratio of the number of hits used in the track fit to the expected number of hits. The Hit fraction (f_{Hit}) must be greater than 0.5.
  - **Polar Angle, θ** :
    The track must lie in the region $|cos(\theta)| < 0.93$, where θ is the angle between the track and the beam axis. This cut is applied to remove tracks reconstructed from noise hits close to the beam pipe.
  - **Momentum, $|\vec{p}|$:**
    Each Charged track is required to have momentum in the range 0.05 - 2.0 GeV/c which should be consistent with that of D meson decay products. The low momentum (< 0.05 GeV/c) cut also removes the tracks which have poor resolution due to multiple scattering.

  - **Impact parameter:**
    Impact parameter, defined as the distance of closest approach of the reconstructed track to the interaction point. The cuts on impact parameter is designed to remove the tracks that don't come from the interaction point. We define good charged tracks by requiring $d_0 < 0.5$ cm and $z_0 < 5$ cm, where d_0 and z_0 represent the impact parameters to the nominal interaction point in the $x - y$ plane and along the z-axis, respectively.

  - **Particle Identification, PID :**
    We use PID information to distinguish between charged pion or kaon. The track will be identified as a charged kaon if it satisfies the following requirements:

$$\begin{aligned} \sigma_K^2 - \sigma_\pi^2 + \mathcal{L}_K - \mathcal{L}_\pi &\leq 0, \\ |\sigma_K| &\leq 3.0. \end{aligned} \tag{7.20}$$

    Similarly, a track will be identified as a charged pion if it satisfies the following requirements:

$$\begin{aligned} \sigma_\pi^2 - \sigma_K^2 + \mathcal{L}_\pi - \mathcal{L}_K &\leq 0, \\ |\sigma_\pi| &\leq 3.0, \end{aligned} \tag{7.21}$$

where $\sigma_{K/\pi}$ is the difference between the expected dE/dx of the track and the actual measured value, $\mathcal{L}_{K/\pi}$ is the likelihood of a tracks hypothesis determined from RICH information.

We use information from RICH along with $n_\gamma \geq 3$ which satisfies the following selection criteria:

$$\begin{aligned} |\vec{p}| &> 0.7\ GeV, \\ |cos\theta| &< 0.8. \end{aligned} \tag{7.22}$$

This ensures tracks have momenta sufficiently above Cherenkov threshold and are within the RICH detector acceptance. Here n_γ is the number of Cherenkov radiation associated with the track. We also require the dE/dx of a particular track is at most 3σ away from the expected dE/dx expected value, given the track momentum.

If these criteria are fulfilled, a combined log likelihood difference is constructed from the dE/dx and RICH information to identify pion/kaon.

- **π^0 and η Meson**
  π^0 and η mesons are identified from the energy deposit in the crystal calorimeter from their decays to di-photons. The following selection criteria have been applied while reconstructing π^0 or η. The invariant mass of π^0 or η must be less than 1 Gev/c^2. The magnitude of pull mass, M_p must be less than 3, where pull mass is defined as:
  $$M_p = \frac{|M_m - M_0|}{\sigma_M}, \tag{7.23}$$
  where M_m and M_0 are the measured mass and nominal mass of π^0 or η respectively and σ_M is the uncertainty associated with the measured mass of π^0 or η. The χ^2 of the mass-constrained fit of the di-photons mass to the parent mass of π^0 or η, must be less than 10,000. The energy deposited by each photon shower in the calorimeter is required to be greater than 30 Mev (50 Mev) for π^0 (η) meson.

- **K_S^0 Meson**
  K_S^0 candidates are reconstructed by combining two oppositely-charged pions. The invariant mass of K_S^0 must lie within $\pm$30 MeV of the nominal K_S^0 mass. These charged tracks are not subjected to any PID requirements described above. Furthermore, the χ^2 of the K_S^0 vertex fit, must be less than 1,000.

- **Composite D Meson:**
  The final state particles that satisfy all the above requirements are used to reconstruct composite D meson candidates from the relevant final states. D meson candidates are identified by using two independent kinematic variables: the

Beam Constrained Mass, ($m_{\rm bc}$) and the Energy Difference (ΔE) defined in the CM frame, as:

$$m_{\rm bc} = c^{-2}\sqrt{E^2_{\rm beam} - |\vec{p}_D|^2 c^2}, \tag{7.24}$$

$$\Delta E = E_D - E_{\rm beam}. \tag{7.25}$$

For correctly reconstructed D mesons, $m_{\rm bc}$ peaks at the nominal mass of the D meson [8] and ΔE peaks at zero.

7.2.4 Selection of fully-reconstructed Double-tag and Single-tag events

Table 7.2 gives the overview of the D^0 and $\bar{D}^0$ final states that have been reconstructed. The unstable final state particles are reconstructed in the following decay modes: $\pi^0 \to \gamma\gamma$, $K^0_{\rm S} \to \pi^+\pi^-$, $\omega \to \pi^+\pi^-\pi^0$, $\eta \to \gamma\gamma$, $\eta \to \pi^+\pi^-\pi^0$ and $\eta' \to \eta(\gamma\gamma)\pi^+\pi^-$. We apply

Table 7.2: D final states reconstructed in this analysis.

Type	Final states
Signal	$\pi^+\pi^-\pi^0$, $K^+K^-\pi^0$
CP-even	K^+K^-, $\pi^+\pi^-$, $K^0_{\rm S}\pi^0\pi^0$, $K^0_{\rm L}\pi^0$, $K^0_{\rm L}\omega$
CP-odd	$K^0_{\rm S}\pi^0$, $K^0_{\rm S}\omega$, $K^0_{\rm S}\eta$, $K^0_{\rm S}\eta'$

additional selection cuts to separation signal from the background. In this section we describe the cuts applied to each final state particle in a fully-reconstructed single-tag or double-tag decay.

- **π^0 and η Mesons**
  An additional shower quality requirement is imposed on the photon candidates used to construct π^0 and η mesons. That is, the quantity $\rm E_9/E_{25}$ must be equal to 0.99 for all π^0 and η candidates. Here $\rm E_9/E_{25}$ is the energy deposited by each shower in the 3×3 grid of calorimeter cells centered on the shower to the 5×5 grid of cells centered on the shower.

- **Specific mass cuts on K^0_S, ω, η, and η' Mesons**
  In order to minimise non-resonant peaking backgrounds in selections of these mesons, additional mass cuts are applied to the invariant mass distributions formed by the daughter candidates. The requirements made on the invariant mass of each particle are listed in Table 7.3.

- **K^0_S Meson**
  In order to eliminate pairs of charged pions that do not originate from a K^0_S decay yet form a combined invariant mass compatible with that of a K^0_S, we require the K^0_S invariant mass to be within ± 7.5 MeV (3σ) about the nominal mass of the K^0_S

Table 7.3: **Mode specific Invariant Mass Cuts in MeV/c^2.**

Particle	**Min.**	**Max.**
K_S	490.1	505.1
ω	762.0	802.0
η	506.0	590.0
η'	950.0	964.0

(497.6 MeV). We apply a cut on the three dimensional flight significance (FS), since K^0_S mesons originating directly from D mesons propagate some distance through the detector before decaying. We require FS should be greater than 2.0 for all K^0_S candidates.

- **Selection of D Mesons**
  After reconstructing the final state particles, we apply the following selection criteria to reconstruct D candidates in the event. In all modes, we select signal candidates that possess m_{bc} in the range $1.86 < m_{bc} < 1.87$ GeV. We also apply most specific cut on ΔE to constrain further. The cuts values of the ΔE distribution of each `DTag` mode are summarized in Table 7.4.

Table 7.4: **ΔE requirements in GeV.**

Mode	**Minimum ΔE**	**Maximum ΔE**
$\pi\pi\pi^0$	-0.058	0.035
$KK\pi^0$	-0.058	0.035
KK	-0.020	0.020
$\pi\pi$	-0.030	0.030
$K_S\pi^0$	-0.071	0.045
$K_S\eta$	-0.055	0.035
$K_S\omega$	-0.025	0.025
$K_S\pi^0\pi^0$	-0.055	0.045
$K_S\eta'$	-0.030	0.020

- **Additional K^0_S veto requirement for $\pi^+\pi^-\pi^0$ mode:** After applying all the above selection requirements, there is still a significant background observed in the $\pi^+\pi^-\pi^0$ signal mode. The decays that contributes to this background are from $K_S\pi^0$ with K_S decaying to $\pi^+\pi^-$. To reject such peaking background, we reject the events that lie within 3σ from the nominal mass of K_S [8].

- **Lepton veto for K^+K^- and $\pi^+\pi^-$:** To suppress the cosmic muons and radiative bhabha backgrounds for modes consisting of two charged tracks, we apply "DTag

Bhabha veto" to reject tracks that are identified as muons or electrons and require no showers above 50 MeV. These backgrounds appear only at high $M_{\rm bc}$. For K^+K^- we require additional geometric requirement to remove doubly radiative Bhabhas based upon bhabha events close to beam pipe.

7.2.5 Selections Involving K_L^0

The selection of $\pi^+\pi^-\pi^0$ vs. K_L^0 and $K^+K^-\pi^0$ vs. K_L^0 CP tags are not performed via. fully reconstructed `DDoubleTag` objects. K_L^0 have a longer life time and they do not decay inside the detector. To reconstruct the K_L^0 events, we utilise a missing mass technique [70]. Given a fully-reconstructed $\pi^+\pi^-\pi^0$, $K^+K^-\pi^0$ events, we reconstruct all other final state particles associated with the CP tag and then calculating the missing mass of K_L^0 using:

$$M^2_{miss} = E^2_{miss}c^{-4} - p^2c^{-2}. \tag{7.26}$$

The M^2_{miss} is used to discriminate between signal and background. For correctly reconstructed events M^2_{miss} will peak at the square of the mass of the K_L^0 [8]. Signal yields are then determined by counting events in the signal region of K_L^0 by using background subtraction technique. We perform selections against $K_L^0\pi^0$ and $K_L^0\omega(\pi^+\pi^-\pi^0)$. Details of the selection of these modes are given below.

$K_L^0\pi^0$

The selection of $K_L^0\pi^0$ is the same as described in Ref. [17]. The π^0 associated with $K_L^0\pi^0$ is selected by considering all opposite-side showers not associated with the $\pi^+\pi^-\pi^0$ or $K^+K^-\pi^0$ candidates.

- K_S^0 **veto:**
  We veto K_S^0 events on the basis of its invariant mass and FS as described in Sec. 7.2.4.

- **Multiple π^0 Candidates**
  Events with multiple π^0 candidates that do not share a common shower between them are vetoed and event of multiple π^0 candidates that do share a common shower, then the candidate with a pullmass closest to nominal is chosen.

- π^0 **momentum:**
  The momentum of the π^0 should lie between 0.75 - 1.00 GeV/c.

The rest of cuts on π^0 are the same as those given in Sec. 7.2.4.

$K_L^0\omega(\pi^+\pi^-\pi^0)$

The selection of $K_L^0\omega(\pi^+\pi^-\pi^0)$ is similar to that of $K_L^0\pi^0$. The main difference is that we require two opposite side tracks, together with π^0 candidate, to reconstruct ω. The additional selections applied to this mode are described below.

- **RICH Hypothesis**
  We apply, ω daughters RICH kaon Hypothesis Cut < 3.0 and the absolute value of ω daughters RICH pion Hypothesis Cut < 3.0

- **ω Candidate**
  Invariant mass requirements, as quoted in Table 7.3, are imposed on all ω candidates coming from $K_L\pi^0$.

- **π^0 Momentum**
  Since the π^0 is a daughter of the three-body ω decay, it has a lower momentum spectrum as compared to that in the $K^0_L\pi^0$ mode. Here we allow the momentum of the π^0 to lie between 0.15 - 0.6 GeV/c.

Best Candidate Selection

After applying all selection criteria still there is possibility of multiple `DTag` candidates while considering all permutations of the charged tracks and neutrals reconstructed within an event. In addition to the correctly reconstructed signal candidate (Best Candidate), these multiple combinatoric candidates, can be produced. So, we select the correctly reconstructed candidate by applying a figure of merit based upon ΔE. We choose the smallest value of figure of merit:

$$\delta = \frac{\Delta E(S) + \Delta E(O)}{2}, \tag{7.27}$$

where $\Delta E(S)$ and $\Delta E(O)$ corresponds to the energy difference of the *signal*-side and *opposite*-side final states, respectively. For single-tag event selection or for the situation when one final state contains a K_L meson, we apply figure of merit based upon:

$$\delta = \Delta E(S). \tag{7.28}$$

Here $\Delta E(S)$ corresponds to the energy difference of the single-tag final state or the final state that contains a K_L meson.

7.2.6 Double-tag Background Evaluation

The double-tag yield is measured using cut and cound method in the $M_{bc(1)}$ vs. $M_{bc(2)}$ plane.

In order to determine the actual signal yield within the double-tag sample it is necessary to subtract the background contamination present in the signal region. Here we divide the M_{bc} plane to various background regions (A, B, C and D) along with signal region (S) in order to identify the level of background present in the signal region and the signal yield.

- **Signal and Peaking background region**
  Signal region (S) is identified where both the D have been correctly identified (i.e.

$m_{bc} - m_D \simeq 0$). and We select S in the region between 1.860 GeV/c^2 to 1.870 GeV/c^2 for both D. This peaks with in 3σ from the nominal D meson mass.
peaking background in the signal region:
This corresponds to D^0 decays where final state particles of the decay exactly matches with that of the signal D^0 decay. These events also peak within invariant mass distributions and thus are indistinguishable from true signal.

- **Flat (Non-Peaking) background region**
This region corresponds to smooth background of misreconstructed events on lower end of one M_{bc} distribution and the signal region of the other. This can be further classified into different categories as described below.

- Sideband A and B are used to determine the backgrounds in which one D has been correctly reconstructed ($m_{bc} - m_D \simeq 0$) and the other D has been misidentified.

- Sideband C is used to determine the track swapped combinatoric background events.

- Sideband D is used to determine the flat flat background from non-$D\bar{D}$ sources (i.e. continuum events). To distinguish between C and D sideband region requirements are placed on the quantity $\delta m_{bc} = |m_{bc}(D_1) - m_{bc}(D_2)|$, where the two D-mesons are denoted D_1 and D_2. The region boundaries are summarized in Table 7.5 with a demonstration plot shown in Fig. 7.5.

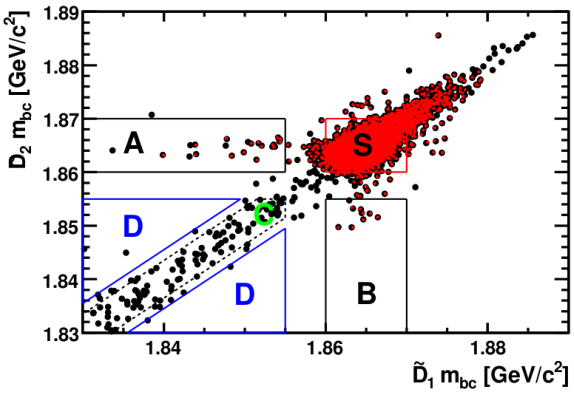

Figure 7.5: A $m_{\rm bc}$ of the signal vs. $m_{\rm bc}$ of the tag for $K^-\pi^+$ vs $\pi^+\pi^-\pi^0$ plot showing signal and various sideband regions.

Since the background in these mass sidebands is approximately flat, so the signal yield is calculated by just subtracting the scaled background events in the signal region from the total events in the signal region. Here the scale factor corresponding to the background events represent the ratio of background in the signal box compared to that in a specific sideband. The resulting equation that is used to calculate the absolute signal yield, Y, after sideband subtraction is:

Table 7.5: Sideband and signal region for $h^+h^-\pi^0$ vs. DTags used to form the double-tag candidates.

Region	$m_{bc}(D_1)$		$m_{bc}(D_2)$		Additional requirements	Comment
	Min.	Max.	Min.	Max.		
S	1.860	1.870	1.860	1.870	-	Signal box.
A	1.830	1.855	1.860	1.870	-	Represents the Low Mass background corresponding to tag $\tilde{D}_1$
B	1.860	1.870	1.830	1.855	-	Represents the Low Mass background corresponding to tag $\tilde{D}_2$.
C	1.830	1.855	1.830	1.855	$\delta m_{bc} \leq 0.0035$	Represents track swapped events.
D	1.830	1.855	1.830	1.855	$\delta m_{bc} \geq 0.0055$	Represents the flat background from non-$D\bar{D}$ sources (i.e. continuum events)

$$\mathrm{Y} = \Big(\mathrm{S} - \frac{\mathrm{R_S}}{\mathrm{R_D}}\mathrm{D}\Big) - \sum_{\mathrm{i=A,B,C}} \frac{\mathrm{R_S}}{\mathrm{R_i}}\Big(\mathrm{i} - \frac{\mathrm{R_i}}{\mathrm{R_D}}\mathrm{D}\Big), \tag{7.29}$$

where S, A, B, C and D are the yields in the corresponding sideband. Here $\mathrm{R_i}$ represents the area of the m_{bc} vs. m_{bc} plane contained within the ith sideband. This technique only takes in to account the flat background present in the signal region except the peaking background. The peaking background which peaks exactly like signal in the signal region is difficult to identify in data. We determine the peaking background contamination from assessment of generic Monte Carlo using truth matching technique. Since we use 10 $\times$ more events in the simulation sample than in the $\psi(3770)$ data sample for our analysis, so we scale the number of simulated events to the full 818 pb^{-1} dataset to estimate peaking background. As the scaling factor of 10 $\times$ MC is ~ 3.27 times that of data. Therefore, we estimate the number of peaking background events in data for each double-tag, from the corresponding generic Monte Carlo sample ($\mathrm{Y_{Peak}}$) estimation by multiplying by $\frac{1}{3.27} \sim 0.306$. The peaking background estimate is then subtracted from the yield calculated in Eq. 7.29 to give the true signal yield, $\mathrm{Y_{true}}$:

$$\mathrm{Y_{true}} = \mathrm{Y} - 0.306 \times \mathrm{Y_{Peak}} \tag{7.30}$$

7.2.7 Double-tag yields

We follow the selection and yield determination procedure given in sec: 7.2.4 and 7.2.6. We reconstruct the $h^+h^-\pi^0$ vs. CP-tag signal candidates to determine the yield in the signal region. Here the CP-tag final state does not contain a K^0_{L} meson. We use sideband subtraction technique given in Eq. 7.29to extract the signal yield from counting

events in the signal and sideband region. Figure 7.6 shows the M_{bc} distributions for CP-tagged signal candidates. Our selection result along with efficiency have been tabulated in Table 7.6 and Table 7.7.

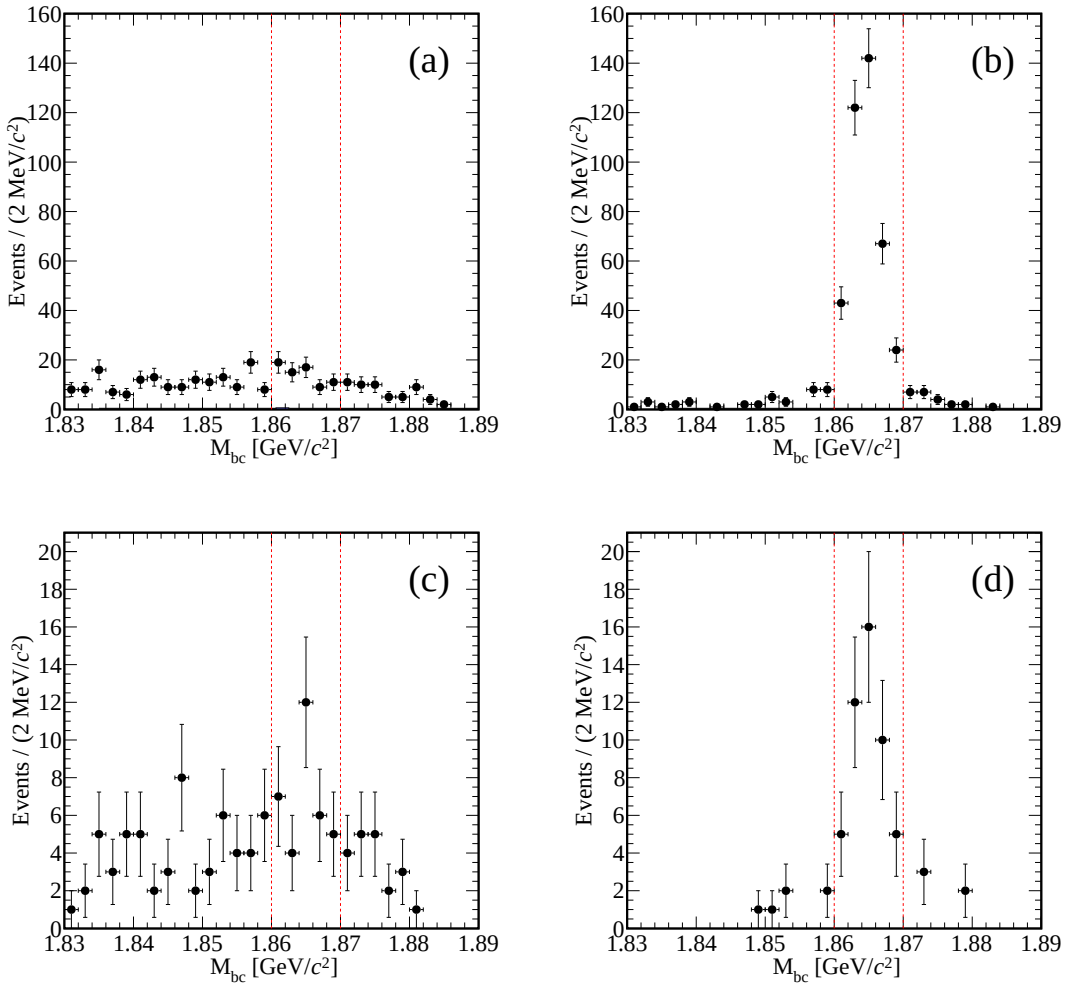

Figure 7.6: M_{bc} distributions for $D \to \pi^+\pi^-\pi^0$ candidates tagged by CP-even (a) and CP-odd (b) eigenstates; corresponding plots for $D \to K^-K^+\pi^0$ for CP-even (c) and CP-odd (d). Tags included a K^0_L are not included.

Table 7.6: Reconstruction efficiency $\epsilon_{rec}(\%)$, yield in signal region (S), Flat background yield (Flat Bkg.), Peaking background yield (P) and background subtracted signal yields (S') for $\pi^+\pi^-\pi^0$ vs. CP-tags after analysing 817 pb^{-1} data sample.

Tag	$\epsilon_{rec}(\%)$	S	Flat Bkg	P	S'
KK	23.94 ± 0.22	28	26.4 ± 5.3	0.00 ± 0.00	1.6 ± 5.6
$\pi\pi$	29.39 ± 0.24	19	3.2 ± 5.7	0.00 ± 0.00	15.8 ± 7.0
$K_S\pi^0\pi^0$	4.97 ± 0.10	3	0.83 ± 3.08	0.3 ± 0.55	1.87 ± 3.47
$K_S\pi^0$	11.89 ± 0.15	211	-3.0 ± 3.2	0.00 ± 0.00	214.0 ± 15.0
$K_S\phi$	6.97 ± 0.12	18	0.0 ± 0.0	1.5 ± 1.2	16.5 ± 4.37
$K_S\omega$	5.89 ± 0.11	99	2.6 ± 1.1	0.9 ± 0.95	95.5 ± 9.95
$K_S\eta(\gamma\gamma)$	11.77 ± 0.15	35	1.7 ± 0.9	0.3 ± 0.55	33.0 ± 5.83
$K_S\eta(\pi\pi\pi^0)$	8.05 ± 0.13	10	1.2 ± 0.9	0.00 ± 0.00	8.8 ± 3.1
$K_S\eta'(\pi^+\pi^-\eta)$	6.23 ± 0.11	18	0.4 ± 0.4	0.00 ± 0.00	17.6 ± 4.2

Table 7.7: Reconstruction efficiency $\epsilon_{rec}(\%)$, yield in signal region (S), Flat background yield (Flat Bkg.), Peaking background yield (P) and background subtracted signal yields (S') for $K^+K^-\pi^0$ vs. CP-tags after analysing 817 pb^{-1} data sample.

Tag	$\epsilon_{rec}(\%)$	S	Flat Bkg	P	S'
KK	16.07 ± 0.18	12	0.7 ± 2.5	0.00 ± 0.00	11.3 ± 4.2
$\pi\pi$	21.47 ± 0.21	12	10.3 ± 3.5	0.00 ± 0.00	1.7 ± 3.7
$K_S\pi^0\pi^0$	3.96 ± 0.10	5	2.2 ± 1.0	0.00 ± 0.00	2.8 ± 2.0
$K_S\pi^0$	8.58 ± 0.13	27	1.0 ± 0.7	0.00 ± 0.00	26.0 ± 5.2
$K_S\omega$	4.17 ± 0.10	12	0.4 ± 0.4	0.00 ± 0.00	11.6 ± 3.4
$K_S\eta(\gamma\gamma)$	8.02 ± 0.13	2	-1.5 ± 1.5	0.00 ± 0.00	3.5 ± 2.4
$K_S\eta(\pi^+\pi^-\pi^0)$	5.50 ± 0.11	1	0.0 ± 0.0	0.00 ± 0.00	1.0 ± 1.0
$K_S\eta'(\pi^+\pi^-\eta)$	4.33 ± 0.10	3	0.0 ± 0.0	0.00 ± 0.00	3.0 ± 1.7

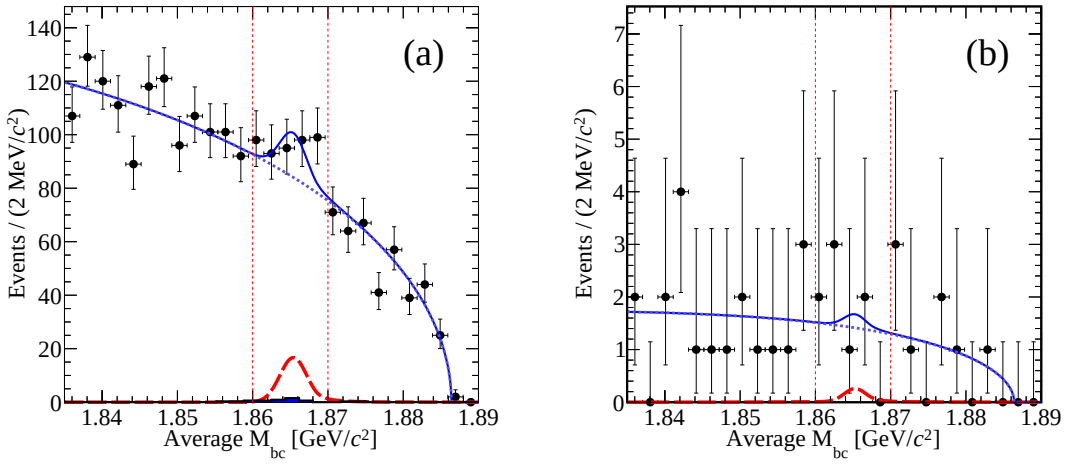

Figure 7.7: Average M_{bc} distributions (points with error bars) for (a) $\pi^+\pi^-\pi^0$ vs. $\pi^+\pi^-\pi^0$ and (b) $K^+K^-\pi^0$ vs. $K^+K^-\pi^0$. Superimposed are the total (solid line), signal (dashed line) and background (dotted line) signal yield fit results. The vertical lines indicate the signal region.

7.2.8 $h^+h^-h^0$ vs $h^+h^-h^0$ yields

The yield determination procedure for $h^+h^-h^0$ vs $h^+h^-h^0$ is different than all other fully reconstructed modes. The reason of which is described below.

$\pi^+\pi^-\pi^0$ vs. $\pi^+\pi^-\pi^0$ candidates contains a significant combinatoric background from continuum $e^+e^- \to u\bar{u},\ d\bar{d}$ events that hadronize to six pions. This combinatoric background does not follow a uniform distribution in M_{bc} as in the other double-tag modes. Therefore, we use an alternative strategy to determine the signal yield. A maximum-likelihood fit to the distribution of the average M_{bc} of the two $D^0 \to \pi^+\pi^-\pi^0$ candidates is used to determine the signal yield. The probability density functions (PDFs) are parametrized by a Crystal Ball function [71] and a threshold Argus function [72] for the signal and combinatoric background components, respectively. Apart from the signal yield all other parameters of the signal PDF are fixed to those obtained from the signal MC sample. All parameters for the background PDF are obtained from the fit to data. The average M_{bc} distribution for $\pi^+\pi^-\pi^0$ vs. $\pi^+\pi^-\pi^0$ candidates is shown in Fig. 7.7(a), along with the result of the fit. No significant signal is observed.

For $K^+K^-\pi^0$ vs. $K^+K^-\pi^0$ decay, though the combinatoric background is smaller, but we employ the same method to determine the signal yield as for $\pi^+\pi^-\pi^0$ vs. $\pi^+\pi^-\pi^0$. The average M_{bc} distribution and fit result for $K^+K^-\pi^0$ vs. $K^+K^-\pi^0$ candidates is shown in Fig. 7.7(b); no significant signal is observed. Selection result along with efficiency have been tabulated in Table 7.8.

Table 7.8: Reconstruction efficiency $\epsilon_{rec}(\%)$, yield in signal region (S), Flat background yield (Flat Bkg.), Peaking background yield (P) and background subtracted signal yields (S') for $h^+h^-\pi^0$ vs. $h^+h^-\pi^0$ after analysing 817 pb^{-1} data sample.

Tag	$\epsilon_{rec}(\%)$	S	Flat Bkg	P	S'
$\pi^+\pi^-\pi^0$	16.71 ± 0.18	336	2147 ± 50	3.67 ± 1.92	34.3 ± 20.1
$K^+K^-\pi^0$	8.12 ± 0.13	5	2.3 ± 3.2	0.00 ± 0.00	2.7 ± 3.6

7.2.9 K_L^0 Tag Background Evaluation

After applying the background suppressing vetos discussed in Section 7.2.5, contamination is still there in the $K_L^0\pi^0$ and $K_L^0\omega(\pi^+\pi^-\pi^0)$ tagged events. Most of the background originates from peaking sources that mimic the $K_L^0\pi^0$ or $K_L^0\omega(\pi^+\pi^-\pi^0)$ final state. We asses the level of contamination from the generic Monte Carlo. The remaining contributions to the total background typically originate from decay modes that possess multiple π^0 daughters which peak in the lower recoil mass region.

$K_L^0\pi^0$

Figure 7.8 (left) shows the distributions in the recoil mass plane resulting from events selected through the mode $\pi^+\pi^-\pi^0$ vs. $K_L^0\pi^0$ after analysis of the 10× luminosity generic MC sample. The sources of various background is lebeled in the figure. We divide the mass spectrum in to three mass windows (P, S, B). The mass range of P, S, B lies between (-0.3 - 0.1) GeV, (0.1 - 0.5) GeV, (0.5 - 0.7) GeV, respectively. We extract the total yields of (P, S, B) in terms of three unknowns ($\mathrm{Y_{K_L}}, \mathrm{Y_{\pi^0\pi^0}}, \mathrm{B_{ELSE}}$):

$$\mathrm{S} = \mathrm{Y_{K_L\pi^0}} + \mathrm{B^S_{PEAK}} + \delta\cdot\mathrm{Y_{\pi^0\pi^0}} + \gamma\cdot\mathrm{B_{ELSE}}, \quad (7.31)$$

$$\mathrm{P} = \mathrm{Y_{\pi^0\pi^0}} + \alpha\cdot\mathrm{Y_{K_L\pi^0}}, \quad (7.32)$$

$$\mathrm{B} = \mathrm{B_{ELSE}} + \mathrm{B^B_{PEAK}} + \beta\cdot\mathrm{Y_{K_L\pi^0}}, \quad (7.33)$$

where $\mathrm{B^{S/B}_{PEAK}}$ represents the peaking background contributions within S/B and α, β, γ

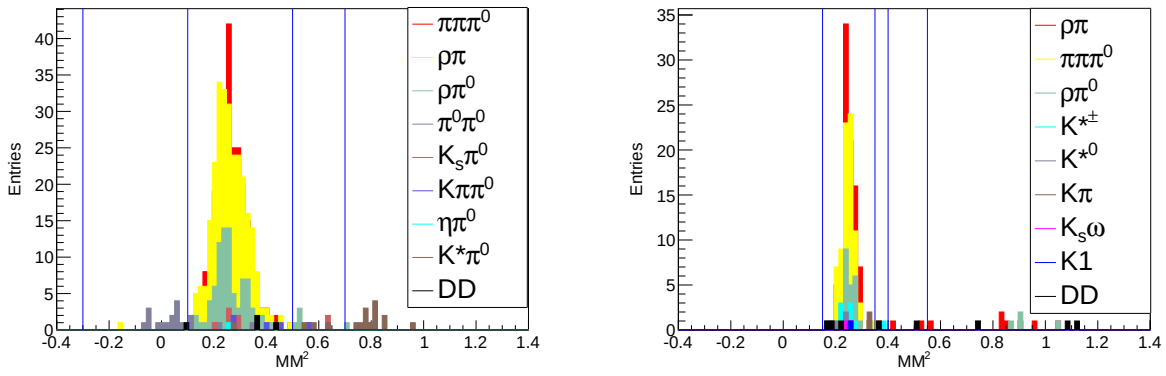

Figure 7.8: Missing mass distributions of signal and all kinds of background resulting from $\pi^+\pi^-\pi^0$ vs. $K_L^0\pi^0$ (left) and $\pi^+\pi^-\pi^0$ vs. $K_L^0\omega(\pi^+\pi^-\pi^0)$ (right) when run over 10× luminosity MC sample. All decays have been lebeled in the figures.

and δ are the ratios of the MC yields for each corresponding distribution, which are defined as:

$$\alpha = \frac{\text{MC Signal in } \mathbf{P}}{\text{MC Signal in } \mathbf{S}}, \tag{7.34}$$

$$\beta = \frac{\text{MC Signal in } \mathbf{B}}{\text{MC Signal in } \mathbf{S}}, \tag{7.35}$$

$$\gamma = \frac{\text{MC B}_{\text{ELSE}} \text{ in } \mathbf{S}}{\text{MC B}_{\text{ELSE}} \text{ in } \mathbf{B}}, \tag{7.36}$$

$$\delta = \frac{\text{MC } \pi^0\pi^0 \text{ in } \mathbf{S}}{\text{MC } \pi^0\pi^0 \text{ in } \mathbf{P}}. \tag{7.37}$$

$K^0_L\omega(\pi^+\pi^-\pi^0)$

Figure 7.8 (right) shows the distributions in the recoil mass plane resulting from events selected through the mode $\pi^+\pi^-\pi^0$ vs. $K^0_L\omega(\pi^+\pi^-\pi^0)$ after analysis of the 10× luminosity generic MC sample.

Determination of the signal yield is performed in an analogous way to that done for $K^0_L\pi^0$. In this case, since there are no events in the P sideband, so only one mass sideband, B is considered. The mass range of S and B lies between (0.15 - 0.35) GeV and (0.40 - 0.55) GeV, respectively. The resulting yield equation is therefore depends only on β, γ, S, B.

$$\mathrm{Y}_{\mathrm{K_L}\omega} = \frac{\left(\mathrm{S} - \mathrm{B}^{\mathrm{S}}_{\mathrm{PEAK}}\right) - \gamma \cdot \left(\mathrm{B} - \mathrm{B}^{\mathrm{B}}_{\mathrm{PEAK}}\right)}{(1 - \beta \cdot \gamma)}. \tag{7.38}$$

7.2.10 Analysis of data to select fully-reconstructed $h^+h^-h^0$ vs K^0_{L} events

We follow the selection and yield determination procedure given in sec: 7.2.5 and 7.2.9. Figure 7.9 shows the M^2_{miss} distributions for CP-tagged signal candidates, where the CP tag final state contains a K^0_{L} meson.

The peaking background estimates are determined from the generic MC sample of $D\overline{D}$ events. We found significant peaking backgrounds in the states tagged by $K^0_L\pi^0$ and $K^0_L\omega$, as shown in Fig. 7.9. The dominate source of peaking background is $D^0 \to K^0_S X$, $K^0_S \to \pi^0\pi^0$ ($X = \pi^0, \omega$) events where the π^0 mesons from the K^0_S decay are not reconstructed.

The measured event yields after background subtraction are given in Table 7.9 and 7.10. No significant signal is seen in any of these modes.

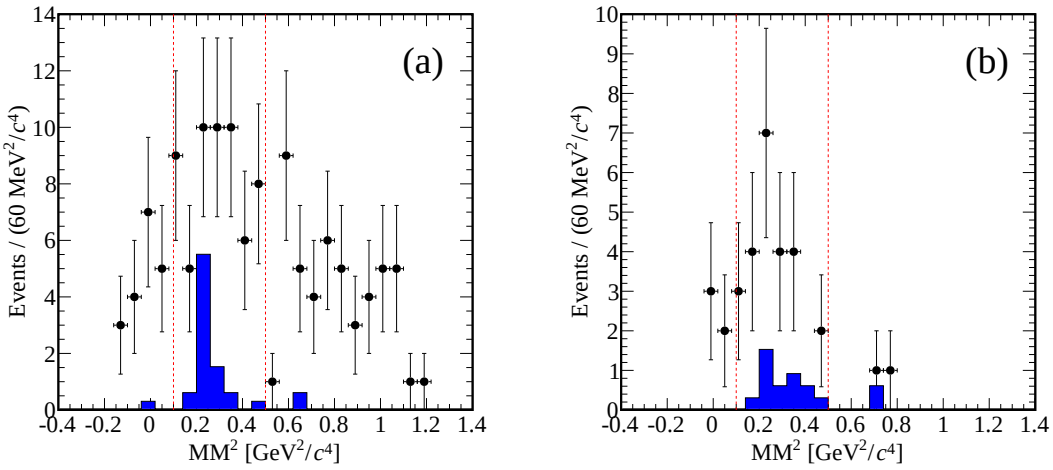

Figure 7.9: $M^2_{\rm miss}$ distributions for $D \to \pi^-\pi^+\pi^0$ (a) and $D \to K^-K^+\pi^0$ candidates tagged by CP eigenstates that contain a $K^0_{\rm L}$. The shaded histogram indicates the peaking background.

Table 7.9: Reconstruction efficiency $\epsilon_{rec}(\%)$, yield in signal region (S), Flat background yield (Flat Bkg.), Peaking background yield (P) and background subtracted signal yields (S') for $\pi^+\pi^-\pi^0$ vs. K_L-tags after analysing 817 pb^{-1} data sample.

Tag	$\epsilon_{rec}(\%)$	S	Flat Bkg	P	S'
$K_L\pi^0$	18.60 ± 0.19	34	16.95 ± 5.01	2.45 ± 1.57	14.61 ± 7.90
$K_L\omega$	6.12 ± 0.11	10	7.86 ± 2.40	6.43 ± 2.53	-4.29 ± 4.01

Table 7.10: Reconstruction efficiency $\epsilon_{rec}(\%)$, yield in signal region (S), Flat background yield (Flat Bkg.), Peaking background yield (P) and background subtracted signal yields (S') for $K^+K^-\pi^0$ vs. K_L-tags after analysing 817 pb^{-1} data sample.

Tag	$\epsilon_{rec}(\%)$	S	Flat Bkg	P	S'
$K_L\pi^0$	11.38 ± 0.15	13	-0.31 ± 0.55	2.75 ± 1.66	10.56 ± 4.03
$K_L\omega$	3.84 ± 0.09	7	2.0 ± 3.2	1.53 ± 1.24	3.47 ± 4.36

Table 7.11: Background subtracted data yield (Y) in the Signal region (1.86-1.87) GeV and corresponding efficiency $\epsilon_{rec}(\%)$.

Decay Mode	**Single-tag result**	
	$\epsilon_{rec}(\%)$	Y
KK	48.71 ± 0.31	11970 ± 116
$\pi\pi$	65.18 ± 0.36	5595 ± 109
$K_S\pi^0\pi^0$	11.62 ± 0.16	7306 ± 125
$K_S\pi^0$	28.32 ± 0.22	20069 ± 146
$K_S\omega$	11.85 ± 0.15	7960 ± 99
$K_S\eta(\gamma\gamma)$	9.95 ± 0.08	2903 ± 71
$K_S\eta(\pi\pi\pi^0)$	3.81 ± 0.05	1161 ± 48
$K_S\eta'(\pi^+\pi^-\eta)$	14.91 ± 0.17	1405 ± 38

7.2.11 Analysis of data to extract single-tag yields

We require the single-tag yield for the CP-eigenstates to normalise the double tag yields appropriately to obtain a value of F_+. The selection of single tags is only possible for modes without a K^0_L in the final state. The selection criteria are identical to those for the double-tag selection.The signal yield is estimated using a maximum likelihood fit to the M_{bc} distribution where the signal is modeled by the sum of a Gaussian and an asymmetric Gaussian and the combinatoric background is modeled by an Argus function. Apart from the signal yield all other parameters of the signal PDF are fixed to those obtained from the signal MC sample. All parameters for the background PDF are obtained from the fit to data. The signal yield is estimated by integrating the best-fit PDF within the interval $1.86 < M_{bc} < 1.87$ GeV/c^2. Peaking backgrounds are estimated from the generic $D\bar{D}$ simulation. Significant contributions are only found for $D^0 \to K^0_S\omega$ and $D^0 \to K^0_S\eta'(\pi^+\pi^-\pi^0)$ candidates corresponding to 1.9% and 3.8% of the signal, respectively; in both cases the dominant source of peaking background are states with intermediate K^*, K_1 and K_2 resonances which lead to $K^0_S\pi^+\pi^-\pi^0$ in the final state. The background-subtracted single-tag yields are given in Table 7.11. Figure 7.10 and 7.11 show the M_{bc} distributions for single-tag candidates except $K_L$tag.

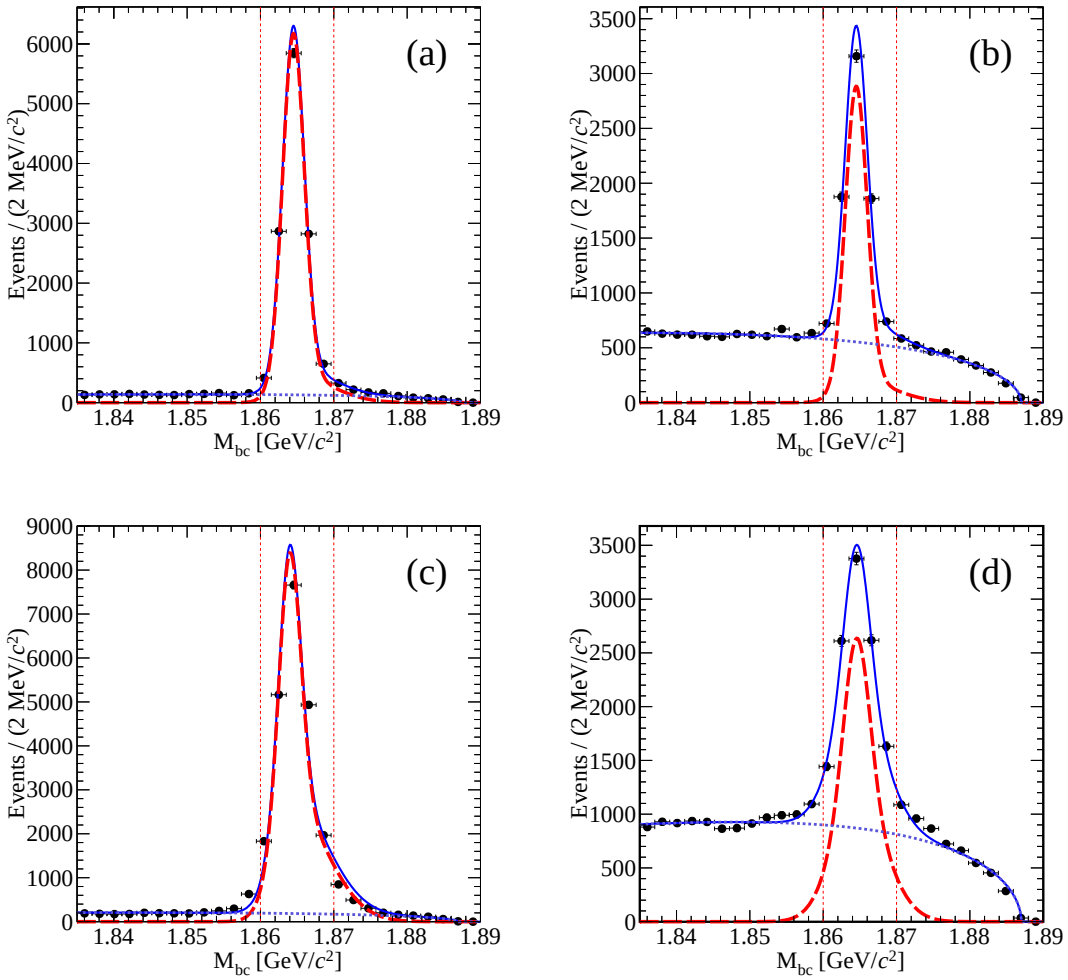

Figure 7.10: M_{bc} distributions for KK (a), $\pi\pi$ (b), $K_S\pi^0$ (c), $K_S\pi^0\pi^0$ (d). Superimposed are the total (solid line), signal (dashed line) and background (dotted line) fit results. The vertical lines indicate the signal region.

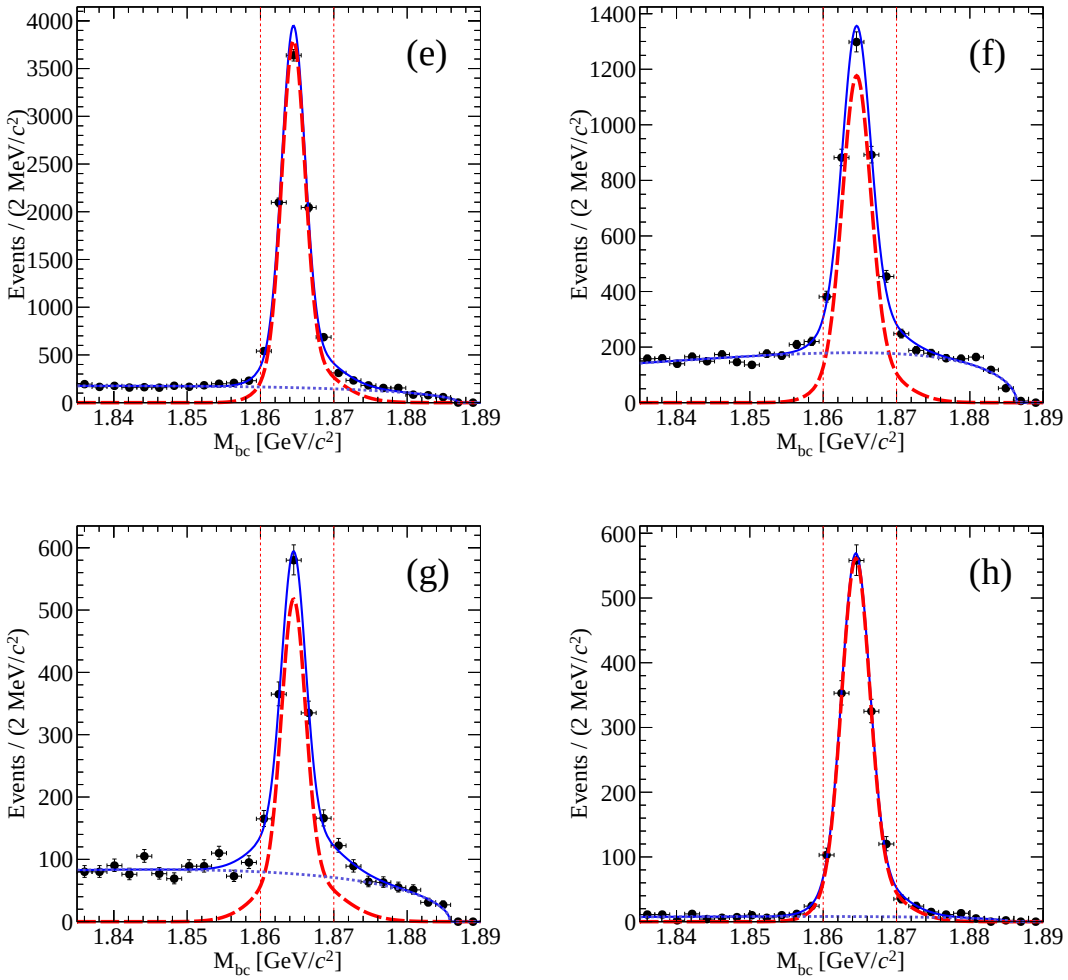

Figure 7.11: M_{bc} distributions for $K_S\omega$ (e), $K_S\eta$ (f), $K_S\eta(\pi\pi\pi^0)$ (g), $K_S\eta'$ (h). Superimposed are the total (solid line), signal (dashed line) and background (dotted line) fit results. The vertical lines indicate the signal region.

7.2.12 Determination of F^+

The yields of double-tagged and single CP-tag candidates are used to determine the quantities N^+ and N^-. We calculate the CP fraction F^+ from these values. The values for N^+ and N^- are calculated from the CP-odd and CP-even tags, respectively, considering the statistical and systematic uncertainties. The measured values for N^+ and N^- for the two signal modes are displayed in Fig. 7.12 It can be seen that there is consistency between the individual tags for each measurement. From these results it is determined that $\mathbf{F^+ = 0.968 \pm 0.017 \pm 0.006}$ for $\pi^+\pi^-\pi^0$ and $\mathbf{F^+ = 0.731 \pm 0.058 \pm 0.021}$ for $K^+K^-\pi^0$, where the first uncertainty is statistical and the second is systematic. These values are slightly higher than, but compatible with, the model predictions reported in sect. 7.1.

7.2.13 Systematic Uncertainties

We calculate the systematic uncertainties (σ_{F_+}) associated with F_+ using:

$$\sigma_{F_+} = \frac{\sqrt{N_-^2\sigma_{N^+}^2 + N_+^2\sigma_{N^-}^2}}{(N^- + N_+)^2}, \tag{7.39}$$

where σ_{F_+} and σ_{F_-} are the uncertainties associated with N_+ and N_-. Here we have assumed there in no correlation between σ_{F_+} and σ_{F_-}. By varying the yields by $\pm 1\sigma$, we find the difference in the value of $N_+(N_-)$ from the nominal value which is taken as the systematic uncertainty. We discuss below the sources of various uncertainties.

- **Single tag fits for non $\mathbf{K_L}$ tag modes**
  We assign a systematic to the single tag yields $S^{\pm}_{\rm meas}$ due to the fit function used to model the M_{bc} distribution of the signal. This shape of the distribution varies depending on whether there are no electromagnetic neutral final-state particles present (K^+K^- and $\pi^+\pi^-$), whether the neutrals are relatively hard ($K^0_S\pi^0(\gamma\gamma)$ and ($K^0_S\eta(\gamma\gamma)$ or soft (all other modes). Uncertainties are assigned of $2.0\%, 2.5\%$ and 5.0%, respectively. $S^{\pm}_{\rm meas}$ is corrected for the effects of $D^0\bar{D}^0$ mixing using $y_D = 0.62 \pm 0.08$ [16].

- **Uncertainties on the $\mathbf{K_L}$ tag**
  Tags involving a K^0_L require special treatment as it is not possible to measure a single tag yield for these modes. The expected value for the tag $K^0_L\pi^0$ without mixing effects, $S^-K^0_L\pi^0$, is given by $2N_{D\bar{D}}\epsilon_{K_L\pi^0}BR_{h^+h^-\pi^0}$. Here $\epsilon_{K_L\pi^0}$ is an effective single tag efficiency, taken to be equal to the ratio of the double-tagged efficiency to the single-tagged signal efficiency, as determined from simulation. The number of $D\bar{D}$ pairs in the sample, $N_{D\bar{D}}$, can be measured from the double-tagged yield of decays into Cabibbo-favored final states. It is found that $S^-K^0_L\pi^0 = 24433 \pm 3934$, where the assigned error reflects the uncertainties in the input factors and assumptions of this calculation. A similar procedure for $K^0_L\omega$ yields $S^-K^0_L\omega = 8923 \pm 4015$.

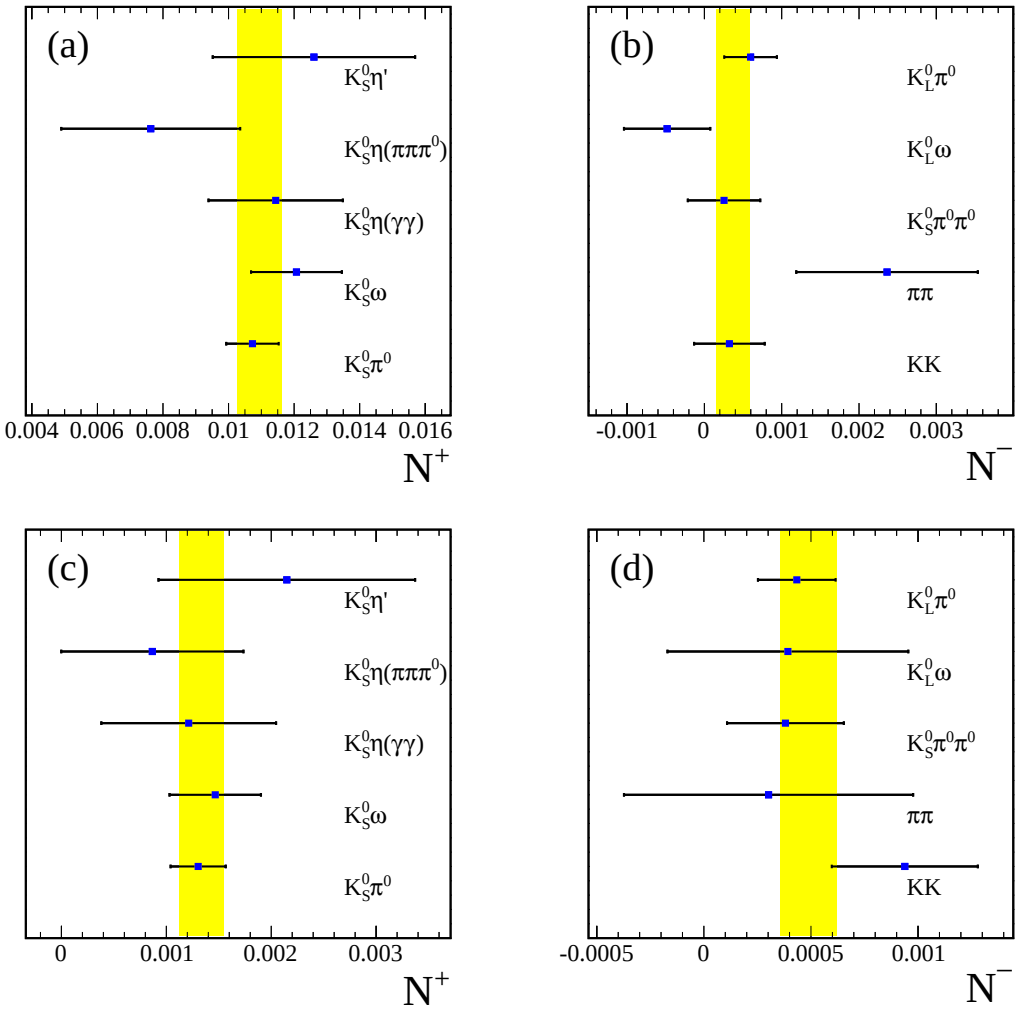

Figure 7.12: $D \to \pi^+\pi^-\pi^0$ results for N^+ (a) and N^- (b). $D \to K^+K^-\pi^0$ results for N^+ (c) and N^- (d). In each plot the vertical yellow band indicates the value obtained from the combination of all tags.

- **Uncertainties due to non-uniformities in the Dalitz acceptance**
  There is a possible source of bias arising from non-uniformities in the Dalitz acceptance. The efficiency of reconstruction at CLEO-c is rather flat across phase space, but residual variations are parameterised and used to weight the amplitude models for the two signal modes, and the resulting effective values of F^+ are then calculated. The potential bias is assessed to be 0.001 for $\pi^+\pi^-\pi^0$, and 0.010 for $K^+K^-\pi^0$. The significant difference between the two values is attribute to the larger fraction of events in the CP-odd Dalitz plot for $D \to K^+K^-\pi^0$, which will be distributed differently to those in the CP-even Dalitz plot. Therefore, the measured value of F^+ is affected more significantly by efficiency variations than for $D \to \pi^+\pi^-\pi^0$.

7.2.14 Implications for the measurement of ϕ_3

Sensitivity to the unitarity triangle angle ϕ_3 is obtained by measuring the relative decay rates of $B^\mp \to D(h^-h^+\pi^0)K^\mp$ decays and related observables. Once more considering the Dalitz plot to be divided into a pair of symmetric bins, as introduced in Sect. 7.1, and making use of the relations of Ref. [20] and Eq. 7.15, it follows that

$$\begin{aligned}\Gamma(B^\mp \to D(h^-h^+\pi^0)K^\mp) &= h_B\Big([1+r_B^2][1-2c_1y_D\sqrt{K_1K_{-1}}] \\ &\quad + 2x_\mp[2c_1\sqrt{K_1K_{-1}} - y_D]\Big) \\ &= h_b\Big([1+r_B^2][1-(2F_+-1)y_D] \\ &\quad + 2x_\mp[(2F_+-1) - y_D]\Big) \end{aligned} \tag{7.40}$$

Here h_B is a normalisation factor, r_B is the ratio of the magnitudes of the $B^+ \to D^0K^+$ and $B^+ \to \bar{D}^0K^+$ amplitudes, δ_B is the strong-phase difference between these amplitudes and $x_\pm = r_B\cos(\delta_B \pm \phi_3)$. This expression includes the effects of $D^0\bar{D}^0$ oscillations at leading order in the mixing parameters [16].

These partial widths and those involving flavor specific D meson decays can be used to construct the partial-widths ratio R_{F_+} and CP-asymmetry A_{F_+}:

$$R_{F_+} \equiv \frac{\Gamma(B^- \to D_{F_+}K^-) + \Gamma(B^+ \to D_{F_+}K^+)}{\Gamma(B^- \to D^0K^-) + \Gamma(B^+ \to \bar{D}^0K^+)}, \tag{7.41}$$

$$A_{F_+} \equiv \frac{\Gamma(B^- \to D_{F_+}K^-) - \Gamma(B^+ \to D_{F_+}K^+)}{\Gamma(B^- \to D_{F_+}K^-) + \Gamma(B^+ \to D_{F_+}K^+)}, \tag{7.42}$$

where D_{F_+} indicates a D meson of CP-even content F_+, established through its decay into the final state $h^+h^-\pi^0$. These observables are directly analogous to the usual so-called GLW [14] observables $R_{\mathrm{CP}\pm}$ and $A_{\mathrm{CP}\pm}$, where the D meson is reconstructed in a pure CP eigenstate. In order to make explicit the relationship to the pure CP-eigenstate case, the effects of mixing are now neglected. Then R_{F_+} and A_{F_+} are found

to have the following dependence on the underlying physics parameters:

$$R_{F_+} = 1 + r_B^2 + (2F_+ - 1) \cdot 2r_B \cos\delta_B \cos\phi_3, \quad (7.43)$$
$$A_{F_+} = (2F_+ - 1) \cdot 2r_B \sin\delta_B \sin\phi_3 / R_{F_+}, \quad (7.44)$$

which reduces to the equivalent expressions for $R_{\mathrm{CP}\pm}$ and $A_{\mathrm{CP}\pm}$ in the case F_+ is 1 or 0. Therefore inclusive final states such as $h^-h^+\pi^0$ may be cleanly interpreted in terms of ϕ_3 and the other parameters of interest, provided that F_+ is known.

Chapter 8

Conclusion

- In summary, we report a study of the mode $B^- \to Dh^-, D \to K^+\pi^-\pi^0$ ($h = K, \pi$), using 772×10^6 $B\overline{B}$ pair collected by the Belle detector. We use a neural network based method to discriminate between signal and background with nine discriminating variables as a input to the network. We applied a two-dimensional fit to ΔE and NB$'$ which are having negligible correlation, to extract the signal yield. We obtain the first evidence of suppressed $B \to DK$ signal with a significance of 3.2σ. We measure the ratio of suppressed to favored $B^- \to DK^-$ branching-fraction, R_{DK} and the direct CP asymmetry A_{DK} for the mode $B^- \to DK^-, D \to K^+\pi^-\pi^0$ as:

$$\begin{aligned} R_{DK} &= [1.98 \pm 0.62(\text{stat.}) \pm 0.24(\text{syst.})] \times 10^{-2}, \\ A_{DK} &= 0.41 \pm 0.30(\text{stat.}) \pm 0.05(\text{syst.}). \end{aligned}$$

  In addition, we report the first measurements of $R_{D\pi}$ and $A_{D\pi}$ for $B^- \to D\pi^-$ decay as:

$$\begin{aligned} R_{D\pi} &= [1.89 \pm 0.54(\text{stat.})^{+0.22}_{-0.25}(\text{syst.})] \times 10^{-3}, \\ A_{D\pi} &= 0.16 \pm 0.27(\text{stat.})^{+0.02}_{-0.03}(\text{syst.}). \end{aligned}$$

  The above results for $B^- \to DK^-$ decay are the important observables for the extraction of ϕ_3 in a model independent method.

- We also report a study of the decays $D \to \pi^-\pi^+\pi^0$ and $D \to K^-K^+\pi^0$ using the data corresponding to an integrated luminosity of 818 pb^{-1} collected by the CLEO-c experiment in e^+e^- collisions at the $\psi(3770)$ resonance. We measured the fractional CP-even content, $F^+ = 0.968 \pm 0.017 \pm 0.006$ for $\pi^+\pi^-\pi^0$ decay and $F^+ = 0.731 \pm 0.058 \pm 0.021$ for $K^+K^-\pi^0$ decay. In the above values of F^+, the first uncertainty is statistical, and the second is systematic. Such self-conjugate inclusive decay channels can be cleanly included in measurements of the unitarity-triangle angle ϕ_3, using $B^\mp \to DK^\mp$ decays. The high value of F_+ obtained for

$D \to \pi^-\pi^+\pi^0$ makes this channel, in particular, a valuable addition to the suite of D-decay modes used in the measurement of ϕ_3 at LHCb and Belle-II.

Appendix A

RooKSFW

The KSFW variable is defined as,

$$\text{KSFW} = \sum_{l=0}^{4} \sum_{m=c,n,\nu} \alpha_{l,m} (R_l^{so})_m + \sum_{l=0,4} \beta_l R_l^{oo} + \gamma \sum_{n=1}^{N} |(P_t)_n|.$$

The various terms are described below. R_l^{so} is defined as

$$R_l^{so} = \begin{cases} \frac{\sum_{j,k} Q_j Q_k |p_k| P_l(\cos\theta_{jk})}{E_{e^+e^-} - E_B} & (l = 1, 3) \\ \\ \frac{\sum_{j,k} |p_j| P_l(\cos\theta_{jk})}{E_{e^+e^-} - E_B} & (l = 0, 2, 4) \end{cases}, \tag{A.1}$$

where $P_l(\cos\theta_{jk})$ are Legendre polynomials of the cosine of the angle between the j^{th} and i^{th} tracks (θ_{jk}), where j and k run over signal B and other B tracks, respectively. Here, p_j (Q_j) and p_k (Q_k) are the momentum (charge) of corresponding particles and $E_{e^+e^-}$ and E_B are the energy in the CoM frame of e^+e^- and B, respectively.

R_l^{so} can be calculated by subdividing the particles from the other B into charged (c), neutral (n) and the missing momentum (ν), which leads to the following three classes:

- $(R_l^{so})_c$ (for l=0 to 4), using only charged tracks of other B
- $(R_l^{so})_n$ (for l=0,2,4), using only photons of other B and
- $(R_l^{so})_\nu$ (for l=0,2,4), using only missing momentum of other B

The parameters $\alpha_{l,c}$, $\alpha_{l,n}$ and $\alpha_{l,\nu}$ are the Fisher coefficients for the charged, neutral, and missing-momentum categories, respectively. There are total 11 parameters for $l = 0, 1, 2, 3$ and 4.

R_l^{oo} can be defined identically to R_l^{so} but now the summations over j and k both run over charged tracks not forming the signal candidate. β_l are the Fisher coefficients. We total have 5 parameters corresponding to R_l^{oo}.

$\sum_{n=1}^{N} |(P_t)_n|$ is the scalar sum of the transverse momenta P_t of all particles in the event multiplied by a Fisher coefficient γ. The n represents particle index, and N is the number of particles in the event.

Therefore, there are a total of 17 parameters used to define the KSFW, which are determined using the signal and continuum MC. The ROOKSFW package directly gives the variable LRKSFW (KSFW Likelihood Ratio) for the events to be signal or continuum background.

Appendix B

Demonstration of the Fit to MC samples

Using the method of configuring PDF described in Sec. 5.2, we demonstrate the fit using two streams of MC.

B.1 Fit to Favored Modes

B.1.1 Signal extraction

Using the PDFs described above we fit to one stream of MC sample and a data sample to extract signal yield. We use $\Upsilon(4S)$ sample of 772×10^6 $B\overline{B}$ pairs.

Fit to $B \to D_{fav}\pi$ mode using one stream of MC

Figure B.1 shows the result of the fit to favored modes on MC. Projections for several regions are shown in Figure B.2 and Figure B.3. Good quality of the fit is indicated by the values of χ^2/ndf. Table B.1 shows the list of the parameters in the fit.

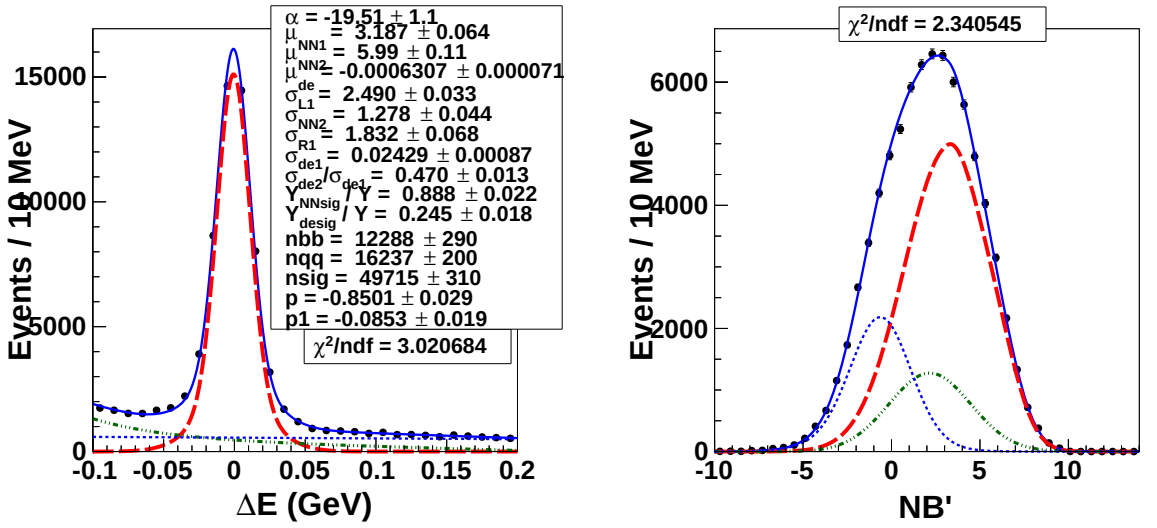

(a) (b)

Figure B.1: (a) ΔE distributions and (b) NB' distribution both of which are obtained by projecting all fitted regions. The fitted sample is shown with dots with error bars and the PDF is shown with the solid blue curve, for which the components are shown with dashed red (Dπ), dashed cyan ($B\overline{B}$ background) and dashed magenta ($q\overline{q}$ background)

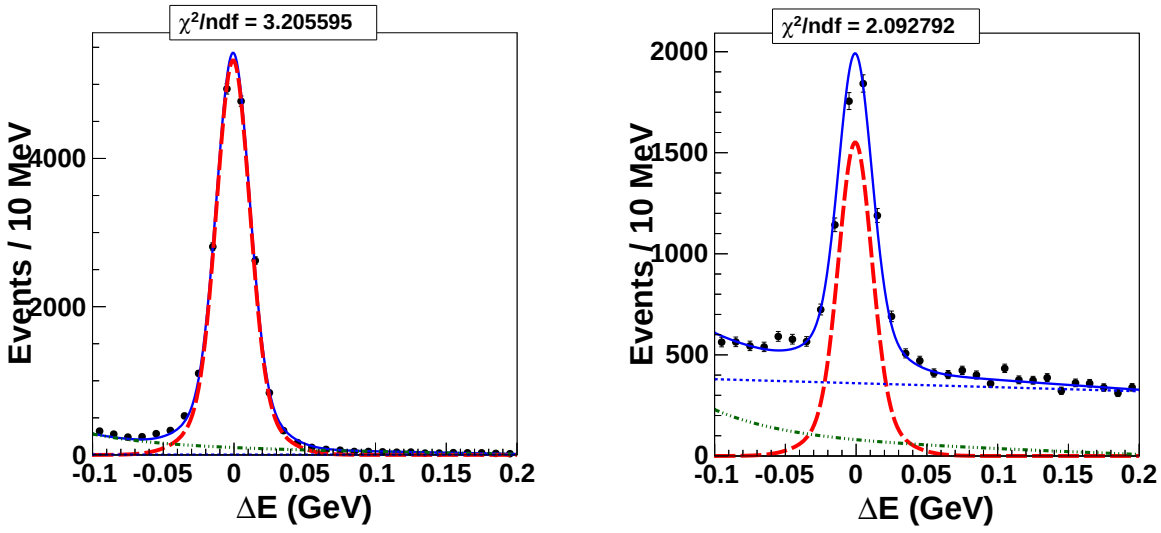

(a) (b)

Figure B.2: The projections for the favored Dπ MC sample. The ΔE distributions for signal and $B\overline{B}$ enhanced ($1 < NB' < 6$), $q\overline{q}$ enhanced ($NB' < 0$) are shown from left to right.

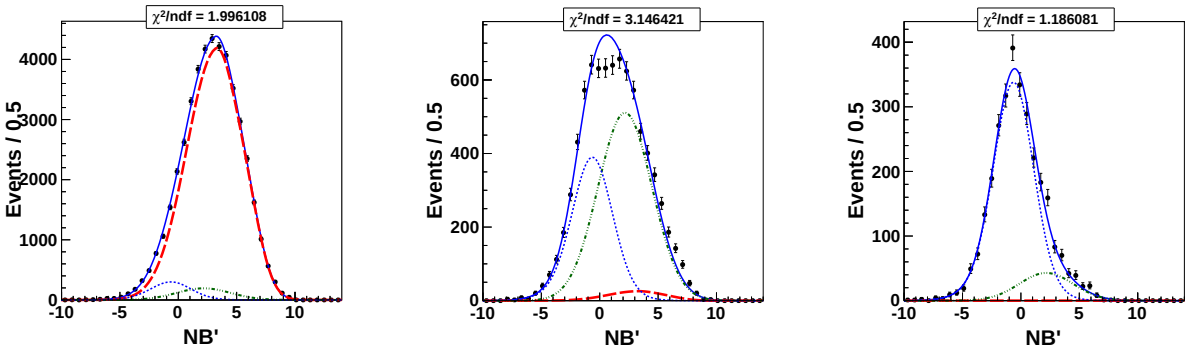

(a) (b) (c)

Figure B.3: The projections for the favored Dπ MC sample. The NB' distributions for signal enhanced ($-0.02 < \Delta E < 0.02$), $B\overline{B}$ enhanced($-0.1 < \Delta E < -0.05$), $q\overline{q}$ enhanced ($\Delta E > 0.15$) are shown from left to right.

Table B.1: The list of parameters as well as the values for the fit to B→ $D_{fav}\pi$ MC. The expected yield for $D\pi$ = 50320, $B\overline{B}$ = 11677 and $q\bar{q}$ = 16395.

Component	PDF type	Floated Parameters	Value
Dπ	General	Yield	49715±310
	Double Gaussian (ΔE)	μ	-0.0006307±0.000071
		σ_1	0.02429±0.00087
		σ_2/σ_1	0.47±0.013
		Area fraction	0.245±0.018
	b.f. Gaussian + Gaussian (NB′)	Area fraction	0.888±0.022
		μ_1	3.187±0.064
		σ_{L1}	2.49±0.033
		σ_{R1}	1.832±0.068
		μ_2	5.99±0.11
		σ_2	1.278±0.044
$B\overline{B}$ in Dπ	General	Yield	12288±290
	Exponential+Linear (ΔE)	expo. coefficient	-19.51±1.1
		Slope	-0.8501±0.029
		Area fraction	0.341 (fixed from $B\overline{B}$ MC)
	Gaussian (NB′)		fixed from $B\overline{B}$ MC PDF values shown in Fig. 5.6:(a)
$q\bar{q}$ in Dπ	General	Yield	16237±200
	Linear	Slope	-0.0853±0.019
	Double Gaussian (NB′)		fixed from qq sideband PDF values shown in Fig. 5.8:(a)

Fit to $B \to D_{fav}K$ mode using one stream of MC

Figure B.4 shows the result of the fit to $D_{fav}K$ mode on MC. Projections for several regions are shown in Figure B.5 and Figure B.6. Good quality of the fit is indicated by the values of χ^2/ndf. Table B.2 shows the list of the parameters in the fit.

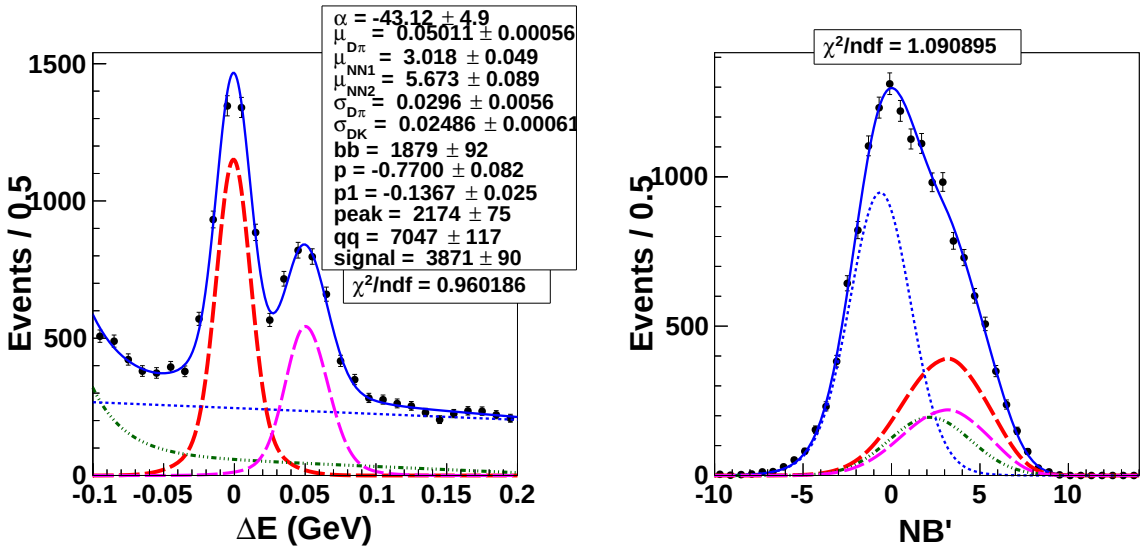

(a) (b)

Figure B.4: (a) ΔE distribution and (b) NB' distribution both of which are obtained by projecting all fitted regions. In these plots, points with error bars represent data while the total best-fit projection is shown with the solid blue curve, for which the components are shown with thicker dashed red (DK signal), thinner dashed magenta ($D\pi$), dashed dot green ($B\bar{B}$ background) and dotted blue ($q\bar{q}$ background).

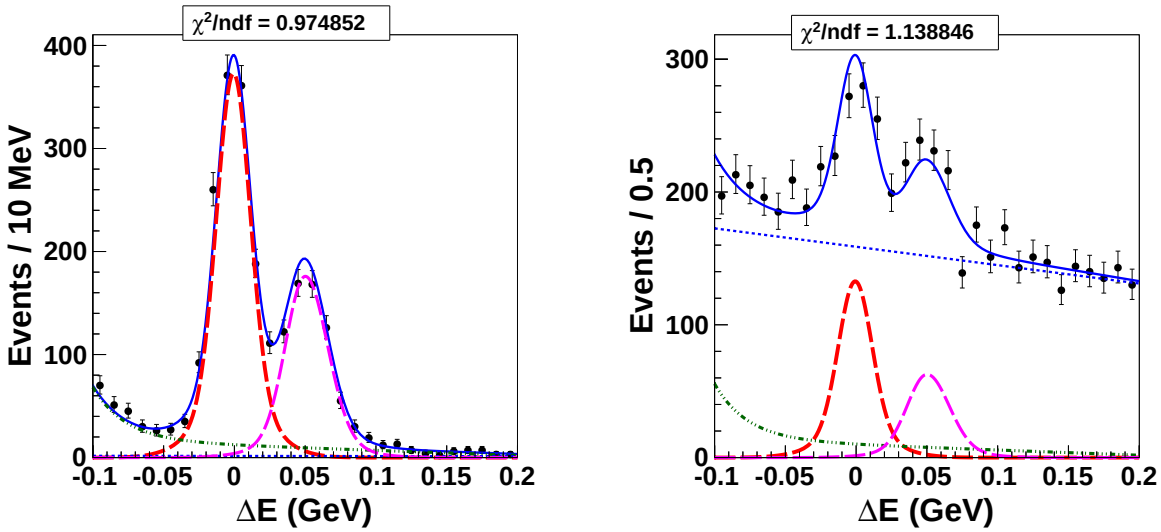

(a) (b)

Figure B.5: The projections for the favored DK data sample. Figure (a) shows ΔE distribution for signal enhanced, Dπ enhanced, $B\bar{B}$ enhanced region ($NB' > 4$) and Figure (b) shows ΔE distribution for $q\bar{q}$ enhanced region ($NB' < 0$)

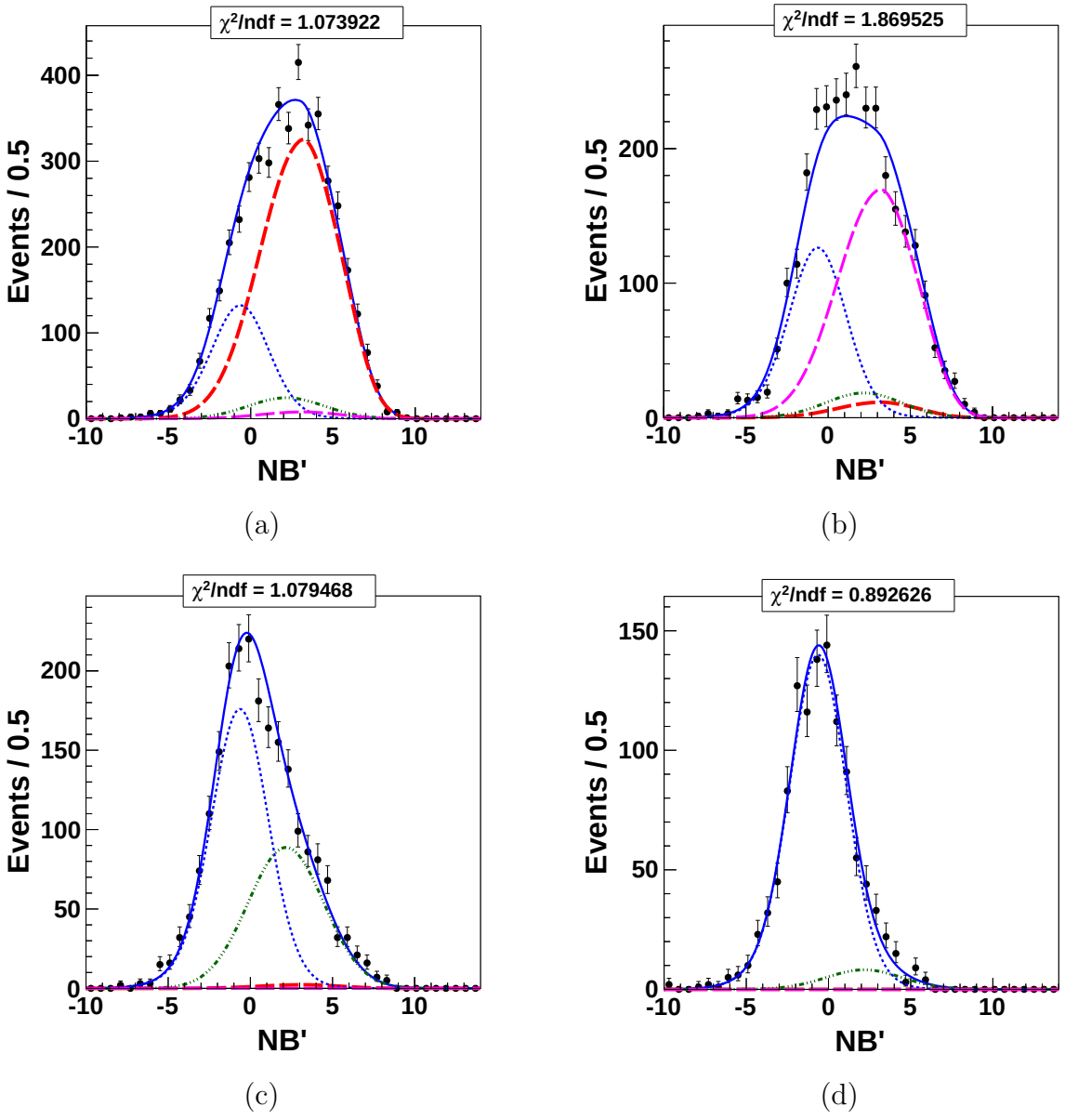

Figure B.6: The projections for the favored DK data sample. The NB' distributions for signal enhanced ($-0.02 < \Delta E < 0.02$), Dπ enhanced ($0.03 < \Delta E < 0.07$), $B\bar{B}$ enhanced ($-0.1 < \Delta E < -0.05$), $q\bar{q}$ enhanced ($\Delta E > 0.15$) are shown from Figure (a) to (d).

Table B.2: The list of parameters as well as the values for the fit to B→ $D_{fav}K$ MC. The expected yield for DK = 3863, $D\pi$ = 2208, $B\overline{B}$ = 1992 and $q\overline{q}$ = 6908.

Component	PDF type	Parameters	Value
DK	General	Yield	3871±90
	Double Gaussian (ΔE)	μ	-0.0006307 (fixed)
		σ_1	0.02486±0.00061
		σ_2/σ_1	0.47 (fixed)
		Area fraction	0.245 (fixed)
	b.f. Gaussian + Gaussian (NB′)	Area fraction	0.888 (fixed)
		μ_1	3.018±0.049
		σ_{L1}	2.49 (fixed)
		σ_{R1}	1.832 (fixed)
		μ_2	5.673±0.089
		σ_2	1.278 (fixed)
Dπ in DK	General	Yield	2174±75
	b.f. Gaussian + Gaussian (ΔE)	μ	0.05011±0.00056
		σ	0.0296±0.0056
		σ_R	0.01541 (fixed)
		σ_L/σ_R	0.895 (fixed)
		Area fraction	0.8303 (fixed)
	b.f. Gaussian + Gaussian (NB′)		same as DK signal component
$B\overline{B}$ in DK	General	Yield	1879±92
	Exponential+Linear (ΔE)	expo. coefficient	-43.12±4.9
		Slope	-0.77±0.08
		Area fraction	0.298 (fixed from $B\overline{B}$ MC)
	Gaussian (NB′)		fixed from $B\overline{B}$ MC PDF values shown in Fig. 5.6:(a)
$q\overline{q}$ in DK	General	Yield	7047±117
	Linear	Slope	-0.1367±0.025
	Double Gaussian (NB′)		fixed from $q\overline{q}$ MC sideband PDF values shown in Fig. 5.8:(a)

B.2 Fit to Suppressed Modes

B.2.1 Signal extraction

Using the PDFs described above we fit to five streams of MC samples.

Fit to $B \to D_{sup}\pi$ mode using five stream of MC

We demonstrate here the fit using 5 streams of MC. Figure B.7 shows the result of the fit to signal enhanced region for suppressed $D\pi$ modes. The projections for the other regions are shown in Appendix C. Among all floated parameters, yield parameters along with the corresponding truth matching yields are shown in Table B.3. The signal yield for all the five streams are consistent with the expected number, which is **205**. Also signal, $B\overline{B}$ and $q\overline{q}$ yields are in good agreement with truth matched value. The residuals for each component of $D_{sup}\pi$ mode are shown in Figure B.8. The last column in Table B.4 shows the list of parameters returned by the fit for one stream MC (a); those parameters that have changed are highlighted.

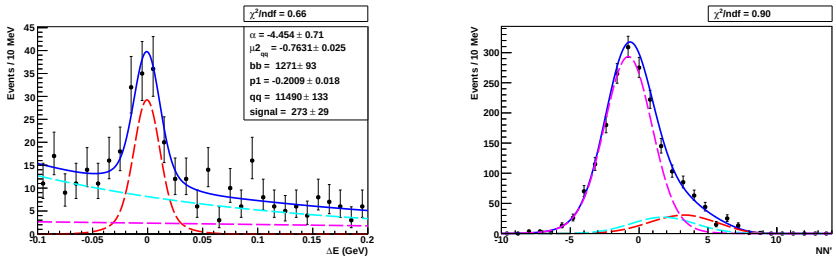

(a) Fit for stream 0

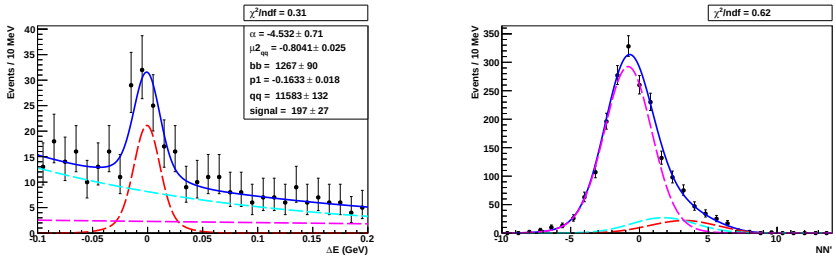

(b) Fit for stream 1

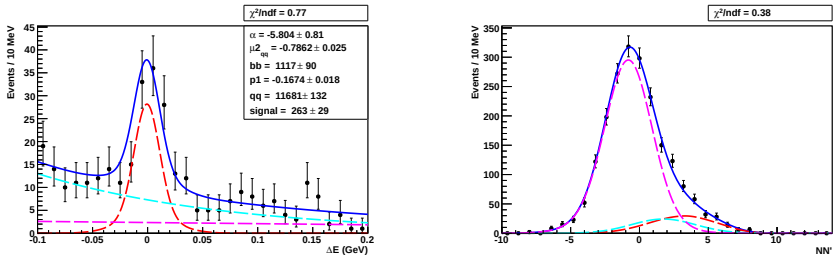

(c) Fit for stream 2

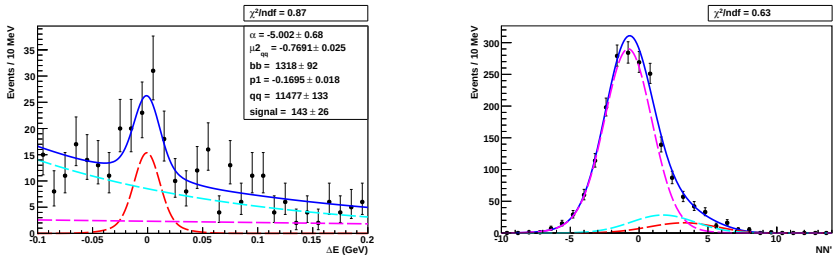

(d) Fit for stream 3

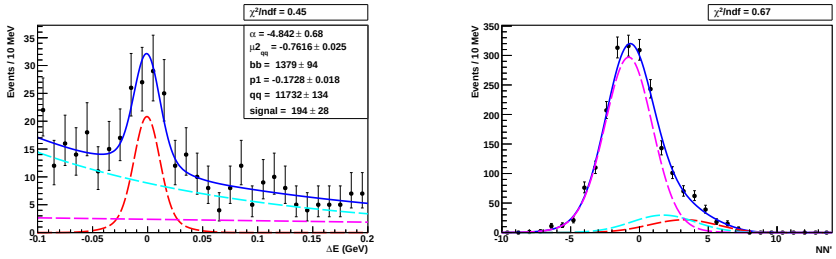

(e) Fit for stream 4

Figure B.7: The projections for the suppressed $D\pi$ mode using MC sample. Left plot shows ΔE distributions for signal enhanced region ($4 < NB' < 14$) and right plot shows NB' distributions for signal enhanced region ($-0.02 < \Delta E < 0.02$)

Table B.3: Yield for each component of suppressed $D\pi$ mode using five streams of MC.

Component	Yield	Value				
		MC (a)	MC (b)	MC (c)	MC (d)	MC (e)
Signal	Fit Yield	273 ± 29	197 ± 27	263 ± 29	143 ± 26	194 ± 28
	Truth Matched	248	192	221	190	184
$B\overline{B}$	Fit Yield	1271 ± 93	1267 ± 90	1117 ± 90	1318 ± 92	1379 ± 94
	Truth Matched	1356	1223	1234	1181	1325
$q\overline{q}$	Fit Yield	11490 ± 133	11583 ± 132	11681 ± 132	11477 ± 133	11732 ± 13
	Truth Matched	11430	11632	11606	11567	11796

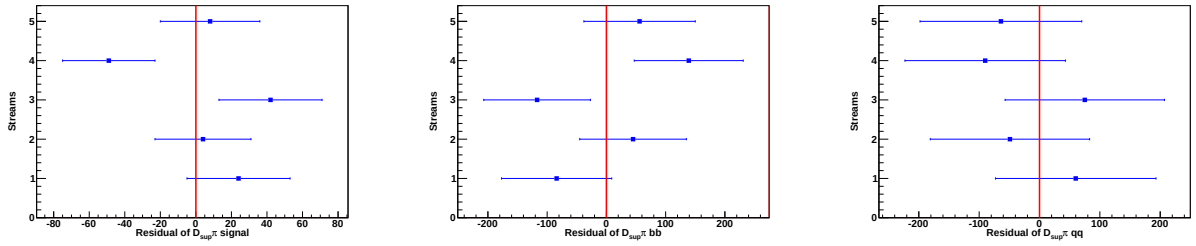

(a) (b) (c)

Figure B.8: Residual plot for each component of $D_{sup}\pi$ mode.(a) residual distribution for signal (b) residual distribution for $B\overline{B}$ (c) residual distribution for $q\overline{q}$

Table B.4: The list of parameters as well as the values for the fit to B→ $D_{sup}\pi$ MC.

Component	PDF type	Parameters	Value
Dπ	General	Yield	273±29
	Double Gaussian (ΔE)	μ	-0.0006307 (fixed)
		σ_1	0.02429(fixed)
		σ_2/σ_1	0.47 (fixed)
		Area fraction	0.245 (fixed)
	b.f. Gaussian + Gaussian (NB′)	Area fraction	0.888 (fixed)
		μ_1	3.187(fixed)
		σ_{L1}	2.49 (fixed)
		σ_{R1}	1.832 (fixed)
		μ_2	5.99 (fixed)
		σ_2	1.278 (fixed)
$B\overline{B}$ in Dπ	General	Yield	1271±93
	Exponential (ΔE)	expo. coefficient	-4.454±0.71
	Gaussian (NB′)		fixed PDF values shown in Fig. 5.7:(a)
$q\bar{q}$ in Dπ	General	Yield	11490±133
	Linear	Slope	-0.2±0.02
	Double Gaussian (NB′)		fixed from $q\bar{q}$ MC sideband with free μ_2 (μ_2 = -0.7631±0.025) PDF values shown in Fig. 5.9:(a)

Fit to $B \to D_{sup}K$ mode using five stream of MC

We demonstrate here the fit using 5 streams of MC. Figure B.10 shows the result of the fit to signal enhanced region for suppressed DK modes. The projections for the other regions are shown in Appendix C. Among all floated parameters, yield parameters along with the corresponding truth matching yield are shown in Table B.5. The signal yields obtained for all the five streams are consistent with the expected signal value, which is **15**. And also signal, $B\overline{B}$, $q\overline{q}$ yields are in good agreement with truth matched value. The residuals for each component of $D_{sup}K$ are shown in Figure B.9. The remaining small bias between $B\overline{B}$ and $q\overline{q}$ is due to the effect of other parameters in the $q\overline{q}$ NB' PDF and similar ΔE shape of combinatorial $B\overline{B}$ background and $q\overline{q}$ background. The last column in Table B.6 shows the list of parameters returned by the fit for one stream MC (a); those parameters that have changed are highlighted.

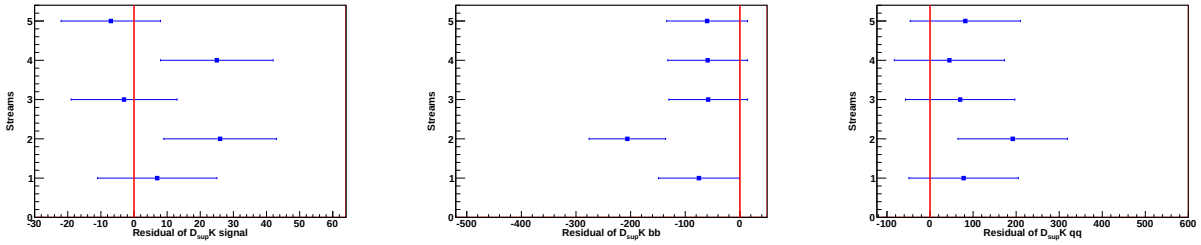

(a) (b) (c)

Figure B.9: Residual plot for each component of $D_{sup}K$ mode using MC with corrected $q\overline{q}$ NB' shape.(a) residual distribution for signal (b) residual distribution for $B\overline{B}$ (c) residual distribution for $q\overline{q}$

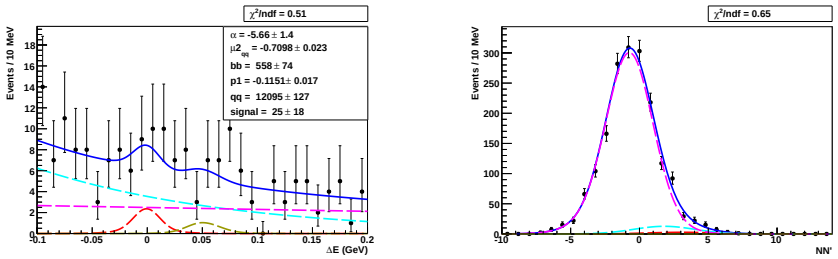

(a) Fit for stream 0

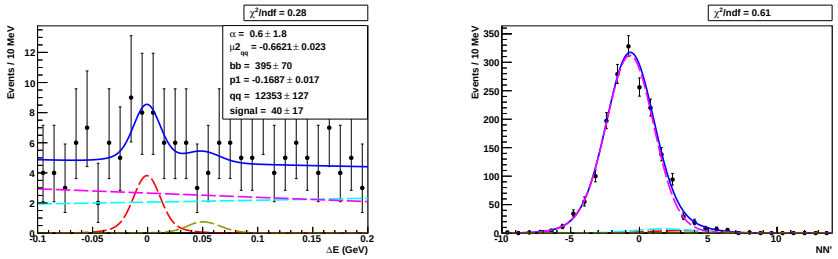

(b) Fit for stream 1

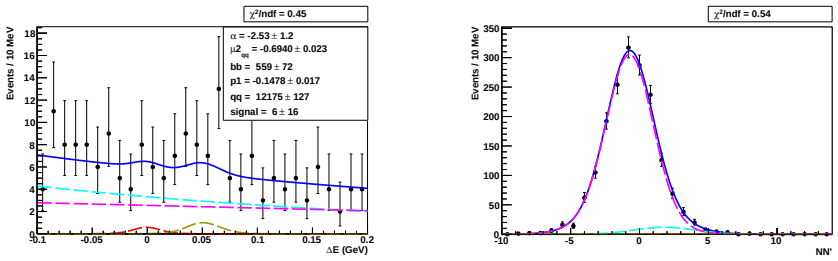

(c) Fit for stream 2

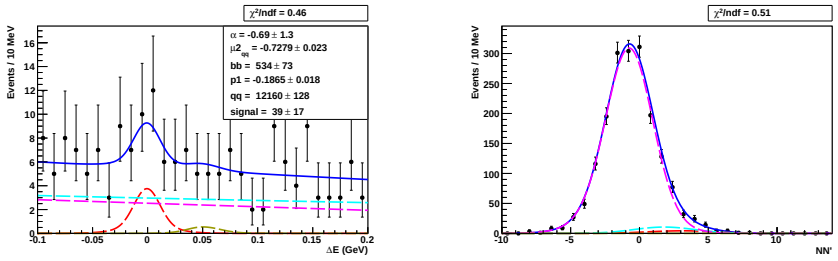

(d) Fit for stream 3

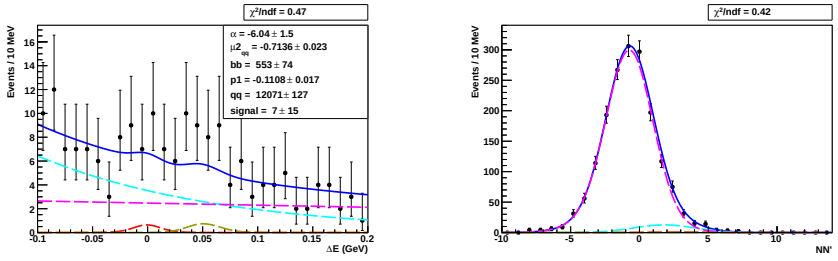

(e) Fit for stream 4

Figure B.10: The projections for the suppressed DK mode using MC sample. Left plot shows ΔE distributions for signal enhanced region ($4 < NB' < 14$) and right plot shows NB' distributions for signal enhanced region ($-0.02 < \Delta E < 0.02$)

Table B.5: Yield for each component of suppressed DK mode using five streams of MC.

Component	Yield	Value				
		MC (a)	MC (b)	MC (c)	MC (d)	MC (e)
Signal	Fit Yield	25 ± 18	40 ± 17	6 ± 16	39 ± 17	7 ± 15
	Expected	18	14	9	14	14
$B\overline{B}$	Fit Yield	558 ± 74	395 ± 70	559 ± 72	534 ± 72	553 ± 74
	Truth Matched	633	601	617	593	613
$q\overline{q}$	Fit Yield	12095 ± 127	12353 ± 127	12175 ± 127	12160 ± 128	12071 ± 12
	Truth Matched	12025	12166	12113	12119	12000

Table B.6: The list of parameters as well as the values for the fit to B→ $D_{sup}K$ MC.

Component	PDF type	Parameters	Value
DK	General	Yield	25±18
	Double Gaussian (ΔE)	μ	-0.0006307 (fixed)
		σ_1	0.02486(fixed)
		σ_2/σ_1	0.47 (fixed)
		Area fraction	0.245 (fixed)
	b.f. Gaussian + Gaussian (NB′)	Area fraction	0.888 (fixed)
		μ_1	3.018(fixed)
		σ_{L1}	2.49 (fixed)
		σ_{R1}	1.832 (fixed)
		μ_2	5.673 (fixed)
		σ_2	1.278(fixed)
Dπ in DK	General	Yield	13 (fixed)
	b.f. Gaussian + Gaussian (ΔE)	μ	0.05011(fixed)
		σ	0.0296(fixed)
		σ_R	0.01541 (fixed)
		σ_L/σ_R	0.895 (fixed)
		Area fraction	0.8303 (fixed)
	b.f. Gaussian + Gaussian (NB′)		same as DK signal component
$B\overline{B}$ in DK	General	Yield	558±74
	Exponential+Linear (ΔE)	expo. coefficient (α)	-5.66±1.4
	Gaussian (NB′)		fixed PDF values shown in Fig. 5.7:(b)
$q\overline{q}$ in DK	General	Yield	12095±127
	Linear	Slope	-0.1151±0.017
	Double Gaussian (NB′)		fixed from $q\overline{q}$ MC sideband with free μ_2 (μ_2 = -0.7098±0.023) PDF values shown in Fig. 5.9:(b)

Appendix C

Projections for suppressed modes

C.1 Projections of fit to Suppressed $D\pi$ Mode

Figure C.5 and C.10 show the projections for $D\pi$ peak, $B\overline{B}$ and $q\overline{q}$ regions for suppressed $D\pi$ and DK mode using five MC streams: stream 0 (top) - stream 5 (bottom) with corrected $q\overline{q}$ NB' shape.

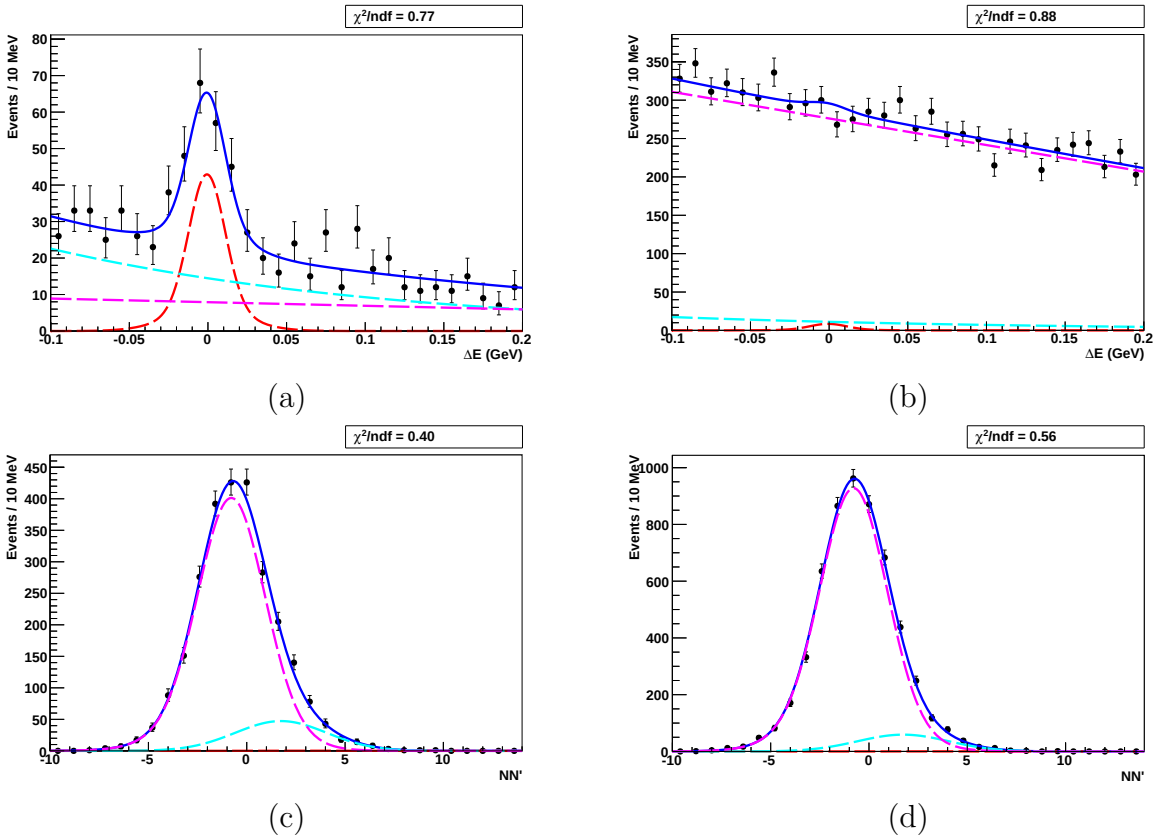

Figure C.1: The projections for suppressed $D\pi$ mode using MC sample of stream 0 with corrected $q\bar{q}$ NB' shape. The ΔE distributions for $B\overline{B}$ enhanced ($0 < NB' < 5$), $q\bar{q}$ enhanced ($-10 < NB' < 0$) are shown from (a) to (b). NB' distributions for $B\overline{B}$ enhanced($-0.1 < \Delta E < -0.05$), $q\bar{q}$ enhanced ($\Delta E > 0.05$) are shown from (c) to (d).

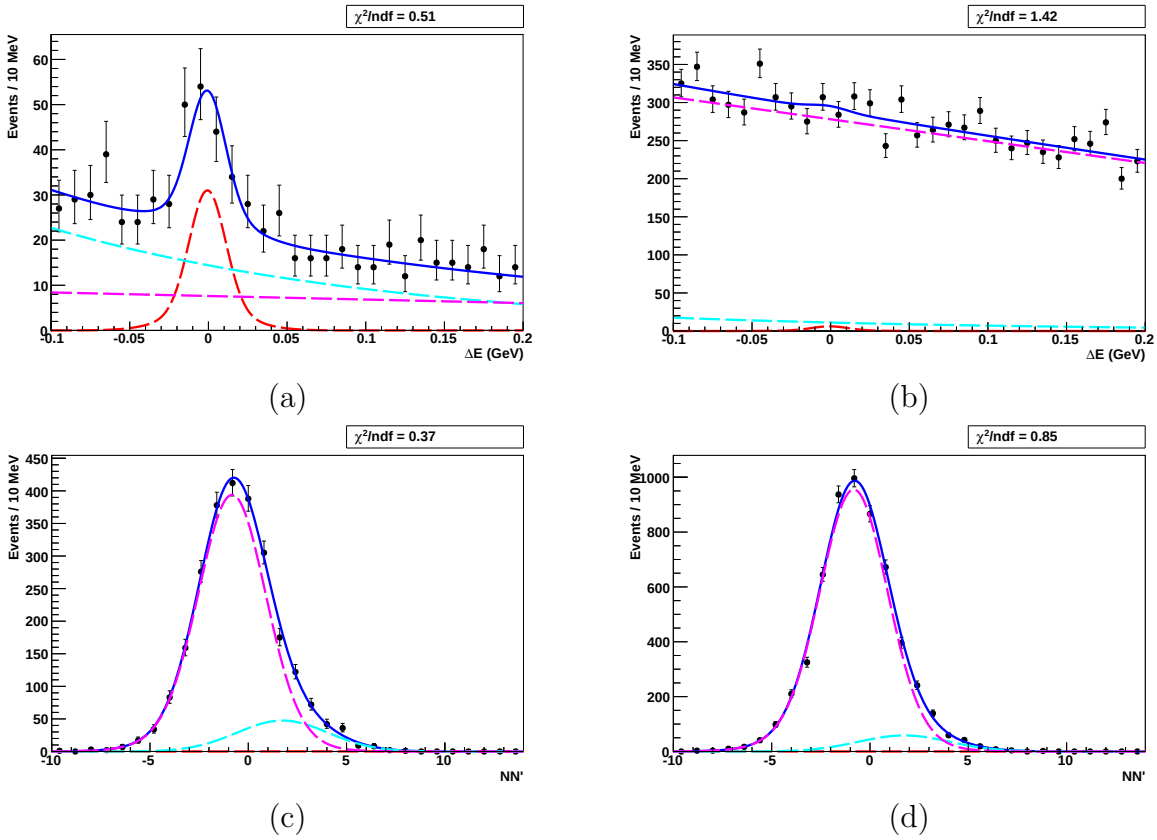

Figure C.2: The projections for suppressed $D\pi$ mode using MC sample of stream 1 with corrected $q\overline{q}$ NB' shape. The ΔE distributions for $B\overline{B}$ enhanced ($0 < NB' < 5$), $q\overline{q}$ enhanced ($-10 < NB' < 0$) are shown from (a) to (b). NB' distributions for $B\overline{B}$ enhanced($-0.1 < \Delta E < -0.05$), $q\overline{q}$ enhanced ($\Delta E > 0.05$) are shown from (c) to (d).

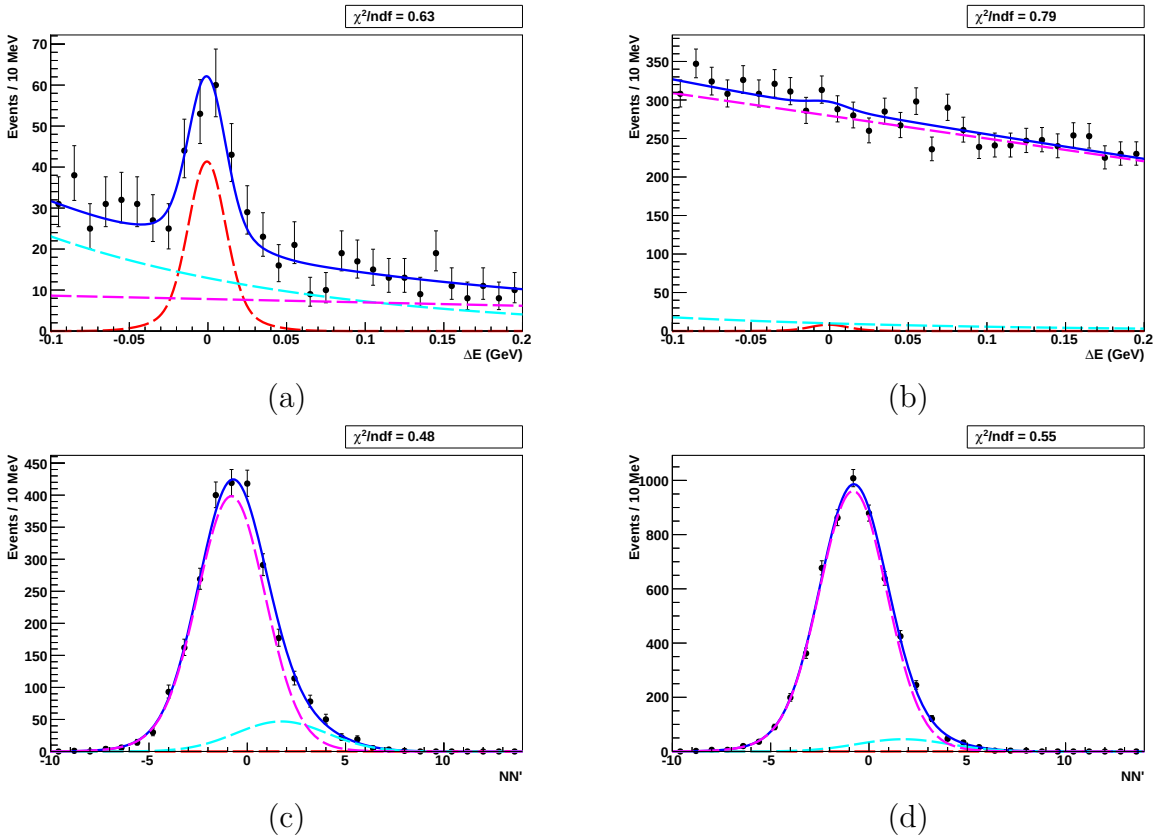

Figure C.3: The projections for suppressed $D\pi$ mode using MC sample of stream 2 with corrected $q\overline{q}$ NB' shape. The ΔE distributions for $B\overline{B}$ enhanced ($0 < NB' < 5$), $q\overline{q}$ enhanced ($-10 < NB' < 0$) are shown from (a) to (b). NB' distributions for $B\overline{B}$ enhanced($-0.1 < \Delta E < -0.05$), $q\overline{q}$ enhanced ($\Delta E > 0.05$) are shown from (c) to (d).

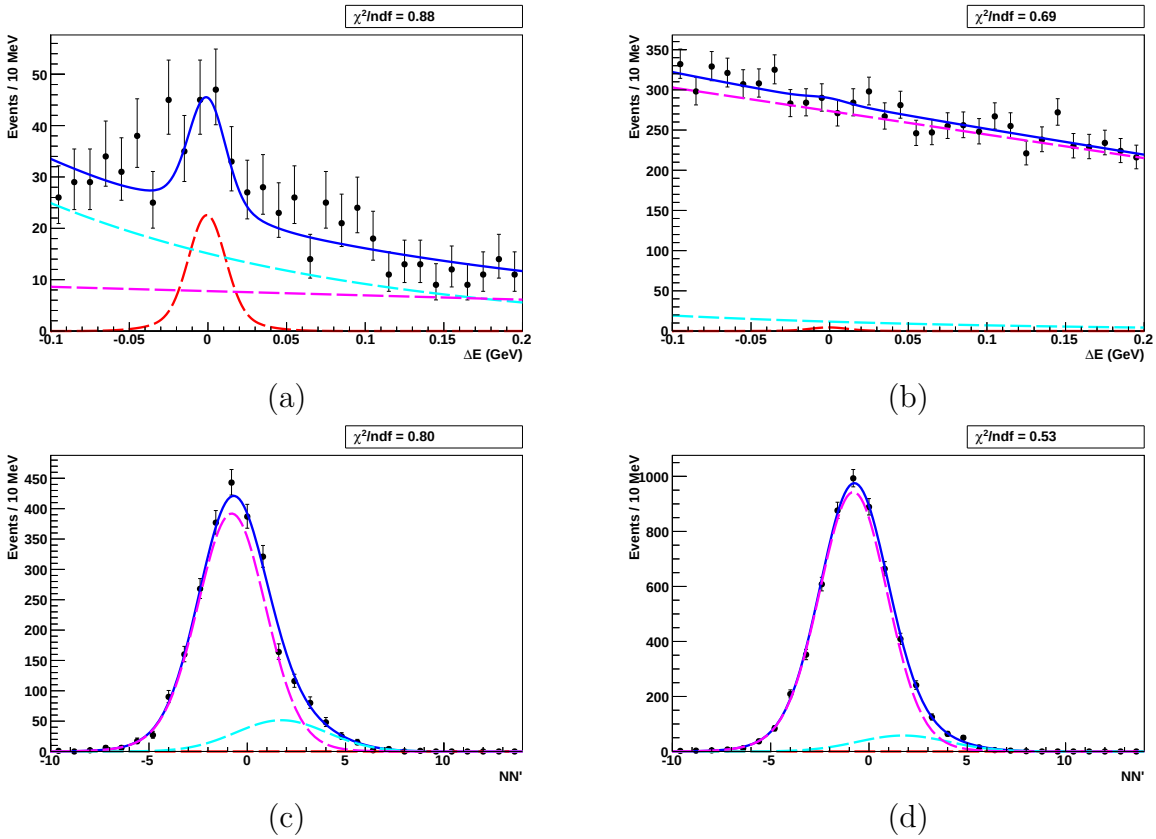

Figure C.4: The projections for suppressed $D\pi$ mode using MC sample of stream 3 with corrected $q\overline{q}$ NB' shape. The ΔE distributions for $B\overline{B}$ enhanced ($0 < NB' < 5$), $q\overline{q}$ enhanced ($-10 < NB' < 0$) are shown from (a) to (b). NB' distributions for $B\overline{B}$ enhanced($-0.1 < \Delta E < -0.05$), $q\overline{q}$ enhanced ($\Delta E > 0.05$) are shown from (c) to (d).

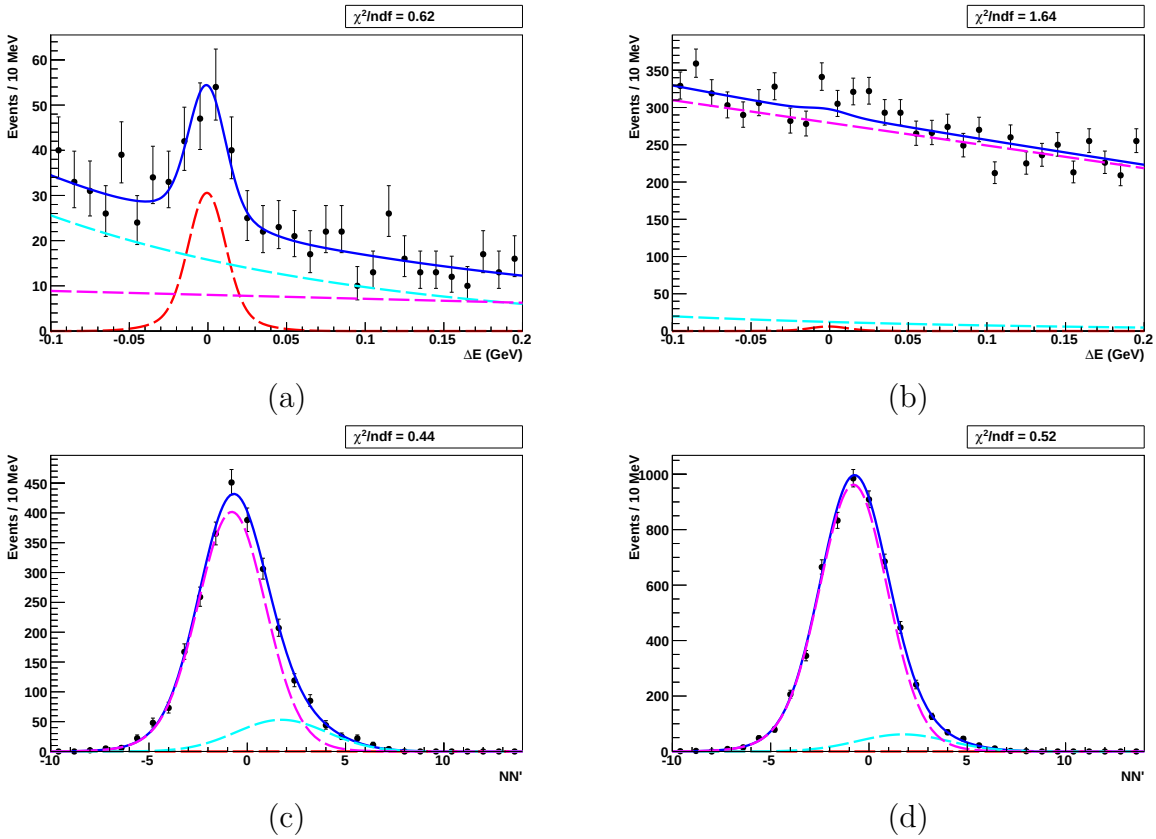

Figure C.5: The projections for suppressed $D\pi$ mode using MC sample of stream 4 with corrected $q\overline{q}$ NB' shape. The ΔE distributions for $B\overline{B}$ enhanced $(0 < NB' < 5)$, $q\overline{q}$ enhanced $(-10 < NB' < 0)$ are shown from (a) to (b). NB' distributions for $B\overline{B}$ enhanced$(-0.1 < \Delta E < -0.05)$, $q\overline{q}$ enhanced $(\Delta E > 0.05)$ are shown from (c) to (d).

C.2 Projections of fit to Suppressed DK Mode

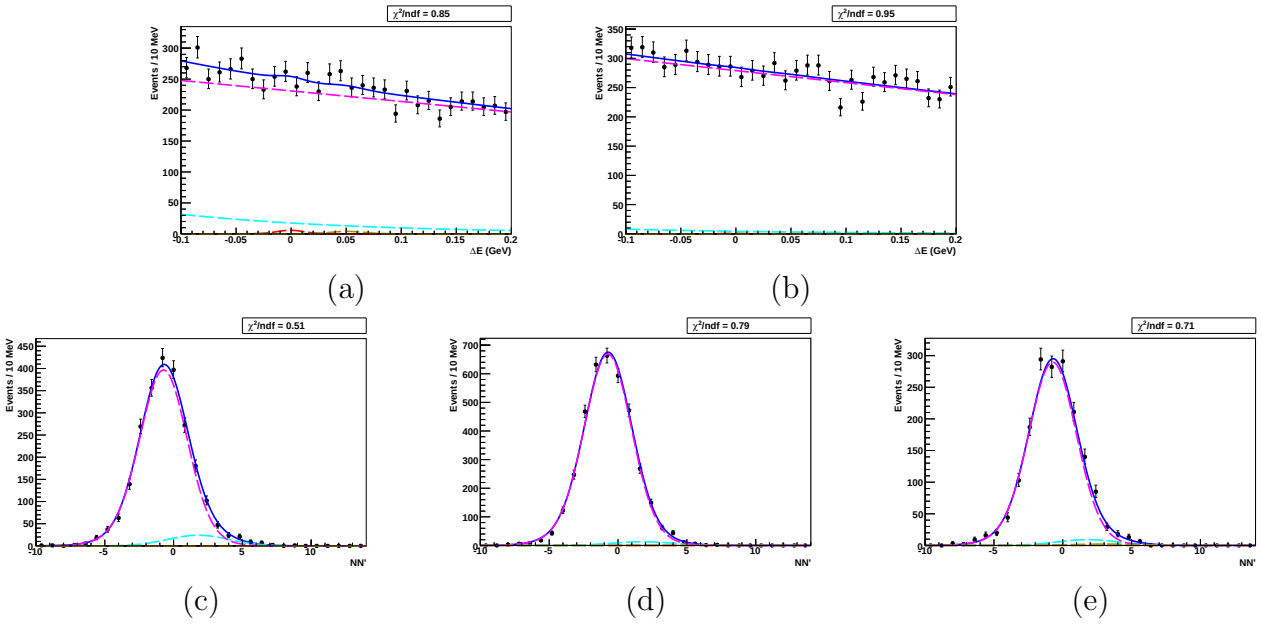

Figure C.6: The projections for suppressed DK mode using MC sample for stream 0 with corrected $q\overline{q}$ NB' shape. The ΔE distributions for $B\overline{B}$ enhanced ($1 < NB' < 5$), $q\overline{q}$ enhanced ($-10 < NB' < 0$) are shown from (a) to (b). NB' distributions for $B\overline{B}$ enhanced ($-0.1 < \Delta E < -0.05$), $q\overline{q}$ enhanced ($\Delta E > 0.1$), $D\pi$ peak enhanced ($0.03 < \Delta E < 0.07$) are shown from (c) to (e).

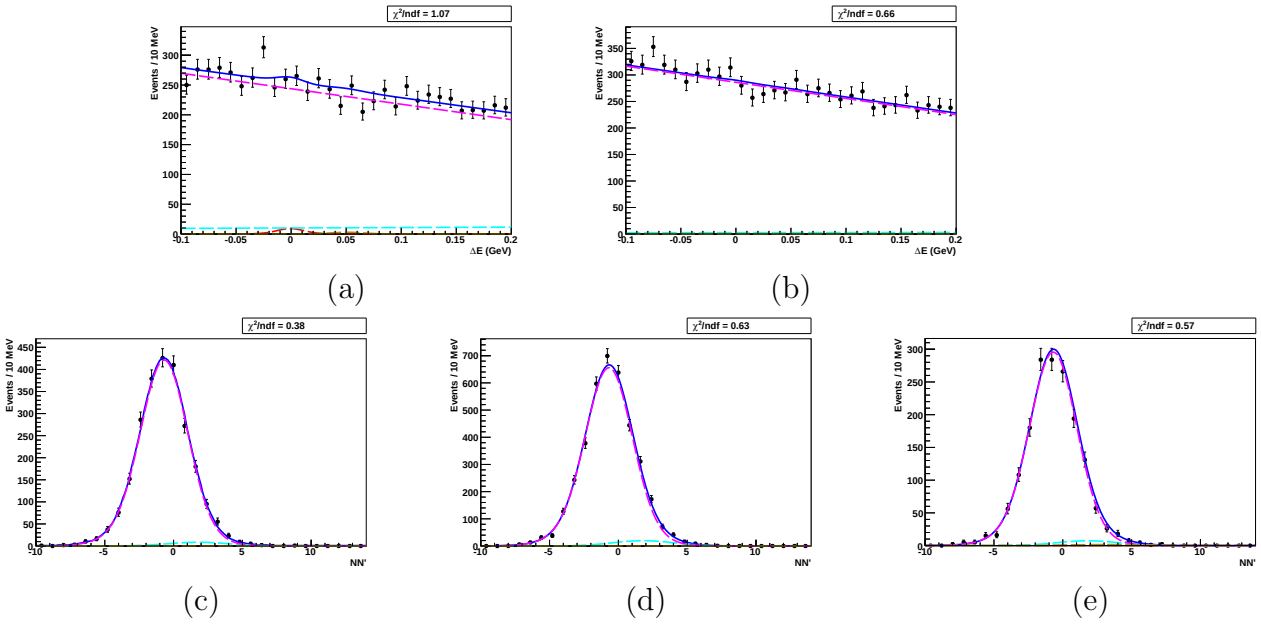

Figure C.7: The projections for suppressed DK mode using MC sample for stream 1 with corrected $q\overline{q}$ NB' shape. The ΔE distributions for $B\overline{B}$ enhanced ($1 < NB' < 5$), $q\overline{q}$ enhanced ($-10 < NB' < 0$) are shown from (a) to (b). NB' distributions for $B\overline{B}$ enhanced ($-0.1 < \Delta E < -0.05$), $q\overline{q}$ enhanced ($\Delta E > 0.1$), $D\pi$ peak enhanced ($0.03 < \Delta E < 0.07$) are shown from (c) to (e).

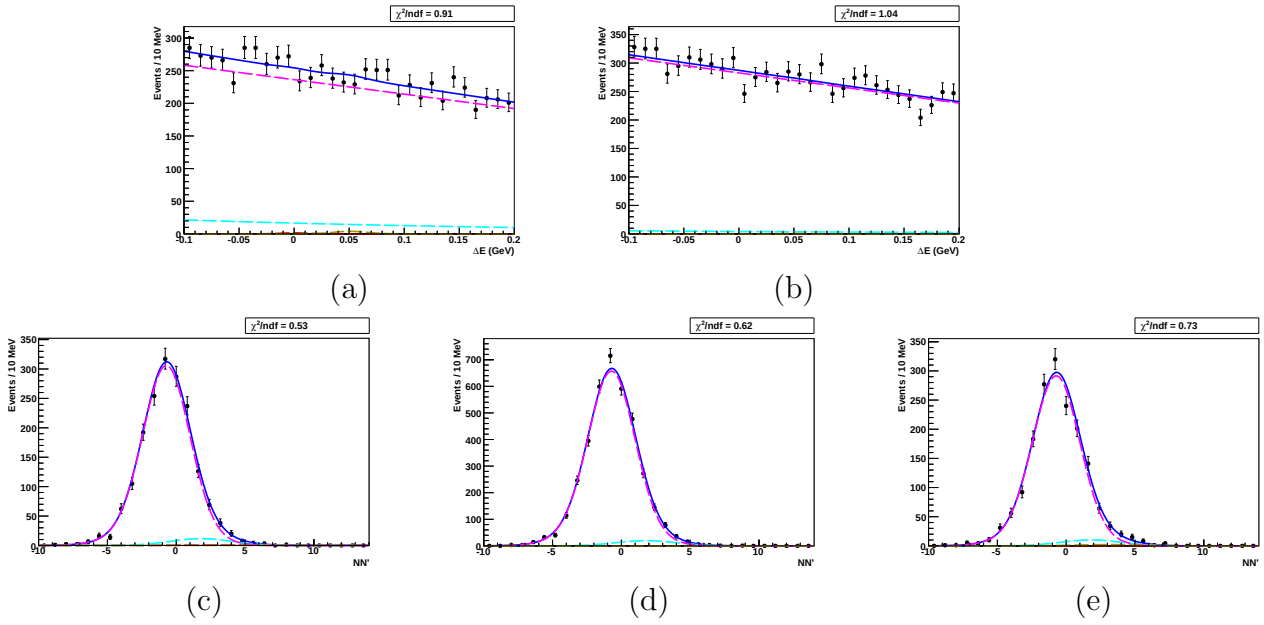

Figure C.8: The projections for suppressed DK mode using MC sample for stream 2 with corrected $q\bar{q}$ NB' shape. The ΔE distributions for $B\overline{B}$ enhanced ($1 < NB' < 5$), $q\bar{q}$ enhanced ($-10 < NB' < 0$) are shown from (a) to (b). NB' distributions for $B\overline{B}$ enhanced ($-0.1 < \Delta E < -0.05$), $q\bar{q}$ enhanced ($\Delta E > 0.1$), $D\pi$ peak enhanced ($0.03 < \Delta E < 0.07$) are shown from (c) to (e).

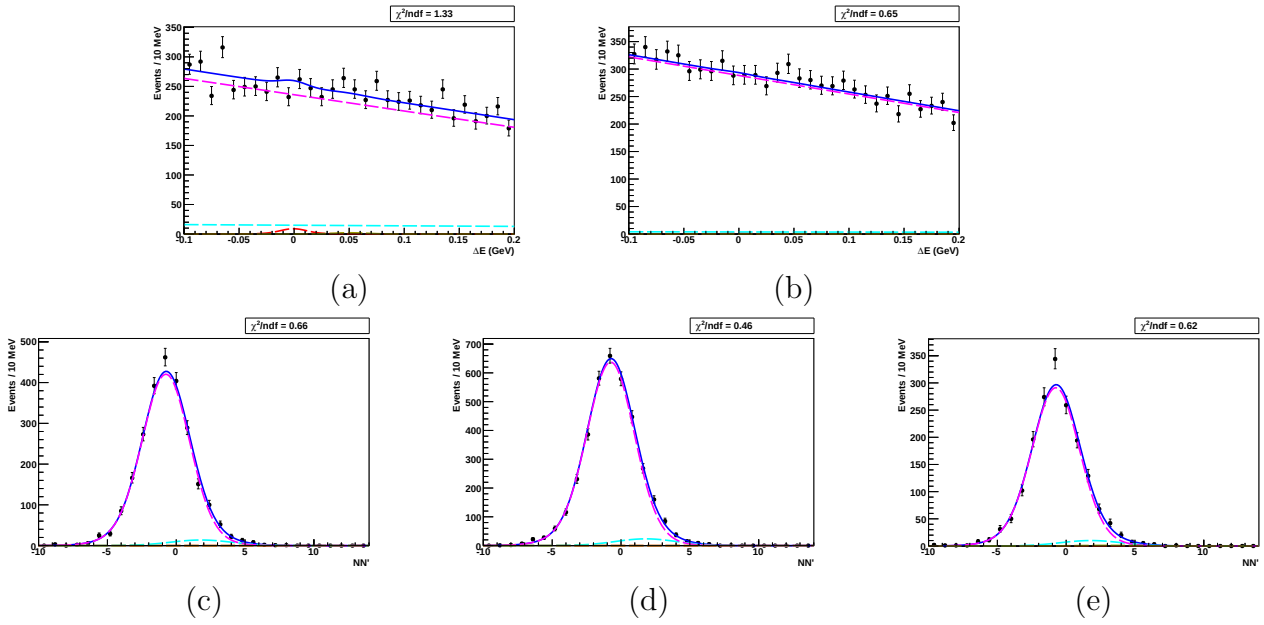

Figure C.9: The projections for suppressed DK mode using MC sample for stream 3 with corrected $q\bar{q}$ NB' shape. The ΔE distributions for $B\overline{B}$ enhanced ($1 < NB' < 5$), $q\bar{q}$ enhanced ($-10 < NB' < 0$) are shown from (a) to (b). NB' distributions for $B\overline{B}$ enhanced ($-0.1 < \Delta E < -0.05$), $q\bar{q}$ enhanced ($\Delta E > 0.1$), $D\pi$ peak enhanced ($0.03 < \Delta E < 0.07$) are shown from (c) to (e).

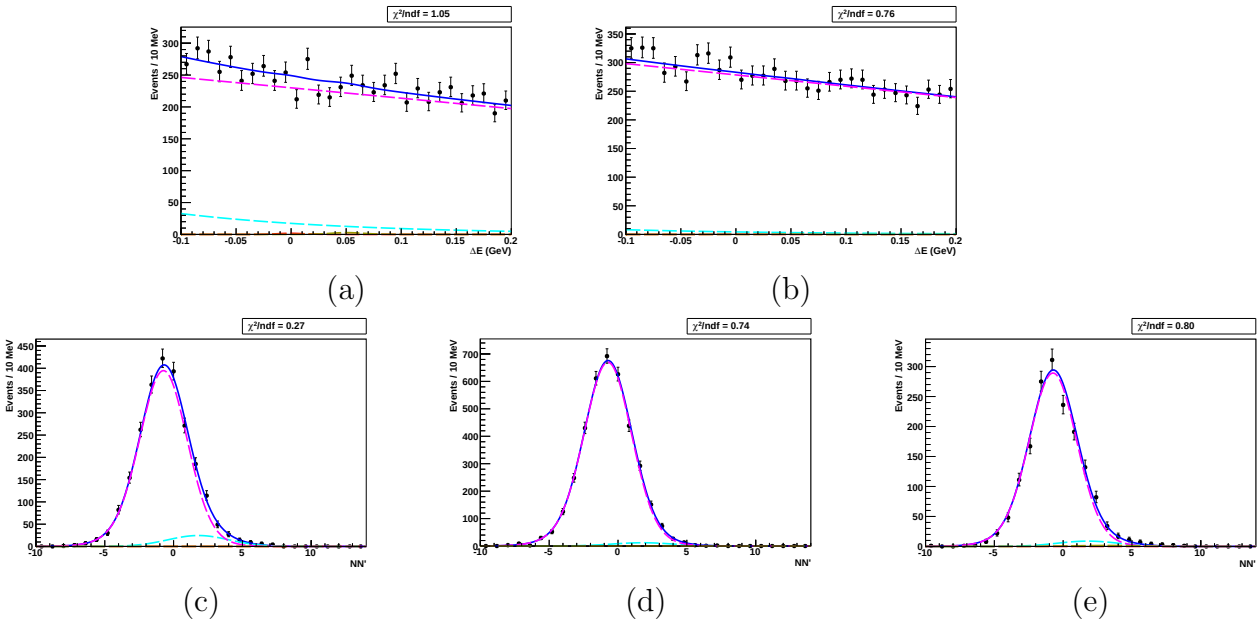

Figure C.10: The projections for suppressed DK mode using MC sample for stream 4 with corrected $q\bar{q}$ NB' shape. The ΔE distributions for $B\overline{B}$ enhanced ($1 < NB' < 5$), $q\bar{q}$ enhanced ($-10 < NB' < 0$) are shown from (a) to (b). NB' distributions for $B\overline{B}$ enhanced ($-0.1 < \Delta E < -0.05$), $q\bar{q}$ enhanced ($\Delta E > 0.1$), $D\pi$ peak enhanced ($0.03 < \Delta E < 0.07$) are shown from (c) to (e).

Bibliography

[1] CKMfitter Group (J. Charles *et al.*), Eur. Phys. J. **C 41**, 1-131 (2005).

[2] D. Atwood, I. Dunietz and A. Soni, Phys. Rev. D **63**, 036005 (2001).

[3] M. Nayak *et al.* (Belle Collaboration), Physical Review D. **88**, 091104(R) (2013).

[4] M. Nayak *et al.*, submitted to Phys. Lett. B, arXiv:1410.3964.

[5] S. L. Glashow, Nucl. Phys. **22**, 579 (1961).

[6] A. Salam, 1969, Proc. of the 8th Nobel Symposium on 'Elementary particle theory, relativistic groups and analyticity', Stockholm, Sweden, 1968, edited by N. Svartholm, p.367-377.

[7] S. Weinberg, Phys. Rev. Lett. **19**, 1264 (1967).

[8] K. A. Olive *et al.* (Particle Data Group), Chin. Phys. C, **38**, 090001 (2014).

[9] T. D. Lee, Chen-Ning Yang, Phys. Rev. **104**, 254-258 (1956).

[10] J. M. Christenson *et al.*, Phys Rev. Lett. **13**, 138 (1964).

[11] N. Cabibbo, Phys. Rev. Lett. **10**, 531 (1963).

[12] M. Kobayashi and T. Maskawa, Prog. Theor. Phys. **49**, 652 (1973).

[13] L. Wolfenstein, Phys Rev. Lett. **51**, 1945 (1983).

[14] M. Gronau and D. London, Phys. Lett. B **253**, 483 (1991); M. Gronau and D. Wyler, Phys. Lett. B **265**, 172 (1991).

[15] A. Giri, Yu. Grossman, A. Soffer, and J. Zupan, Phys. Rev. D68, 054018 (2003).

[16] Matteo Rama, Phys. Rev. D**89**, 014021 (2014).

[17] J. Libby *et al.*, Phys. Lett. **B 731** (2014) 197.

[18] B. Aubert *et al.* (BABAR Collaboration), Phys. Rev. D **76**, 111101 (2007).

[19] J. P. Lees *et al.*(BaBar Collaboration), Phys. Rev. D **84**, 012002 (2011).

[20] A. Bondar and A. Poluektov, Eur. Phys. J. **C 55** (2008) 51, A. Bondar and A. Poluektov, Eur. Phys. **C 47** (2006) 347.

[21] D. Atwood and A. Soni, Phys. Rev. **D 68** (2003) 033003.

[22] B. Aubert *et al.* (BaBar collaboration), Phys. Rev. Lett. **99** (2007) 251801.

[23] M. Gaspero, B. Meadows, K. Mishra and A. Soffer, Phys. Rev. **D 78** (2008) 014015.

[24] B. Aubert *et al.* (BaBar collaboration), Phys. Rev. **D 76** (2007) 011102.

[25] S. Kurokawa and E. Kikutani, Nucl. Instrum. Methods Phys. Res., Sect. A **499**, 1 (2003).

[26] `http://openi.nlm.nih.gov/detailedresult.php?img=3422684_pjab-88-283-g003&req=4`

[27] A. Abashian *et al.* (Belle Collaboration), Nucl. Instrum. Methods Phys. Res., Sect. A **479**, 117 (2002).

[28] `http://legacy.kek.jp/intra-e/press/2009/KEKBluminosity2.html`

[29] `http://www.lns.cornell.edu/public/lab-info/upsilon.html`

[30] G. Alimonti *et al.*, Nucl. Instrum. Methods Phys. Res., Sect. A **453**, 71 (2000).

[31] Y. Ushiroda, Nucl. Instrum. Methods Phys. Res., Sect. A **511**, 6 (2003).

[32] Horii Yasuyuki (2010) *First Evidence of the Suppressed B Meson Decay* $B^- \to DK^-$ *Followed by* $D \to K^+\pi^-$ *and Extraction of the CP-Violating Angle* ϕ_3, PhD theis, Tohoku University.

[33] H. Hirano *et al.*, Nucl. Instrum. Methods Phys. Res., Sect. A **455**, 294 (2000).

[34] T. Iijima *et al.*, Nucl. Instrum. Methods Phys. Res., Sect. A **453**, 321 (2000).

[35] H. Kichimi *et al.*, Nucl. Instrum. Methods Phys. Res., Sect. A **453**, 315 (2000).

[36] `http://sabotin.ung.si/~sstanic/belle/nim/total/node65.html`

[37] H. Ikeda *et al.*, Nucl. Instrum. Methods Phys. Res., Sect. A **441**, 401 (2000).

[38] R. Akhmetshin *et al.*, Nucl. Instrum. Methods Phys. Res., Sect. A **455**, 324 (2000).

[39] A. Abashian *et al.*, Nucl. Instrum. Methods Phys. Res., Sect. A **449**, 112 (2000).

[40] Y. Ushiroda *et al.*, Nucl. Instrum. Methods Phys. Res., Sect. A **438**, 460 (1999).

[41] T. Tsuboyama, Nucl. Instrum. Meth. A **447** (2000) 26.

[42] `http://belle.kek.jp/group/trg/images/trig_gscheme_loi.jpg`

[43] M. Nakao *et al.*, IEEE Trans. Nucl. Sci.**47**, 61 (2000).

[44] D. J. Lange, Nucl. Instrum. Meth. A**462**, 152 (2001).

[45] R. Brun *et al., GEANT 3 : users guide Geant 3.10, Geant 3.11* (CERN-DD-EE-84-01, 1984).

[46] D.J. Lange, *The EvtGen particle decay simulation package*, Nucl. Instrum. Meth. **A 462** (2001) 152.

[47] R. Brun *et al.*, GEANT 3.21, CERN Program Library Long Writeup W5013, unpublished.

[48] Y. Horii *et al.* (Belle Collaboration), Phys. Rev. Lett. **106**, 231803 (2011).

[49] E. Nakano, Nucl. Instrum. Methods Phys. Res. Sect. A **494**, 402 (2002).

[50] M. J. Oreglia, Ph.D. thesis, Report No. SLAC-R-236 (1980); J. E. Gaiser, Ph.D. thesis, Report No. SLAC-R-255 (1982).

[51] G.C. Fox and S. Wolfram, Phys. Rev. Lett. **41**, 1581 (1978).

[52] H. Kakuno *et al.*, Nucl. Instrum. Meth. A **533**, 516 (2004), arXiv:hep-ex/0403022.

[53] M. Feindt and U. Kerzel, Nucl. Instrum. Methods Phys. Res., Sect. A **559**, 190 (2006).

[54] `http://root.cern.ch/root/html/ROOFIT_ROOFIT_Index.html`

[55] `http://root.cern.ch/drupal/`

[56] Y. Horii *et al.* (Belle Collaboration), Phys Rev. D **78**, 071901(R) (2008)

[57] D. Atwood and A. Soni, Phys Rev. D **68**, 033003 (2003).

[58] Y. Amhis *et al.* (HFAG), arXiv:1207.1158, online updates at http://www.slac.stanford.edu/xorg/hfag. update.

[59] `http://www.lns.cornell.edu/public/CLEO/spoke/CLEOc/ProjDesc.html`

[60] `http://www.lepp.cornell.edu/Research/CESR/WebHome.html`

[61] `http://www.classe.cornell.edu/Research/CLEO/Detector.html`

[62] D. Peterson *et al.* (CLEO collaboration), Nucl. Instrum. Meth. A **409**, 204 (1998).

[63] D. Peterson *et al.* (CLEO collaboration), Nucl. Instrum. Meth. A **478**, 142 (2002).

[64] M. Artuso *et al.* (CLEO collaboration), Nucl. Instrum. Meth. A **554**, 147 (2005).

[65] M. Artuso *et al.* (CLEO collaboration), Nucl. Instrum. Meth. A **461**, 545 (2001).

[66] E. Blucher *et al.* (CLEO collaboration), Nucl. Instrum. Meth. A **249**, 201 (1986).

[67] D.J. Lange, *The EvtGen particle decay simulation package*, Nucl. Instrum. Meth. **A 462** (2001) 152.

[68] R. Brun *et al.*, GEANT 3.21, CERN Program Library Long Writeup W5013, unpublished.

[69] D.M. Asner *et al.* (CLEO collaboration), Phys. Rev. **D 78** (2008) 012001.

[70] Q. He *et al.* (CLEO Collaboration), Phys. Rev. Lett. **100** (2008) 091801.

[71] T.Skwarnicki, Ph.D Thesis, DESY F31-86-02(1986), Appendix E.

[72] H. Albrecht *et. al* (ARGUS Collaboration), Phys. Lett. **B 340** (1994) 217.